

AN HVDC OFF-SHORE WIND GENERATION SCHEME WITH HIGH VOLTAGE
HYBRID GENERATOR

AN HVDC OFF-SHORE WIND GENERATION SCHEME WITH HIGH VOLTAGE
HYBRID GENERATOR

BY

Omid Beik, B.Sc., M.Sc.

A Thesis Submitted to the School of Graduate Studies in Partial Fulfilment of the
Requirements for the Degree of Doctor of Philosophy

McMaster University

February 2016

McMaster University DOCTOR OF PHILOSOPHY (Electrical Engineering), Hamilton,
Ontario, 2016.

TITLE: An HVDC Off-shore Wind Generation Scheme with
High Voltage Hybrid Generator

AUTHOR: Omid Beik
B.Sc. (Yazd University)
M.Sc. (Shahid Beheshti University, Abbaspour School
of Engineering)

SUPERVISOR: Dr. Nigel Schofield

NUMBER OF PAGES: xxx, 292

Abstract

This thesis proposes a high voltage DC generation system for off-shore wind applications. The proposed scheme consists of a high voltage (HV) hybrid generator, a passive rectifier, DC/DC converters and HVDC interconnection and transmission. The HV hybrid generator prime mover is a wind turbine that may incorporate a gear-stage or be a direct drive system. Mathematical models for the wind turbine operation are extracted from published literature and verified via comparisons with published commercial wind turbine characteristics. Two regions of operation for the wind turbine are proposed; a limited speed region and a high speed operation region. In the high speed region, the turbine rotor operates above the nominal speed and hence machine torque is reduced for a constant generated power output. This operating region would necessitate detailed aerodynamic and mechanical design of the turbine system which is out of the scope of this thesis. However, the operating principals are explored to study the operational implication of this mode on the HV hybrid generator design. The detailed machine design study focusses on the limited speed region which is current industry practice for wind turbine control and operation.

The proposed wind generation scheme is studied and compared with a commercial off-shore wind system installed in the UK. The analyses are carried out considering system steady-state operation for full-, three-quarter-, half- and one-quarter loads to identify the system envelope specification requirements, key technology gaps, benefits and system performance and deduce component ratings. Dynamic analysis is not addressed in this thesis. The proposed system results in higher efficiency, lower mass for the turbine power-train and also interconnection and transmission cables. However, of greater significance is the reduction in power conversion plant at the turbine a feature that could reduce cost and improve system reliability. Specifically, the active power electronic converters and turbine transformer used in existing commercial systems are eliminated in the proposed system, therefore system complexity and component count are reduced.

The proposed system offers a variable controlled voltage to the local wind farm interconnection and a fixed voltage for transmission through variable step-ratio DC/DC

converters. The proposed hybrid generator is a high voltage machine with two rotor components namely a wound field (WF) rotor and a permanent magnet (PM) rotor. The PM rotor provides a fixed voltage at a given fixed speed while the DC wound field adjusts the machine total output voltage within a specified range. Therefore, the machine output voltage is actively controlled to a desired level as the generator rotor speed varies during normal wind speed variations. Both rotors share a common stator wound with 9-phase distributed winding. It is shown that the 9-phase machine results in higher output voltage and hence it is more power dense when compared to a 3-phase machine. The hybrid generator design is based on an industrial high voltage machine, test results from which provides verification of the proposed design feasibility. Performance of the HV hybrid generator when connected via a passive rectifier is compared to the case when the machine is connected via a voltage source converter with pulse width modulation (PWM) current and over-modulated voltage control schemes.

Two designs for the HV hybrid generator are proposed; a surface PM rotor and an embedded PM rotor design. The DC wound field rotor design is the same in both designs. Finite element analysis (FEA) is used to study the machine electro-magnetic performance and MATLAB Simulink to process the results data. Machine losses including copper, windage and friction are calculated while the iron losses are predicted analytically from the machine field solution information and materials characteristics.

Different insulation systems for the HV winding are studied based on commercial high voltage winding practice with the conclusion that the winding scheme is highly practicable.

Acknowledgments

First and foremost, I would like to thank my supervisor, Dr. N. Schofield for his invaluable encouragement, support and guidance. Nigel, without your help the completion of this thesis would have been even more difficult to say the least and I wish you every luck in training up your new students.

I would like to thank members of the Power Conversion Group at The University of Manchester who supported me during the time I was at The University of Manchester.

I would also like to thank staff and faculty members at the Department of Electrical and Computer Engineering, McMaster University for their support.

I would like to thank my friends and colleagues from McMaster University and The University of Manchester for all the fun and support.

Over the course of my Ph.D. studies I have received three McMaster International Excellence Awards, and two Graduate Scholarships. I would like to acknowledge McMaster University and the Natural Sciences and Engineering Research Council of Canada (NSERC) for provision of a NSERC Ph.D. Scholarship for my studies.

Finally, I would like to thank my family and my parents in particular. Their love and support has been much appreciated.

Table of Contents

Abstract.....	iii
Acknowledgments.....	v
Table of Contents.....	vi
List of Figures.....	xi
List of Tables.....	xviii
Nomenclature.....	xxii
Declaration.....	xxx
Chapter 1: Wind Energy Systems.....	1
1.1 Introduction.....	1
1.2 Motivation and Research Contributions.....	6
1.3 Developments in the Wind Generation Systems.....	8
1.4 Thesis Outline.....	15
Chapter 2: Wind Turbine Systems.....	17
2.1 Introduction.....	17
2.2 Wind Turbine Power and the Betz Limit.....	17
2.3 Wind Turbine Power Coefficient.....	23
2.3.1 Tip Speed Ratio.....	23
2.3.2 Mathematical Expression for Wind Turbine Power Coefficient.....	27
2.4 Wind Turbine Operation.....	30
2.4.1 Limited Speed Operation.....	36
2.4.2 High Speed Operation.....	42
2.5 Summary.....	46

Chapter 3: Proposed Wind Generation System	47
3.1 Introduction	47
3.2 Overview of the Walney Off-shore Wind Farm.....	47
3.3 Walney System Component Model.....	52
3.3.1 Induction Generator (IG) Model.....	53
3.3.2 VSC Model	54
3.3.3 Transformer Model	55
3.3.4 AC Cables Model.....	56
3.3.5 DC-link Model.....	57
3.4 Walney System Analysis at Different Loads	61
3.4.1 Full-load Results	61
3.4.2 Results for Three-quarter-, Half- and One-quarter- Load.....	65
3.5 Proposed Off-shore HVDC Wind Generation System.....	71
3.5.1 Hybrid Generator (HG).....	72
3.5.2 Gearbox.....	74
3.5.3 Voltage Control Scenarios	75
3.5.4 DC/DC Converter	76
3.5.5 Turbine Safety Considerations.....	78
3.6 Proposed System Analysis	79
3.6.1 DC Cable Calculations.....	81
3.6.2 Results for Full-, Three-quarter-, Half- and One-quarter- Load.....	83
3.7 Comparison between Proposed system and Walney Wind Farm.....	90
3.8 Summary....	93

Chapter 4: Hybrid Generator (HG) Concept and Benchmark Machine	94
4.1 Introduction	94
4.2 Electric Machines and Converters for Wind Turbines.....	95
4.2.1 Doubly-Fed Induction Generators (DFIGs).....	95
4.2.2 VSC Coupled Induction and Synchronous Generators.....	96
4.2.3 Comparison of Generators	100
4.3 Hybrid Generator (HG) Concept and Prototype	102
4.3.1 Machine Concept	102
4.3.2 HG Prototype Machine and Experimental Test facility.....	104
4.3.3 Simulation Model and Results	107
4.4 High Voltage Benchmark Synchronous Generator (SG)	113
4.4.1 General Details.....	113
4.4.2 Winding Arrangement	118
4.4.3 Magnetic Field Distribution and Flux-density	122
4.4.4 Flux-linkage and Back-EMF.....	126
4.4.5 Torque Calculations	129
4.4.6 Inductances	133
4.4.7 Modelling of Benchmark SG.....	137
4.5 Summary....	141
Chapter 5: Hybrid Generator (HG) Design.....	142
5.1 Introduction	142
5.2 HG Design Philosophies	143
5.2.1 HG Design Philosophy for Limited Speed Region.....	143
5.2.2 HG Design Philosophy for High Speed Region	146

5.3	Design of 3-phase HG with 100% Wound Field (WF).....	148
5.3.1	Generator Connected to a Passive Rectifier.....	148
5.3.2	Generator Connected to a VSC.....	153
5.4	Design of 9-phase HG with 100% Wound Field (WF).....	159
5.4.1	Comparison of 3-phase and 9-phase Machines	165
5.4.2	Generator Connected to a Passive Rectifier.....	169
5.5	Design of HG PM Rotor with NdFeB Surface Magnets	175
5.5.1	Sintered NdFeB Characteristics	175
5.5.2	Flux-linkage, Back-EMF and Torque	183
5.5.3	Inductances	188
5.6	Design of HG PM Rotor with Ferrite Embedded Magnets.....	191
5.7	Design of HG PM Rotor with NdFeB Embedded Magnets	197
5.7.1	Flux-linkage, Back-EMF and Torque	199
5.7.2	Inductances	204
5.8	Final HG Considerations.....	206
5.8.1	WF and PM Split Ratio.....	209
5.8.2	HG Loss Audit	213
5.9	Summary.....	220
Chapter 6: HG High Voltage Insulation Systems.....		221
6.1	Introduction	221
6.2	Analysis of the Proposed HV System Employing a 6.35 kV HG	222
6.3	HV Winding Types	226
6.4	Insulation Systems.....	229
6.4.1	Strand, Turn and Groundwall Insulation	231

6.4.2	Semiconductive Slot and Voltage Stress Grading Insulation	239
6.4.3	Transposition.....	241
6.5	HG Insulation	243
6.6	Summary....	252
Chapter 7: Conclusions and Future Work.....		253
7.1	Summary and Conclusions.....	253
7.2	Publications.....	257
7.3	Future Work	258
References.....		259
Appendices.....		275
A.1	MATLAB Program: Turbine Power Coefficient.....	275
A.2	MATLAB Program: Turbine Power versus Speed	276
A.3	MATLAB Program: Walney Off-shore Wind Farm Full-load Analysis	278
A.4	MATLAB Program: Proposed Wind Generation Scheme Full-load Analysis	286
A.5	Example of FEA Torque Analysis Coupled with MATLAB Program.....	289

List of Figures

Fig. 1.1. Wind energy conversion.....	2
Fig. 1.2. Main components in an Alstom wind turbine	3
Fig. 1.3. Wind turbine components.....	4
Fig. 1.4. Wind farms	5
Fig. 1.5. Early wind turbines were used by Persians in the Siestan region	8
Fig. 1.6. DOL wind turbines	9
Fig. 1.7. DFIG and power electronic converters.....	10
Fig. 1.8. Wind turbine power-train with fully rated power electronic VSC's	11
Fig. 2.1. Air flow with velocity of v through an area of A	18
Fig. 2.2. Increase in cross-sectional area	19
Fig. 2.3. Turbine power coefficient variation with respect to the ratio of wind velocities before and after the turbine	22
Fig. 2.4. Blade pitch angle	23
Fig. 2.5. Wind turbine power and torque coefficients' curves.....	25
Fig. 2.6. Turbine power and power coefficient for Enercon E-82.....	26
Fig. 2.7. Turbine power coefficient curves	29
Fig. 2.8. Wind turbine power and torque characteristics for $\beta=0$	32
Fig. 2.9. Siemens SWT-3.6-107, 3.6 MW wind turbine power curve with respect to wind velocity.....	33
Fig. 2.10. Turbine power coefficient with respect to wind velocity variations at different rotor speeds for $\beta=0$	34
Fig. 2.11. Turbine power curves with-respect-to wind velocity variations at different rotor speeds (in rad/s) for $\beta=0$	34
Fig. 2.12. Turbine power curves at wind velocity 15 m/s.....	37
Fig. 2.13. Turbine power curves at 19 (m/s).....	37
Fig. 2.14. Turbine power curves at 25 (m/s).....	38
Fig. 2.15. Per unit power and torque characteristics of the wind turbine when operating in Limited Speed region.....	39

Fig. 2.16. Rotor speed for the Limited Speed Operation region.....	40
Fig. 2.17. Per unit power and torque characteristics of the wind turbine when operating in High Speed region.....	44
Fig. 2.18. Rotor speed for the Limited and High Speed Operation regions	45
Fig. 3.1. Walney off-shore wind farm.....	48
Fig. 3.2. Walney wind farm turbine arrangements	49
Fig. 3.3. Walney wind turbine connection to terrestrial grid	51
Fig. 3.4. Walney 1 site layout	52
Fig. 3.5. Walney 1 site layout	53
Fig. 3.6. Balanced, per-phase, steady-state equivalent circuit IG model.....	53
Fig. 3.7. VSC model	55
Fig. 3.8. Balanced, per-phase, steady-state transformer equivalent circuit model	55
Fig. 3.9. Cable balanced, per-phase, steady-state, Pi equivalent circuit model	57
Fig. 3.10. Proposed wind generation scheme with high voltage hybrid generator (HG), HVDC interconnection and HVDC transmission.....	71
Fig. 3.11. Schematic view of the HG.....	73
Fig. 3.12. HG in a wind turbine	73
Fig. 3.13. Example planetary and helical gearbox implementation.....	74
Fig. 3.14. Three-phase, single active bridge (SAB) topology for DC/DC converter	76
Fig. 3.15. Three phase dual active bridge (SAB) topology for DC/DC converter	77
Fig. 3.16. LC circuit based DC/DC converter with Thyristors.....	78
Fig. 3.17. Schematic of proposed system	80
Fig. 4.1. DFIG configuration	95
Fig. 4.2. IG connected to grid via two fully rated VSC.....	96
Fig. 4.3. PM generator connected to grid via two fully rated VSC	97
Fig. 4.4. Direct drive PM and geared DFIG	98
Fig. 4.5. PM generator connected to grid via passive rectifier, DC/DC converter, VSC ..	98
Fig. 4.6. Wound field SG connected to grid via passive rectifier and fully rated VSC.....	99
Fig. 4.7. Hybrid generator (HG) concept.....	103

Fig. 4.8. Prototype HG details	106
Fig. 4.9. HG prototype and test-rig	107
Fig. 4.10. HG MATLAB Simulink.....	108
Fig. 4.11. WF excitation current with respect to DC-link voltage for varying DC-link powers at 3000 RPM.....	108
Fig. 4.12. HG WF current and DC-link voltage variations at 3000 RPM speed	109
Fig. 4.13. HG simulated phase voltage and current, DC-link voltage and current at 3000 RPM for a delivered power of 2 kW.....	111
Fig. 4.14. HG simulated and measured phase voltage and current, DC-link voltage and current at 3000 RPM for a delivered power of 2 kW, point (C).....	112
Fig. 4.15. Front-end cross-section of the benchmark SG	117
Fig. 4.16. Benchmark SG stator tooth/slot details	117
Fig. 4.17. Benchmark SG rotor pole structure	118
Fig. 4.18. Fractional-slot, short-pitched stator winding for the benchmark SG	119
Fig. 4.19. Stator phase coil connections for benchmark SG.....	120
Fig. 4.20. Stator slot showing cross section of coil, conductor and strands	120
Fig. 4.21. Rotor and stator windings.....	121
Fig. 4.22. Rotor coil connections for benchmark SG	121
Fig. 4.23. Benchmark SG field distribution at full field	122
Fig. 4.24. Air-gap flux-density versus rotor electrical angle for two electrical cycles....	123
Fig. 4.25. Stator and rotor sections for flux-density measurement.....	124
Fig. 4.26. Flux-density versus rotor field current for air-gap, back-iron and tooth.....	125
Fig. 4.27. Phase winding open-circuit flux-linkage for benchmark SG at full-field	126
Fig. 4.28. Phase winding open-circuit back-EMF at full-field and nominal rotor speed of 600 RPM.....	128
Fig. 4.29. Phase winding open-circuit back-EMF versus rotor field current.....	129
Fig. 4.30. Benchmark SG cogging torque for the adjusted and constant air-gap rotor topologies.....	130

Fig. 4.31. Benchmark SG torque components at full rotor field current and full-load stator winding currents.....	131
Fig. 4.32. Benchmark SG total torque at full-field and varying load	131
Fig. 4.33. Peak torque variation with-respect-to stator load current.....	132
Fig. 4.34. Benchmark SG total torque at full-load stator current and varying rotor field current	132
Fig. 4.35. Benchmark SG total torque at full-load stator current and varying rotor field current	133
Fig. 4.36. SG synchronous reactance as function of field current	134
Fig. 4.37. Unsaturated phase self-inductance for the benchmark SG.....	136
Fig. 4.38. Benchmark SG connected to 11 kV infinite bus-bar	138
Fig. 4.39. MATLAB model for benchmark SG connected to 11 kV infinite bus-bar	138
Fig. 4.40. Power-angle characteristics for the benchmark SG connected to an infinite bus-bar	139
Fig. 4.41. Benchmark SG back-EMF, phase voltage and current.....	140
Fig. 5.1. Voltage variation of a fully WF (SG) for a turbine operating in the limited speed region	144
Fig. 5.2. Voltage variations for a HG with 75% induced voltage due to PM rotor and 25% induced voltage due to WF rotor for a turbine operating in the limited speed region	145
Fig. 5.3. Voltage variations for a fully WF (SG) for a turbine operating in the high speed region	147
Fig. 5.4. Voltage variations for a HG with PM and WF rotor parts for a turbine operating in the high speed region	147
Fig. 5.5. 3-phase HG WF connected to a passive rectifier	148
Fig. 5.6. MATLAB model for the 3-phase HG WF connected to a rectifier or VSC.....	150
Fig. 5.7. No-load DC-link voltage at the rectifier output.....	150
Fig. 5.8. DC-link power vs. DC-link voltage variations at the rectifier output	152
Fig. 5.9. Phase back-EMF, phase voltage and current for a DC-link voltage of 14 kV and 0.44 p.u. inductance for a 3-phase HG WF connected to a passive rectifier	152

Fig. 5.10. DC-link power and current for a DC-link voltage of 14 kV and 0.44 p.u. inductance for a 3-phase HG WF connected to a passive rectifier	153
Fig. 5.11. Three-phase stator HG WF connected to a VSC.....	154
Fig. 5.12. Phase back-EMF, voltage and current for a 3-phase HG WF connected to a VSC with PWM control, modulation index 0.95, DC-link voltage 14 kV, inductance 0.44 p.u. and load angle 60°	155
Fig. 5.13. DC-link power and current for the same conditions as in Fig. 5.12.....	156
Fig. 5.14. Amplitude of the phase voltage fundamental component variations with respect to modulation index	156
Fig. 5.15. Phase back-EMF, voltage and current for a 3-phase HG WF connected to a VSC with over-modulated control, modulation index 100, DC-link voltage 14 kV, inductance 0.44 p.u. and load angle 60°	157
Fig. 5.16. DC-link power and current for the same conditions as in Fig. 5.15.....	158
Fig. 5.17. DC-link power with respect to load angle for PWM and over-modulated control for 3-phase HG WF connected to VSC, DC-link voltage 14 kV, inductance 0.44 p.u. ..	158
Fig. 5.18. Fractional-slot, short-pitched stator winding for the 9-phase HG WF.....	160
Fig. 5.19. Phase flux-linkage for the HG WF at a full-field current 486.23 A.....	166
Fig. 5.20. Phase back-EMF for the HG WF at a full-field current 486.23 A	166
Fig. 5.21. Phasor diagram for 3-phase winding, 5-set and 4-set pattern.....	167
Fig. 5.22. Phasor diagram for 9-phase winding, 2-set and 1-set patterns	168
Fig. 5.23. Per-phase self-inductance for one phase of the 9-phase HG WF.....	169
Fig. 5.24. Coil representation for 9-phase inductance calculations	169
Fig. 5.25. MATLAB model for the 9-phase HG WF connected to a rectifier.....	172
Fig. 5.26. No-load rectified DC-link voltage for the 3- and 9-phase HG WF.....	172
Fig. 5.27. Phase back-EMF, phase voltage and current for a 9-phase HG WF connected to a passive rectifier and a DC-link voltage of 14 kV.....	174
Fig. 5.28. DC-link power and current for a 9-phase HG WF connected to a passive rectifier and with a DC-link voltage of 14 kV.....	174
Fig. 5.29. B-H characteristic for NdFeB N35H.....	176

Fig. 5.30. Surface PM rotor structure	178
Fig. 5.31. Air-gap flux-density versus magnet thickness for sintered NdFeB surface magnet PM rotor	180
Fig. 5.32. Air-gap flux-density for NdFeB surface magnet PM rotor	181
Fig. 5.33. Field distribution for NdFeB surface magnet PM rotor	181
Fig. 5.34. Demagnetizing field distribution for NdFeB surface magnet PM rotor	183
Fig. 5.35. Phase winding flux-linkage versus rotor position	185
Fig. 5.36. Phase winding open-circuit back-EMFs.....	185
Fig. 5.37. Cogging torque waveforms	187
Fig. 5.38. Electromagnetic torque at full-load peak stator current 170.67 A for 9-phase and 512 A for 3-phase, and rotor field current 486.23 A for the HG WF	187
Fig. 5.39. Self- and mutual-inductances for the HG PM with surface magnets	188
Fig. 5.40. B-H characteristic for Ferrite AC-5.....	191
Fig. 5.41. Ferrite magnet arrangement in HG PM ‘high field’ embedded rotor design ..	192
Fig. 5.42. Typical no-load magnetic field distribution for the HG PM with embedded sintered Ferrite magnets.....	193
Fig. 5.43. HG PM average air-gap flux-density with respect to embedded Ferrite magnet size	195
Fig. 5.44. HG PM average air-gap flux-density with respect to number of embedded Ferrite magnet rotor poles.....	196
Fig. 5.45. No-load flux distribution for HG PM with embedded NdFeB rotor design....	198
Fig. 5.46. No-load air-gap flux-density with respect to rotor electrical angle for the HG PM embedded NdFeB rotor design	198
Fig. 5.47. Per-phase flux-linkage for the 9-phase HG WF, 9-phase HG PM with surface NdFeB magnets and 9-phase HG PM with embedded NdFeB magnets	200
Fig. 5.48. Per-phase open-circuit back-EMF for the 9-phase HG WF, 9-phase HG PM with surface NdFeB magnets and 9-phase HG PM with embedded NdFeB magnets.....	200
Fig. 5.49. Cogging torque (at zero stator current).....	202

Fig. 5.50. Electromagnetic torque at full-load peak stator current of 170.67 A for the 9-phase stator winding	203
Fig. 5.51. Salient and excitation torque components in the 9-phase HG PM with embedded NdFeB	203
Fig. 5.52. Per-phase self-inductance for the HG PM with embedded NdFeB magnets ..	205
Fig. 5.53. HG rotor and stator end winding extension.....	210
Fig. 5.54. Manufacturer's iron loss data for United Laminated Steel	214
Fig. 5.55. Predicted versus manufacturer's datasheet iron loss density.....	216
Fig. 6.1. Stator winding connections	226
Fig. 6.2. A Random-wound stator.....	228
Fig. 6.3. A form-wound coil	228
Fig. 6.4. A typical Roebel bar winding.....	228
Fig. 6.5. Three-phase benchmark SG or HG WF slot insulation system.....	230
Fig. 6.6. 3-phase HG WF strand voltage	232
Fig. 6.7. 3-phase benchmark SG (or HG WF) turn and phase voltages	234
Fig. 6.8. AB Powerformer stator slots	234
Fig. 6.9. Lumped capacitance model between strands and grounded stator core.....	236
Fig. 6.10. Groundwall-to-grounded stator core model with an air pocket.....	237
Fig. 6.11. Coil-to-coil capacitor core model	238
Fig. 6.12. Coil capacitor model along the HG axial length	238
Fig. 6.13. Semiconductive resistance and air gap capacitor model	239
Fig. 6.14. Semiconductive, stress grading and groundwall insulations for the 3-phase HG WF stator coil.....	240
Fig. 6.15. Coil transposition.....	242
Fig. 6.16. Coil transposition via knuckle	242
Fig. 6.17. Coil cross-section for 3-phase SG and 9-phase HG	244
Fig. 6.18. Coil cross-section for 13.2 kV, 26.4 kV and 38.1 kV HG.....	249
Fig. 6.19. Stator cross-sectional view for different HG winding designs.....	250

List of Tables

Table 2.1. Operational parameters for the Siemens SWT-3.6-107, 3.6 MW turbine	33
Table 3.1. Summary of Walney wind farm summary of details.....	49
Table 3.2. Details of Siemens SWT-3.6-107 wind turbine.....	50
Table 3.3. Induction generator (IG) parameters.....	54
Table 3.4. Transformer parameters at 50 Hz	56
Table 3.5. Cable equivalent circuit parameters at 50 Hz	57
Table 3.6. DC-link calculations	60
Table 3.7. Walney 1, full-load analysis results: voltages and currents.....	62
Table 3.8. Walney 1, full-load analysis results: power and losses	63
Table 3.9. Walney 1, three-quarter-load analysis results: voltages and currents.....	65
Table 3.10. Walney 1, three-quarter-load analysis results: power and losses	66
Table 3.11. Walney 1, half-load analysis results: voltages and currents	67
Table 3.12. Walney 1, half-load analysis results: power and losses.....	68
Table 3.13. Walney 1, one-quarter-load analysis results: voltages and currents.....	69
Table 3.14. Walney 1, one-quarter-load analysis results: power and losses.....	70
Table 3.15. Proposed system cables specifications	83
Table 3.16. Proposed system full-load analysis.....	84
Table 3.17. Rotor speed, HG voltage and DC/DC converter ratio at different loads	85
Table 3.18. Proposed system three-quarter-load analysis.....	86
Table 3.19. Proposed system half-load analysis	87
Table 3.20. Proposed system one-quarter-load analysis.....	88
Table 3.21. Comparison between Walney and proposed system.....	91
Table 3.22. Mass comparison	92
Table 4.1. Comparison of different generators for wind turbine application as reported in [56] and the benchmark HV Siemens generator used in this study	101
Table 4.2. HG prototype and brushless exciter specifications.....	105

Table 4.3. Comparison of simulated and measured results for HG prototype at different DC-link voltage, 3000 RPM and delivering 2 kW	110
Table 4.4. Benchmark SG specifications	114
Table 4.5. Benchmark SG dimensions.....	115
Table 4.6. Walney wind farm IG specifications	116
Table 4.7. Flux-density for different machine sections	123
Table 4.8. Flux-density for different field currents.....	125
Table 4.9. Phase winding open-circuit back-EMF for different rotor field currents	128
Table 4.10. Benchmark SG inductances and resistance	137
Table 4.11. Comparison between benchmark SG simulated results and datasheet	140
Table 5.1. DC-link and machine voltages for the 3-phase HG WF connected to a passive rectifier	151
Table 5.2. Maximum DC-link power for the 3-phase HG WF connected to a passive rectifier and VSC	159
Table 5.3. 9-phase winding specifications for the HG WF.....	163
Table 5.4. Rotor field winding specifications for the HG WF.....	165
Table 5.5. RMS and peak voltages for 3- and 9-phase HG WF at full-field of 486.23 A and 600 RPM.....	167
Table 5.6. Comparison of three-phase and nine-phase machines at an average DC-link voltage of 14 kV.....	173
Table 5.7. Neodymium-Iron-Boron magnet N35H properties at 80 °C	177
Table 5.8. Magnet thickness and average air-gap flux-density for NdFeB surface magnet PM rotor	180
Table 5.9. Flux-density for different sections for NdFeB surface magnet PM rotor.....	182
Table 5.10. Sintered NdFeB magnet dimensions for the surface magnet PM machine ..	184
Table 5.11. Inductances for the HG PM with surface magnets	190
Table 5.12. Ferrite magnet AC-5 properties at 80 °C	192
Table 5.13. Magnet size and average air-gap flux-density for the HG PM with embedded sintered Ferrite PM rotor.....	195

Table 5.14. Average air-gap flux-density for the HG PM with embedded PM rotor and different number of poles (Ferrite length 670.968 mm and thickness 40 mm)	196
Table 5.15. Average air-gap flux-density for the HG PM with different rotor designs (for all designs magnet length is 670.968 mm, and thickness 40 mm).....	199
Table 5.16. Flux-density for different sections for the HG PM with NdFeB magnets....	199
Table 5.17. RMS and peak voltages for 9-phase HG with various rotors	202
Table 5.18. Peak cogging and total torque for different designs	202
Table 5.19. Peak salient, excitation and total torque for different designs	204
Table 5.20. HG PM with embedded NdFeB inductances	205
Table 5.21. Main machine specifications at 5.75 MW	208
Table 5.22. Main machine specifications at 3.6 MW	208
Table 5.23. Specification details for the HG Designs.....	210
Table 5.24. HG wound field rotor winding specifications.....	211
Table 5.25. HG stator winding specifications.....	212
Table 5.26. HG per-phase stator equivalent synchronous inductance	212
Table 5.27. HG copper, friction and windage losses at nominal speed, full-load RMS stator current and rotor full-field DC current.....	213
Table 5.28. Constants of the loss coefficients.....	216
Table 5.29. Flux-density for different sections for the HG.....	217
Table 5.30. Volume and mass audit of the HG designs.....	218
Table 5.31. HG iron losses.....	219
Table 5.32. HG total losses	219
Table 6.1. Proposed system cable specifications with a 6.35 kV HG	222
Table 6.2. Proposed system full-load analysis with a 6.35 kV HG	223
Table 6.3. Comparison between system with a 6.35 kV HG and with a 38.1 kV HG at full-load.....	224
Table 6.4. Turn, coil and strand voltages.....	232
Table 6.5. Strand-to-groundwall capacitors parametric values	236
Table 6.6. RMS phase, coil, turn and strand voltage	244

Table 6.7. Coil, turn and strands for 9-phase HG with phase RMS voltage 6.6 kV.....	246
Table 6.8. Voltage scaling steps for the 9-phase HG.....	247
Table 6.9. HG coil and turn insulations	251

Nomenclature

Symbol	Meaning	Unit
DAB	Dual Active Bridge	-
DFIG	Doubly-fed Induction Generator	-
DOL	Direct Online	-
EMF	Electromotive force	V
FEA	Finite Element Analysis	-
GB	Gear Box	-
HG	Hybrid Generator	-
HS	High Speed	-
HV	High Voltage	-
HVDC	High Voltage DC	-
IG	Induction Generator	-
IGBT	Insolated-Gate Bipolar Transistor	-
MPPT	Maximum Power Point Tracking	-
NdFeB	Neodymium-Iron-Boron	-
O.C.	Open Circuit	-
PD	Partial Discharge	-
PM	Permanent Magnet	-
PWM	Pulse Width Modulation	-
RMS	Root Mean Square	-
RPM	Revolution per Minuet	-
SAB	Single Active Bridge	-
SG	Synchronous Generator	-
SRC	Series Resonant Circuit	-
ZCS	Zero Current Switching	-
VSC	Voltage Source Converter	-

WF	Wound Field	-
PMG	Permanent Magnet Generator	-
U	Energy in an air parcel	Joules (J)
P_w	Wind power	W
P_t	Turbine power	W
\dot{m}	Mass flow	kg/s
F	Force that the air exerts on wind turbine	N
C_p	Turbine power coefficient	p.u.
C_p^{\max}	Maximum turbine power coefficient	p.u.
T_t	Turbine torque	N.m
C_τ	Turbine torque coefficient	p.u.
β	Turbine blade pitch angle	Degrees
λ	Blade tip speed ratio	p.u.
u	Tangential velocity of the blade tip	m/s
$c_1, c_2, c_3, c_4, c_5, c_6$	Constants in turbine power coefficient equation	p.u.
$P_{nominal}$	Rated turbine power	MW
v_{cut-in}	Turbine cut-in velocity	m/s
v_{rated}	Turbine rated velocity	m/s
$v_{cut-out}$	Turbine cut-out velocity	m/s
λ_{opt}	Optimum blade tip speed ratio	p.u.
ω_{cut-in}	Rotor speed at cut-in wind velocity	rad/s
ω_b	Rotor rated speed	rad/s
$\omega_{cut-out}$	Highest rotor speed	rad/s
R_1	Stator resistance	Ω
R_2	Rotor resistance referred to stator	Ω
R_c	Loss resistance	Ω

X_m	Magnetizing reactance	Ω
X_1	Stator leakage reactance	Ω
X_2	Rotor leakage reactance referred to stator	Ω
R_T	Transformer equivalent resistance referred to primary	Ω
X_T	Transformer equivalent leakage reactance referred to primary	Ω
a	Transformer ratio	
V_{dc1}	Walney DC-link voltage at Converter 1 terminals	V
m_{a1}	Amplitude modulation index for Converter 1 in Walney	p.u.
V_{L1}	IG RMS line-to-line voltage	V
$\hat{V}_{control}$	Amplitude of control signal	V
\hat{V}_{tri}	Amplitude of carrier signal	V
ω_{gen}	IG operating speed	rad/s
ω_{max}	IG maximum speed	rad/s
I_{dc}	Walney DC-link current	A
P_{dc1}	Walney input power to the DC-link	MW
A_{dc}	Walney DC-link cable cross-section area	mm ²
J_{dc}	Walney DC-link cable current density	A/mm ²
R_{dc}	Walney DC-link cable resistance	m Ω
ρ_{cu}	Copper resistivity	$\mu\Omega\text{m}$
l_{dc}	Walney DC-link cable length	m
$P_{loss-dc}$	Walney DC-link power loss	kW
V_{dc2}	Walney DC-link voltage at Converter 2 terminals	V
ΔV_{dc}	DC-link voltage drop	V

n_t	Turns (transfer) ratio of the DC/DC	p.u.
\hat{V}_{ph}	Machine peak phase voltage	V
J_{ac}^{array}	Walney inter-array cable current	A/mm ²
I_{ac}^{array}	Walney inter-array cable current	A
A_{ac}^{array}	Walney inter-array cable cross-section area	mm ²
$I_{dc}^{turbine}$	Proposed system individual turbine current	A
$P_{turbine}$	Turbine power	MW
I_{dc}^{array}	Proposed system inter-array cable current	A
A_{dc}^{array}	Proposed system inter-array cable cross-section area	mm ²
A_{dc}^{tower}	Proposed system turbine cable cross-section area	A/mm ²
$J_{ac}^{circuit}$	Walney transmission cable current density	A/mm ²
$I_{ac}^{circuit}$	Walney Circuit 2 cable current	A
$A_{ac}^{circuit}$	Walney Circuit 2 cable cross-section area	mm ²
$A_{dc}^{circuit}$	Proposed system Circuit 2 cable cross-section area	mm ²
$I_{dc}^{circuit}$	Proposed system Circuit 2 cable current	A
J_{ac}^{trans}	Walney transmission cable current density	A/mm ²
I_{ac}^{trans}	Walney transmission cable current	A
A_{ac}^{trans}	Walney transmission cable cross-section area	mm ²
A_{dc}^{trans}	Proposed system transmission cable cross-section area	mm ²
I_{dc}^{trans}	Proposed system transmission cable current	A
V_{cable}	Cable volume	m ³
δ_{cu}	Copper density	kg/m ³
ϕ	Machine phase flux linkage per turn	Wb
θ_e	Rotor electrical angle	rad or deg.

ω_e	Machine electrical rotor speed	rad/s
ω_m	Machine mechanical rotor speed	rad/s
n	Machine rotor speed	RPM
L_a, L_b, L_c	Phase inductances for phase A, B and C respectively for 3-phase system	mH
M_{ab}, M_{ac}, M_{bc}	Mutual inductances between phases for 3-phase system	mH
L_0	Average phase self-inductance	mH
L_2	Phase inductance amplitude variations above average for 3-phase system	mH
L_d	Machine d-axis inductance	mH
L_q	Machine q-axis inductance	mH
L_s	Machine synchronous inductance	mH
k_s	Saturation factor	p.u.
I_{f_rated}	Field current at rated stator load current	A
I_{f_lin}	Field current that produces rated back-EMF on the linear air-gap characteristic	A
E_{lin}	Back-EMF produced by rated rotor field current on the air-gap linear characteristic	kV
E_{rated}	Rated back-EMF	kV
L_{ss}	Saturated inductance	mH
L_{su}	Unsaturated inductance	mH
V_{dc}^{ave}	Rectified average DC-link voltage	V
V_{LL}^{rms}	RMS line-to-line voltage	V
\hat{V}_{ctrl}	Control signal amplitude	V
$\hat{V}_{saw-tooth}$	Carrier signal amplitude	V
$R_{turn}^{9\phi}$	9-phase phase resistance	Ω
l_{turn}	Length of a turn in a stator coil	mm

A_{turn}	Cross section of a turn in a stator coil	mm^2
l_a	Machine active axial length	mm
$R_{coil}^{9\phi}$	9-phase coil resistance	Ω
N_{stator}	Number of turns in stator coil	p.u.
$l_{interconnection}$	Stator winding interconnection length	Mm
$R_{interconnection}^{9\phi}$	9-phase winding interconnection resistance	Ω
$R_{ph}^{9\phi}$	9-phase per phase winding resistance	Ω
α_T	Temperature coefficient of resistance	$^{\circ}\text{C}^{-1}$
R_{turn}^{rotor}	Rotor winding turn resistance	Ω
l_{turn}^{rotor}	Length of a turn in a rotor coil	mm
A_{turn}^{rotor}	Cross section of a turn in a rotor coil	mm^2
l_w^{poles}	Width of rotor pole	mm
R_{coil}^{rotor}	Rotor coil resistance	Ω
N_{rotor}	Number of turns in a rotor coil	p.u.
$R_{interconnection}^{rotor}$	Rotor winding interconnection resistance	Ω
$l_{interconnection}^{rotor}$	Rotor winding interconnection length	mm
R_{rotor}	Rotor winding resistance	Ω
L_i	Self-inductance for phase i (i = 1, ..., 9)	mH
M_{ij}	Mutual inductance between phase i and j (i = 1, ..., 9 and j = 1, ..., 9)	mH
L_0^9	Average phase inductance for the 9-phase winding	mH
\bar{L}_g^9	Phase inductance amplitude variations above average for the 9-phase winding	mH
μ_r	Magnet relative permeability	p.u.
μ_0	Vacuum permeability	H/m
B_r	Remanence	T
H_c	Coactivity	kA/m

H_{lim}	Magnetic intensity demagnetization limit	kA/m
B_{lim}	Flux-density demagnetization limit	T
σ_m	Magnet electrical conductivity	MS/m
B_m	Magnet flux-density	T
l_g	Air-gap thickness (length)	mm
l_m	Magnet length	mm
l_m^{\min}	Magnet minimum thickness	mm
L_i^{PMs}	Self-inductance for i^{th} phase for the HG PM with surface magnets	mH
M_{ij}^{PMs}	Mutual inductance between phases i and j for the HG PM with surface magnets	mH
L_s^{PMs}	The synchronous inductance for the HG PM with surface magnet	mH
L_{self}^{PMe}	Phase self-inductance for HG PM with embedded NdFeB magnets	mH
L_0^{PMe}	Average phase inductance for HG PM with embedded NdFeB magnets	mH
L_2^{PMe}	Phase inductance amplitude variations above average for HG PM with embedded NdFeB magnets	mH
L_d^{PMe}	d-axis inductance for HG PM with embedded NdFeB magnets	mH
L_q^{PMe}	q-axis inductance HG PM with embedded NdFeB magnets	mH
L_s^{PMe}	The synchronous inductance for the HG PM with surface magnet	mH
Q	Electric loading	A/mm
B_{ave}	Air-gap average flux-density (magnetic loading)	T

P_{cu}^s	Stator winding copper loss	kW
P_{cu}^r	Rotor winding copper loss	kW
I_s	Stator RMS full-load phase current	A
I_r	Rotor DC field current at full-load	A
P_{iron}^d	Iron loss density	W/kg
k_e, k_h, k_a, k_d	Frequency dependent loss-coefficients	p.u.
$a_{ei}, a_{hi}, a_{ai}, a_{di}$	Constants of the loss coefficients where $i=0,1,2$	p.u.
ϵ	Insulating material permittivity	F/m
ϵ_r	Insulating material relative permittivity	p.u.
ϵ_0	Air permittivity	F/m
C_s	Strand insulation capacitor	μF
C_c	Conductor insulation capacitor	μF
C_g	Groundwall insulation capacitor	μF
C_{air}	Air pocket capacitor	μF
C_{sep}	Insulating slot separator capacitor	μF
C_{eqs}	Equivalent capacitor	μF
R_{semi}	Semiconductive resistance	Ω

Declaration

No portion of the work referred to in this thesis has been submitted in support of an application for another degree or qualification of this or any other place of learning.

Chapter 1

Wind Energy Systems

1.1 Introduction

Wind energy systems have been the center of much attention in recent years resulting in many research publications and an increasing number of installed systems by industrial manufacturers, electrical grid operators and utilities [1-7]. Wind energy is a renewable and sustainable source of energy that is environmentally clean with regard to CO₂ production [8]. However, wind energy varies with the wind velocity therefore it needs to be appropriately harvested to be useful [9]. Wind turbines are used to capture the kinetic wind energy and transform it to mechanical energy which is then converted to electrical energy by electrical generators. The flow chart in Fig. 1.1(a) shows a conversion scheme from wind to electrical energy. Basic power conversion train for a wind turbine is presented in Fig. 1.1(b). Wind turbine blades capture the energy in the wind by slowing down wind velocity. This energy is then transferred to the turbine rotor which spins a generator and electrical energy is produced. A gearbox is sometimes used to increase the turbine rotor speed to higher speed for suitable for the generator. If no gearbox is used the turbine generator is called direct drive generator (DDG). Existing turbine power-trains use industrially rated generator technologies such as the induction generator (IG) [4], synchronous generator (SG) [5], doubly fed induction generator (DFIG) [6], and permanent magnet (PM) generator [7] either with or without a gearbox. The turbine hub, shaft and other rotating parts are referred to as wind turbine rotor. Fig. 1.1(c) shows a 2.7 MW commercial wind turbine, ECO 122-2.7 MW, manufactured by Alstom. The turbine

conversion power-train is located at the top of the turbine tower i.e. in the Nacelle. Approximate length, size and mass of main turbine structure for the Alstom ECO 122-2.7 MW is shown in Fig. 1.1(c).

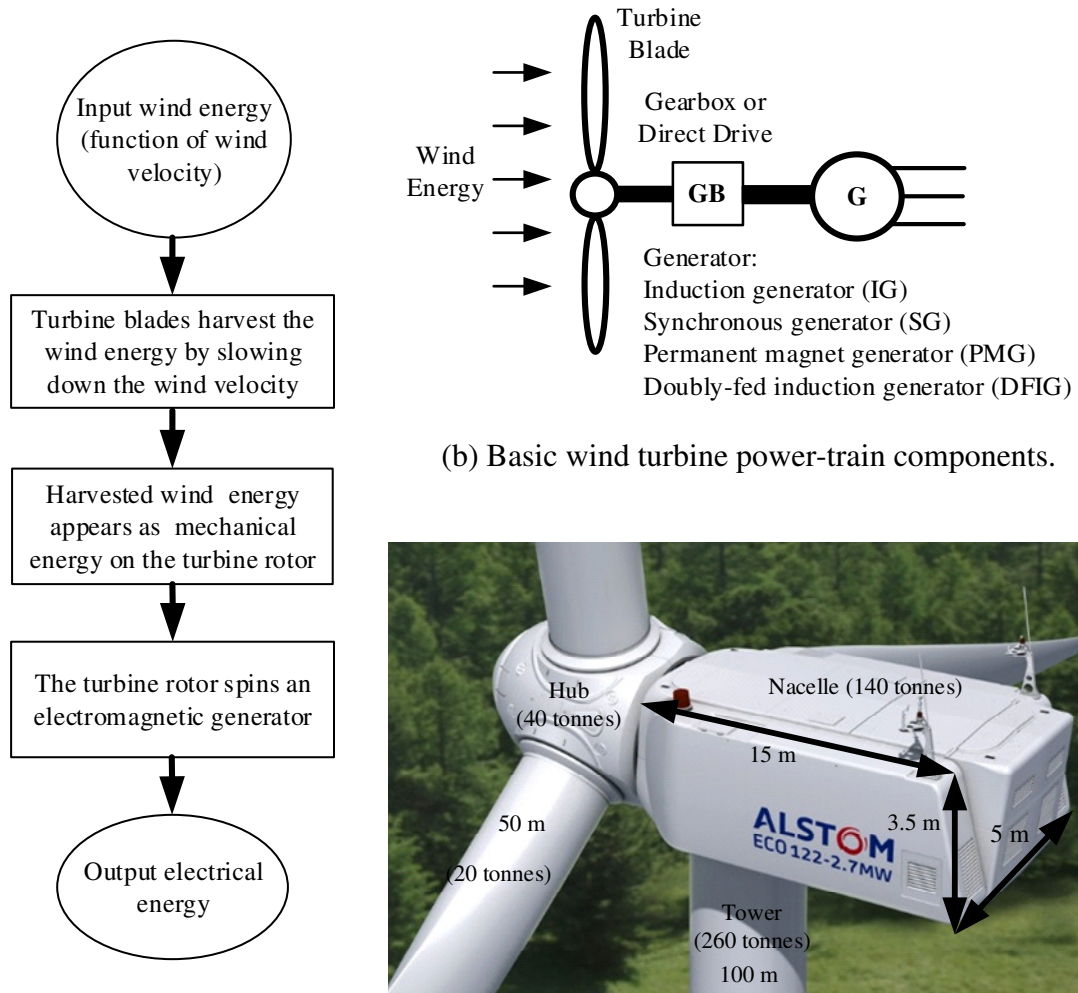


Fig. 1.1. Wind energy conversion.

Modern wind turbines normally have three blades with the capability of changing the angle of the blades with respect to the plane of the rotation of the turbine. This angle is called the pitch angle and is an important parameter in wind turbine control. Fig. 1.2 shows main components inside an Alstom wind turbine.

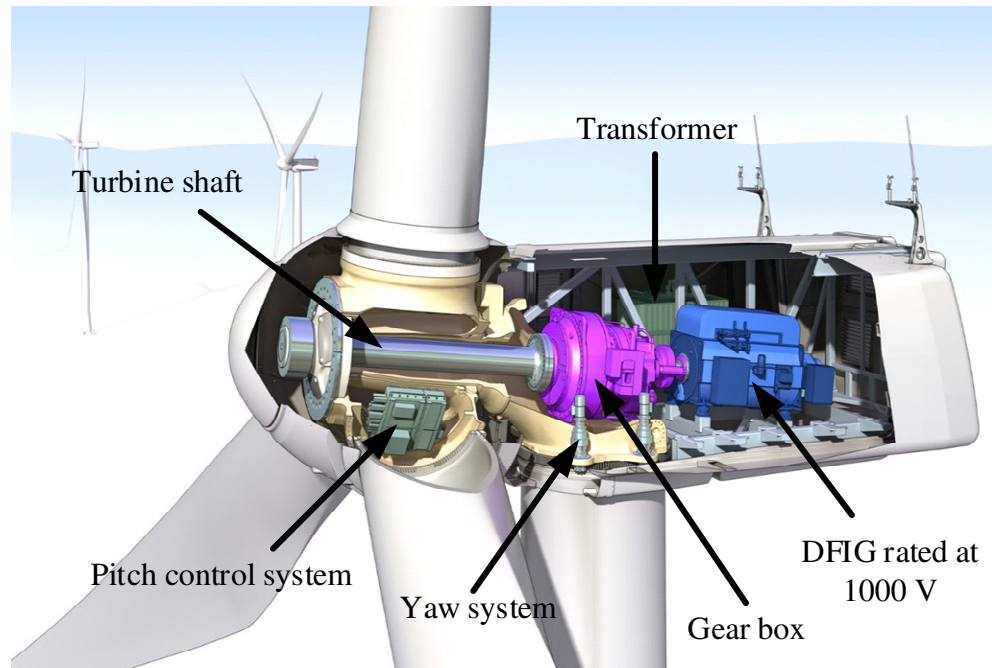
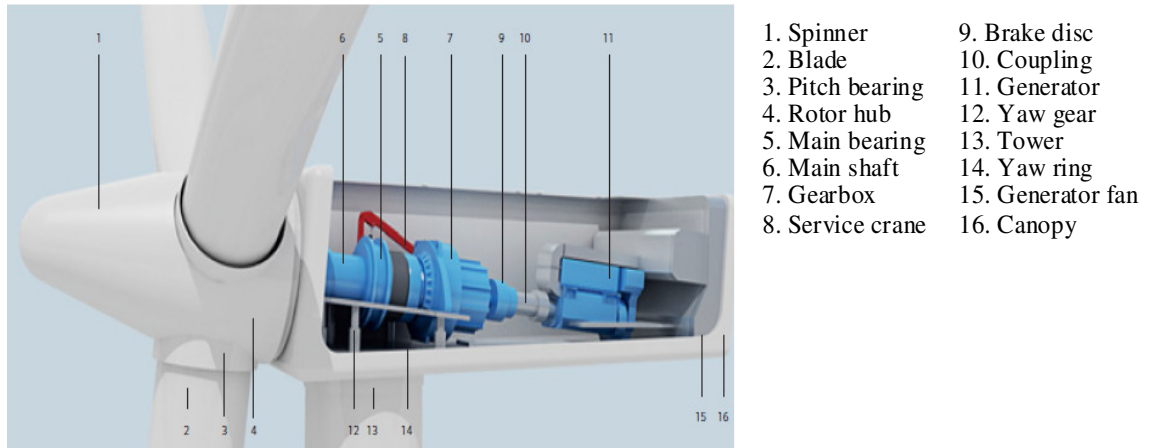


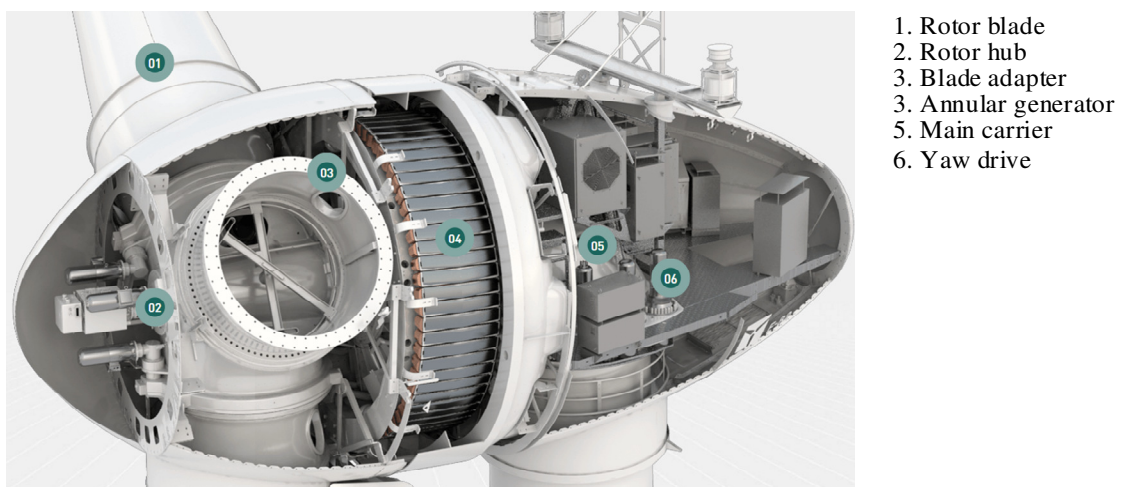
Fig. 1.2. Main components in an Alstom wind turbine [3].

The pitch control system changes the direction that the turbine blades are facing the wind. Therefore, by adjusting the pitch angle of a turbine desired amount of energy is harvested from the wind. At zero pitch angle the blades are fully facing the wind hence maximum wind energy is captured and as the pitch angle increases the energy harvested is reduced. The pitch angle is one of the tools that is used to control the power output of a wind turbine. The yaw control system rotates the turbine top parts (Nacelle, blades and hub) with respect to the turbine tower. In case the wind direction changes the yaw system moves the turbine towards the wind velocity direction or out of it if desired. The generator low output voltage is stepped-up using a transformer to a level suitable for transmission. The turbine transformer is placed at the bottom of the turbine tower in some wind turbines. For the same

power the direct drive generator has usually a bigger diameter than a gearbox coupled generator while its axial length is smaller. Fig. 1.3 compares a 3.6 MW commercial wind turbine with gearbox coupled generator manufactured by Siemens, SWT-3.6-107 3.6 MW, with a 2 MW wind turbine with direct generator manufactured by Enercon.



(a) Siemens SWT-3.6-107 3.6 MW wind turbine [10].



(b) Enercon E-82 2 MW wind turbine [11].

Fig. 1.3. Wind turbine components.

To collect the wind energy in a desired large amount a number of wind turbines are normally clustered in a group and installed at an off-shore or on-shore ‘wind farm’ or ‘wind park’ an example of each is shown in Fig. 1.4.



(a) Brazos on-shore wind farm, US [1].

(b) Walney off-shore wind farm, UK [2].

Fig. 1.4. Wind farms.

There has been concerns about the on-shore wind parks mainly due to turbine noise, visual impacts on the environment in which the turbine is installed [12], harms to birds and also affecting neighboring property prices and limited land [12]. Therefore, much of the work in wind generation systems has shifted towards the off-shore wind installations. In the off-shore locations the wind is usually stronger and steadier hence more power can be captured [12]. However, it is worth noticing that the cost of installations in the off-shore sites is normally higher than that of on-shore farms.

1.2 Motivation and Research Contributions

The author of this thesis has contributed to future wind generation systems by introducing a new off-shore, high voltage DC generating system and a new high voltage generator concept for wind turbine applications. As far as the author is aware there has been no published data on high voltage (HV) generator design (22 kV and above) for wind turbine applications. A major obstacle to this has been the lack of commercially available power electronic switches at high voltage and high power. However, in the proposed system, the active converter is replaced with passive (diode) rectifiers that are commercially available. The novel generator technology proposed in this this thesis is referred to as a hybrid generator (HG). The HG uses two rotor parts, a permanent magnet (PM) and a DC wound field (WF) rotor, hence the hybrid term refers to combination of PM and WF rotors. The PM rotor has a fixed field and induces a fixed voltage into the stator as a function of rotor speed. The WF rotor is fed by a controlled DC current and induces a controlled variable voltage. Therefore, the machine output voltage is controlled over a limited speed range. A major requirement in existing wind generation schemes is that the turbine electrical supply system is required to operate at or near a constant voltage for all wind speed conditions. This is to ensure operation of the back-to-back VSC's and ancillary components in the system including monitoring, measurements and maintenance equipment. However, by controlling the induced voltage due to the WF in the proposed HG, the machine output voltage and hence interconnecting system voltage is allowed to vary but in a controlled manner. To-date HVDC is mainly used for the transmission connections. Elimination of the two back-to-back VSC's that are common in existing wind conversion systems has allowed the author to use HVDC connections for interconnection cables as well as the transmission cables. The proposed system contributes to mass reduction in the turbine Nacelle by using a HV generator and the turbine tower by eliminating the step-up transformer. The proposed system thus offers a much simplified power conversion system for wind generation, in particular the gearbox (GB), low voltage generator, back-to-back VSC's and turbine transformer typical of existing commercial systems are replaced with a HV HG, a gearbox with lower gear ratio, and a passive rectifier. The new power conversion

system for off-shore applications further opens up new research areas. The high voltage, high power DC/DC converters used in the proposed system are an interesting technology that are subject of much research and development effort in the field of HVDC transmission and distribution. Finally, the thesis proposes a new operational region for wind turbines, here referred to as the high speed region, where the turbine rotor speed is allowed to exceed the nominal value, thus resulting in lower torque requirements for the machine in the constant power generation region.

1.3 Developments in the Wind Generation Systems

Early wind mills date back to the year 644 A. D. used by Persians (Iranians) in the today's Persian-Afghan border region of Seistan shown in Fig. 1.5 [9].



Fig. 1.5. Early wind turbines were used by Persians in the Siestan region (Photo courtesy of Google Map).

The early wind mills were used locally for different purposes such as grinding wheat and pumping water but producing electricity [9]. Around 1890s first wind turbines were manufactured to produce electricity using DC generators [9]. Design of wind turbines developed through the years by improved conversion power-train such as mechanics, new generators, power electronics and control systems. One of the early modern wind turbine technology used induction generator directly connected to the grid known as direct online (DOL) [13] as shown in Fig. 1.6. The DOL system was limited in energy conversion and required machine speed control via variable gearbox and blade pitch control. In the DOL IG magnetizing current and reactive current is supplied by local grid. In an improved DOL

connection the reactive power were countered by variable (switched) capacitance connected in parallel to machine terminals.

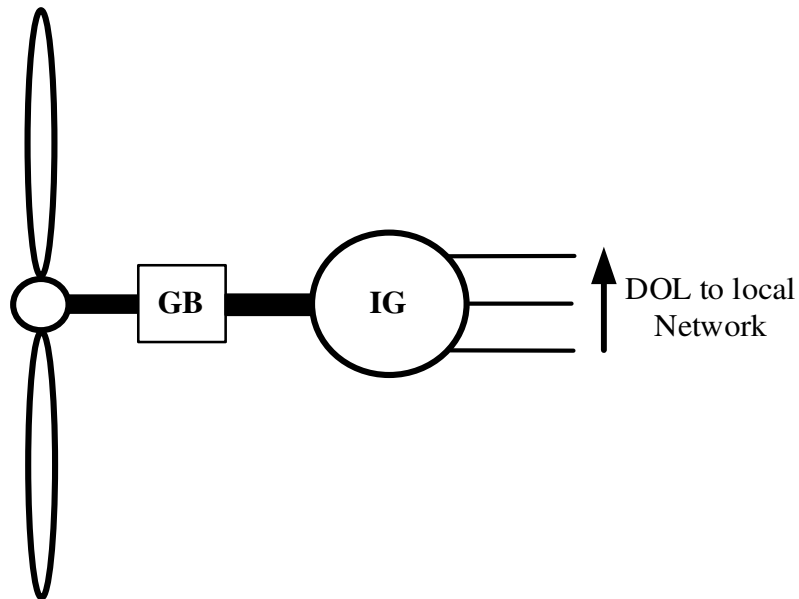


Fig. 1.6. DOL wind turbines.

The DOL systems were later improved using DFIG and power electronic converters shown in Fig. 1.7. The two converters in the scheme presented in Fig. 1.7 are so call connected back-to-back. Each converter typically processes $1/3^{\text{rd}}$ of the rated DFIG power [12]. The two converters decouple the rotor from machine output and allow the variable speed operation of DFIG within limited speed range [12], [14-20]. By injecting a variable frequency and amplitude voltage into the DFIG rotor the machine output voltage and frequency are control to fixed values [14-20].

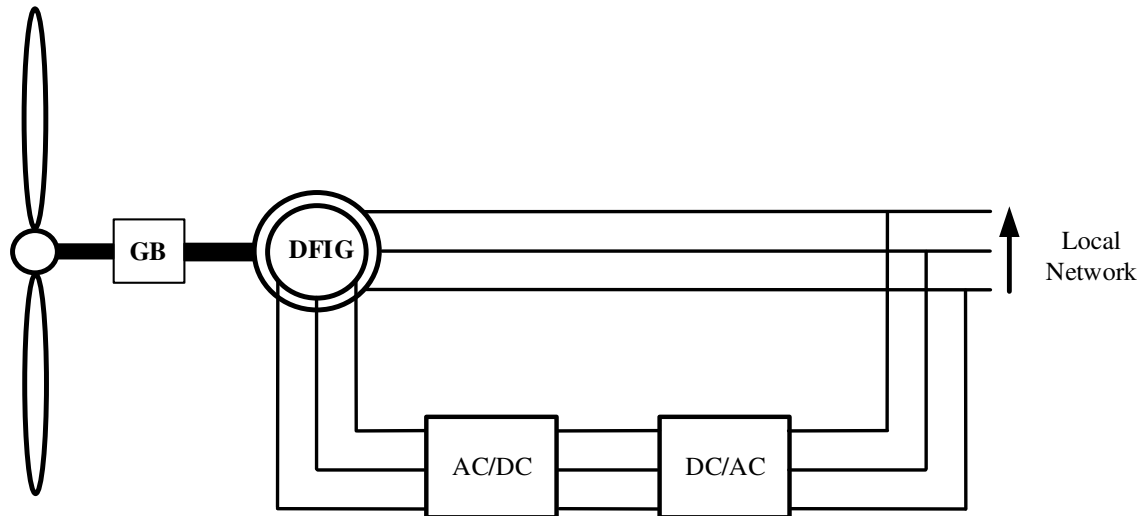


Fig. 1.7. DFIG and power electronic converters.

The wind turbine power-trains based on DFIG are used in the today's systems. However, wind turbine systems with fully rated power electronic converters, shown in Fig. 1.8, are current industry practice for many wind generation systems. The two converters are voltage source converter (VSC) being connected back-to-back. For the current systems the generator is usually an IG, a PM or a SG. Due to varying nature of the wind velocity the generator output voltage amplitude and frequency is variable. The generator side VSC i.e. VSC1 in Fig. 1.8 converts generator variable frequency and voltage amplitude to a fixed DC-link voltage. VSC2 converts DC-link voltage to a fixed frequency and voltage amplitude at the transformer input. The VSC's decouples the generator from the grid, enabling variable speed operation. The DC-link voltage is maintained at its nominal value via grid connected VSC2. The transformer steps-up the voltage to a level suitable for transmission and sent it to the local grid.

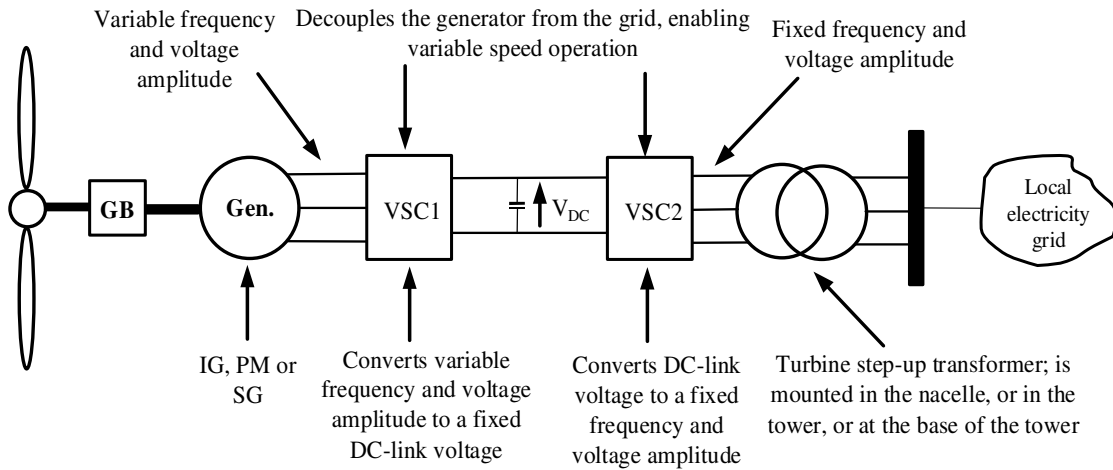


Fig. 1.8. Wind turbine power-train with fully rated power electronic VSC's.

To-date studies have investigated many areas related to wind generation including, but not limited to, the control and stability of wind farms [21-22], power electronic converters for the turbine-generator power-trains [23-25] and DC grids for wind generation [26-34]. Liu et al [21] addresses wind farm stability and control using an impedance-based criterion where the VSC based HVDC transmission is used in an off-shore wind farm. For existing commercial wind generation systems, the aggregated power at the off-shore substation is transmitted to the shore via either high voltage AC (HVAC) or HVDC systems. Above a so called 'break-even distance' HVDC will have lower costs than HVAC systems, providing the same transmission power capacity is considered. However, with existing technologies the HVDC terminal station costs are generally more than those of AC systems [23], although this trend may change in the future with the development of higher voltage and current handling power electronic devices and converters. The choice between HVDC and AC system depends on several factors including voltage and power level, cost of devices, installations and labor costs, loss analysis and control capabilities [23]. However, trends suggest that as more systems are commercialized, HVDC converter station costs will continue to reduce making it the favored choice in the future.

Feldman et al [24] presents a hybrid modular multilevel VSC for the HVDC with voltage control option for real and reactive power. A review of different converter topologies, control method and efficiency is provided in [25] that includes (i) a PMG connected to passive rectifier back-to-back with thyristor (SCR) converter, (ii) PMG connected to a passive rectifier back-to-back with a voltage source inverter (VSI), (iii) PMG connected to a passive rectifier back-to-back with a VSI and chopper in between, (iv) PMG connected to two back-to-back VSC, (v) DFIG with a rectifier and a SCR, (vi) DFIG with two back-to-back VSC (vii) DFIG with a matrix converter, (viii) IG connected to a passive rectifier and a VSC, and (ix) SG connected to passive rectifier with a DC/DC boost converter and an inverter. Advantages and disadvantages of different generator-converter topology is also addressed in [25]. The HVDC system proposed in [27] reduces the number of VSC in the system by using a higher rated VSC for a group of wind turbines. However, such a scheme results in lower (electrical) control functionality at the individual turbines. Veilleux [28] proposed a series HVDC interconnection system using PMG, passive recitifer and DC/DC converter for each turbine such that the off-shore platform is eliminated. However, not having a platform off-shore increases the system maintenance and serviceability. Moreover, the reliability of such system is at risk if the series connection fails. A HVDC system is proposed by ABB known as Windformer [29] that uses PMG connected to a passive rectifier which makes the Windformer unable of controlling the generator output voltage due to fixed PM excitation and lack of active power electronic converter hence it is infeasible to implement. The ABB Windformer was initially proposed in 2000 but has not been installed or investigated further.

Muyeen et al [30] investigates dynamic and transient analyses of an off-shore wind farm with on three-level neutral point clamped VSC HVDC transmission where the maximum power point tracking (MPPT) control of the wind turbine is implemented via VSC's while [31-334] provide a review of HVDC systems based on different topologies, application and models. Meyer et al [35] proposes a system of parallel DC interconnections where different topologies based on location of DC/DC converter is investigated and the topology where the DC/DC converters are placed on an off-shore substation is chosen. The DC grid

proposed by [35] employs DC/DC converters with a so-called single active bridge (SAB) topology [36]. Other topologies for high voltage, high power DC/DC converters have also been proposed based on dual active bridge (DAB) and resonant circuits [37-40].

DC/DC converter based on two resonant circuits is discussed by in [38] while Meyer [40] studies a series resonant DC/DC converter based on a modified topology of a three-phase series resonant circuit (SRC) system. Max [41] discusses design and control considerations for a SAB DC/DC converter where the losses are evaluated and a variable frequency control method results in low losses. Two topologies for resonant switched-capacitor DC/DC converter are proposed in [42] while [43] provides design of a bidirectional resonant 30 kW DC/DC converter where it is capable of DC fault isolation. A series and a cascade topology for multiple modules DC/DC converter is offered by [44] where the converter achieves high gains at high voltages. Ortiz et al [45] present design of a high power DC/DC converter where DAB and SRC configurations are investigated with zero current switching (ZCS) and the converter efficiency reaches 98.6%.

Different generator topologies and their comparison have also been proposed and demonstrated, although in small laboratory prototype scale [46-47]. Chau et al [46] proposed a hybrid excitation PM generator for the wind turbine application where a DC wound field winding is used in the stator in series with PM. The field winding regulates the machine fixed output voltage due to the PM excitation. However, the topology is complex and the paper offers a low voltage low power machine design. The hybrid excitation PM machine proposed in [47] has two stators and an outer rotor with 24 salient poles with no windings. The outer stator has a three-phase winding while the inner stator uses both PM and DC wound field windings. The configuration is complex and the machine is a low voltage low power generator. Pillai et al [48] discusses different generator topology for the wind turbine applications including cage and wound rotor IG, DFIG, PM and investigates the SG in more details. Benefits presented for the SG in [48] includes better power capability, transformer free since the HV SG is commercialized and widely in use, harmonic free and better fault current capability. However, on the disadvantages it discusses increased drive train mass and complexity for the SG compared to other generator

topologies. Margaris [49] studies a direct drive wound field SG connected to a grid via a passive rectifier, DC/DC converter and a VSC where three different control strategies are discussed (i) constant output voltage by SG excitation, maximum power point tracking by DC/DC converter and constant DC-link voltage using the VSC (ii) power control using SG excitation, voltage control by DC/DC converter and DC-link voltage control by VSC (iii) output voltage control by SG excitation, DC-link voltage control by DC/C converter and power control by the VSC. Achilles et al [50] discusses a model used for both dynamic and steady state analysis of a SG connected to a grid using a passive rectifier, DC/DC converter to and a VSC. Behnke [51] develops a reduced order model for the SG connected a grid via VSC's to study system response to disturbances. Performance of wind turbine during grid voltage disturbance and speed variations is studied. Spooner [52] proposed direct drive lightmass PM generator where the stator has no iron while Brisset [53] discusses different topologies for axial-flux direct drive PM generator for wind turbine application. The machine stator has 9-phase concentric winding and choice of configurations is based on finite element analysis (FEA). A comparison between large scale geared and direct-drive generators for wind turbine applications has been presented in [54-56], however, the comparison does not include a total wind generation scheme hence the comparison is not comprehensive and cannot be generalized. Liserre [57] provides an overview of wind turbines in terms of generator technology, power electronic interface and control strategies for the system. It also briefly discusses system issues including harmonics and faults. Most turbine-generator systems are rated to an upper voltage limit of 1000 VAC. Although there are some experimented or prototype installations using higher voltage generators, such as a SG example operating at 13.8 kV [58].

1.4 Thesis Outline

This Chapter has presented a general overview of the wind generation industry to-date to introduce the subject area, energy conversion schemes and systems currently existing worldwide. The discussion is not presented as a comprehensive review of the industry, but as an introduction to the topic. A more detailed discussion of a wind energy form will be presented in later Chapters, in particular Chapter 3, where the Walney off-shore system is studied in some detail.

Chapter 2 discusses the basics of wind turbine systems and their components. A commercial wind turbine is characterized using mathematical models derived from the turbine mechanics. Different models reported in the literature for turbine power are evaluated and turbine power and torque characteristics studied. Two operating schemes are studied for wind turbines (i) normal rated speed and (ii) high speed regions of operations. The normal turbine operation is chosen for further studies and taken forward to subsequent Chapters.

Chapter 3 discusses an off-shore HVDC wind generation scheme proposed by the author. The Walney off-shore wind farm in the UK is chosen as benchmark system against which comparisons with the proposed HVDC wind generation system are made. Both the proposed and Walney wind farm systems are modelled and power flow analyses at different loads are carried out to evaluate the system in terms of performance and required plant. System loss, mass and efficiency are analyzed and comparisons summarized.

Chapter 4 presents an overview of different electric generator topologies and power electronics interface for wind turbine applications. The hybrid generator (HG) concept is discussed and a low power, low voltage prototype is tested and results are compared with that of MATLAB simulations. The scope of the thesis does not permit the build and test of a full power HG hence, an industrial high voltage synchronous generator design is used to benchmark the high voltage HG. In Chapter 4 the benchmark machine is analyzed and results compared against published data to validate the analysis procedures. Having established validity of the design tools and procedure the benchmark machine design is

used in Chapter 5 to develop the proposed high voltage HG and in Chapter 6 to study winding insulation systems.

Chapter 5 presents design of a high voltage high power HG for the proposed HVDC wind generation system. A multiphase (9-phase) stator winding is considered for the HG, a choice that results in improved machine power density above 3-phase implementations. Moreover, the multiphase design improves the machine rectified output power quality thus reducing the mass and volume of passive (electrolyte) capacitors. FEA is used as a tool for electromagnetic analysis where machine air-gap flux-density, per-phase flux-linkage, torque and inductances are calculated. MATLAB Simulink is used to evaluate and process results data and to confirm machine operational characteristics. Two rotor sections i.e. WF and PM are designed separately and then combined to form the HG. For the PM rotor a surface PM and an embedded PM rotor design is considered. Sintered NdFeB and Ferrite magnets are used for the PM rotors to compare their relative merits. The combined HG consideration is made where the WF and PM rotor split ratio is deduced for the chosen 3.6 MW example generator such that the desired output specification is met. Loss analysis for copper, windage and friction and iron losses are presented at the end of Chapter 5.

Design of high voltage insulation systems are presented in Chapter 6. Circuit models for the machine winding insulations are presented. Since this is a theoretical study the benchmark SG insulation system is used to benchmark the new designs and thus give some validation to the designs proposed. The machine voltage and hence insulation is increased in steps to obtain desired output voltage. It is assumed that the insulation requirements vary linearly with voltage and changes in the number of strands, conductor cross-sections and coil dimensions are discussed. Slot size and machine mass variations due to the coil height increase are also investigated.

Finally, Chapter 7 concludes the thesis research findings, main achievements and presents recommendations for future work.

Chapter 2

Wind Turbine Systems

2.1 Introduction

This Chapter will present the equations used to analyze wind turbine systems and apply them to confirm the general operating characteristics of two commercial systems used in the wind industry, the Enercon E-82, 2MW turbine [11] and the Siemens SWT-3.6-107, 3.6 MW turbine [10]. With this validation, the models are then used to identify the general industry operating principles of wind turbines, referred to herein as (i) the Limited Speed Operating Regime, and to propose an alternative (ii) High Speed Operating Regime. These two operating regimes are further utilized in Chapter 4 to develop the power- and torque-speed requirements of the Hybrid Generator.

2.2 Wind Turbine Power and the Betz Limit

A wind turbine is an energy converter that transforms the kinetic energy of the wind into mechanical energy that is then used as the prime mover to an electric generator. The electric generator subsequently converts mechanical to electrical energy [9]. However, all the available energy in the wind cannot be harvested as observed by the German scientist Albert Betz [59] who showed that an ideal loss-less wind turbine can only convert 59.3% of the total wind energy. Referring to the schematic diagram of Fig. 2.1, the kinetic energy in a moving parcel of air is given by [60]:

$$U = \frac{1}{2} m v^2 \quad (\text{Joules}) \quad (2.1)$$

which, considering the mass equation:

$$m = \rho A x \quad (\text{kg}) \quad (2.2)$$

Becomes:

$$U = \frac{1}{2} m v^2 = \frac{1}{2} (\rho A x) v^2 \quad (\text{Joules}) \quad (2.3)$$

where,

m : Parcel mass (kg)

v : Parcel speed (m/s)

A : Cross-sectional area (m²)

ρ : Air density (kg/m³)

x : is the thickness of the parcel (m)

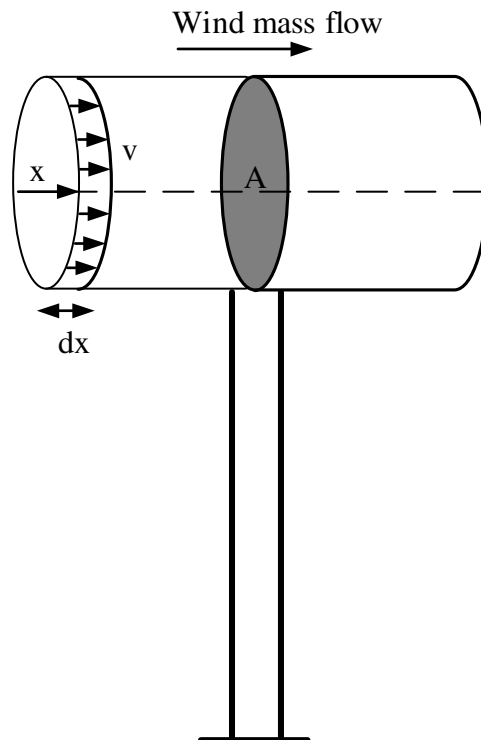


Fig. 2.1. Air flow with velocity of v through an area of A .

The power in the wind is obtained by taking the time derivative of the kinetic energy [60] as follows:

$$P_w = \frac{dU}{dt} = \frac{1}{2} v^2 \frac{dm}{dt} \quad (\text{W}) \quad (2.4)$$

where the mass flow is:

$$\dot{m} = \frac{dm}{dt} = \rho A \frac{dx}{dt} \quad (\text{kg/s}) \quad (2.5)$$

Linear velocity is:

$$\frac{dx}{dt} = v \quad (\text{m/s})$$

Hence,

$$P_w = \frac{dU}{dt} = \frac{1}{2} \rho A v^3 \quad (\text{W}) \quad (2.6)$$

The wind turbine harvests energy from the wind by slowing down the wind velocity. Therefore, with an unchanged mass flow, the cross-sectional area behind the turbine increases as a result of velocity reduction [9] as shown in Fig. 2.2.

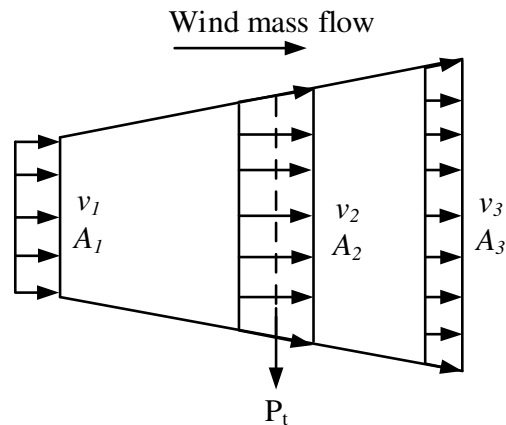


Fig. 2.2. Increase in cross-sectional area.

The power extracted from the wind is then related to the power difference of air before and after the turbine [9]. Thus, referring to Fig. 2.2:

$$P_t = \frac{1}{2} \rho A_1 v_1^3 - \frac{1}{2} \rho A_3 v_3^3 = \frac{1}{2} \rho (A_1 v_1^3 - A_3 v_3^3) \quad (\text{W}) \quad (2.7)$$

For an unchanged mass flow [9]:

$$\dot{m} = \rho A_1 v_1 = \rho A_3 v_3 \quad (\text{kg/s}) \quad (2.8)$$

Therefore:

$$P_t = \frac{1}{2} \rho A_1 v_1 (v_1^2 - v_3^2) \quad (\text{W}) \quad (2.9)$$

or in terms of mass flow:

$$P_t = \frac{1}{2} \dot{m} (v_1^2 - v_3^2) \quad (\text{W}) \quad (2.10)$$

The force that the air exerts on wind turbine can be expressed as [9]:

$$F = \dot{m} (v_1 - v_2) \quad (\text{N}) \quad (2.11)$$

This force is counteracted by an equal force exerted by the wind turbine on the air flow.

Therefore:

$$P_t = F v_2 = \dot{m} (v_1 - v_2) v_2 \quad (\text{W}) \quad (2.12)$$

Equating equations (2.10) and (2.12) results in:

$$v_2 = \frac{(v_1 + v_3)}{2} \quad (\text{m/s}) \quad (2.13)$$

Therefore:

$$\dot{m} = \rho A_2 v_2 = \rho A_2 \left(\frac{v_1 + v_3}{2} \right) \quad (\text{kg/s}) \quad (2.14)$$

Thus, the wind turbine power can be expressed as:

$$P_t = \frac{1}{2} \dot{m} (v_1^2 - v_3^2) = \frac{1}{4} \rho A_2 (v_1^2 - v_3^2) (v_1 + v_3) \quad (\text{W}) \quad (2.15)$$

According to equation (2.6) the power in the wind can be expressed as:

$$P_w = \frac{1}{2} \rho A_1 v_1^3 \quad (\text{W}) \quad (2.16)$$

The ratio of the wind turbine power to the available power in the wind is called the wind turbine power coefficient C_p [9]:

$$C_p = \frac{P_t}{P_w} \quad (2.17)$$

Using equations (2.15) and (2.16) the wind turbine power coefficient is calculated from [9]:

$$C_p = \frac{1}{2} \left(1 + \frac{v_3}{v_1} \right) \left[1 - \left(\frac{v_3}{v_1} \right)^2 \right] \quad (2.18)$$

The turbine power coefficient variation with respect to the ratio of velocities before and after the turbine is plotted in Fig. 2.3. Here, C_p is maximum at a velocity ratio that is $v_3 / v_1 = 1/3$, hence the maximum turbine power coefficient is:

$$C_p^{\max} = \frac{16}{27} = 0.593 \text{ per unit} \quad (2.19)$$

This is the ‘Betz limit’ or ‘Betz factor’ as referred to previously. Therefore, an ideal loss-less wind turbine can harvest a maximum of 59.3% of the wind energy.

The net extractable turbine power therefore is expressed as:

$$P_t = \frac{1}{2} \rho A v^3 C_p \quad (\text{W}) \quad (2.20)$$

For non-ideal turbines, where there is further loss of energy conversion, the turbine power coefficient is modified.

Using the turbine rotational speed ω (rad/s), the turbine torque, T_t , is obtained from:

$$T_t = \frac{P_t}{\omega} = \frac{1}{2} \rho A v^3 \frac{C_p}{\omega} = \frac{1}{2} \rho A v^3 C_\tau \quad (\text{N.m}) \quad (2.21)$$

where $C_\tau = \frac{C_p}{\omega}$ is the turbine torque coefficient.

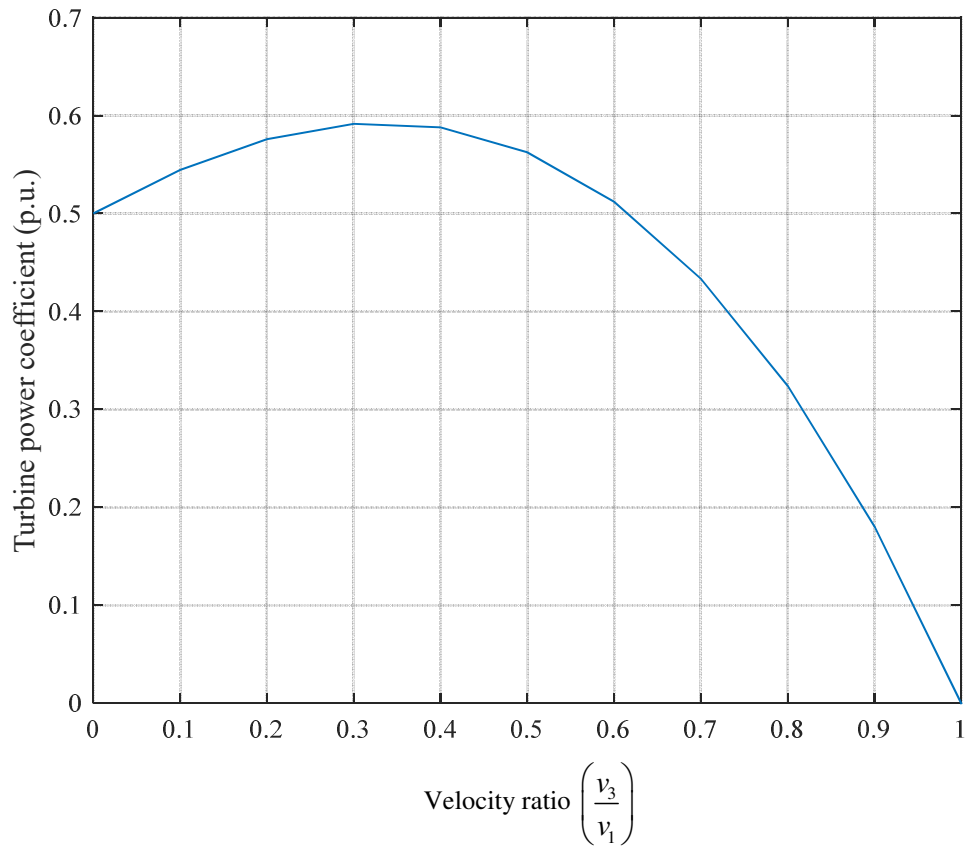


Fig. 2.3. Turbine power coefficient variation with respect to the ratio of wind velocities before and after the turbine.

2.3 Wind Turbine Power Coefficient

The wind turbine power coefficient defines the portion of the power that is extracted from the wind. The power coefficient therefore, depends on the aerodynamic design of the wind turbine. In order to obtain the turbine power coefficient, different measurements at various wind velocities are taken and the turbine power coefficient estimated from the post process analysis. Analytical methods may also be applied to model the turbine power coefficient. Normally, manufacturers provide the turbine power along with the power coefficients at different velocities.

2.3.1 Tip Speed Ratio

The turbine power coefficient C_p , is normally expressed as a function of two parameters, blade pitch angle, β , and blade tip speed ratio, λ . The blade pitch angle is defined as the angle between the blade cross-section chord and the plane of rotation [9], [61-63] as depicted in Fig. 2.4.

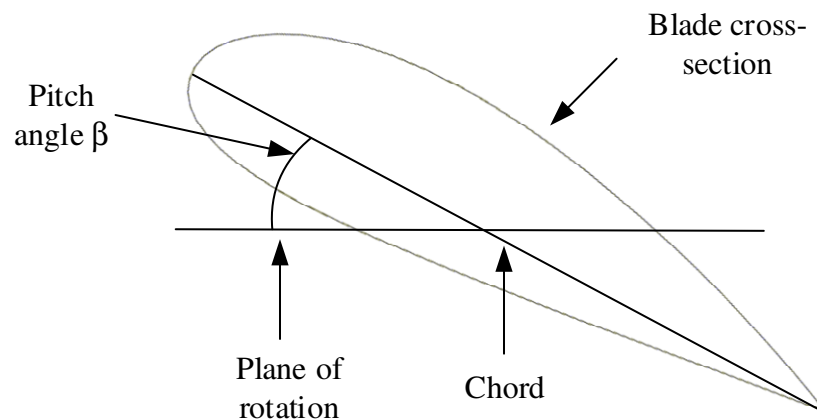


Fig. 2.4. Blade pitch angle.

The tip speed ratio is defined as follows:

$$\lambda = \frac{u}{v} = \frac{R \omega}{v} \quad (2.22)$$

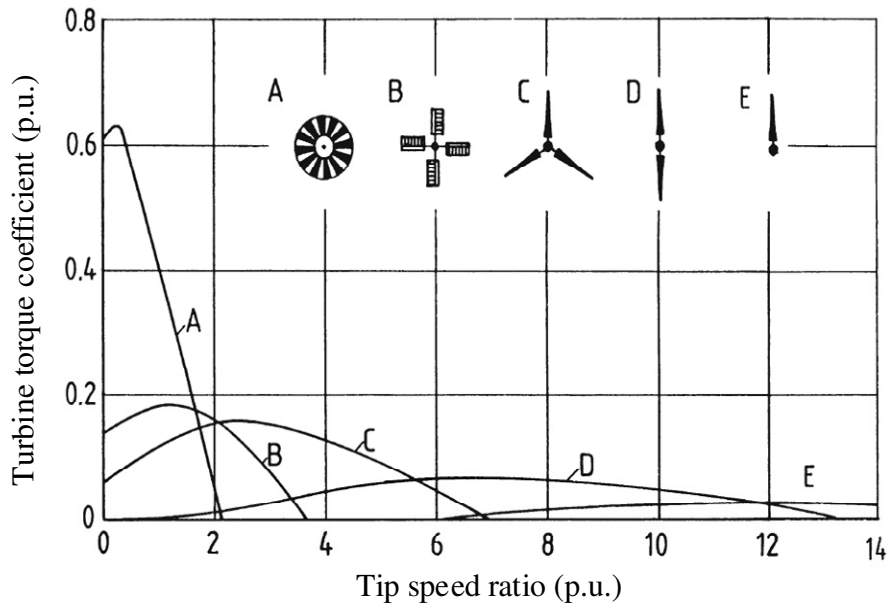
where,

u : is the tangential velocity of the blade tip

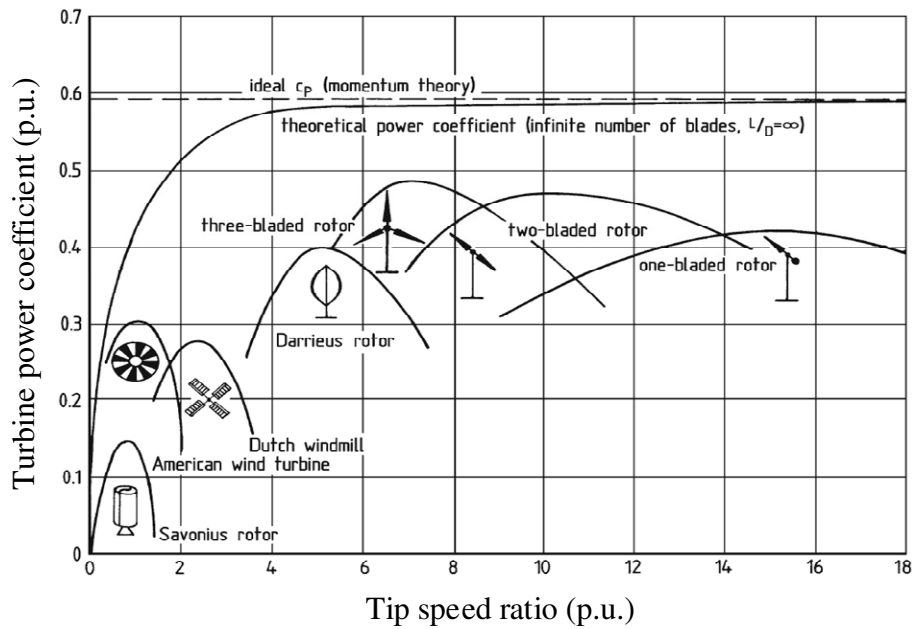
R : is the rotor radius (\approx blade length)

The rotor radius includes the hub radius plus the blade length, but in large wind turbines the blade length is much longer than the hub radius, hence it is acceptable to assume that R is the total blade length.

The turbine power coefficient is different for various turbine designs and configurations. Typical wind turbine power coefficient (C_p) and also torque coefficient (C_t) curves for different turbine configurations are presented in Fig. 2.5 [9]. The upper limit for the turbine power coefficient is the Betz limit. As it can be seen the three-blade wind turbine has the highest power coefficient amongst various designs, hence modern wind turbines generally use three-blade designs.



(a) Torque coefficient.



(b) Power coefficient.

Fig. 2.5. Wind turbine power and torque coefficients' curves [8].

One difficulty in assessing manufacturer's turbines is that the relevant turbine pitch blade angles at which the power coefficients are obtained are not usually provided. As an example the turbine power and the power coefficient for Enercon E-82 2 MW [11] is presented in Fig. 2.6.

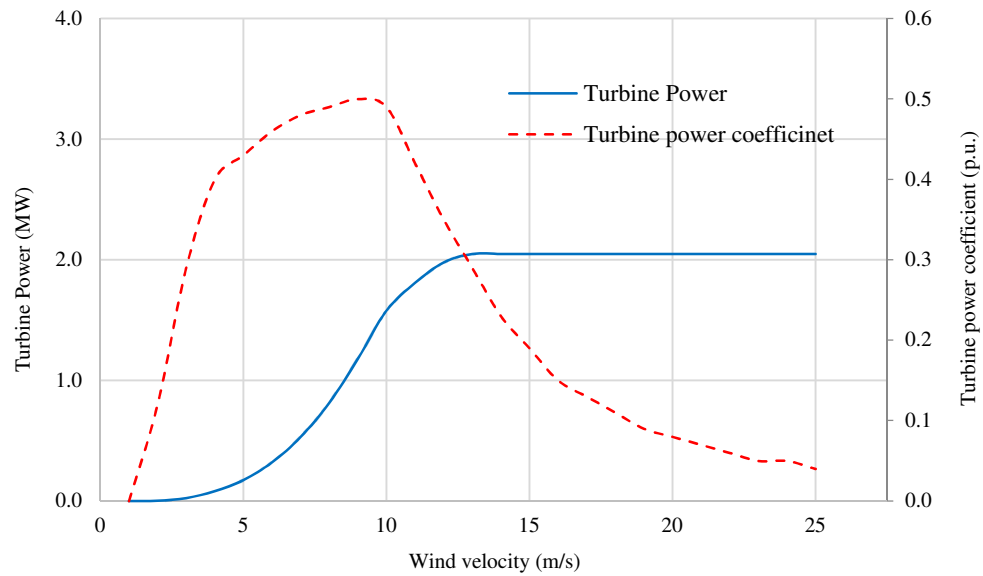


Fig. 2.6. Turbine power and power coefficient for Enercon E-82 [11].

2.3.2 Mathematical Expression for Wind Turbine Power Coefficient

The power coefficient of wind turbines can be approximated by nonlinear functions as discussed in great detail by O. Wasynczuk in 1981 [64] and P. M. Anderson [65] in 1983, who reported the power coefficient for a MOD-2 wind turbine that is an upwind, 2-blade, 2500 kW wind turbine installed and tested in the USA [66]. Upwind is a term used when the wind turbine is facing the wind in front of the electric machine while for downwind turbines the electric machine is behind the turbine in terms of wind flow. The equation for the power coefficient from [64-65] is:

$$C_p = 0.5 \left(\Gamma - 0.022 \beta^2 - 5.6 \right) e^{-0.17\Gamma} \quad (2.23)$$

where,

$$\Gamma = \frac{v}{\omega}$$

S. Heier [61] proposed the following model for the wind turbine power coefficient:

$$C_p(\lambda, \beta) = c_1 \left(c_2 - c_3 \beta - c_4 \beta^x - c_5 \right) e^{-c_6} \quad (2.24)$$

Using parameters stated in equation (2.25), equation (2.24) fits to equation (2.23):

$$\begin{aligned} c_1 &= 0.5 & c_2 &= \frac{v}{\omega} & c_3 &= 0 & c_4 &= 0.022 \\ c_5 &= 5.6 & c_6 &= 0.17 \frac{v}{\omega} & x &= 2 \end{aligned} \quad (2.25)$$

The power coefficient following parameters have been proposed by S. Hiere [61], Z. Lubosny [63] and B. Almang [67]:

$$c_1 = 0.5 \quad c_2 = \frac{116}{\lambda_1} \quad c_3 = 0.4 \quad c_4 = 0 \quad c_5 = 5 \quad c_6 = \frac{21}{\lambda_1} \quad (2.26)$$

$$\frac{1}{\lambda_1} = \frac{1}{\lambda + 0.08 \beta} - \frac{0.035}{\beta^3 + 1}$$

Further, a modified version of the turbine power coefficient and parameters is reported in the literature [68-69] as follows:

$$C_p(\lambda, \beta) = c_1 (c_2 - c_3 \beta - c_4 \beta^x - c_5) e^{-c_6} + c_7 \lambda$$

$$c_1 = 0.5176, c_2 = \frac{116}{\lambda_1}, c_3 = 0.4, c_4 = 0, c_5 = 5, c_6 = \frac{21}{\lambda_1}, c_7 = 0.0068 \quad (2.27)$$

$$\frac{1}{\lambda_1} = \frac{1}{\lambda + 0.08 \beta} - \frac{0.035}{\beta^3 + 1}$$

The maximum of the turbine power coefficient stated in equation (2.24) when applying parameters in equation (2.26) is 0.41 p.u., while using equation (2.27) a maximum of 0.48 p.u. is achieved. Note that the turbine power coefficient cannot be higher than the Betz limit, i.e. 0.593 p.u. Today's wind turbine design's trend suggests C_p values in the range of 0.47-0.5 p.u. [10-11], [58]. Therefore, in this study equation (2.27) for the wind turbine power coefficient is used for further analysis.

The power coefficients can be different for various turbines [61], [63]. The C_p equations provide an approximation to the actual turbine power coefficient, hence the equations and their parameters can vary depending on the design of the turbine. As an example the maximum value of C_p for Enercon E-82 2 MW wind turbine is 0.5 that does not match the maximum C_p in equation (2.27). Other methods of approximating the turbine power coefficient such as curve fitting [70] and exploiting the drag and lift characteristics of the turbine [63] have been proposed. However, if the C_p data and pitch angles for different wind velocities and rotor speeds are provided by manufacturers, analysis of the wind turbine should rely on real data. But in many cases the manufacturers only provide a curve of power coefficient versus wind velocity without pitch angles and rotor speeds, thus approximation equations are used.

By varying the tip speed ratio, λ , the turbine power coefficient curves for different pitch angles using equation (2.27) are plotted in Fig. 2.7. The turbine power coefficient curve at

$\beta = 0$ achieves the highest value compared to curves at other pitch angles hence a wind turbine harvests the highest power when it operates at zero pitch angle.

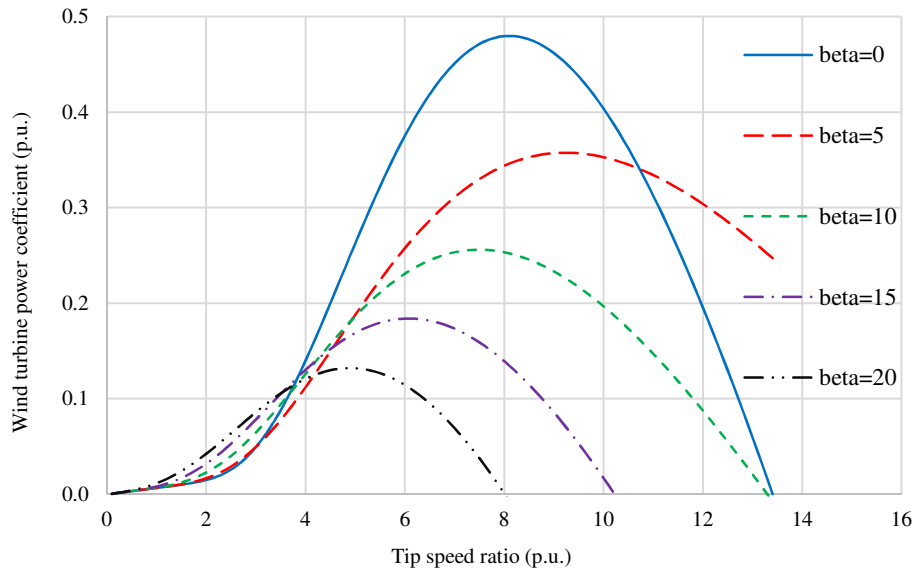


Fig. 2.7. Turbine power coefficient curves.

2.4 Wind Turbine Operation

By replacing wind velocity from equation (2.22) to equations (2.20) and (2.21) the turbine power and torque are respectively expressed as:

$$P_t = \frac{1}{2} \rho \pi R^5 \omega^3 \frac{C_p(\lambda, \beta)}{\lambda^3} \quad (\text{W}) \quad (2.28)$$

$$T_t = \frac{P_t}{\omega} = \frac{1}{2} \rho \pi R^5 \omega^2 \frac{C_p(\lambda, \beta)}{\lambda^3} \quad (\text{N.m}) \quad (2.29)$$

where, the air density in normal conditions is $\rho = 1.225$ (kg/m³) [9], [61-63]. The turbine power and torque are cubic and square function of the turbine rotor speed (and wind velocity) respectively.

Using blade a length of $R=41$ (m) for the Enercon E-82 2 MW [11] the wind turbine power and torque characteristics versus rotor speed, for $\beta = 0$ and at different wind velocities are plotted in Fig. 2.8. The so called maximum power point tracking (MPPT) of the turbine is achieved by controlling the turbine system such that it operates at the maximum points of the power curves shown in Fig. 2.8(a), i.e. every point on the MPPT corresponds to a maximum power being extracted from the wind at a specific wind velocity. Commercial wind turbines are normally rated to operate over a variable wind velocity range that defines the minimum and maximum operating points for the turbine. The minimum wind velocity at which the turbine starts delivering power is called the ‘cut-in velocity and the maximum wind velocity for turbine operation is called the ‘cut-out velocity’. Although the output power of the wind turbine varies with wind velocity, industrial turbines are generally designed and controlled to deliver a constant power referred to as ‘rated power’ over a variable range of wind velocity. Rated here usually refers to the system mechanical, thermal and electromagnetic capabilities.

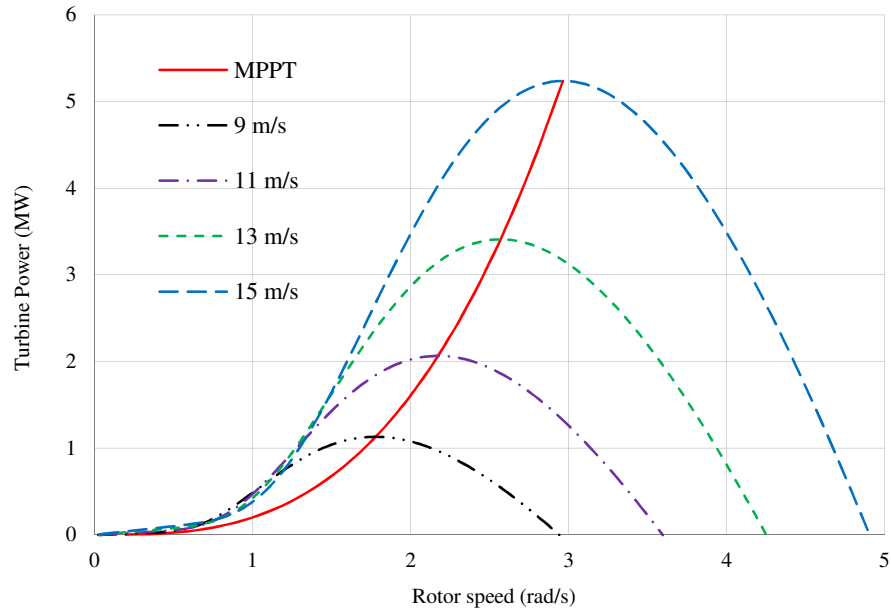
For the purpose of comparison and further discussion, the wind velocity at which the turbine starts delivering rated power will be defined in this thesis as the ‘rated power base velocity’, or simply the ‘rated velocity’. This definition is industry practice [10-11] and is clarified by reference to the power versus wind velocity characteristic for the Siemens

SWT-3.6-107 3.6 MW wind turbine [10], as illustrated in Fig. 2.9, while Table 2.1 presents the Siemens SWT-3.6-107 3.6 MW wind turbine operational parameters.

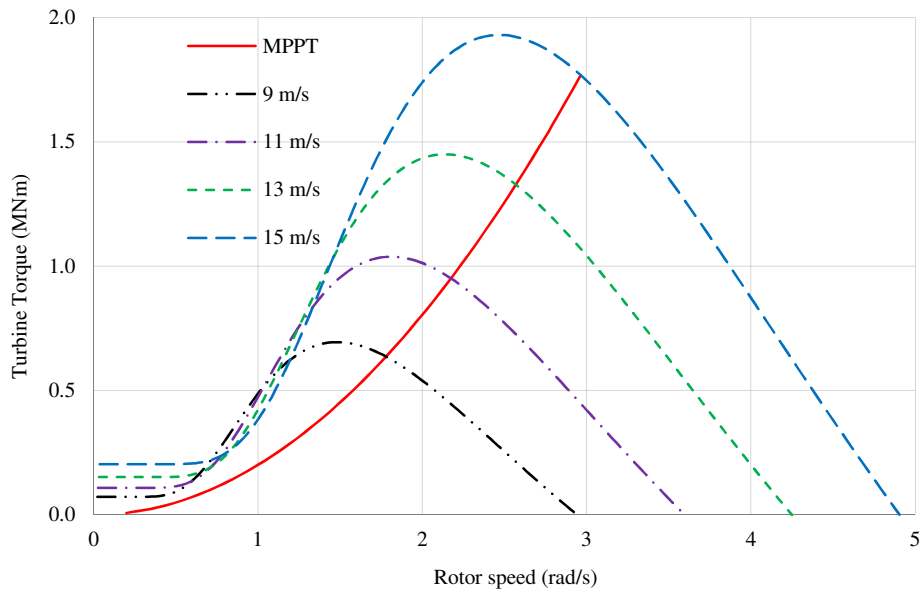
Therefore, using equation (2.20) and according to Fig. 2.9, the power versus wind velocity characteristics of a wind turbine is mathematically expressed as follows:

$$P_t = \begin{cases} 0 & v \leq v_{cut-in} \\ \frac{1}{2} \rho \pi R^5 \omega^3 C_p(\lambda, \beta) & v_{cut-in} \leq v \leq v_{rated} \\ P_{nominal} & v_{rated} \leq v \leq v_{cut-out} \\ 0 & v \geq v_{cut-out} \end{cases} \quad (\text{W}) \quad (2.30)$$

Fig. 2.10 illustrates turbine power coefficient curves with respect to wind velocity at different rotor speeds for the Enercon E-82 wind turbine (rated at 2 MW). Using these curves, turbine power with-respect-to wind velocity variation at different rotor speeds are plotted in Fig. 2.11, from which it is seen that in order to extract the maximum power at a specific wind velocity, the rotor speed should be at a certain value which is referred to as the ‘optimum rotor speed’. Therefore, for each wind velocity there is an optimum rotor speed and the wind turbine is controlled to operate at optimum rotor speeds.



(a) Turbine power curves.



(a) Turbine torque curves.

Fig. 2.8. Wind turbine power and torque characteristics for $\beta=0$.

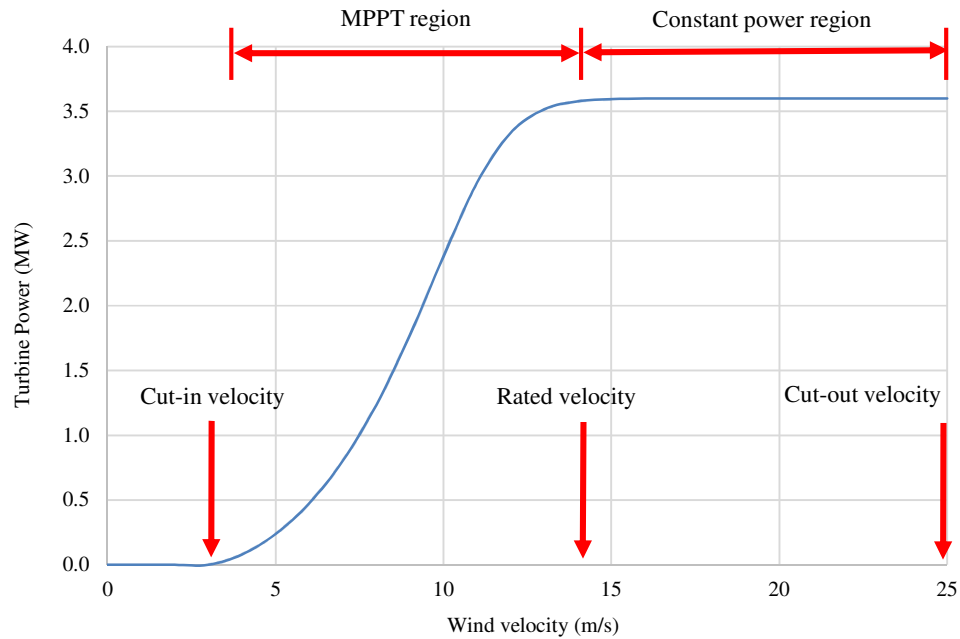


Fig. 2.9. Siemens SWT-3.6-107, 3.6 MW wind turbine power curve with respect to wind velocity [10].

Table 2.1. Operational parameters for the Siemens SWT-3.6-107, 3.6 MW turbine

Parameter	Symbol	Value
Optimum tip speed ratio	λ_{opt}	8.1
Maximum turbine power coefficient	C_p^{max}	0.48
Wind velocity (m/s)	v	0-25
Cut-in velocity (m/s)	v_{cut-in}	3-5
Rated velocity (m/s)	v_{rated}	13-14
Cut-out velocity (m/s)	$v_{cut-out}$	25
Rated power (MW)	$P_{nominal}$	3.6
Air density (kg/m^3)	ρ	1.225

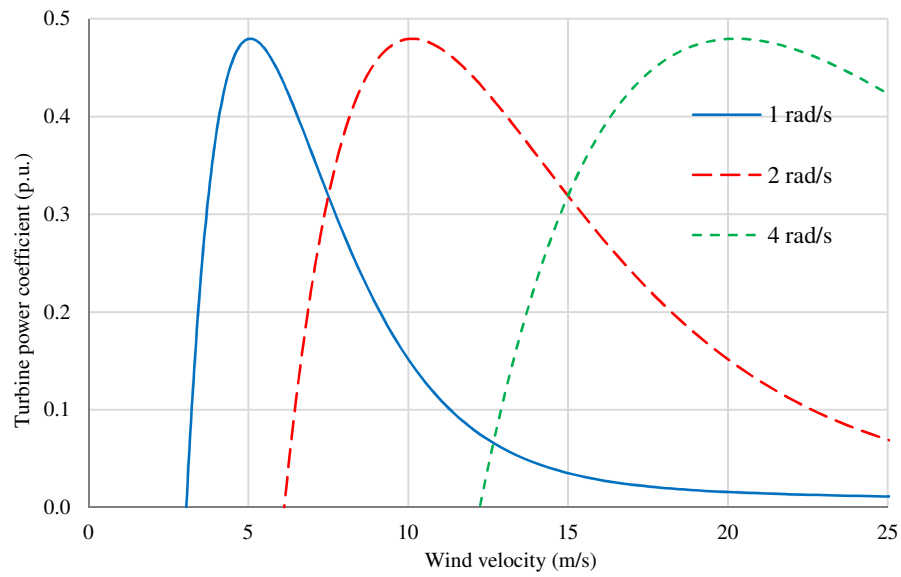


Fig. 2.10. Turbine power coefficient with respect to wind velocity variations at different rotor speeds for $\beta=0$.

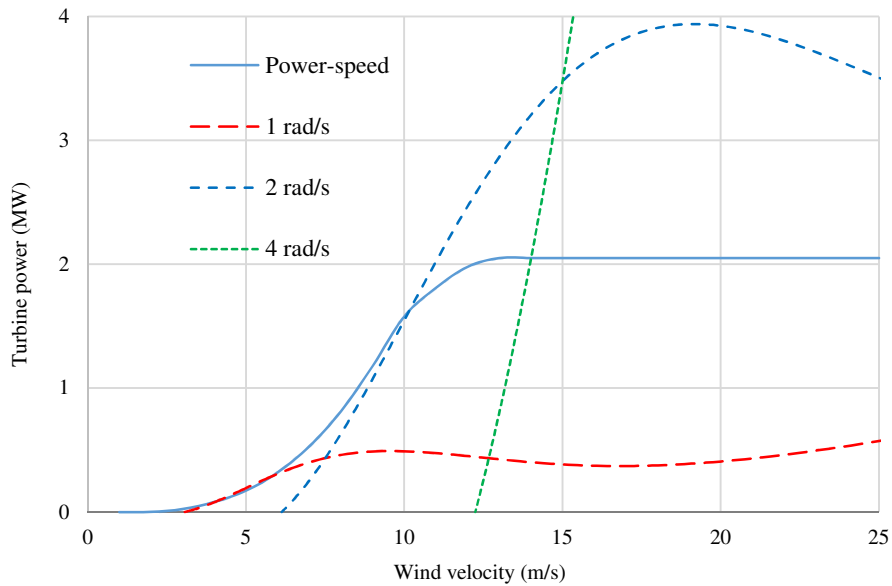


Fig. 2.11. Turbine power curves with-respect-to wind velocity variations at different rotor speeds (in rad/s) for $\beta=0$.

Referring to Fig. 2.9, from cut-in to rated wind velocity the turbine is controlled via MPPT, hence, power varies with wind velocity as defined by:

$$P_i = \frac{1}{2} \rho \pi R^2 v^3 C_p^{\max} \quad (\text{W}) \quad (2.31)$$

where, C_p^{\max} is the maximum turbine power coefficient.

Hence, the turbine power is a cubic function of the wind velocity. For wind velocities above the rated velocity, the wind turbine is controlled to deliver a constant power, as shown in Fig. 2.9.

Commercial manufacturers use a control method that is explained in this study as ‘Limited Speed Operation’ region. The ‘Limited Speed Operation’ is regarded as the standard industry practice to control turbines to deliver fixed power. However, a new control method for operating at wind velocities above the rated velocity is proposed in this study and referred to as ‘high speed operation’. This control function allows the wind turbine to operate at higher rotor speeds while delivering a fixed power output. Note that for both Limited and High Speed Operation regions the wind turbine is controlled to ideally operate with MPPT from cut-in to the rated velocity. Hence, only when above the rated velocity will the control methods differ for Limited and High Speed Operation.

2.4.1 Limited Speed Operation

For the Limited Speed Operation Scheme, the turbine blade pitch angle is controlled such that turbine operates on the MPPT curve from cut-in up to rated velocity. Therefore, as the wind velocity increases, the turbine rotor speed and hence the power extracted from the wind increases. However, once at rated wind velocity and above, the turbine speed is maintained around a fixed upper speed, referred to here as the ‘turbine rated speed’, or simply ‘rated speed’. For wind velocities above rated velocity the turbine blade pitch angle is controlled to maintain turbine speed at rated and the turbine delivers a fixed rated power. It might be practically infeasible to control the turbine to operate exactly at the rated speed and a limited speed variation of 10% around the turbine rotor rated speed is usually allowed [71].

In order to illustrate operation of a wind turbine in the Limited Speed Operation region, the following case using the Enercon E-82 commercial wind turbine is analyzed and presented. The rated wind velocity for the turbine under study is 13 (m/s). Figs. 2.12 to 2.14 show turbine power curves at different blade pitch angles and for velocities above rated. If the blade pitch angle is maintained when the wind velocity increases to 15 (m/s) the turbine rotor speed and hence output power increase. However, to keep a constant output power and control the rotor at rated speed, the blade pitch angle is changed from zero to $\beta=15^\circ$, as shown in Fig. 2.12. For higher wind velocities the blade pitch angle increases further to keep the turbine power and the speed around their nominal rated values. For example at 19 and 25 m/s the blade pitch angle is increased to $\beta=25^\circ$ and $\beta=33^\circ$ respectively, as shown in Figs. 2.13 and 2.14 respectively. Fig. 2.15 illustrates the turbine per unit power-speed and torque-speed characteristics for the Limited Speed Operation control regime. The speed variation around rated speed is about 10%, as explained previously arising from the result of practical implementation of the rotor blade pitch angle control.

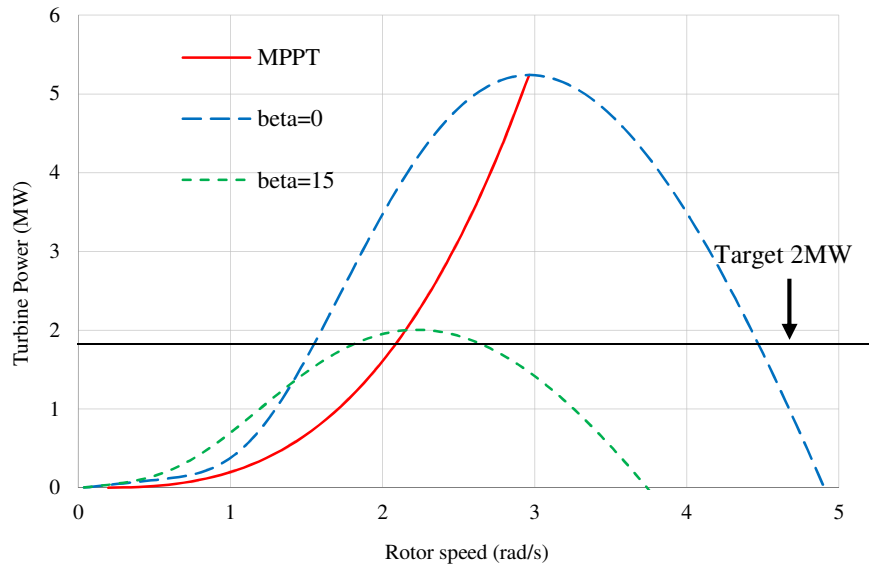


Fig. 2.12. Turbine power curves at wind velocity 15 m/s.

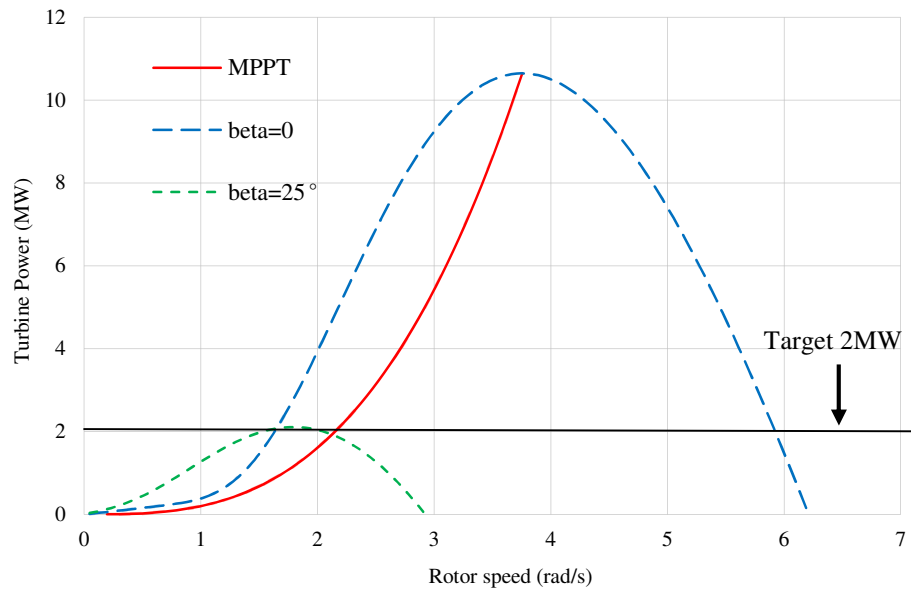


Fig. 2.13. Turbine power curves at 19 (m/s).

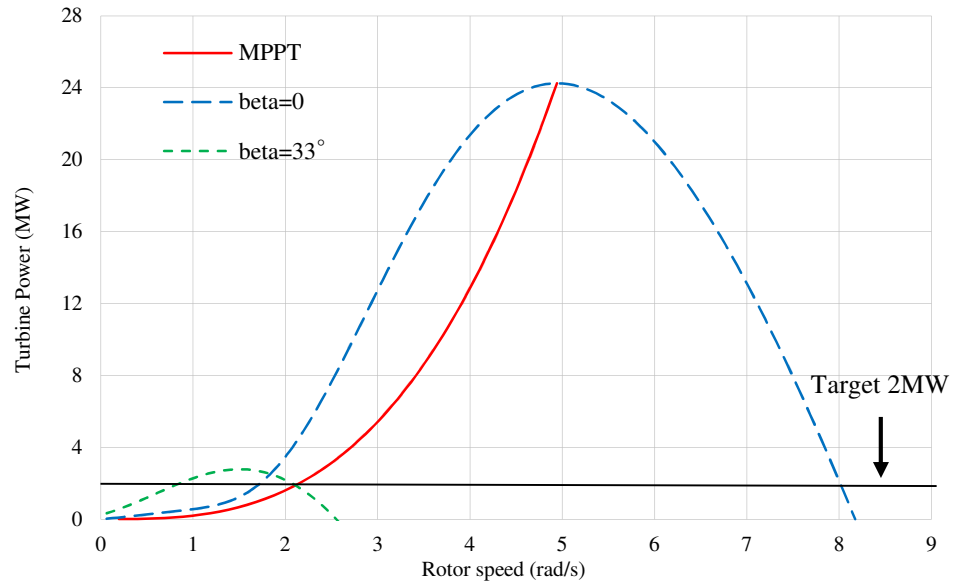
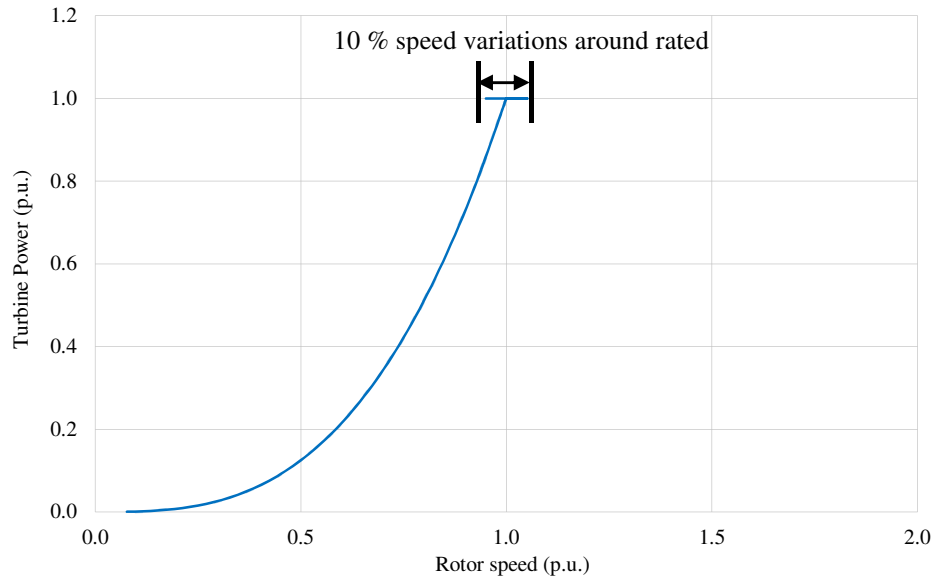
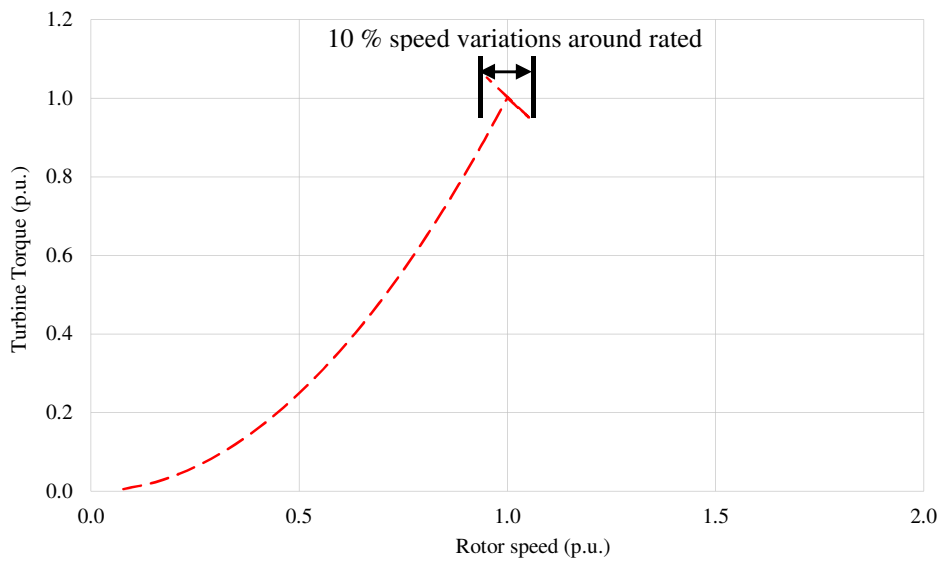


Fig. 2.14. Turbine power curves at 25 (m/s).



(a) Power-speed.



(b) Torque-speed.

Fig. 2.15. Per unit power and torque characteristics of the wind turbine when operating in Limited Speed region.

It may be inferred from Fig. 2.15 that from cut-in to rated wind velocity the turbine power is a cubic function of the turbine speed while the turbine torque is a square function of turbine speed, as per equations (2.28) and (2.29) respectively. For wind velocities higher than rated, power is controlled to be nearly constant while the turbine speed has small changes around the rated speed, which yield a small torque variation. Turbine rotor speed with respect to the wind velocity variations for Limited Speed Operation is plotted in Fig. 2.16.

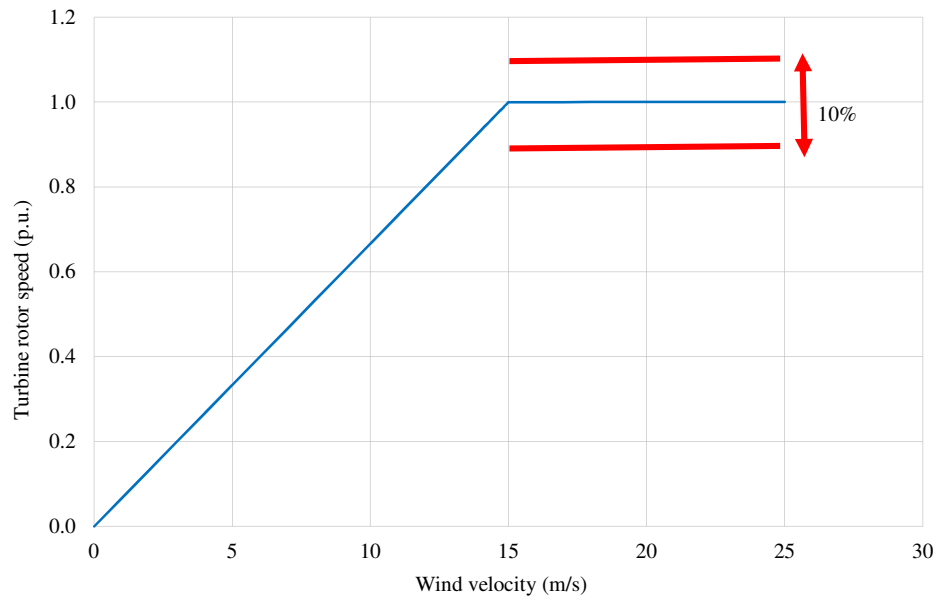


Fig. 2.16. Rotor speed for the Limited Speed Operation region.

Using equation (2.28) -(2.29) and according to Fig. 2.16, following expressions for power- and torque-speed characteristics of a turbine in the Limited Speed Operation are derived:

$$P_t = \begin{cases} 0 & \omega \leq \omega_{cut-in} \\ \frac{1}{2} \rho \pi R^5 \omega^3 \frac{C_p(\lambda, \beta)}{\lambda^3} & \omega_{cut-in} \leq \omega \leq \omega_b \\ P_{nominal} & \omega = \omega_b (\pm \alpha \%) \\ 0 & \text{otherwise} \end{cases} \quad (\text{W}) \quad (2.32)$$

$$T_t = \begin{cases} 0 & \omega \leq \omega_{cut-in} \\ \frac{1}{2} \rho \pi R^5 \omega^2 \frac{C_p(\lambda, \beta)}{\lambda^3} & \omega_{cut-in} \leq \omega \leq \omega_b \\ \frac{P_{nominal}}{\omega_b (\pm \alpha \%)} & \omega = \omega_b (\pm \alpha \%) \\ 0 & \text{otherwise} \end{cases} \quad (\text{N.m}) \quad (2.33)$$

where,

ω_{cut-in} : is the rotor speed at cut-in wind velocity (rad/s)

ω_b : is the rotor rated speed (rad/s)

α : is the percentage of the speed variations around the rated speed

2.4.2 High Speed Operation

Commercial wind turbines normally operate in the Limited Speed Operation region. The High Speed Operating Region is a new control concept, the operation of which is presented in this thesis. For wind velocities up to rated, the operation of the wind turbine in High Speed Region is as that of the Limited Speed Operation scheme. The only difference in the two schemes is when the turbine operates above the rated wind velocity. Therefore, from cut-in to the rated wind velocity, the blade pitch angle is controlled such that maximum power is extracted from the wind and the turbine operates on the MPPT curve. However, for wind velocities above rated, the turbine speed is allowed to increase while harvesting rated power from the wind by controlling the blade pitch angle. By way of example, consider the results shown in Fig. 2.12. At a wind velocity of 15 (m/s) the blade pitch angle is increased to 15° to maintain the turbine power output at 2 MW, i.e. control in the Limited Speed region. However, if the blade pitch angle is held at zero, the turbine rotor would accelerate to $\omega = 4.5$ (rad/s) if the power output was maintained at 2MW. This speed is obviously higher than that at rated wind velocity. The rotor speed at rated wind velocity for the Enercon E-82 is $\omega = 2$ (rad/s). Similarly to harvest 2 MW from the turbine at velocities of 19 m/s (Fig. 2.13) and 25 m/s (Fig. 2.14) and $\beta = 0$, the turbine rotor speed would have to be controlled at $\omega = 5.9$ (rad/s) and $\omega = 8$ (rad/s) respectively. The per unit power-speed and torque-speed characteristic of the wind turbine when operating in the high operation speed region are plotted in Fig. 2.17, where it can be seen that above the rated speed, turbine torque reduces as a result of increased rotor speed at constant power. If, to be consistent with the Limited Speed Operating scheme, the rated turbine rotor speed is referred to as 1 p.u., then for the Enercon E-82 studied here, maintaining the turbine blade pitch angle at zero results in the rotor speed increasing up to 2.66 p.u. at the wind cut-out velocity of 25 m/s. An alternative High Speed Operating regime would be to limit the increase in speed above the rated speed via control of the turbine blade pitch angle. This angle could be modified to limit speed, as illustrated in Fig. 2.17 showing the power-speed (a), and torque-speed (b) profiles for both of the High Speed (HS) Operating regimes, i.e. without (i) and

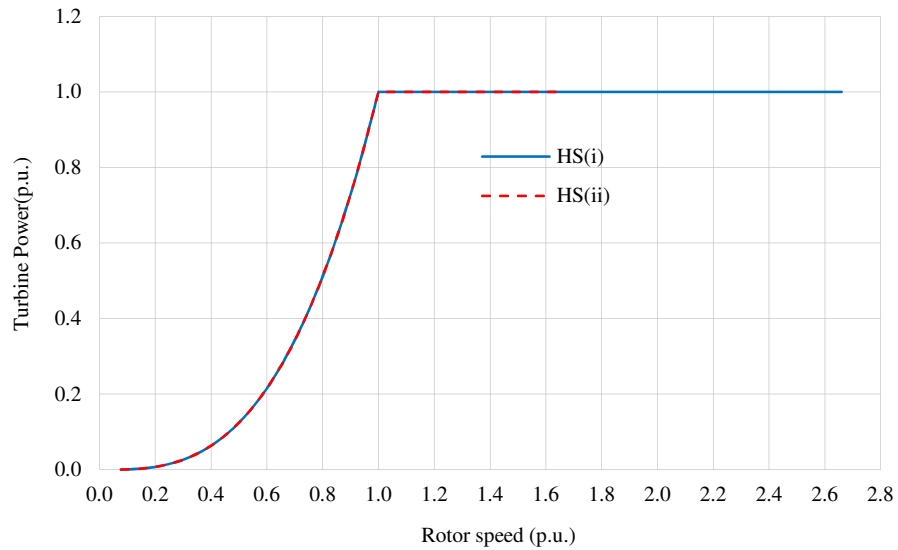
with (ii) blade pitch control. In this example, the highest turbine rotor speed is 2.66 p.u. for HS(i) and 1.67 p.u. for HS(ii).

Fig. 2.18 shows rotor speed with-respect-to wind velocity variation for both the Limited and the two High Speed Operation regimes. According to Fig. 2.17 following expressions for power and torque-speed characteristics of a turbine in the high speed operation regime is derived:

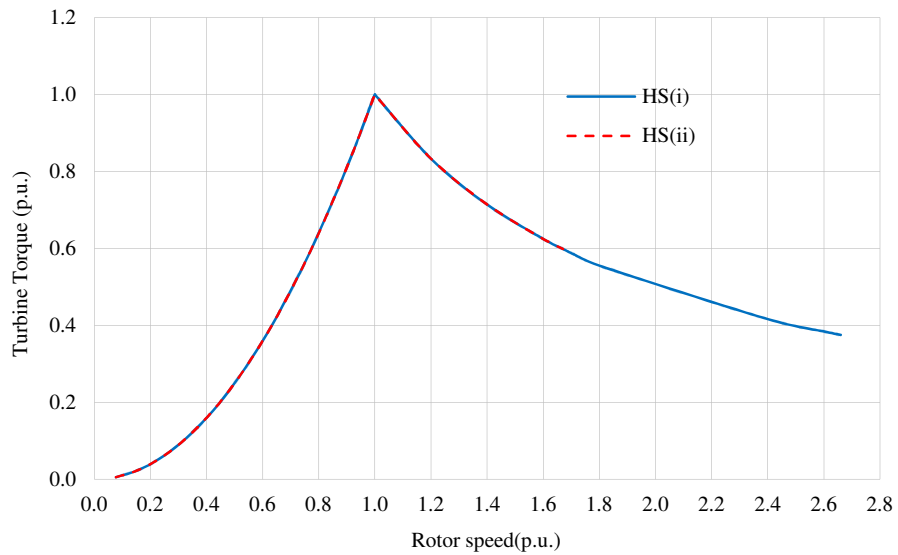
$$P_t = \begin{cases} 0 & \omega < \omega_{cut-in} \\ \frac{1}{2} \rho \pi R^5 \omega^3 \frac{C_p(\lambda, \beta)}{\lambda^3} & \omega_{cut-in} \leq \omega < \omega_b \\ P_{nominal} & \omega_b \leq \omega \leq \omega_{cut-out} \\ 0 & \omega > \omega_{cut-out} \end{cases} \quad (\text{W}) \quad (2.34)$$

$$T_t = \begin{cases} 0 & \omega < \omega_{cut-in} \\ \frac{1}{2} \rho \pi R^5 \omega^2 \frac{C_p(\lambda, \beta)}{\lambda^3} & \omega_{cut-in} \leq \omega < \omega_b \\ \frac{P_{nominal}}{\omega_b (\pm \alpha \%)} & \omega_b \leq \omega \leq \omega_{cut-out} \\ 0 & \omega > \omega_{cut-out} \end{cases} \quad (\text{N.m}) \quad (2.35)$$

The High Speed region of operation is not usually implemented by high power wind turbine system manufacturers, but it has been discussed by Schofield et al [72] for small wind applications (up to 5 kW) where it may be interesting from the machine point of view due to the reduced torque at higher speeds and possible control simplifications. However, a major challenge for this operating regime is the impact of higher rotor speeds on the wind turbine mechanics, the assessment of which is out of the scope of this study and is an area of future research, as captured in Chapter 6. Although the mechanical implementation of the High Speed Operating Regime is not further investigated, the impact of the scheme on generator power-speed and torque-speed specifications is discussed for completeness.



(a) Power versus speed.



(a) Torque versus speed.

Fig. 2.17. Per unit power and torque characteristics of the wind turbine when operating in High Speed region.

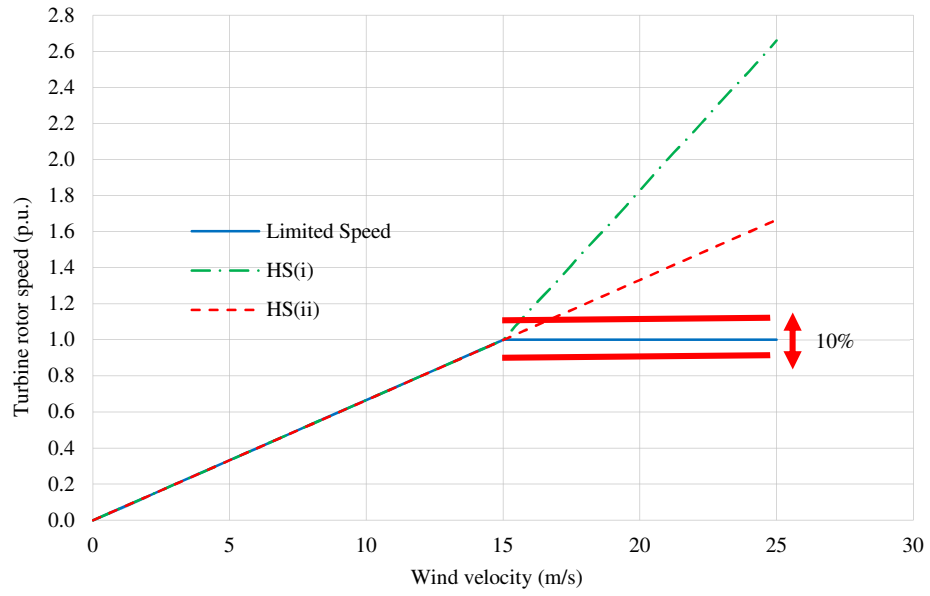


Fig. 2.18. Rotor speed for the Limited and High Speed Operation regions.

2.5 Summary

In this Chapter wind turbines are introduced and the basics of wind energy conversion discussed. Using basic mechanic concepts an expression for harvested wind power is developed from sources in the literature and used to show the Betz limit and the performance of different turbine configurations and designs from which it is confirmed that modern 3-blade turbines yield higher power, hence their utilization by most of high power wind generation industry.

Analytical models for the turbine characteristics including power-speed and torque-speed are derived and mathematical models which may be used in optimization analysis and modelling are given. Public domain data for the Enercon E-82, a commercial 2 MW wind turbine system [11], is used to validate the developed analytic models in the form of a case study exploring the system operational performance. Power-speed, torque-speed, power versus wind velocity at different rotor speeds and turbine power coefficient characteristics of the Enercon E-82 wind turbine are calculated. Two wind turbine operational regimes are explored and presented, the Limited Speed and High Speed schemes. The Limited Speed regime is that which is widely implemented by the wind industry, while the High Speed regime is a new control approach studied in this thesis. In contrast with the Limited Speed regime, the turbine rotor speed is allowed to exceed the rated speed in the High Speed region (hence the rated speed has to be redefined as the base speed) which results in reduced torque, an interesting concept in terms of the generator design. However, for the High Speed operating regime the turbine mechanics would require redesign; hence the mechanics of this concept are not further analyzed and assessed in this thesis.

Chapter 3

Proposed Wind Generation System

3.1 Introduction

In this Chapter a new off-shore wind generation scheme comprising of a high voltage hybrid generator (HG), HVDC interconnections and transmission is proposed. The proposed system is compared with a commercial wind generation system in terms of losses, component count, efficiency and mass. Steady-state analysis is presented to identify the system envelope rating specification requirements, key technology gaps, benefits and system performance. The Walney wind farm [2] is chosen as the commercial benchmark system against which comparisons are made. In this Chapter the Walney wind farm is modelled using operational data from the commercial components, then different loading conditions are investigated by performing load flows. MATLAB code is developed and used to calculate voltages, currents and losses at different points in the network from which system performance is analyzed and assessed. Then, the proposed high voltage system is introduced and modeled. Similar analyses are carried out for the proposed system and comparisons made with the Walney benchmark system.

3.2 Overview of the Walney Off-shore Wind Farm

The Walney wind farm, shown in Fig. 3.1, is at present one of the largest off-shore wind farms in the UK, located in the Irish Sea about 15 km off the UK coast near Barrow-in-

Furness, Cumbria [2]. The total installation consists of two wind farms, Walney 1 and Walney 2, each with 51 turbines giving 102 turbines in total.



Fig. 3.1. Walney off-shore wind farm [2].

The wind turbine arrangements for Walney 1 and Walney 2 are shown in Fig. 3.2. The Walney wind farm turbines are connected to two off-shore substations, one for each farm, via under sea AC cables. The off-shore substations collect the output from all turbines at 33 kV and step-up the voltage to 132 kV for transmission to the on-shore substation using AC cables buried under the sea. The Walney 1 off-shore substation is connected to the UK national grid at Heysham via a 44.4 km long buried cable.

The Walney wind farm is claimed to be operational for 25 years from the start of 2012. Table 3.1 presents summary details of the Walney wind farm while Table 3.2 presents details of the Siemens 3.6 MW wind turbine SWT-3.6-107 which is used in Walney 1 wind farm. In this thesis the Walney 1 wind farm is chosen as a representative commercial benchmark against which the new high voltage scheme is assessed.

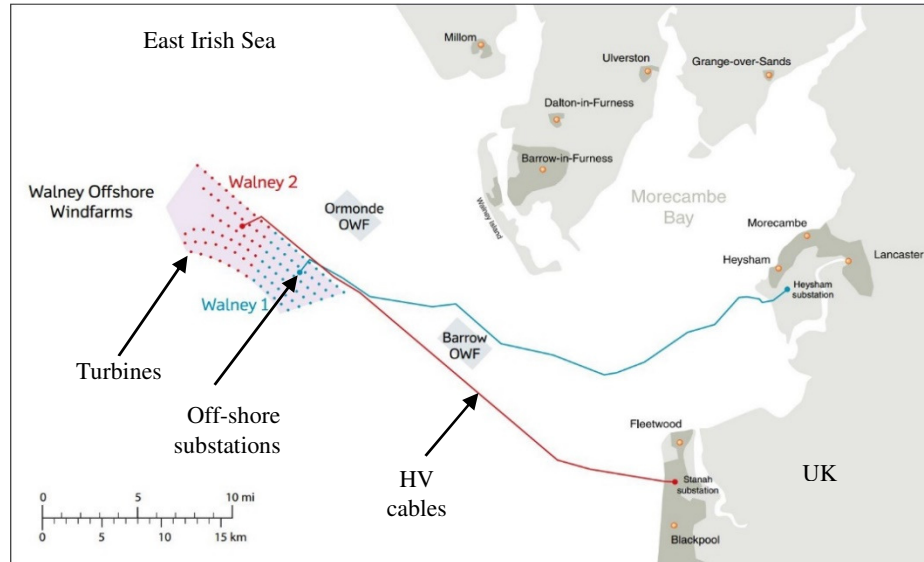


Fig. 3.2. Walney wind farm turbine arrangements [2].

Table 3.1. Summary of Walney wind farm summary of details [2]

Item	Walney 1	Walney 2
Wind turbine type	Siemens SWT-3.6-107	Siemens SWT-3.6-120
Number of turbines	51	51
Output power (MW)	183.6	183.6
Transmission type	MVAC / HVAC	
Operating voltage level (kV)	33 / 132	
Off-shore substation (MVA)	2 × 120	2 × 120
Distance between turbines (m)	749-958	
Distance from sub. to shore (km)	44.4	43.7
Approximate total area (km ²)	34	39
Approximate water depth (m)	21-26	

Table 3.2. Details of Siemens SWT-3.6-107 wind turbine [10]

Operating data	
Cut-in wind speed (m/s)	3-5
Nominal power at (m/s)	13-14
Cut-out wind speed (m/s)	25
Average wind speed at 84 m (m/s)	> 9
Generator, converter and transformer	
Generator type	IG
Generator rated power (MW)	3.6
Generator rated voltage (V)	690 (RMS Line-to-Line)
Generator number of poles	4
Frequency (Hz)	50
Generator rated speed (RPM)	1500
Power electronic converter	Full scale back-to-back VSCs
Location of VSC's	One in nacelle, one in tower
Turbine transformer location	Tower base
Transformer voltage ratio (kV)	47.83 (=0.69/33)
Rotor	
Rotor speed (RPM)	5-13
Rotor diameter (m)	107
Blade length (m)	52
Rotor type	3-blade horizontal axis
Rotor position	Upwind
Hub height	83.5 m
Power regulation	Full span pitch regulation
Gearbox ratio	1:119
Gearbox type	3-stage planetary/helical
Mechanical brake	Hydraulic disc brake

Fig. 3.3 simply illustrates the electrical installation of the Walney 1 wind farm showing the major system components. The power-train in this system uses an induction generator (IG) that is interfaced to the fixed frequency grid via two fully rated VSC's (Converter 1 and Converter 2) in a back-to-back configuration. The two VSCs decouple the IG output from the fixed-frequency, (essentially) fixed-voltage grid facilitating variable speed operation of the wind turbine. The maximum rated output voltage of each IG is 690 V. This is converted via the two VSC's to DC and then back to a 690 V maximum, 3-phase voltage that is stepped-up to 33 kV by a transformer located in the turbine tower base. VSCs are bulky and costly for high voltage and high power applications. In fact, the power electronic switching devices that are the building blocks of the VSCs in the Walney system are not commercially available to-date at high voltages, hence high voltage, high power VSCs necessitate series connected, modular or multilevel structures to realize the voltage requirements and a number of parallel units to achieve the required power levels. This is one factor that constrains the wind industry to low voltage commercial industrial VSC designs and the necessary step-up transformer to realize reasonable transmission voltage levels. Further, VSCs also have reliability issues in terms of passive capacitors sited on the DC-link. These components are one of the major causes of failure in industrial VSC drive systems [73] compromising wind turbine service life and necessitating maintenance/refit schedules. Given the low voltage nature of the wind energy conversion, high currents have to be handled in the turbine tower; currents in the order of 3,000 Amps for each 3.6 MW turbine as discussed later.

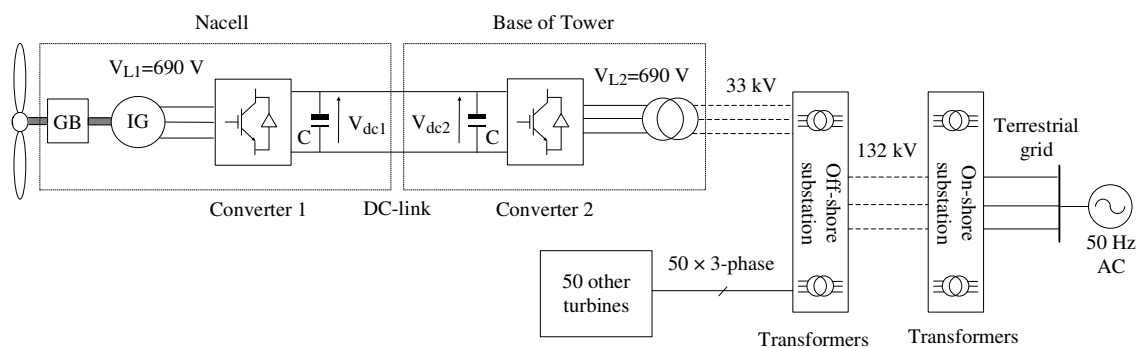


Fig. 3.3. Walney wind turbine connection to terrestrial grid.

3.3 Walney System Component Model

The site layout for the Walney 1 wind farm is illustrated in Fig. 3.4. Walney 1 consist of six circuits. Circuit 1 and Circuit 2 have six and five wind turbines respectively whereas the other circuits have 10 turbines. The electrical single line diagram of Walney 1 is illustrated in Fig. 3.5 showing the detailed components of Circuit 2. Each turbine is equipped with an induction generator, two back-to-back VSC's, Converter 1 and Converter 2, and a transformer. The IG and Converter 1, Fig. 3.5, are located in the Nacelle while Converter 2 and transformer are at the bottom of turbine tower. In this section models for all the component are presented.

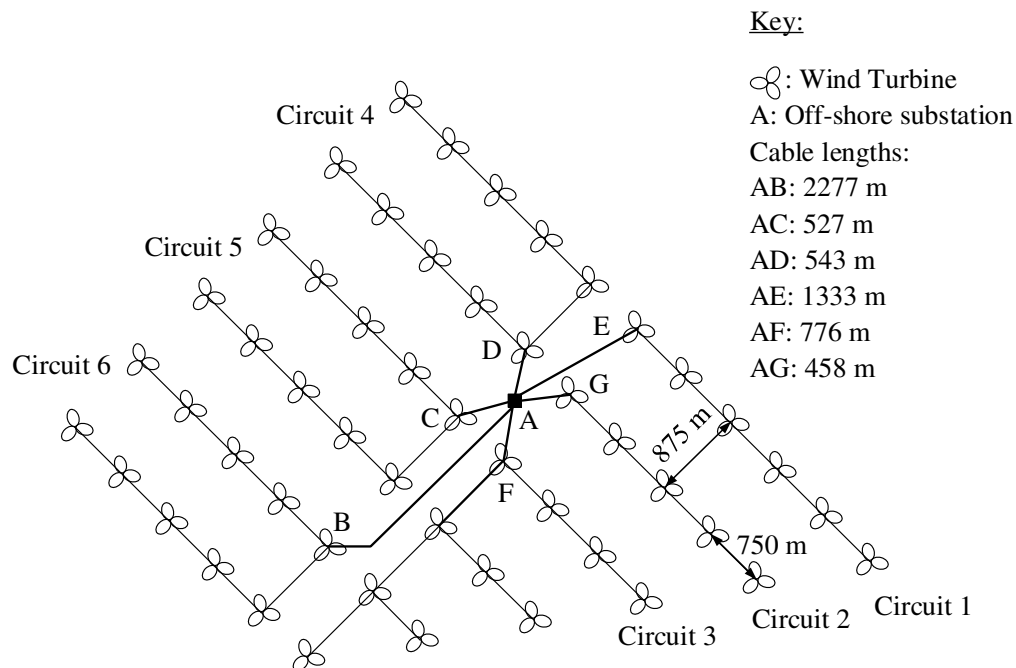


Fig. 3.4. Walney 1 site layout.

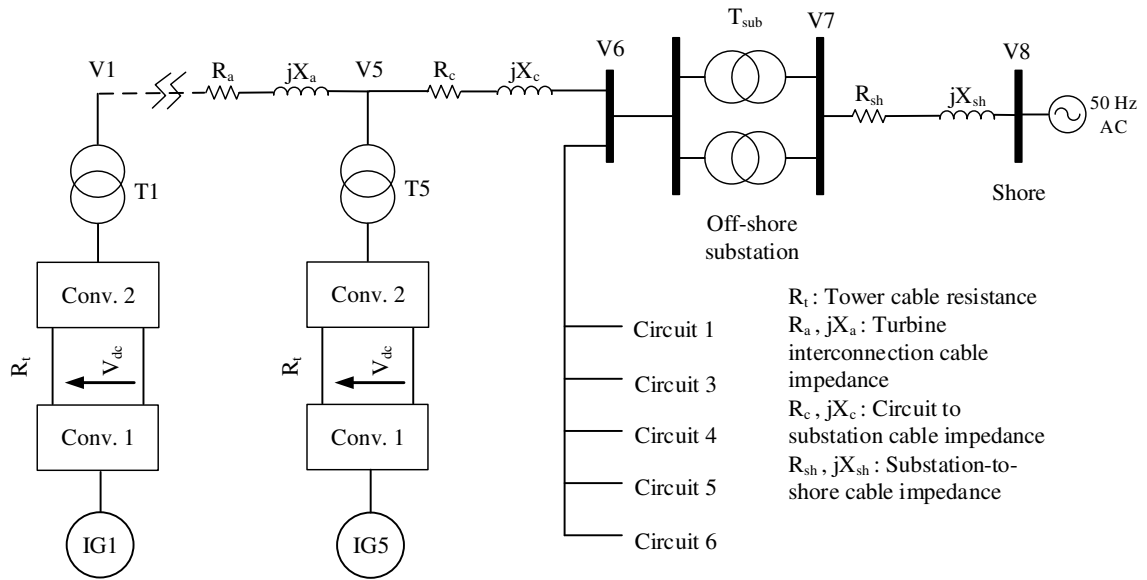


Fig. 3.5. Walney 1 site layout.

3.3.1 Induction Generator (IG) Model

The turbine generators used in Walney 1 are squirrel cage IG manufactured by Siemens, the conventional, balanced per-phase, steady-state equivalent circuit model for which is as shown in Fig. 3.6 and parameters listed in Table 3.3 [10].

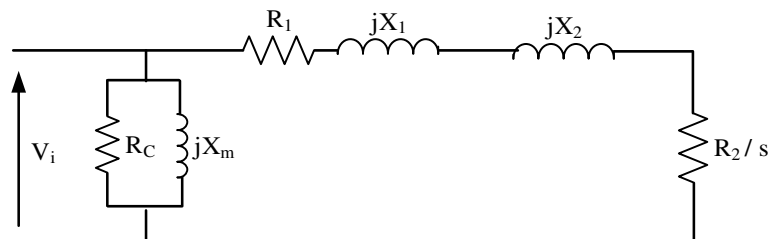


Fig. 3.6. Balanced, per-phase, steady-state equivalent circuit IG model.

Table 3.3. Induction generator (IG) parameters [10]

Description	Parameter	Value (Ω)
Stator resistance	R_1	0.0019
Rotor resistance referred to stator	R_2	0.0019
Loss resistance	R_c	4.41
Magnetizing reactance	X_m	1.16
Stator leakage reactance	X_1	0.048
Rotor leakage reactance referred to stator	X_2	0.035

3.3.2 VSC Model

Referring to Fig. 3.5 the two power electronic VSC's decouple the variable frequency output of the generator from the fixed frequency grid. Converter 1 controls the speed of the generator to extract the maximum power from the wind via MPPT while Converter 2 regulates the DC-link voltage to keep it constant. Converter 2 therefore maintains a constant DC-link voltage at all times, i.e. from full-load to no-load. Thus, all circuits from the DC-link to the point of connection at the on-shore grid are always excited to full nominal voltage. Pulse Width Modulation (PWM) vector control of the two VSC's is implemented to maximize power conversion of the induction generator and the DC-link to AC output of Converter 2. Converter 1 is placed in the nacelle while Converter 2 is located at the bottom of the turbine tower adjacent to the tower transformer. The output of Converter 2 is synchronized to the on-shore 50 Hz grid. The back-to-back VSC model is presented in Fig. 3.7. Each converter consists of three phase legs and there are two power electronic switching devices, e.g. S1 and S2, per leg. To allow higher power each power electronic switch consists of a number Insulated-Gate Bipolar Transistors (IGBT's). The anti-parallel diodes, e.g. D1 and D2, are freewheeling diodes that allow the flow of reverse energy when appropriate. The PWM signals for the IGBT's gates are generated by comparing a control

(modulating) signal which is essentially normalized phase voltage of the AC terminals with a high frequency saw-tooth (triangular) carrier signal. Note, in the industry these power electronic switching devices are often referred to as valves, a throw-back to earlier valve technologies. In the steady-state system analysis presented later the VSC's are modeled via their input, output and efficiencies.

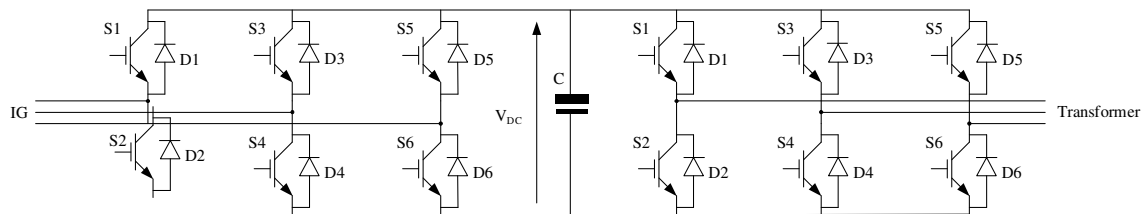


Fig. 3.7. VSC model.

3.3.3 Transformer Model

Each turbine has an associated 4.5 MVA, 0.69/33 kV tower mounted transformer manufactured by Siemens. Further, the off-shore substation has 2 transformers each rated at 120 MVA, 33/132 kV manufactured by ABB. The conventional, balanced, per-phase equivalent circuit used to model the turbine and the off-shore substation transformers is shown in Fig. 3.8 and their parameters are listed in Table 3.4. Note, that the output of Converter 2 is fixed at on-shore electrical utility grid frequency of 50 Hz.

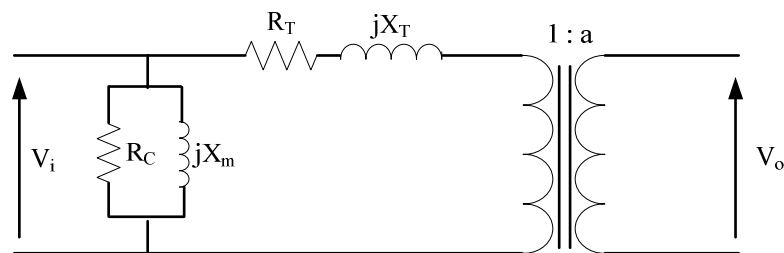


Fig. 3.8. Balanced, per-phase, steady-state transformer equivalent circuit model.

Table 3.4. Transformer parameters at 50 Hz [10], [74]

Description	Parameter	Value	
		Turbine transformer	Substation transformer
Rated power (MVA)	-	4.5	2 × 120
Rated voltage (kV)	-	0.69 / 33	33 / 132
No load losses (kW)	-	3.7	63.3
Load losses (kW)	-	46.5	370
Percentage impedance (%)	-	6.4	10.5
Iron loss resistance (Ω)	R_c	128.68	1741.71
Magnetizing reactance (Ω)	X_m	10.62	213.5
Transformer equivalent resistance referred to primary (Ω)	R_T	0.001	0.002
Transformer equivalent leakage reactance referred to primary (Ω)	X_T	0.00677	0.089
Transformer ratio	a	$\frac{33}{0.69} = 47.83$	$\frac{132}{33} = 4$

3.3.4 AC Cables Model

The inter-array cables connecting the turbines in Fig. 3.4 are composed of 3×150 mm² copper conductors while each circuit is connected to the off-shore substation using a cable composed of 3×500 mm² copper conductors. The cable connecting the off-shore substation to shore is 44.4 km in length and is composed of 3×630 mm² copper conductors. The balanced, per-phase Pi (π) equivalent circuit model of the cables is shown in Fig. 3.9 and their parameters are listed in Table 3.5.

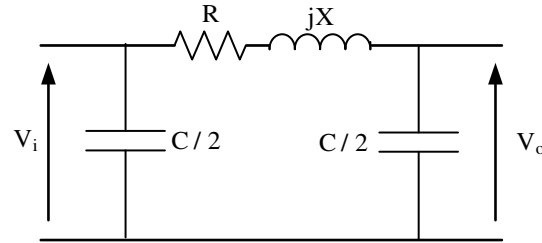


Fig. 3.9. Cable balanced, per-phase, steady-state, Pi equivalent circuit model.

Table 3.5. Cable equivalent circuit parameters at 50 Hz [75-76]

Description/ Parameters		Circuit 2		Off-shore substation to on-shore
		Inter-array between turbines	Inter-array to off- shore substation	
Cable length (km)	-	0.75	0.458	44.4
Material	-	Copper		
Cable size (mm ²)	-	3 × 150	3 × 500	3 × 630
Rated voltage (kV)	-	33	33	132
AC resistance (Ω /km)	R	0.16	0.0515	0.028
Reactance (Ω /km)	X	0.116	0.0974	0.116
Capacitance (μF /km)	C	0.191	0.3	0.21

3.3.5 DC-link Model

The connection between Converter 1 and Converter 2 is via a DC-link. Information for the DC-link cable was not accessible to the author. Therefore, in order to calculate the DC-link cable impedance, the DC-cable cross section of the DC-cable is estimated using voltage

and power information as follows. Considering the PWM switching scheme for the VSC the DC-link voltage at the output of the Converter 1, Fig. 3.5, is given by [77]:

$$V_{dc1} = \frac{2\sqrt{2}}{\sqrt{3}m_{a1}} V_{L1} \quad (\text{V}) \quad (3.1)$$

where,

V_{L1} : is the IG RMS line-to-line voltage fundamental component

m_{a1} : is amplitude modulation index for Converter 1

The amplitude modulation index is defined as the ratio of amplitudes of control signal over carrier signal. Alternatively, the amplitude modulation index can be defined as the ratio of the IG operating speed over maximum speed where a simple V/f control scheme is implemented:

$$m_{a1} = \frac{\hat{V}_{control}}{\hat{V}_{tri}} = \frac{\omega_{gen}}{\omega_{max}} \quad (3.2)$$

where,

$\hat{V}_{control}$: is the amplitude of the control signal

\hat{V}_{tri} : is the amplitude of the carrier signal

ω_{gen} : is the IG operating speed

ω_{max} : is the IG maximum speed

The DC-link current is calculated as follows:

$$I_{dc} = \frac{P_{dc1}}{V_{dc1}} \quad (\text{A}) \quad (3.3)$$

where P_{dc1} is the input active power to the DC-link from Converter 1.

The average current through the DC-link capacitor is zero therefore the DC current throughout the entire length of the DC-link is the same. Assuming operation at the maximum IG output speed and voltage, the output DC link voltage from Converter 1 is 1126.77 V. The two capacitors in the DC-link support a constant DC-link voltage and reduce voltage ripple. Note that the IG is assumed to be closely connected to Converter 1

such that the resistances of the connecting inter-leads are negligible. Considering a maximum generated power output of each IG of 3.6 MW, the DC-link cable conductor cross-section area and resistance are thus calculated [78]:

$$A_{dc} = \frac{I_{dc}}{J_{dc}} \quad (\text{mm}^2) \quad (3.4)$$

$$R_{dc} = \frac{\rho_{cu} l_{dc}}{A_{dc}} \quad (\Omega) \quad (3.5)$$

where,

ρ_{cu} : is the electrical resistivity of the DC-link cable

l_{dc} : is the DC-link cable length that runs from the nacelle to the bottom of the tower

J_{dc} : is the DC-link cable current density that is assumed to be 1.0 A/mm² i.e. the same as the AC cables current density in order to have the same thermal performance for the cables.

The power loss and voltage drop in the DC-link cable are calculated from:

$$P_{loss-dc} = 2 R_{dc} I_{dc}^2 \quad (\text{W}) \quad (3.6)$$

$$V_{dc2} = V_{dc1} - 2 R_{dc} I_{dc} \quad (\text{V}) \quad (3.7)$$

where the factor 2 is due to the sum of the resistances of the two equal cable conductors in the DC-link i.e. the go and return conductors. The DC-link calculation results are given in Table 3.6.

Table 3.6. DC-link calculations

Parameter	Description	Value
V_{L1}	IG RMS Line voltage (V)	690
m_{a1}	Converter 1 Modulation index	1.0
V_{dc1}	Converter 1 DC-link voltage (V)	1126.77
P_{dc1}	Input power to the DC-link (MW)	3.6
I_{dc}	DC-link current (A)	3195
J_{dc}	DC-link cable current density (A/mm ²)	1.0
A_{dc}	DC-link cable cross-section area (mm ²)	3195
ρ_{cu}	Copper resistivity ($\mu\Omega\text{m}$)	0.0172
l_{dc}	DC cable length (m)	83.5
R_{dc}	DC-link cable resistance (m Ω)	0.45
V_{dc2}	Converter 2 DC-link voltage (V)	1123.9
ΔV_{dc}	DC-link voltage drop (V)	2.87
$P_{loss-dc}$	DC-link power loss (kW)	9.2

3.4 Walney System Analysis at Different Loads

The Walney 1 wind farm has been modeled using equivalent models for the induction generator, power electronic converters, DC-link cables, transformer and cables as discussed previously. MATLAB programs have been written to perform the system power flow study. Different loading conditions were studied and analysis conducted with the following assumptions:

- (1) The distance between the induction generator and Converter 1 in the nacelle is negligible and hence neglected.
- (2) The distance between Converter 2 and the transformer at the bottom of the tower is also negligible and hence neglected.
- (3) Converter 2 is controlled to deliver a unity power factor output for all turbines and at all loading conditions, except for the no-load case.
- (4) Therefore, based on (3), all of the circuits connect to the off-shore substation with the same power factor.
- (5) The length of the undersea transmission cable is the distance from the off-shore substation to an immediate substation on-shore. In other words, the distance that might exist from the shore termination station to the on-shore substation is not considered.
- (6) The turbines produce no power at no-load hence, since the system is energized, the power to supply the system losses, monitoring, measuring devices and for other ancillary services is taken from the on-shore grid to which the wind farm is connected.

3.4.1 Full-load Results

The results of the system analysis at full-load operation is presented in Tables 3.7 and 3.8. Here, full-load assumes that all the IG's in the wind farm generate 3.6 MW to their respective Converter 1. Full-load condition may occur when the turbines are operating within a certain wind velocity range i.e. between 13-25 (m/s) for Siemens SWT-3.6-107

wind turbine. The frequency of this loading condition is not considered here since the primary objective of the analysis is to deduce the system operating envelope.

Table 3.7. Walney 1, full-load analysis results: voltages and currents

Turbine					
Turbine No.	1	2	3	4	5
IG line voltage (V)	690	689.7	689.2	688.4	687.37
IG phase current (A)	3075.7	3076.9	3079.2	3082.7	3087.5
DC-link voltage at Converter 2 (V)	1123.9	1123.5	1122.6	1121.3	1119.6
DC-link current (A)	3052.65				
Converter 2 line voltage (V)	688.24	687.98	687.45	686.7	685.61
Converter 2 power factor	1.0				
Converter 2 phase current (A)	2835	2836	2838.2	2841.4	2845.8
Transformer output voltages and currents					
Phase voltage and angle (kV), (deg.)	18.90, -2.79	18.89, -2.80	18.88, -2.84	18.86, -2.89	18.83, -2.95
Transformer line voltage (kV)	32.74	32.73	32.71	32.67	32.62
Power factor (leading)	0.9981	0.9981	0.9980	0.9980	0.9979
Phase current (A)	59.22	59.24	59.28	59.35	59.45
Inputs at the off-shore substation					
Phase voltage and angle (kV, degrees)	18.83, -2.99				
Input line voltage at the off-shore substation (kV)	32.61				
Power factor	1.0				
Phase current from Circuit 2 (A)	296.30				
Outputs from the off-shore substation					
Phase voltage and angle (kV, degrees)	75.34, -3.40				
Off-shore substation line voltage (kV)	130.48				
Phase current (A)	751.46				
Power factor (leading)	0.998				
Inputs at the on-shore substation					
Phase voltage and angle (kV, degrees)	74.19, -6.33				
Line voltage at the on-shore substation (kV)	128.50				
Power factor (lagging)	0.99				
Phase current (A)	763.10				

Table 3.8. Walney 1, full-load analysis results: power and losses

Power and losses in the nacelle and tower					
Turbine power (kW)		3,600			
IG output power (kW)		3,492			
Converter 1 output power (kW)		3,439.62			
Converter 2 output power (kW)		3,379.39			
IG efficiency (%) and losses (kW)		97	108.00		
Converter 1 efficiency (%) and losses (kW)		98.5	52.38		
Converter 2 efficiency (%) and losses (kW)		98.5	51.46		
DC-link power loss (kW)		8.77			
Turbine transformer efficiency (%)		99.18			
Turbine transformer loss					
Transformer No.	1	2	3	4	5
Loss (kW)	27.74	27.76	27.79	27.84	27.90
Turbine link cable					
From--to	1 to 2		2 to 3	3 to 4	4 to 5
Inter-array cable loss (kW)	1.26		5.05	11.36	20.21
Cable loss, Circuit 2 to the off-shore substation (kW)					6.21
Input power and losses at off-shore sub. from Circuit 2					
Power (kW)	16,713.83		Losses (kW)	1,286.17	
Input power and losses at off-shore sub. from Circuits 1-6					
Power (kW)	170,481.05		Losses (kW)	13,118.95	
Off-shore substation transformers efficiency (%)					99.27
Loss at off-shore substation (kW)					1,248.35
Cable losses, Off-shore to on-shore substations (kW)					2,110.20
Total power at on-shore substation (kW)					167,346.54
Total losses at on-shore substation (kW)					16,477.50
Total system efficiency (%)					91.15

Referring to the system schematic shown in Fig. 3.5 and the results of Tables 3.7 and 3.8, the following points are observed from the system full-load analysis:

- (1) The scalar voltage drop from the first turbine to the off-shore substation input is 0.4% at full-load, i.e.:

$$\left(\frac{V_1 - V_6}{V_1} \right) 100 = \left(\frac{32.74 - 32.61}{32.74} \right) 100 = 0.4 \% \quad (3.8)$$

This is a considerably small drop voltage resulting in a small voltage difference at the output of each turbine.

- (2) The phase voltage angle decreases from the turbines to the off-shore substation and from the off-shore substation to the on-shore substation, i.e.:

$$\begin{aligned} \text{angle} (V_1) > \text{angle} (V_2) > \text{angle} (V_3) > \text{angle} (V_4) > \\ \text{angle} (V_5) > \text{angle} (V_6) > \text{angle} (V_7) > \text{angle} (V_8) \end{aligned} \quad (3.9)$$

This results in an active power flow from Turbine 1 to the off-shore substation and from the off-shore substation to the on-shore at full-load operation.

- (3) The power factor at the output of the turbine transformer is leading as defined by the measurements at the transformer terminals assuming transformer-to-shore power flow. Moreover, the power factor at the output bus-bar of the off-shore substation is leading resulting in reactive power being absorbed by the off-shore substation. The power factor at the on-shore bus-bar is lagging. Therefore, the line capacitance of the cable connecting the off-shore substation to the on-shore substation is providing some the reactive compensation for the system at full-load operation.

- (4) Loss analysis shows that:

- The total loss for the Walney 1 system is 16,477.50 kW.
- Circuits 1-6 loss contribute to 79.62% of the total loss.
- The two off-shore substation transformers contribute to 7.58% of the total loss.
- Losses in the cable connecting the off-shore to on-shore substations contribute to 12.80% of the total loss.
- Walney 1 efficiency is 91.15% at full-load.

The off-shore substation and the cable connecting the off-shore substation to the on-shore bus-bar make up a large portion of the total system loss at full-load operation. Note that the result is specific to this benchmark system and is not to be a generic conclusion for other systems.

3.4.2 Results for Three-quarter-, Half- and One-quarter- Load

Power flow results for the Walney wind farm at three-quarter-, half- and one-quarter-load are presented in Tables 3.9 to 3.14. At three-quarter-load generator power is 2.7 MW while the generator produces 1.8 MW and 0.9 MW at half- and quarter-loads respectively. Note that the PWM vector control of the IG by Converter 1 keeps a constant 97% efficiency for the machine as the load changes. Also, the efficiency of the VSC's for other loads is the assumed to be same as full-load i.e. 98.5 % [79].

Table 3.9. Walney 1, three-quarter-load analysis results: voltages and currents

Turbine					
Turbine No.	1	2	3	4	5
IG line voltage (V)	690	689.80	689.41	688.82	688.04
IG phase current (A)	2306.76	2307.41	2308.72	2310.70	2313.33
DC-link voltage at Converter 2 (V)	1123.89	1123.57	1122.93	1121.97	1120.69
DC-link current (A)	2289.49				
Converter 2 line voltage (V)	688.24	688.05	687.65	687.07	686.28
Converter 2 power factor	1.0				
Converter 2 phase current (A)	2126.17	2126.77	2127.99	2129.81	2132.25
Transformer output voltages and currents					
Phase voltage and angle (kV), (deg.)	18.93, -2.09	18.92, -2.10	18.91, -2.12	18.90, -2.16	18.88, -2.21
Transformer line voltage (kV)	32.78	32.77	32.76	32.73	32.69
Power factor	1				
Phase current (A)	44.40	44.41	44.44	44.48	44.53
Inputs at the off-shore substation					
Phase voltage and angle (kV, degrees)	18.87, -2.24				
Input line voltage at the off-shore substation (kV)	32.68				
Power factor	1.0				
Phase current from Circuit 2 (A)	222.06				
Outputs from the off-shore substation					
Phase voltage and angle (kV, degrees)	75.51, -2.54				
Off-shore substation line voltage (kV)	130.78				
Phase current (A)	562.61				
Power factor (leading)	0.997				
Inputs at the on-shore substation					
Phase voltage and angle (kV, degrees)	74.54, -4.71				
Line voltage at the on-shore substation (kV)	129.11				
Power factor (lagging)	0.97				
Phase current (A)	582.34				

Table 3.10. Walney 1, three-quarter-load analysis results: power and losses

Power and losses in the nacelle and tower					
Turbine power (kW)			2,700		
IG output power (kW)			2,619		
Converter 1 output power (kW)			2,579.72		
Converter 2 output power (kW)			2,534.54		
IG efficiency (%) and losses (kW)			97	81.00	
Converter 1 efficiency (%) and losses (kW)			98.5	39.29	
Converter 2 efficiency (%) and losses (kW)			98.5	38.60	
DC-link power loss (kW)			6.58		
Turbine transformer efficiency (%)			99.32		
Turbine transformer loss					
Transformer No.	1	2	3	4	5
Loss (kW)	17.21	17.21	17.22	17.24	17.27
Turbine link cable					
From--to	1 to 2		2 to 3	3 to 4	4 to 5
Inter-array cable loss (kW)	0.71		2.84	6.38	11.35
Cable loss, Circuit 2 to the off-shore substation (kW)					3.49
Input power and losses at off-shore sub. from Circuit 2					
Power (kW)	12,561.79		Losses (kW)	938.21	
Input power and losses at off-shore sub. from Circuits 1-6					
Power (kW)	128,130.21		Losses (kW)	9,569.79	
Off-shore substation transformers efficiency (%)					99.03
Loss at off-shore substation (kW)					1,241.92
Cable losses, Off-shore to on-shore substations (kW)					1,186.61
Total power at on-shore substation (kW)					125,792.79
Total losses at on-shore substation (kW)					11,998.32
Total system efficiency (%)					91.35

The voltage drops from turbine one to the off-shore substation at different loads is:

$$(1) \text{ Three-quarter load: } \left(\frac{V_1 - V_6}{V_1} \right) 100 = \left(\frac{32.78 - 32.68}{32.78} \right) 100 = 0.31 \% \quad (3.10)$$

$$(2) \text{ Half load: } \left(\frac{V_1 - V_6}{V_1} \right) 100 = \left(\frac{32.83 - 32.76}{32.83} \right) 100 = 0.21 \% \quad (3.11)$$

$$(3) \text{ one-quarter load: } \left(\frac{V_1 - V_6}{V_1} \right) 100 = \left(\frac{32.88 - 32.85}{32.88} \right) 100 = 0.1 \% \quad (3.12)$$

Therefore, as the load decreases the voltage drop from the turbines to the off-shore substation reduces. Hence, as the load decreases the system nodal voltages increase. For all loads the absolute value of the voltage angle decreases from turbine to the on-shore substation.

Table 3.11. Walney 1, half-load analysis results: voltages and currents

Turbine					
Turbine No.	1	2	3	4	5
IG line voltage (V)	690	689.87	689.61	689.22	688.70
IG phase current (A)	1537.84	1538.13	1538.70	1539.57	1540.74
DC-link voltage at Converter 2 (V)	1123.89	1123.68	1123.26	1122.62	1121.77
DC-link current (A)	1526.32				
Converter 2 line voltage (V)	688.24	688.11	687.85	687.46	686.94
Converter 2 power factor	1.0				
Converter 2 phase current (A)	1417.45	1417.71	1418.25	1419.05	1420.12
Transformer output voltages and currents					
Phase voltage and angle (kV), (deg.)	18.95, -1.39	18.95, -1.40	18.94, -1.41	18.93, -1.44	18.92, -1.47
Transformer line voltage (kV)	32.83	32.82	32.81	32.79	32.77
Power factor	1				
Phase current (A)	29.58	29.59	29.60	29.62	29.64
Inputs at the off-shore substation					
Phase voltage and angle (kV, degrees)					18.92, -1.49
Input line voltage at the off-shore substation (kV)					32.76
Power factor					1.0
Phase current from Circuit 2 (A)					147.87
Outputs from the off-shore substation					
Phase voltage and angle (kV, degrees)					75.69, -1.69
Off-shore substation line voltage (kV)					131.10
Phase current (A)					374.37
Power factor (leading)					0.99
Inputs at the on-shore substation					
Phase voltage and angle (kV, degrees)					74.92, -3.10
Line voltage at the on-shore substation (kV)					129.76
Power factor (lagging)					0.91
Phase current (A)					407.84

Table 3.12. Walney 1, half-load analysis results: power and losses

Power and losses in the nacelle and tower					
Turbine power (kW)			1,800		
IG output power (kW)			1,746.00		
Converter 1 output power (kW)			1,719.81		
Converter 2 output power (kW)			1,689.69		
IG efficiency (%) and losses (kW)		97	54.00		
Converter 1 efficiency (%) and losses (kW)		98.5	26.19		
Converter 2 efficiency (%) and losses (kW)		98.5	25.73		
DC-link power loss (kW)			4.38		
Turbine transformer efficiency (%)			99.43		
Turbine transformer loss					
Transformer No.	1	2	3	4	5
Loss (kW)	9.69	9.69	9.69	9.69	9.70
Turbine link cable					
From--to		1 to 2	2 to 3	3 to 4	4 to 5
Inter-array cable loss (kW)		0.31	1.26	2.83	5.04
Cable loss, Circuit 2 to the off-shore substation (kW)					1.55
Input power and losses at off-shore sub. from Circuit 2					
Power (kW)	8,389.03		Losses (kW)	610.97	
Input power and losses at off-shore sub. from Circuits 1-6					
Power (kW)	85,568.13		Losses (kW)	6,231.87	
Off-shore substation transformers efficiency (%)			98.55		
Loss at off-shore substation (kW)			1,239.36		
Cable losses, Off-shore to on-shore substations (kW)			530.17		
Total power at on-shore substation (kW)			83,822.82		
Total losses at on-shore substation (kW)			8,001.40		
Total system efficiency (%)			91.31		

For all loads the IG's receive reactive power. Transformer reactive power is off-set by the interconnection line capacitance. The power factor at the off-shore substation input is unity for all loads, however the off-shore substation output power factor is leading. Therefore, for all loads reactive power for the off-shore substation transformers is being supplied by the transmission line capacitance connecting the off-shore to on-shore substation. Nonetheless, the power factor at the on-shore substation is lagging which means the wind farm injects reactive power to the grid.

The total system efficiency for different loads is:

$$(1) \text{ Three-quarter load: } \quad 91.35 \% \quad (3.13)$$

$$(2) \text{ Half load: } \quad 91.31 \% \quad (3.14)$$

$$(3) \text{ One-quarter load: } \quad 90.23 \% \quad (3.15)$$

The system efficiency reduces slightly as the load is decreased. Hence, similar benefits and system performance is seen at all loads. However, note that the IG and VSC efficiencies are kept constant at all loads.

Table 3.13. Walney 1, one-quarter-load analysis results: voltages and currents

Turbine					
Turbine No.	1	2	3	4	5
IG line voltage (V)	690	689.94	689.81	689.62	689.36
IG phase current (A)	768.92	768.99	769.13	769.35	769.64
DC-link voltage at Converter 2 (V)	1123.89	1123.79	1123.58	1123.27	1122.85
DC-link current (A)	763.16				
Converter 2 line voltage (V)	688.24	688.18	688.05	687.86	687.60
Converter 2 power factor	1.0				
Converter 2 phase current (A)	708.72	708.79	708.92	709.12	709.39
Transformer output voltages and currents					
Phase voltage and angle (kV), (deg.)	18.98, -0.69	18.98, -0.70	18.98, -0.71	18.97, -0.72	18.97, -0.73
Transformer line voltage (kV)	32.88	32.88	32.87	32.86	32.85
Power factor	1				
Phase current (A)	14.77	14.78	14.78	14.78	14.79
Inputs at the off-shore substation					
Phase voltage and angle (kV, degrees)					18.96, -0.74
Input line voltage at the off-shore substation (kV)					32.85
Power factor					1.0
Phase current from Circuit 2 (A)					73.75
Outputs from the off-shore substation					
Phase voltage and angle (kV, degrees)					75.89, -0.84
Off-shore substation line voltage (kV)					131.44
Phase current (A)					188.13
Power factor (leading)					0.97
Inputs at the on-shore substation					
Phase voltage and angle (kV, degrees)					75.33, -1.50
Line voltage at the on-shore substation (kV)					130.47
Power factor (lagging)					0.73
Phase current (A)					252.59

Table 3.14. Walney 1, one-quarter-load analysis results: power and losses

Power and losses in the nacelle and tower					
Turbine power (kW)			900		
IG output power (kW)			873.00		
Converter 1 output power (kW)			859.90		
Converter 2 output power (kW)			844.85		
IG efficiency (%) and losses (kW)			97	27.00	
Converter 1 efficiency (%) and losses (kW)			98.5	13.10	
Converter 2 efficiency (%) and losses (kW)			98.5	12.87	
DC-link power loss (kW)			2.19		
Turbine transformer efficiency (%)			99.39		
Turbine transformer loss					
Transformer No.	1	2	3	4	5
Loss (kW)	5.18	5.18	5.18	5.18	5.18
Turbine link cable					
From--to		1 to 2	2 to 3	3 to 4	4 to 5
Inter-array cable loss (kW)		0.08	0.31	0.70	1.25
Cable loss, Circuit 2 to the off-shore substation (kW)					0.38
Input power and losses at off-shore sub. from Circuit 2					
Power (kW)	4,195.61		Losses (kW)	304.39	
Input power and losses at off-shore sub. from Circuits 1-6					
Power (kW)	42,795.27		Losses (kW)	3,104.73	
Off-shore substation transformers efficiency (%)			97.10		
Loss at off-shore substation (kW)			1,240.68		
Cable losses, Off-shore to on-shore substations (kW)			140.31		
Total power at on-shore substation (kW)			41,415.46		
Total losses at on-shore substation (kW)			4,485.71		
Total system efficiency (%)			90.23		

3.5 Proposed Off-shore HVDC Wind Generation System

The preceding section analyzed the Walney benchmark system against which the proposed HVDC wind generation scheme is compared. The proposed HVDC wind generation scheme comprises of a high voltage HG, passive rectification, DC/DC converters, HVDC interconnection and HVDC transmission systems. A schematic view of the proposed system based on the Walney wind farm is illustrated in Fig. 3.10.

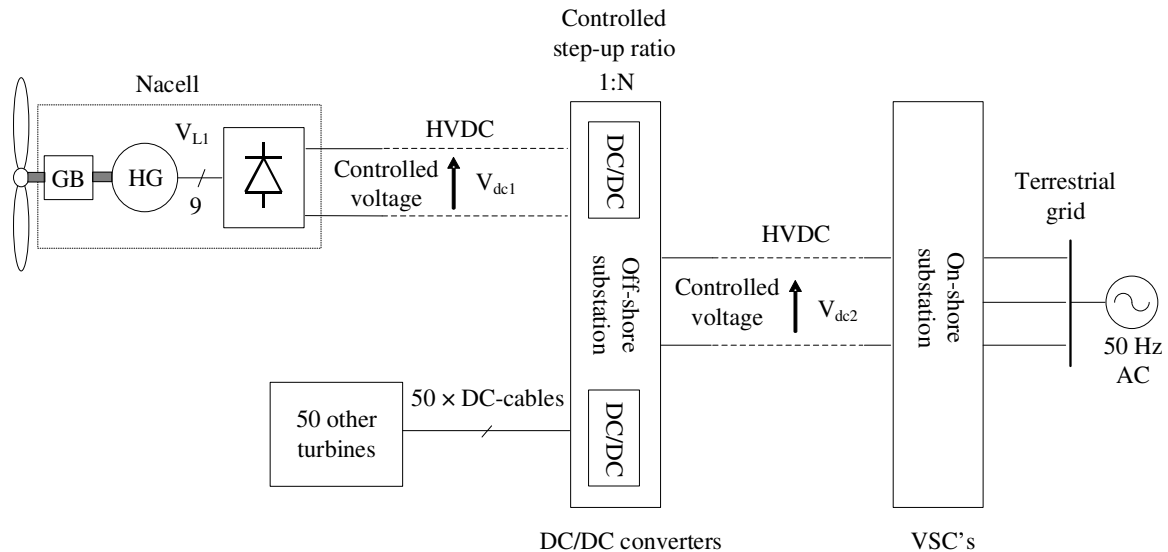


Fig. 3.10. Proposed wind generation scheme with high voltage hybrid generator (HG), HVDC interconnection and HVDC transmission.

The proposed HVDC wind generation scheme potentially results in reduced system cost due to reduced component count and complexity. Compared to the Walney system energy conversion components, Fig. 3.3, the HG and passive rectifier in the proposed system replace the IG, back-to-back VSC's and tower mounted transformer, yielding a much simplified hardware scheme and comprising of no active electronics and electrolyte DC-link capacitor. The HG output rectifier is mounted close or integral to the HG machine assembly i.e. in the machine housing. To minimize passive components and improve

generated DC power quality, a 9-phase winding design is chosen for the HG. For the same ampere-turns per phase and total copper losses the 9-phase winding yields a 4.2% higher DC-link voltage (and hence power) when compared to a 3-phase winding solution due to an improved winding distribution factor. The peak-peak to average DC-link voltage ripple is also reduced from 14% for the 3-phase design to 1.53% for the 9-phase design, effectively negating the requirement for DC-link smoothing capacitance. This will be discussed in detail in Chapter 5. The scheme proposed in this study is different from other proposed DC schemes in particular the ABB Windformer system [29] that was initially reported in 2000 but has not been further developed or installed. The ABB Windformer system uses a PM generator connected to a rectifier without any control of the system DC-link. This feature makes the Windformer system infeasible to implement because of the unregulated generator output voltage, unlike the system proposed in this study that has dynamic regulation of the generator output voltage via the wound field (WF) component of the HG.

3.5.1 Hybrid Generator (HG)

A brief discussion of the HG concept is presented in this section. However, the detailed design and analysis of the HG is addressed in Chapter 5. The HG is a multiphase, high voltage generator that uses two rotor sections, namely a PM rotor and a WF rotor, to provide the total machine excitation. Hence, the name hybrid refers to the combination of these two rotors excitation schemes. The PM and WF rotor sections exist on one rotor assembly inside one machine housing. Thus, the rotors rotate with the same speed. A schematic view of the HG is depicted in Fig. 3.11. DC current for the WF rotor excitation is provided via a brushless exciter system common to industrial synchronous machine systems.

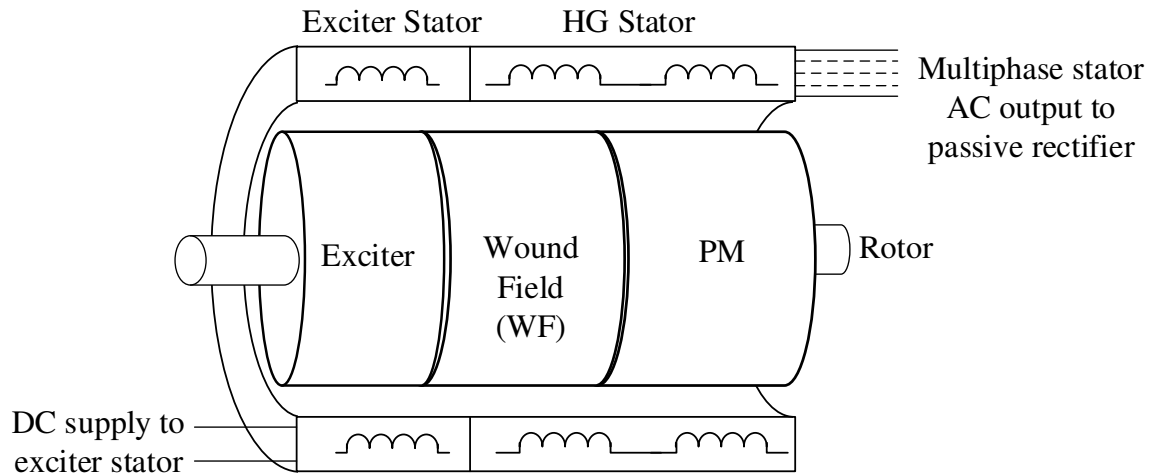


Fig. 3.11. Schematic view of the HG.

Therefore, the HG combines the output voltage due to a fixed field from the PM rotor and a controlled variable voltage due to the variable field of the WF rotor. The total machine output voltage is the sum of the voltages due to PM and WF sections. The WF therefore contributes a controllable variable voltage at the stator output over a limited range. The range of the total voltage variation depends on the design of the WF rotor of the HG. Fig. 3.12 shows the HG in a wind turbine system.

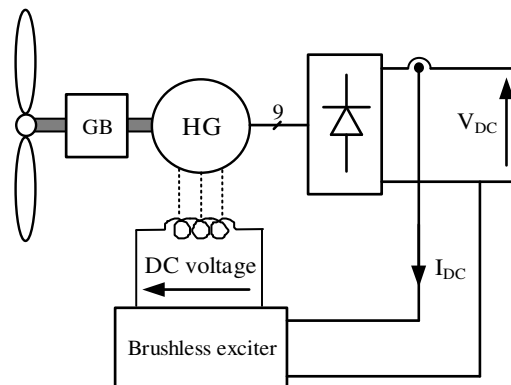


Fig. 3.12. HG in a wind turbine.

3.5.2 Gearbox

The gearbox used in the benchmark (Walney) wind turbines is a Siemens manufactured 3-stage planetary/helical gearbox with a ratio of 1:119 [10]. Fig. 3.13 illustrates example planetary and helical gear designs. Since, the nominal turbine rotor speed is 13 RPM for the Siemens wind turbine, this input to the low speed gearbox shaft is increased to around 1500 RPM on the high speed gearbox output shaft to drive the IG. This speed is defined as the IG nominal speed. Other gearbox ratios with lower stages have been proposed in the literature [56], [80]-[83]. Polinder [56] considers different generators and gearboxes including a doubly fed induction generator with a 3-stage and single-stage gearbox having nominal rated speeds of with 1200 RPM and 90 RPM rates speed respectively, a direct drive synchronous and a PM generator with 15 RPM rated speed and a PM generator with single stage gearbox with a rated speed of 90 RPM. In [56] the ratio of single stage and 2-stage gearbox is 6 and 80 respectively. A comprehensive study of other gearbox stages and ratios are discussed in detail in [84]. However, for this study a 2-stage gearbox with a ratio of 46.154 is chosen to increase the turbine rotor speed of 13 RPM to a rated speed of 600 RPM for the HG. This ratio is chosen such that the HG rated speed is consistent with a wound field SG chosen to benchmark the HG electro-magnetic design, as discussed in Chapter 4.

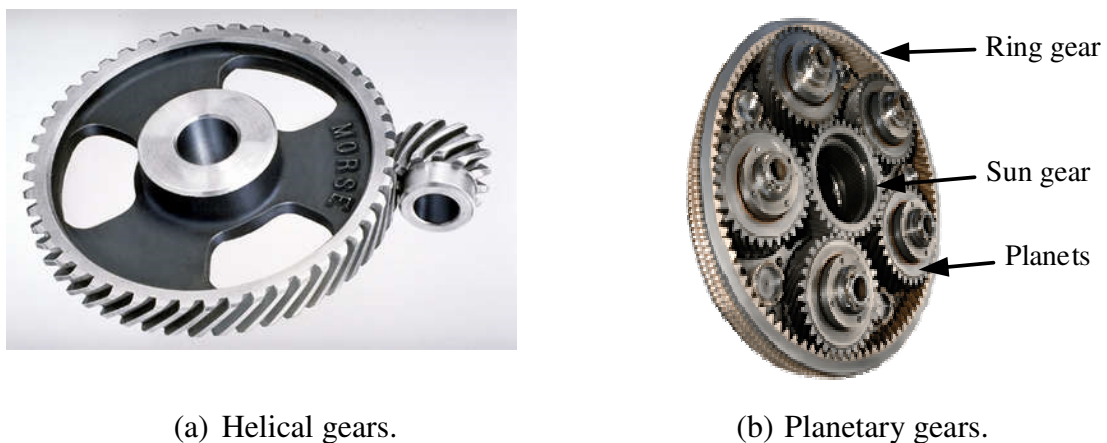


Fig. 3.13. Example planetary and helical gearbox implementation [85].

3.5.3 Voltage Control Scenarios

Although the Walney IG's are generating at a variable voltage, the remaining electrical system is required to be operated at constant voltage, i.e. at around the nominal rated voltage at all times and for all wind speed conditions. This is to ensure operation of the back-to-back VSC's and ancillary components in the system including monitoring, measurements and maintenance equipment. For the proposed HV scheme the system voltage are allowed to vary. Two control methods could be considered for the HG output DC-link voltage:

(1) Fixed voltage

(2) Variable (but controlled) voltage

(1) Fixed voltage. In the fixed voltage approach the rectified output voltage of the HG is kept around its nominal DC value at all wind speed conditions i.e. from cut-in to cut-out velocities. This is implemented by controlling the HG WF current. In this case the voltage transfer ratio of the DC/DC converters, Fig. 3.10, is fixed at 1:4, chosen to be the same as the Walney wind farm turbine transformer step-up ratio (i.e. 33/132), a ratio that is easily implementable by DC/DC converter circuits. Note that there will be small differences in voltage transfer ratios amongst the system DC/DC converters to maintain power flow and avoid rectifier turn-off due to variations in the wind farm turbine speeds (and hence generated DC voltage perturbations). The DC/DC converter voltage transfer ratio is realized by pulse width modulation (PWM) of the converter power electronic devices. This control function produces a switching duty ratio 'D' that is directly related to the voltage transfer ratio of the DC/DC converters [77]:

$$\text{Voltage transfer ratio} = n_t D \frac{V_{input}}{V_{output}} \quad (3.16)$$

where n_t is the turns (transfer) ratio of the DC/DC isolation transformer.

(1) Variable but controlled voltage. In the second control scheme the rectified output voltage of the HG system varies with wind velocity below the rated velocity, refer to Fig. 2.11. Above the rated velocity the WF is controlled to keep the DC-link at nominal maximum. Although again, there will be small perturbations around the maximum value due to wind transients. Therefore, the voltage across the interconnection cables between the wind turbines and the off-shore-substation are variable but controlled. However, the voltage across the transmission cables connecting the off-shore to on-shore substation is controlled to be fixed via the DC/DC converters at the off-shore substation, thus they have to have a variable voltage transfer ratio that is greater than 1:4, achieved by choice of the DC/DC isolation transformer turns ratio, or by a 2- or multi-stage DC/DC converter. For this study, the variable voltage control scenario with variable voltage transfer ratio DC/DC converter at the off-shore substation is chosen since this configuration results in a lower WF current requirement and hence machine mass for the HG and ensures that the off-shore to on-shore cable is operated at full voltage, thus minimizing Ohmic loss. These features are discussed in detail in Chapter 5, but brought forward here as input to the systems study.

3.5.4 DC/DC Converter

Different topologies have been proposed for DC/DC converters at high voltage and high power [36-45]. The single active bridge DC/DC converter topology uses an input VSC, an intermediate transformer and an output rectifier, as shown in Fig. 3.14.

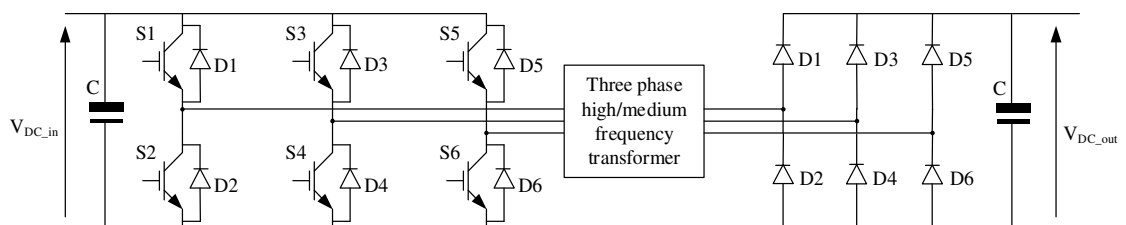


Fig. 3.14. Three-phase, single active bridge (SAB) topology for DC/DC converter.

The input VSC converts DC to an AC voltage with medium or high frequency [40], where this voltage is stepped-up by the intermediate transformer and then rectified by a passive rectifier. The topology shown in Fig. 3.14 is a three phase SAB. Single phase SAB topologies can also be realized by a single phase VSC, single phase transformer and rectifier. However, the higher the number of phases improves the volume power processing capability and can improve DC quality if interleaving technologies are implemented [86]. Power and frequency control is realized using the active power electronic switches in this topology.

If the output rectifier in the SAB is replaced with a VSC a dual active bridge topology is realized for the DC/DC converter as shown in Fig. 3.15. Similar to the SAB a single phase DAB can also be implemented.

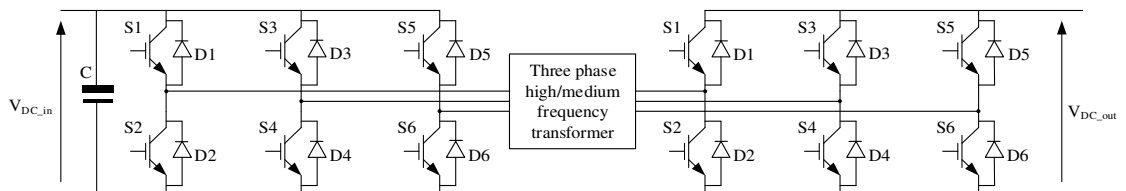


Fig. 3.15. Three phase dual active bridge (SAB) topology for DC/DC converter.

Jovic [87-88] has proposed a high power DC/DC converter topology with high step-up ratio DC/DC converter that utilizes thyristors and LC circuits. The DC/DC converter does not include a step-up transformer, as shown in Fig. 3.16. Jovic has shown that this proposed topology can achieve efficiencies of 95% for a 5 MW DC/DC converter while stepping-up 4 kV to 80 kV, i.e. gain of 20.

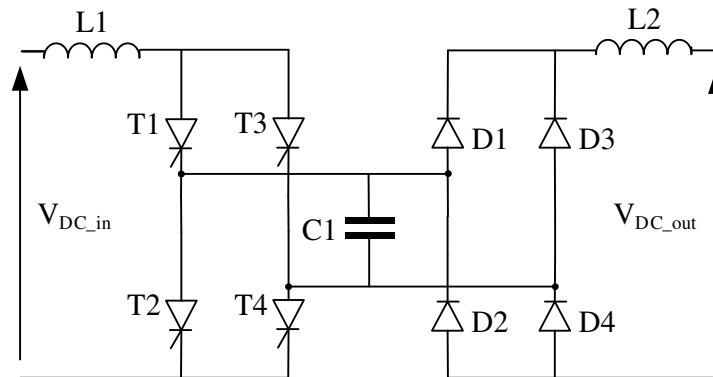


Fig. 3.16. LC circuit based DC/DC converter with Thyristors.

Different topologies for high voltage DC/DC converters and their comparison in terms of losses and efficiency have been addressed by [89-90]. Note that detailed design of the system DC/DC converters is out of scope of this study. However, the DC/DC converters in this study are modeled as a component with specific parameters and efficiency characteristics as reported in literature [89-90].

3.5.5 Turbine Safety Considerations

For the Walney wind farm generators, variable power-speed operation of the wind turbine is implemented by the back-to-back VSC's as well as mechanical controls such as blade pitch-angle control. In the proposed system, the WF voltage and mechanical blade pitch control are the main mechanisms for generator output power-speed control. This results in component reduction, which in turn results in lower power-train mass. As with the Walney scheme, wind turbine control above cut-out speed would be mainly performed by mechanical control mechanisms i.e. pitch and yaw control. Once the cut-out velocity is exceeded, the WF current in the HG is reduced to zero and the turbine blades pitched towards feather position and/or the nacelle is moved out of the wind to limit the over speed of the turbine. Moreover, a mechanical brake is provided on the shaft as an ultimate mechanical control in both Walney and the proposed scheme.

3.6 Proposed System Analysis

The proposed system is analyzed and compared with the Walney wind farm keeping the geometrical topology of the wind farm i.e. distances, site layout, turbine arrangements etc., unchanged. The single line diagram of the proposed system is shown in Fig. 3.17. The analysis studies are carried out with following assumptions:

- (1) The passive rectifier is integral to the generator and installed in the nacelle, hence the distance between the HG and rectifier is neglected.
- (2) At full-load the voltage is at its rated value and the voltage transfer ratio of the off-shore substation DC/DC converters is nominally 1:4. As the wind velocity changes and the voltage drops the DC/DC voltage transfer ratio increases.
- (3) The nominal output power of each turbine in the proposed system is the same as that of the Walney system, i.e. 3.6 MW. Therefore, the HG and passive rectifier in the proposed system are rated at 3.6 MW.
- (4) The rated RMS line-to-line voltage of the IG in Walney system is 690 V. However, the wind farm interconnection cables' voltage and hence the turbine transformer output voltage are usually rated for RMS line-to-line voltages up to 66 kV (RMS phase voltage 38.1 kV) [1-3], [10-11], [58], [91]. The turbine transformer is eliminated in the proposed system and the 9-phase HG is rated at 38.1 kV RMS per phase (quoted in per phase since generator line-to-line voltages are not all equal).

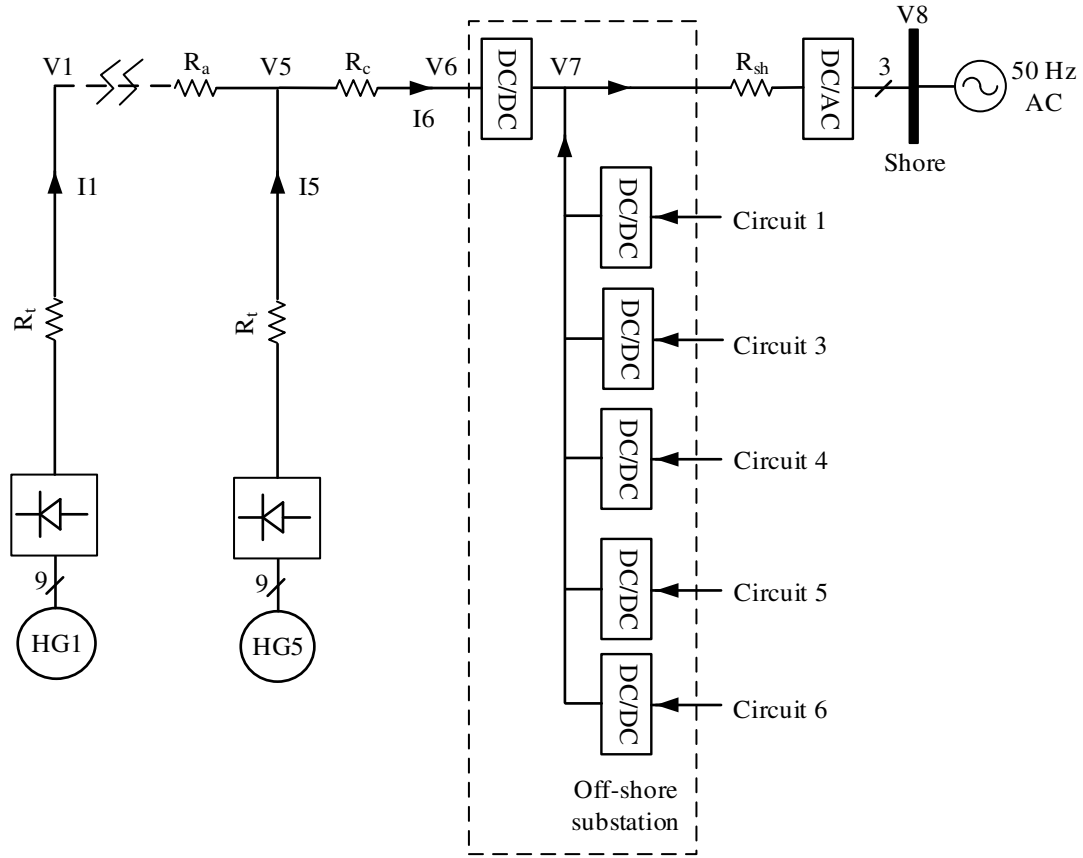


Fig. 3.17. Schematic of proposed system.

Considering the 9-phase HG connected to a passive rectifier, the DC voltage at the rectifier terminals is obtained via [77]:

$$V_{dc} = \frac{2 m \sin(\pi / m)}{\pi} \hat{V}_{ph} \quad (\text{V}) \quad (3.17)$$

where,

m : is the number of phases

\hat{V}_{ph} : is the peak phase voltage

Therefore, for a 38.1 RMS kV phase voltage and 9-phase machine the resultant DC output voltage is:

$$V_{dc} = 105.6 \quad (\text{kV}) \quad (3.18)$$

3.6.1 DC Cable Calculations

In order to calculate the required cable cross-sectional areas and cable resistances, the cable current densities are assumed to be the same as the corresponding cables in Walney 1 wind farm at their highest loading, hence skin effects are neglected in order to calculate a conservative estimate. This ensures the same copper thermal performance for both the AC and DC cables. Since the wind farm topology is unchanged, the length of the cables in the proposed system is the same as the AC cable lengths in the Walney 1 wind farm. In Walney the highest loaded inter-array cable is the one that connects Turbine 4 to Turbine 5, Fig. 3.15, the current in this cable at full-load is the sum of currents from Turbines 1 to 4. Using the calculated currents stated in Table 3.7 and cross-section area of the AC cables listed in Table 3.5, the AC cable current density is deduced to be:

$$J_{ac}^{array} = \frac{I_{ac}^{array}}{A_{ac}^{array}} = \frac{273.09}{150} = 1.58 \quad (\text{A/mm}^2) \quad (3.19)$$

where,

I_{ac}^{array} : Inter-array cable current

A_{ac}^{array} : Inter-array cable cross-section area

The inter-array DC current for the highest loaded cable in Fig. 3.17 is again the sum of currents from Turbines 1 to 4. Individual turbine current is calculated using turbine output power and rectified voltage:

$$I_{dc}^{turbine} = \left(\frac{P_{turbine}}{V_{dc}} \right) = \left(\frac{3.6 \times 10^6}{105.6 \times 10^3} \right) = 34.1 \quad (\text{A}) \quad (3.20)$$

Hence:

$$I_{dc}^{array} = 4 I_{dc}^{turbine} = 4 (34.1) = 136.36 \quad (\text{A}) \quad (3.21)$$

where,

$I_{dc}^{turbine}$: is the turbine output current

$P_{turbine}$: is the turbine power

Therefore, the inter-array cable cross-sectional area is:

$$A_{dc}^{array} = \frac{I_{dc}^{array}}{J_{ac}^{array}} = \frac{136.36}{1.58} = 86.31 \quad (\text{mm}^2) \quad (3.22)$$

Current density for the tower cable is considered to be the same as the one for inter-array cable. Therefore, the tower cable cross-sectional area is:

$$A_{dc}^{tower} = \frac{I_{dc}^{turbine}}{J_{ac}^{array}} = \frac{34.1}{1.58} = 21.58 \quad (\text{A/mm}^2) \quad (3.23)$$

The current in the cable connecting Circuit 2 to the off-shore substation is sum of currents in Turbines 1 to 5. Using current values stated in Table 3.7 and cross-section area quoted in Table 3.5:

$$J_{ac}^{circuit} = \frac{I_{ac}^{circuit}}{A_{ac}^{circuit}} = \frac{296.54}{500} = 0.6 \quad (\text{A/mm}^2) \quad (3.24)$$

Therefore, the cross-sectional area of the DC cable connecting Circuit 2 to the off-shore substation in Fig. 3.17 is:

$$A_{dc}^{circuit} = \frac{I_{dc}^{circuit}}{J_{ac}^{circuit}} = \frac{5(34.1)}{0.6} = 284.2 \quad (\text{mm}^2) \quad (3.25)$$

where,

$I_{ac}^{circuit}$: is the current in the cable connecting Circuit 2 to the off-shore substation

$A_{ac}^{circuit}$: is the cross-section area for the cable connecting Circuit 2 to the off-shore substation

Similarly, for the transmission cable connecting off-shore to on-shore substation, the current density using Tables 3.7 and 3.5 is:

$$J_{ac}^{trans} = \frac{I_{ac}^{trans}}{A_{ac}^{trans}} = \frac{715.46}{630} = 1.2 \quad (\text{A/mm}^2) \quad (3.26)$$

Thus, the current in the cable connecting off-shore to on-shore substation for the proposed system is the sum of currents from 51 turbines and with consideration to a step-up ratio of 4 for the DC/DC converters. Therefore, the cross-sectional area of the corresponding DC cable for the proposed off-shore to on-shore transmission cable is:

$$A_{dc}^{trans} = \frac{I_{dc}^{trans}}{J_{ac}^{trans}} = \frac{51(34.1)(1/4)}{1.2} = 362.31 \quad (\text{mm}^2) \quad (3.27)$$

where I_{dc}^{trans} is the current in the cable connecting off-shore to on-shore substation.

The cable resistance for each DC cable is calculated using equation (3.5). Note that the total length of a DC cable is double the length of the point-to-point connection since there are two DC wires for each cable connection. A summary of proposed system DC cable calculations is listed in Table 3.15.

Table 3.15. Proposed system cables specifications

Description	Tower	Circuit 2		Off-shore substation to on-shore
		Inter-array between turbines	Inter-array to off-shore substation	
Cable length (km)	0.0835	0.750	0.458	44.4
Material	Copper			
Copper resistivity ($\mu\Omega\text{m}$)	0.0172			
Rated voltage (kVDC)	110	110	110	425
Current density (A/mm^2)	1.58	1.58	0.6	1.2
Cross-section area (mm^2)	21.58	86.31	284.2	362.31
DC cables resistance (Ω)	0.13	0.3	0.055	4.2

3.6.2 Results for Full-, Three-quarter-, Half- and One-quarter- Load

The analysis results for the proposed system analysis at full-load is presented in Table 3.16. At full-load all generators in the system generate 3.6 MW to their respective rectifier. As mentioned previously, as the wind velocity changes the output voltage of the turbine HG changes. For the Siemens SWT-3.6-107 wind turbine the turbine rotor speed changes from 5 RPM at cut-in to 13 RPM at rated speed. The output voltage of the HG changes linearly with turbine rotor speed. Moreover, as discussed in Chapter 2, turbine power is a cubic function of the turbine rotor speed. Therefore, the output voltage of the HG changes with cubic root of power. As discussed previously the voltage across interconnection cables varies but the off-shore substation output voltage is constant. Therefore, the DC/DC converter step-up ratio varies as the wind velocity changes. Table 3.17 presents rotor speed, HG output voltage and DC/DC converter ratio at different loads.

Table 3.16. Proposed system full-load analysis

Turbine					
Turbine No.	1	2	3	4	5
HG phase voltage (kV)	38.11	38.10	38.09	38.08	38.08
HG DC voltage (kV)	105.6	105.59	105.57	105.54	105.54
HG DC current output (A)	32.90	32.91	32.91	32.92	32.92
DC voltage at the tower base, kV	105.6	105.59	105.57	105.54	105.50
Interconnection and Transmission					
Input DC voltage at the off-shore substation (kV)				105.49	
Input DC current, Circuit 2 at off-shore sub. (A)				164.57	
Output DC voltage at the off-shore sub. (kV)				421.93	
Output DC current at the off-shore sub. (A)				413.36	
Input DC voltage at the on-shore sub. (kV)				420.22	
Input DC current at the on-shore sub. (A)				413.36	
Power and losses in the nacelle and tower					
Turbine power (kW)				3,600	
HG output power (kW)				3,492	
Rectifier output power (kW)				3,474.54	
HG efficiency (%) and losses (kW)				97	108
Rectifier efficiency (%) and losses (kW)				99.5	17.46
Tower cable power loss (kW)				0.14	
Turbine link cable					
From--to		1 to 2	2 to 3	3 to 4	4 to 5
Inter-array cable loss (kW)		0.32	1.30	2.92	5.20
Cable loss, Circuit 2 to the off-shore substation (kW)				1.49	
Input power and losses at off-shore sub. from Circuit 2					
Power (kW)	17,360.76		Losses (kW)	639.24	
Input power and losses at off-shore sub. from Circuits 1-6					
Power (kW)	177,079.75		Losses (kW)	6,520.25	
DC/DC converters efficiency at off-shore sub. (%)				98.5	
Loss at off-shore substation (kW)				2,656.20	
Cable losses, Off-shore to on-shore sub. (kW)				717.66	
Total power at on-shore substation (kW)				173,705.90	
Total losses at on-shore substation (kW)				9,894.10	
Total system efficiency (%)				94.61	

Table 3.17. Rotor speed, HG voltage and DC/DC converter ratio at different loads

Loading			Rotor speed		HG voltage		Off-shore substation voltage kV	DC/DC converter step-up ratio
Item	p.u.	kW	p.u.	RPM	p.u.	kV		
Full	1.00	3600	1.00	13	1.00	105.6	420	4
Three-quarter	0.75	2700	0.91	11.83	0.91	96.1		4.4
Half	0.5	1800	0.79	10.27	0.79	83.42		5
One-quarter	0.25	900	0.63	8.19	0.63	66.53		6.3
Cut-in	0.05	180	0.38	5	0.38	40.13		10.5

Power flow results for the proposed system at three-quarter, half and one-quarter loads are presented in Tables 3.18, 3.19 and 3.20 respectively. Voltage drop at the tower base from turbine one to the off-shore substation at different loads is:

$$(1) \text{ Full-load: } \left(\frac{V_1 - V_6}{V_1} \right) 100 = \left(\frac{105.6 - 105.49}{105.6} \right) 100 = 0.1 \% \quad (3.28)$$

$$(2) \text{ Three-quarter load: } \left(\frac{V_1 - V_6}{V_1} \right) 100 = \left(\frac{96.09 - 96}{96.09} \right) 100 = 0.09 \% \quad (3.29)$$

$$(3) \text{ Half load: } \left(\frac{V_1 - V_6}{V_1} \right) 100 = \left(\frac{83.42 - 83.35}{83.42} \right) 100 = 0.08 \% \quad (3.30)$$

$$(4) \text{ one-quarter load: } \left(\frac{V_1 - V_6}{V_1} \right) 100 = \left(\frac{66.53 - 66.48}{66.53} \right) 100 = 0.075 \% \quad (3.31)$$

Therefore, as the load decreases, the voltage drop from the turbines to the off-shore substation reduces as result of lower currents flowing the system. Note that for all loads the voltage decreases from Turbine 1 to the off-shore substation i.e.:

$$\begin{aligned} V_1 &> V_2 > V_3 > V_4 > V_5 > V_6 \\ V_7 &> V_8 \end{aligned} \quad (3.32)$$

Therefore, a power flow from turbines to the grid occurs at all loads.

Table 3.18. Proposed system three-quarter-load analysis

Turbine					
Turbine No.	1	2	3	4	5
HG phase voltage (kV)	34.68	34.67	34.67	34.66	34.66
HG DC voltage (kV)	96.10	96.09	96.07	96.05	96.05
HG DC current output (A)	27.12	27.12	27.13	27.13	27.13
DC voltage at the tower base, kV	96.09	96.09	96.07	96.05	96.01
Interconnection and Transmission					
Input DC voltage at the off-shore substation (kV)				96	
Input DC current, Circuit 2 at off-shore sub. (A)				135.63	
Output DC voltage at the off-shore sub. (kV)				422.42	
Output DC current at the off-shore sub. (A)				309.70	
Input DC voltage at the on-shore sub. (kV)				421.12	
Input DC current at the on-shore sub. (A)				309.70	
Power and losses in the nacelle and tower					
Turbine power (kW)				2,700	
HG output power (kW)				2,619	
Rectifier output power (kW)				2,605.91	
HG efficiency (%) and losses (kW)				97	81
Rectifier efficiency (%) and losses (kW)				99.5	13.10
Tower cable power loss (kW)				0.10	
Turbine link cable					
From--to		1 to 2	2 to 3	3 to 4	4 to 5
Inter-array cable loss (kW)		0.22	0.88	1.99	3.53
Cable loss, Circuit 2 to the off-shore substation (kW)				1.01	
Input power and losses at off-shore sub. from Circuit 2					
Power (kW)	13,021.41		Losses (kW)		478.59
Input power and losses at off-shore sub. from Circuits 1-6					
Power (kW)	132,818.43		Losses (kW)		4,881.57
DC/DC converters efficiency at off-shore sub. (%)				98.5	
Loss at off-shore substation (kW)				1,992.28	
Cable losses, Off-shore to on-shore sub. (kW)				402.85	
Total power at on-shore substation (kW)				130,423.31	
Total losses at on-shore substation (kW)				7,276.69	
Total system efficiency (%)				94.72	

The loss analysis at full-load shows that:

- The total loss for the proposed system is 9,894.10 kW.
- Circuits 1-6 loss contribute to 65.9% of the total loss.

- The off-shore substation DC/DC converter loss contributes to 26.38% of the total system loss.
- The losses in the cable connecting the off-shore to on-shore substation contributes to 7.25% of the total system loss.

Table 3.19. Proposed system half-load analysis

Turbine					
Turbine No.	1	2	3	4	5
HG phase voltage (kV)	30.1	30.1	30.1	30.09	30.09
HG DC voltage (kV)	83.43	83.42	83.40	83.39	83.39
HG DC current output (A)	20.82	20.83	20.83	20.83	20.83
DC voltage at the tower base, kV	83.42	83.41	83.40	83.39	83.36
Interconnection and Transmission					
Input DC voltage at the off-shore substation (kV)				83.35	
Input DC current, Circuit 2 at off-shore sub. (A)				104.12	
Output DC voltage at the off-shore sub. (kV)				416.77	
Output DC current at the off-shore sub. (A)				209.28	
Input DC voltage at the on-shore sub. (kV)				415.89	
Input DC current at the on-shore sub. (A)				209.28	
Power and losses in the nacelle and tower					
Turbine power (kW)				1,800	
HG output power (kW)				1,746	
Rectifier output power (kW)				1,737.27	
HG efficiency (%) and losses (kW)				97	54
Rectifier efficiency (%) and losses (kW)				99.5	8.73
Tower cable power loss (kW)				0.06	
Turbine link cable					
From--to		1 to 2	2 to 3	3 to 4	4 to 5
Inter-array cable loss (kW)		0.13	0.52	1.17	2.08
Cable loss, Circuit 2 to the off-shore substation (kW)				0.6	
Input power and losses at off-shore sub. from Circuit 2					
Power (kW)	8,681.57		Losses (kW)	318.43	
Input power and losses at off-shore sub. from Circuits 1-6					
Power (kW)	88,551.99		Losses (kW)	3,248.01	
DC/DC converters efficiency at off-shore sub. (%)				98.5	
Loss at off-shore substation (kW)				1,328.28	
Cable losses, Off-shore to on-shore sub. (kW)				183.96	
Total power at on-shore substation (kW)				87,039.75	
Total losses at on-shore substation (kW)				4,760.25	
Total system efficiency (%)				94.81	

Table 3.20. Proposed system one-quarter-load analysis

Turbine					
Turbine No.	1	2	3	4	5
HG phase voltage (kV)	24.01	24	24	24	24
HG DC voltage (kV)	66.53	66.52	66.52	66.50	66.50
HG DC current output (A)	13.06	13.06	13.06	13.06	13.06
DC voltage at the tower base, kV	66.53	66.52	66.51	66.50	66.49
Interconnection and Transmission					
Input DC voltage at the off-shore substation (kV)				66.48	
Input DC current, Circuit 2 at off-shore sub. (A)				65.30	
Output DC voltage at the off-shore sub. (kV)				418.85	
Output DC current at the off-shore sub. (A)				104.13	
Input DC voltage at the on-shore sub. (kV)				418.42	
Input DC current at the on-shore sub. (A)				104.13	
Power and losses in the nacelle and tower					
Turbine power (kW)				900	
HG output power (kW)				873	
Rectifier output power (kW)				868.63	
HG efficiency (%) and losses (kW)				97	27
Rectifier efficiency (%) and losses (kW)				99.5	4.37
Tower cable power loss (kW)				0.02	
Turbine link cable					
From--to		1 to 2	2 to 3	3 to 4	4 to 5
Inter-array cable loss (kW)		0.05	0.02	0.46	0.82
Cable loss, Circuit 2 to the off-shore substation (kW)				0.23	
Input power and losses at off-shore sub. from Circuit 2					
Power (kW)	4,341.30		Losses (kW)	158.70	
Input power and losses at off-shore sub. from Circuits 1-6					
Power (kW)	44,281.21		Losses (kW)	1,618.79	
DC/DC converters efficiency at off-shore sub. (%)				98.5	
Loss at off-shore substation (kW)				664.22	
Cable losses, Off-shore to on-shore sub. (kW)				45.54	
Total power at on-shore substation (kW)				43,571.45	
Total losses at on-shore substation (kW)				2,328.55	
Total system efficiency (%)				94.93	

The system total efficiency for different loads is:

1) Full load: 94.61% (3.33)

2) Three-quarter load: 94.72% (3.34)

3) Half load: 94.81% (3.35)

4) One-quarter load: 94.93% (3.36)

The system efficiency is similar at different loads. Hence, similar benefits and system performance is seen at all loads. Note that the HG, rectifier and DC/DC converter efficiencies are constant at all loads.

3.7 Comparison between Proposed system and Walney Wind Farm

Table 3.21 compares results of the proposed HVDC system and Walney wind farm in terms of total power, losses and efficiency at different loads. The proposed system increases the wind farm efficiency by 3.8% at full-load. Also, the system efficiency is increased by 3.7%, 3.8% and 5.2% at three-quarter-, half- and one-quarter-load respectively. Therefore, the proposed system results in similar benefits at all loads compared to the Walney system. Note that the voltage throughout the system for the Walney is fixed. However, the interconnection voltage varies in the proposed system while the off-shore to on-shore transmission voltage is fixed. Table 3.22 presents a mass comparison of the proposed HVDC and Walney systems. Mass of different components for the turbine is quoted here using Siemens turbine datasheets [74], [92-93] and private correspondences with Siemens. The VSC's mass and volume are estimated from commercial VSC datasheets available on-line from ABB [94]. Rectifier mass is calculated based on datasheet for high voltage diodes available on [95].

Cable volume is calculated as follows:

$$V_{cable} = A_{cable} l_{cable} \quad (\text{m}^3) \quad (3.37)$$

The cable mass is then calculated as:

$$\text{Mass}_{cable} = \delta_{cu} V_{cable} \quad (\text{kg}) \quad (3.38)$$

where,

A_{cable} : is cable cross-section (m^2)

l_{cable} : is cable length (m)

δ_{cu} : is the copper density taken as 8960 (kg/m^3)

Mass for different cables in the Walney and proposed system is listed in Table 3.22. The analysis demonstrates the improvements of the proposed HVDC system when compared to the benchmark Walney 1. For example, the proposed system results in 16% and 2.3% mass reduction for the power-train and total turbine structure respectively. The power-train in

Walney includes a gearbox, an IG, two VSC's and a transformer i.e. 5 series connected components while for the proposed system it includes a gearbox, an HG and a rectifier i.e. 3 series connected components. Therefore, the proposed system results in a lower component count. Note that the proposed system uses DC/DC converters at the off-shore platform as compared with two transformers. In addition, the cable system copper mass is 75.8% lower.

Table 3.21. Comparison between Walney and proposed system

Item	Walney 1	Proposed system
Voltage scenario	Interconnections: variable Transmission: fixed	Interconnections: variable Transmission: fixed
Full-load		
Total installed capacity (kW)	183,600	183,600
Total power (kW)	167,346.54	173,705.90
Total system loss (kW)	16,477.50	9,894.10
Efficiency %	91.15	94.61
Three-quarter-load		
Total power (kW)	125,792.79	130,423.31
Total system loss (kW)	11,998.32	7,276.69
Efficiency %	91.35	94.72
Half-load		
Total power (kW)	83,822.82	87,039.75
Total system loss (kW)	8,001.40	4,760.25
Efficiency %	91.31	94.81
One-quarter-load		
Total power (kW)	41,415.46	43,571.45
Total system loss (kW)	4,485.71	2,328.55
Efficiency %	90.23	94.93

Table 3.22. Mass comparison

Item	Walney system		Proposed system	
	Mass (Tonnes)	Mass (%)	Mass (Tonnes)	Mass (%)
Power-train, turbine and tower mass				
Blades × 3	54	12.13	54	12.42
Hub mass	38.5	8.65	38.5	8.85
Shaft	27.5	6.18	27.5	6.32
Gearbox	42.5	9.55	28.3	6.5
IG	10	2.25	-	-
HG	-	-	24.2	5.6
Two VSC's	2.4	0.54	-	-
Rectifier	-	-	0.25	0.06
Turbine transformer	8	1.80	-	-
Blades and hub bolts	2.16	0.49	2.16	0.50
Tower*	260	58.42	260	59.78
Total	445.06	100	434.91	100
Cable mass**				
Tower cable	4.78	0.49	0.03	0.01
Inter-array cables between turbines	133.06	13.56	12	5.06
Cable, Circuits to off-shore	91.24	9.3	9.89	4.17
Cable, off-shore sub. to shore	751.89	76.65	215.33	90.76
Total	980.97	100	237.25	100

*83.5 m above mean sea level

**Copper density is taken as 8960 kg/m³

3.8 Summary

A new wind generation scheme based on a high voltage HG, HVDC interconnection and transmission is proposed in this Chapter. The new system is compared with a commercial system, Walney 1, chosen as a representative benchmark of existing industry practice. Analysis results from the two systems show that the proposed system results in 3.8% higher energy conversion efficiency assuming all turbines are operating at, or near, their full-load thermal rating. Results for the proposed wind generation scheme at other loads have also been assessed and show similar efficiency gains and benefits.

The study highlights the potential reduction of system plant within the nacelle and turbine tower, features that will improve the serviceability and maintenance of the wind farm over time. The proposed scheme has 2.3% lower mass for the turbine and 75.8% lower mass for the cable systems. These are achieved by using higher voltage for generation, interconnection and transmission.

However, the major contribution of the new proposed system is the elimination of active VSC's within the nacelle and tower and replacing them with passive rectifiers built into the HG or located close to the machine terminals. The proposed HG uses two rotor field excitations, PM and WF with a 9-phase stator that yields improved power quality while essentially eliminating the electrolytic smoothing devices (DC-link capacitance) that would otherwise be required.

The VSC's and electrolytic capacitors are major causes of variable speed drive system failures [73], hence the claim for improved serviceability, maintenance and lower operational cost. It is proposed that the turbine interconnection voltage is allowed to vary (but controlled), compared to the essentially fixed interconnection voltage for the benchmark AC system. For the proposed scheme, the active power electronic converters (high voltage, high power DC/DC converters) are located at the off-shore sub-station where access for maintenance and repair is easier and more cost effective. It is envisaged that these savings will make a significant contribution to overall cost reduction of the wind farm and system, although this is not assessed nor quantified in this thesis study.

Chapter 4

Hybrid Generator (HG) Concept and Benchmark Machine

4.1 Introduction

In this Chapter an overview of different electric generator topologies and power electronics interface for wind turbine applications is presented to give some background to the proposed hybrid generator (HG) concept. The HG is discussed and a MATLAB/Simulink model presented to investigate the machine's operational characteristics. The simulation model is validated by way of a low power (3 kW), low voltage (maximum phase peak voltage of 88.5 V at rated speed of 3000 RPM) laboratory prototype. The laboratory prototype wound field excitation is provided by an external DC source connected via rotating slip-rings and brush-gears. A brushless exciter system is designed and results are presented. The scope of the thesis does not permit the build and test of a full power HG comparable with one suitable for the Walney wind generation system. Hence, an industrial high voltage synchronous generator design is used to benchmark the high voltage HG. The benchmark machine is a 11 kV, 5.52 MW Siemens SG chosen since its power and speed ratings are close to those typical of wind generation system applications. The benchmark machine is analyzed and results compared against published data to validate the analysis procedures. Having established validity of the design tools and procedure the benchmark machine design is used in Chapter 5 to develop the proposed high voltage HG and in Chapter 6 to study winding insulation systems.

4.2 Electric Machines and Converters for Wind Turbines

4.2.1 Doubly-Fed Induction Generators (DFIGs)

Different turbine generator topologies, both direct drive and geared, have been proposed in the literature and developed by manufactures for wind turbine applications [3], [10-11], [25], [48], [91-92], [96-99]. Fig. 4.1 shows a doubly-fed induction generator (DFIG) connected to the grid via two back-to-back VSC's that can be controlled to operate in four quadrants [48], [96].

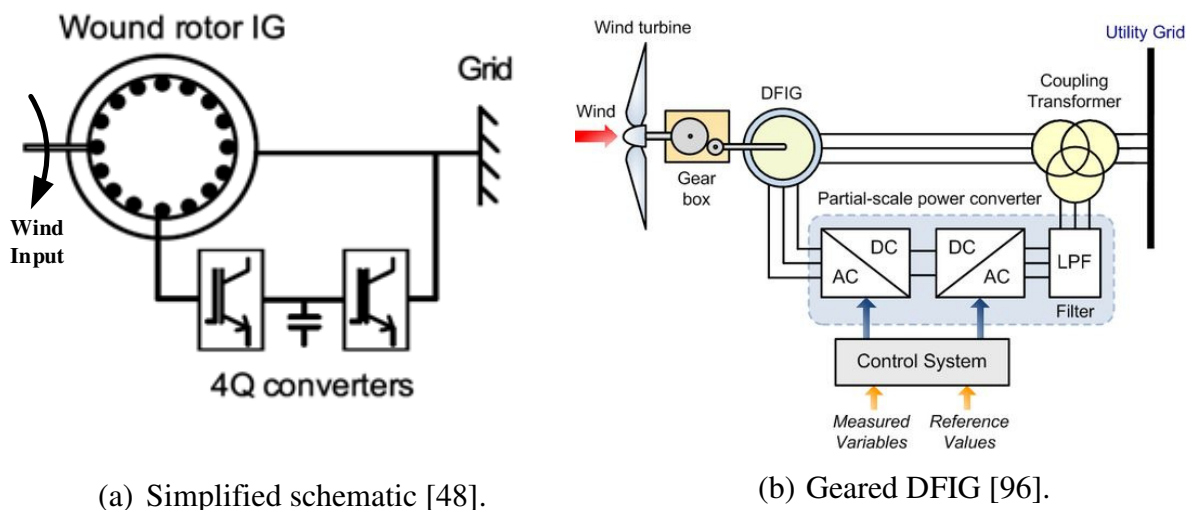


Fig. 4.1. DFIG configuration.

The DFIG has a three-phase stator and wound rotor windings. The four-quadrant VSC's connect the rotor variable voltage and frequency output back to the fixed voltage and frequency mains supply via a coupling transformer and enable the control of both the generator torque and reactive power flow. The rotor speed is controlled by absorbing or injecting active power to the DFIG rotor. A typical DFIG speed range is $\pm 30\%$ around synchronous speed [48] and since only a portion of the generated active power flows through the rotor the DFIG-side VSC power ratings are only around 30% of the generator

rating [48]. However, usually the VSC's are oversized due to increased demand in reactive power controllability, wider speed range and low voltage ride through requirements [48].

4.2.2 VSC Coupled Induction and Synchronous Generators

In order to achieve a wider operating range of speed the induction generator (IG), permanent magnet (PM) or wound field synchronous generator (SG) are connected to the grid via two fully rated converters in a back-to-back configuration. Fig. 4.2 shows a squirrel cage rotor IG in a wind turbine connected to the grid via two back-to-back VSC's. Note that the rating of each converter in this configuration has to be the rating of the generator since the total generator power flows through each converter.

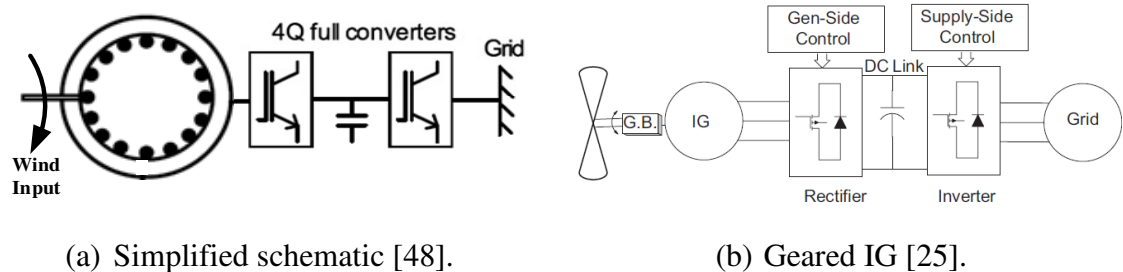


Fig. 4.2. IG connected to grid via two fully rated VSC.

The IG is a mature technology and are relatively inexpensive, robust and require low maintenance [25]. In the configuration shown in Fig. 4.2 the IG-side converter controls the IG speed via vector control to extract maximum wind power. The grid-side converter performs active and reactive power control. A comparison in terms of hardware components, operation and energy output between DFIG and IG are presented in [97]. There are pros and cons for each scheme, for example, the energy output from the DFIG is limited due to limited speed variation range. However, the converters in DFIG schemes are not fully rated, so it is a lower cost scheme. This said, most large wind farms are employing the dual converter scheme of Fig. 4.2, as per the Walney farms due to the increased energy

conversion capability. For such large wind farms as the Walney, life-time energy conversion clearly drives system choice as opposed to initial equipment capital costs. Fig. 4.3 presents a wind conversion scheme employing a PM generator connected to the grid via two fully rated VSC's. The functionality of the conversion system in Fig. 4.3 is similar to that of Fig. 4.2 hence, the machine-side converter controls the rotor speed to extract a maximum power from wind while the grid-side converter controls the active and reactive power flow and maintain a fixed DC-link voltage.

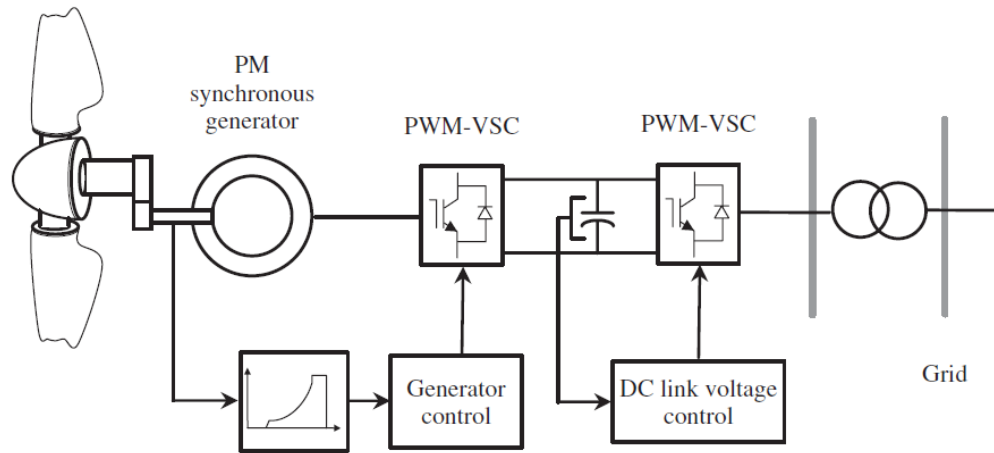


Fig. 4.3. PM generator connected to grid via two fully rated VSC [26].

PM machines have higher flux-densities compared to IG's and DFIG's, they are usually more power-dense compared to other generator technologies, don't need external supply and slip rings and avoid reactive power compensation [25]. Fig. 4.4 shows a 6 MW direct drive PM generator for the Alstom Haliade 150-6MW wind turbine [98], where the machine has larger diameter compared to its axial length due to low rotor speed, i.e. maximum 11.5 RPM. However, the 2 MW geared DFIG from DeWind D8.2 wind turbine [58] with a nominal rotor speed of 1700 RPM has a longer axial length compared to its diameter. Fig. 4.5 shows another scheme where the PM generator is connected to the grid via a passive rectifier, a DC/DC converter (chopper/booster) and a VSC. In this scheme the PM generator vector control is implemented through the VSC while the DC/DC converter maintains a fixed DC-link voltage. Note that current industrial turbines are controlled to

operate in the limited speed operation regime (as discussed in Chapter 2) hence the PM generator maximum speed is the machine rated speed and no field weakening of the machine is required.

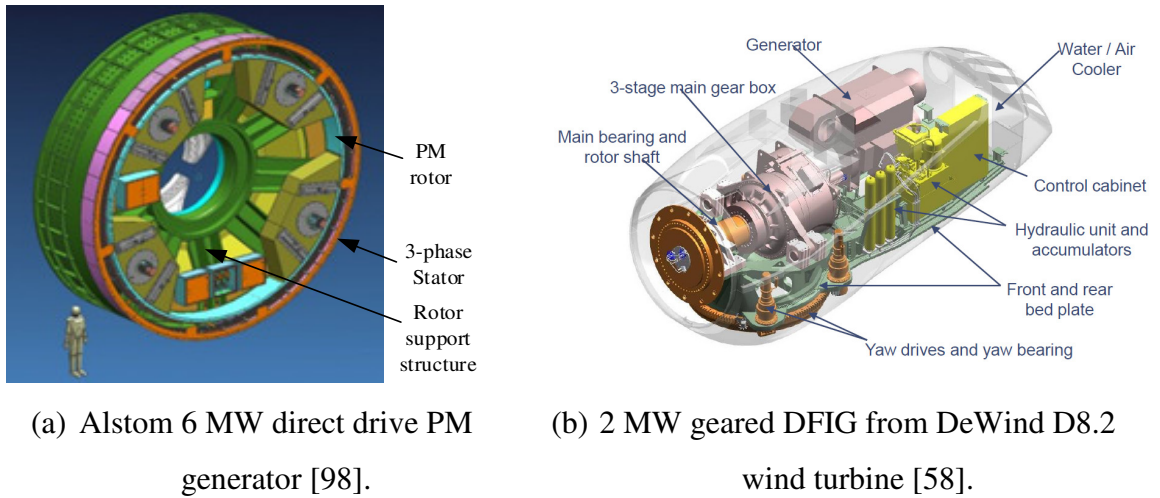


Fig. 4.4. Direct drive PM and geared DFIG.

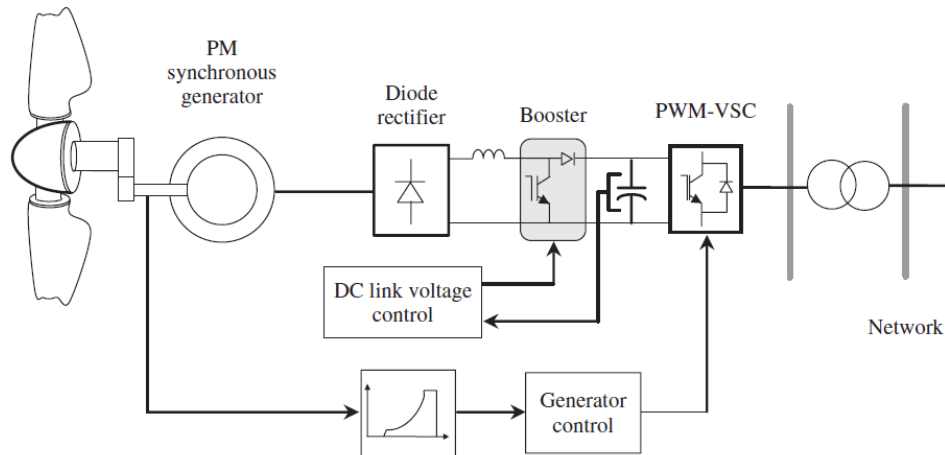
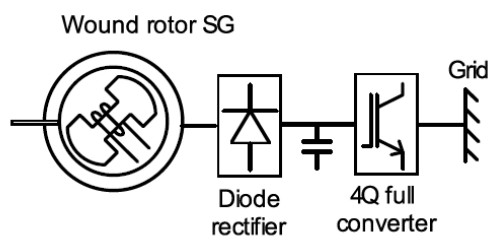


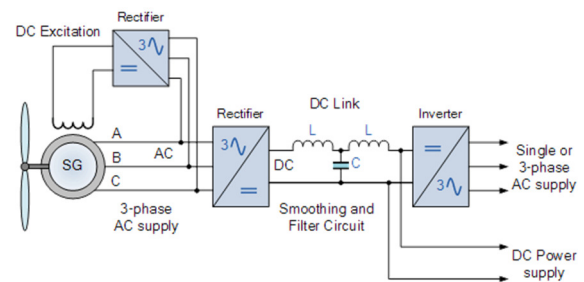
Fig. 4.5. PM generator connected to grid via passive rectifier, DC/DC converter and a VSC [26].

Fig. 4.6 shows a wound field SG connected to the grid via a passive rectifier and a VSC. Using the wound field SG the machine-side VSC that was required for PM generator is

eliminated due to capability of the SG to have an active output voltage control via controlling the machine rotor field. However, in order to improve and facilitate the system control a DC/DC converter can be used as in the system shown in Fig. 4.5. The wound field SG is capable of providing its own field excitation by means of a brushless exciter mounted on its shaft. Unlike the PM generator the wound field SG output voltage can be controlled via controlling the machine field current independent of the load. However, for the same output power wound field SG's are normally heavier than PM rotors, typically bulkier and have higher rotor losses [48].



(a) Simplified model [48].



(b) Direct drive SG [99].

Fig. 4.6. Wound field SG connected to grid via passive rectifier and a fully rated VSC.

4.2.3 Comparison of Generators

A theoretical comparison of different turbine generator topologies is presented by Polinder et al. in [56]. Polinder studies five different generator systems for a 3 MW rated output power and a 15 RPM turbine shaft speed. The generators include:

- A DFIG with a three-stage gearbox (DFIG3G) and gear ratio of 1:80, i.e. a machine speed of 1200 RPM.
- A DFIG with a single-stage gearbox (DFIG1G) and a gear ratio of 1:6, i.e. a machine speed of 90 RPM.
- A direct drive wound field SG (DDSG) with nominal speed of 15 RPM.
- A direct drive PM generator (DDPMG) with nominal speed of 15 RPM.
- And a PM generator with single-stage gearbox (PMG1G) and gear ratio of 1:6, i.e. a machine speed of 90 RPM.

The comparison is based on machine mass, energy yield, losses and cost. Table 4.1 summarizes Polinder's comparison. Note that these comparisons cannot be generalized. For example the DFIG3G is the lightest but for a fair mass comparison the mass of gearbox-generator-converter systems need to be taken into account since the direct drive machine are normally heavier. Moreover, technical characteristics and benefits need to be investigated for a complete analysis. Data for the HV Siemens generator used as a benchmark validation and is available to the authors is also included in Table 4.1 to confirm machine suitability. Gearbox mass for the Siemens SWT-3.6-107 wind turbine that is used in Walney wind farm is also stated in Table 4.1.

Table 4.1. Comparison of different generators for wind turbine application as reported in [56] and the benchmark HV Siemens generator used in this study

Item	DFIG3G	DDSG	DDPMG	PMG1G	DFIG1G	Benchmark SG
Stator radius (m)	0.42	2.5	2.5	1.8	1.8	2.7
Active axial length (m)	0.75	1.2	1.2	0.4	0.6	0.4
Air-gap thickness (mm)	1	5	5	3.6	2	7
Mass* (tonnes)	5.25	45.1	24.1	6.11	11.37	7.02
Cost** (kEuros)	1870	2117	1982	1883	1837	-
Annual energy yield (GWh)	7.73	7.88	8.04	7.84	7.80	-
Turbine speed (RPM)	15					-
Rated generator power (MW)	3					5.52
Machine speed (RPM)	1200	15	15	90	90	600
Gearbox ratio	1:80	1:1	1:1	1:6	1:6	-
Gearbox mass for the Siemens SWT-3.6-107 wind turbine gear ratio (1:119)						
42.5 (tonnes)						

*Mass includes mass of Iron, Copper and PM material only, for the benchmark SG mass does not include mass of rotor iron.

**Cost includes cost of generator material, construction, gearbox, power electronics, and other wind turbine parts.

4.3 Hybrid Generator (HG) Concept and Prototype

4.3.1 Machine Concept

Section 3.5 discussed the proposed off-shore wind generation system that could potentially result in reduced system cost due to reduced component count and complexity. The proposed system uses a multi-phase HG, the AC output of which is passively rectified for transmission from the turbine tower. The HG is an AC machine having a multiphase, high voltage winding and uses two rotor sections, namely a PM rotor and a WF rotor, to provide the total machine excitation. Hence, the name hybrid generator refers to the combination of these two rotors excitation schemes. The PM and WF rotor sections exist on one rotor assembly inside one machine housing. Thus, the rotors rotate with the same speed. A schematic view of the HG is depicted in Fig. 4.7(a). DC current for the WF rotor excitation is provided via a brushless exciter system common to industrial synchronous machine systems. Therefore, the HG combines the output voltage due to a fixed field from the PM rotor and a controlled variable voltage due to the variable field of the WF rotor. The total machine output voltage is the sum of the voltages due to PM and WF sections. The WF therefore contributes a controllable variable voltage at the stator output over a limited range. The range of the total voltage variation depends on the design of the WF rotor of the HG. Fig. 4.7(b) shows the HG in a wind turbine system.

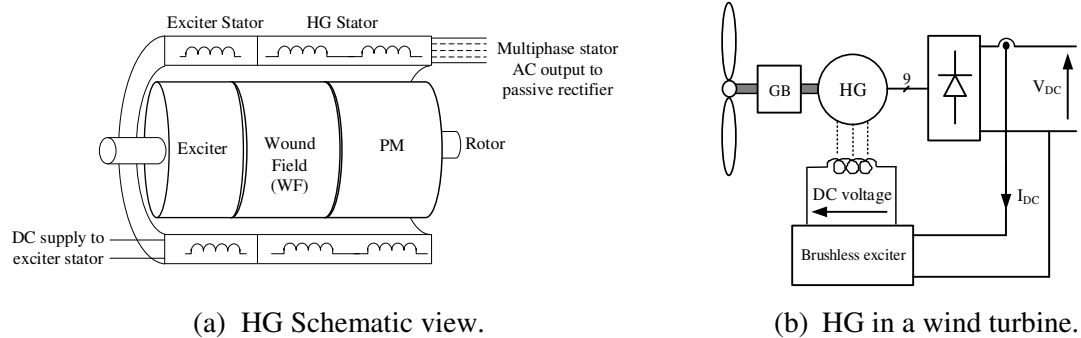


Fig. 4.7. Hybrid generator (HG) concept.

In general PM machines have a fixed rotor field excitation that induces a fixed voltage into the stator winding at a fixed speed. Hence, in order to control the machine output voltage/current a fully rated power electronic converter is required [100]-[101]. However, if the power electronic converter is eliminated an alternative solution to regulate machine output voltage and hence power is the HG configuration with a passive rectifier, shown schematically in Fig. 4.7(a) and Fig. 4.7(b) for a wind turbine application. Referring to Fig. 4.7(b) the output voltage of the machine induced by the PM excitation is regulated by the wound field (WF) excitation. The WF is fed a DC current through a brushless exciter and a rotating rectifier. The brushless exciter has a DC stator that is fed through the output of the HG as shown in Fig. 4.7(b). The machine terminal voltage is converted to a DC voltage via a passive rectification stage. The brushless exciter has an AC rotor that may use a 3- or multiphase configuration. Output of the brushless exciter rotor is then connected to a rotating rectifier that in turn provides the DC supply to the HG WF. A multiphase design for the brushless exciter can give good DC output quality with lower voltage ripple and higher output voltage than compared to three-phase exciter, hence eliminating the need for passive capacitors at its output.

4.3.2 HG Prototype Machine and Experimental Test facility

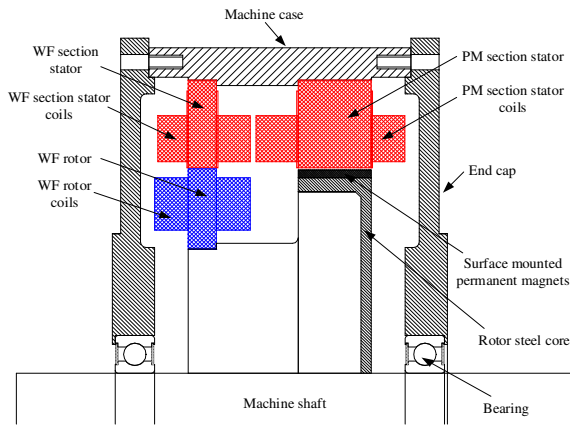
To investigate the feasibility of the proposed HG concept a low power prototype HG was simulated and test validated in the laboratory. The original design of the prototype HG was to address an automotive application and was constrained to use a specific stator lamination and pole number configuration [102]. These design issues are outside the scope of this thesis and not wholly relevant to the design of a HG for wind applications. Where design decisions are relevant they are discussed in detail in Chapter 5.

The objectives of this thesis were to develop a simulation model for the HG, use the model to investigate the machine operational characteristics when acting as a generator into a variable DC-link supply, validate model experimentally and then propose the operational philosophy with regard-to field control-to-DC-link interaction.

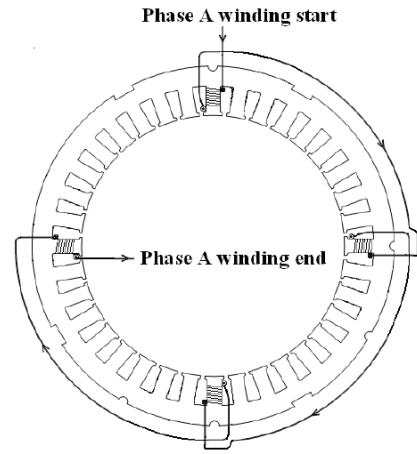
The prototype HG was designed with a 30% WF to 70% PM voltage ratio and as a 9-phase generator with 32 poles. The stator lamination has 36 slots with concentric coils. The PM rotor has 32 sintered NdFeB magnets and the WF rotor uses a 32-slot laminations each wound with simple concentrated coils to form a 32-pole configuration as per the PM rotor section. Note that the PM and WF rotor share the same stator. For the prototype HG, the DC current for the WF is supplied via slip rings and brushes. However, a brushless exciter utilizing the same stator and rotor WF laminations has been designed by the author as discussed in [103]. Table 4.2 lists the HG prototype and brushless exciter specifications while Fig. 4.8 shows prototype HG details. The HG 9-phase output is full-bridge rectified and connected to a controlled DC source that emulates the system DC-link. Fig. 4.9 shows the HG laboratory prototype and test-rig. The HG assembly is housed in a single casing. The test-rig comprises of the laboratory prototype HG, in-line torque measurement transducer and a 4 kW electronically controlled industrial induction machine. The induction machine acts as a variable speed prime-mover emulating the wind turbine mechanical input to the HG.

Table 4.2. HG prototype and brushless exciter specifications

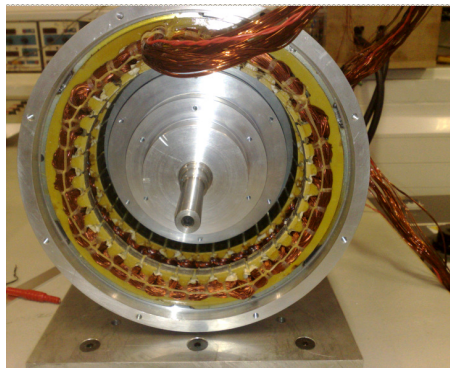
Description	Value
PM rotor axial length, mm	25
WF rotor axial length, mm	10
Brushless exciter axial length, mm	4
Number of turns per stator coil for the HG	14
Number of turns per stator coil for the brushless exciter	50
Number of turns per rotor coil for the WF	80
Number of turns per rotor coil for the brushless exciter	73
Number of HG and exciter stator slots	36
Number of WF and exciter rotor lamination slots	32
Number of HG stator phases	9
Number of exciter rotor phases	16
Number of HG poles	32
Number of brushless exciter poles	36



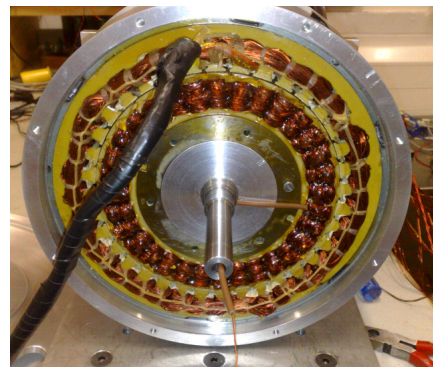
(a) Mechanical general assembly.



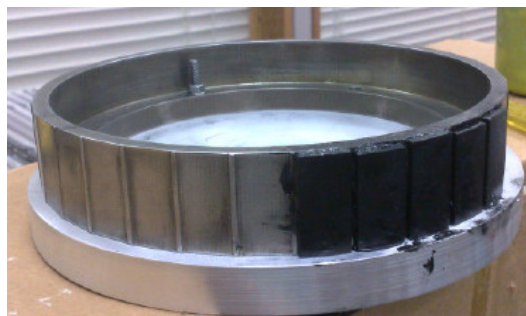
(b) 1-phase of 9-phase stator winding.



(c) Assembly showing stator and PM rotor.



(d) Assembly showing stator and WF rotor.



(e) PM rotor assembly.



(f) WF rotor assembly.

Fig. 4.8. Prototype HG details.

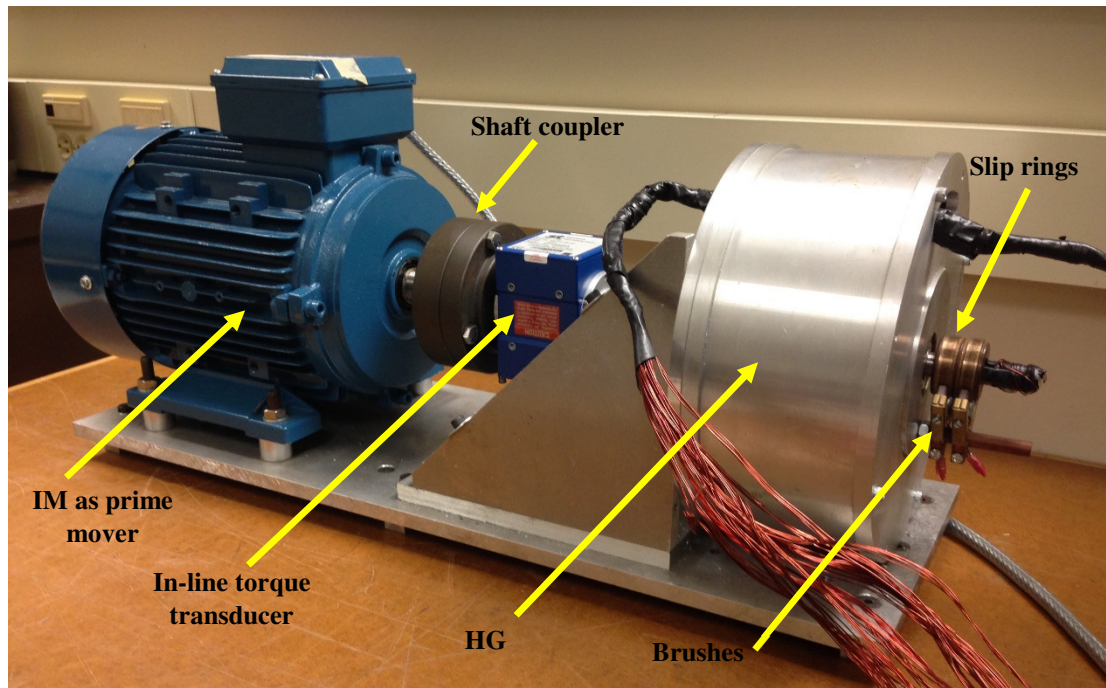


Fig. 4.9. HG prototype and test-rig.

4.3.3 Simulation Model and Results

A MATLAB Simulink model for the HG is shown in Fig. 4.10. The model implements the prototype HG machine (parameters), a representative 9-phase passive rectifier and DC-link source having some series impedance indicative of the experimental test facility. The HG was analyzed for various delivered electrical powers between 0.5 and 3.2 kW and for various DC-link voltage. For each delivered electrical power the rotor field current was chosen to match the HG output DC voltage to that of the test DC-link voltage. Fig. 4.11 shows the set of simulated data at a fixed rotor speed of 3000 RPM. The characteristic is a set of V-curves, although these V-curves are not to be confused with classical V-curves for conventional wound rotor synchronous machines.

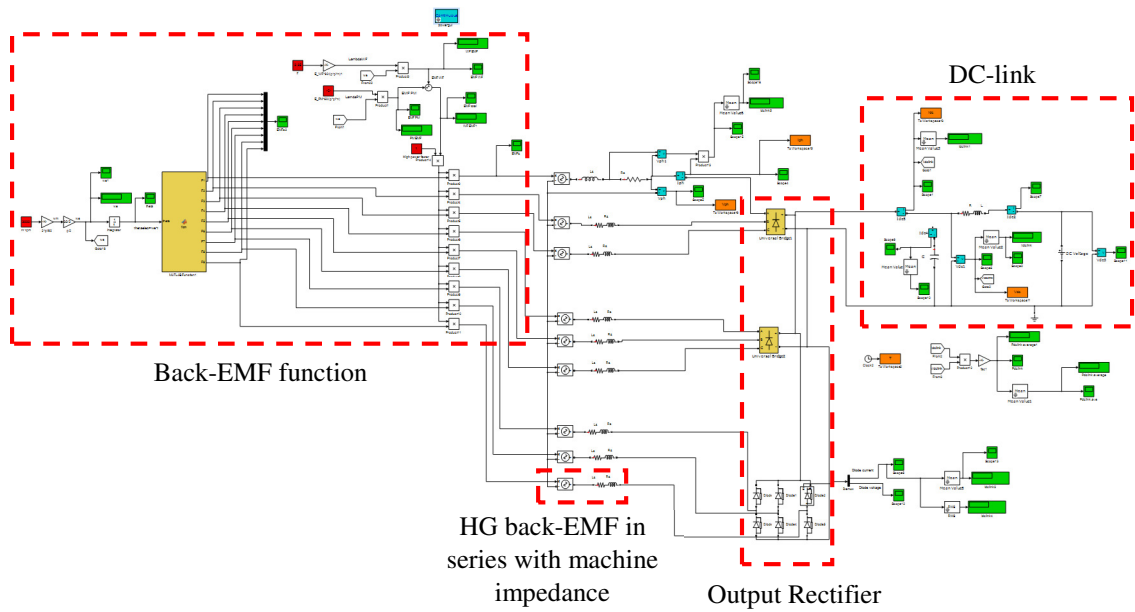


Fig. 4.10. HG MATLAB Simulink.

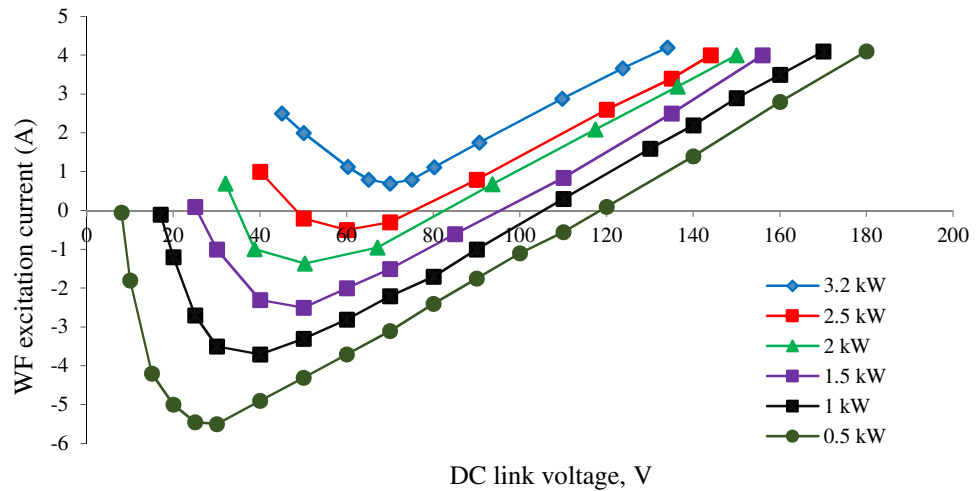


Fig. 4.11. WF excitation current with respect to DC-link voltage for varying DC-link powers at 3000 RPM.

Fig. 4.12 presents measured and simulated results for the HG WF excitation current versus DC-link voltage variation at a nominal speed of 3000 RPM when delivering a fixed power of 2 kW to the DC-link. The HG was tested to confirm the generator operational characteristics within a laboratory environment; hence the rectified DC output of the generator at a fixed speed of 3000 RPM is in the region of 40 to 140 Volts depending on WF excitation. In practice, this variation exceeds the application requirements (i.e. $\pm 30\%$ voltage variations), but is tested here to illustrate the generator characteristic outside the application requirements.

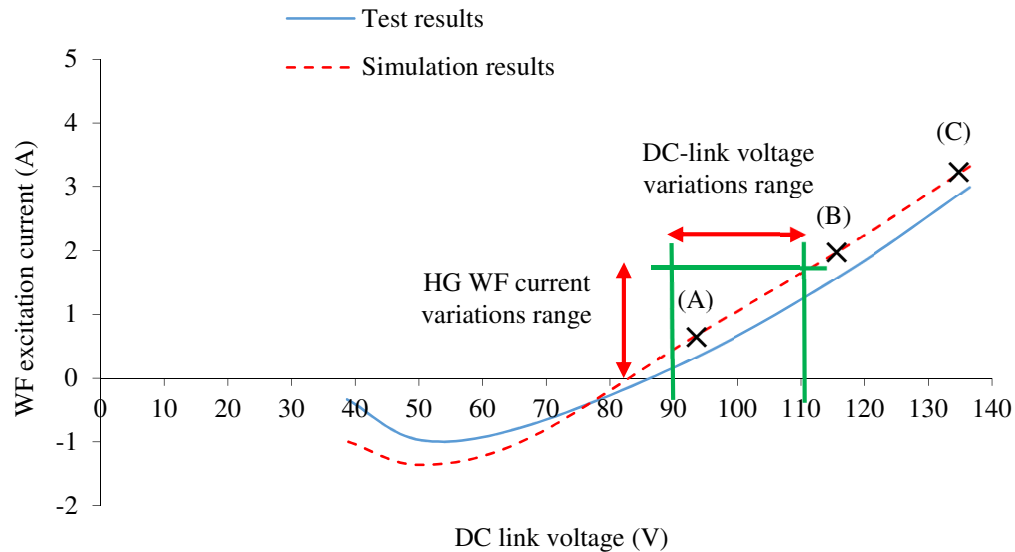


Fig. 4.12. HG WF current and DC-link voltage variations at nominal 3000 RPM speed.

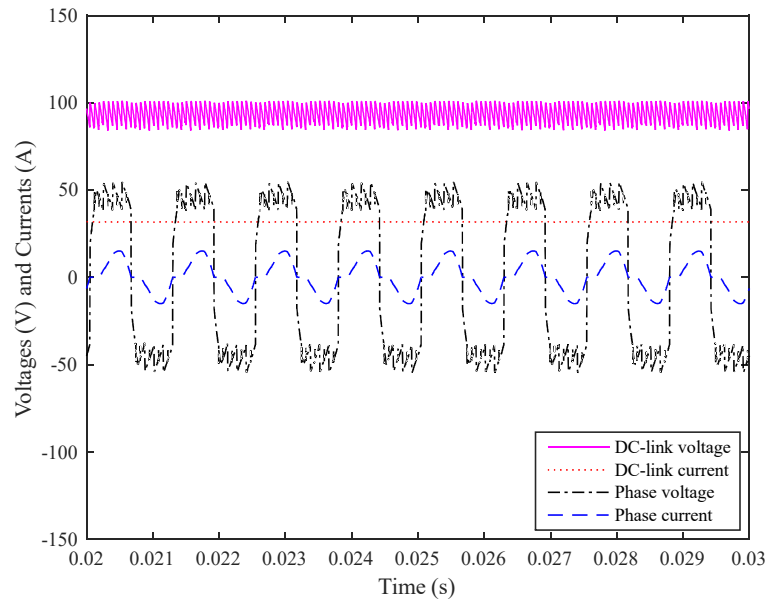
For the wind farm application, the maximum DC-link voltage variation at each speed due to the WF is only 25% (this will be discussed in Chapter 5) which results in a practical limit to the WF current, as illustrated in Fig. 4.12. Therefore, as the wind velocity and hence HG rotor speed varies, the resulting DC-link voltage variation can be modified by variation of the WF rotor current to maintain output voltage and generation. Table 4.3 compares simulated and measured results at three different DC-link voltage operating points, (A), (B) and (C) of Fig. 4.12, and at a fixed speed of 3000 RPM when delivering 2 kW electrical

power. Fig. 4.13 shows simulated waveforms for the HG output phase voltage, phase current and also rectified DC voltage and current at 3000 RPM speed while delivering 2 kW power to the DC-link and for a DC-link average voltage of (a) 93.6 V point (A) and (b) 117.4 V, point (B). Fig. 4.14 presents simulated and measured results when again delivering 2 kW at a speed of 3000 RPM and a DC-link voltage of 136.4 V, point (C). The results of Fig. 4.14 show the good agreement between simulated (a) and measured (b) data.

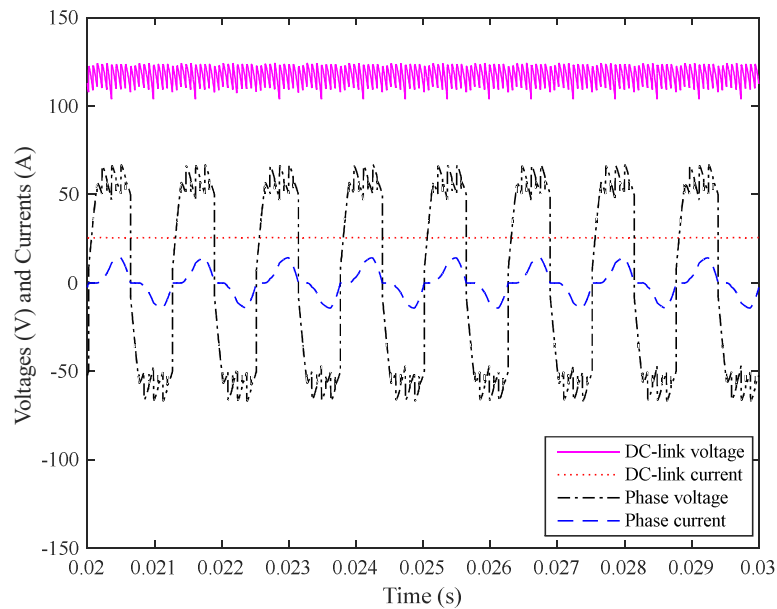
Table 4.3. Comparison of simulated and measured results for HG prototype at different DC-link voltage, 3000 RPM and delivering 2 kW

Op. point	DC-link				HG					
	Average voltage (V)		Average current (A)		RMS voltage (V)		RMS current (A)		WF DC current (A)	
	Sim.	Me.	Sim.	Me.	Sim.	Ms.	Sim.	Me.	Sim.	Me.
(A)	93.6	93.6	22.14	22.18	53.44	46.11	4.31	5	0.68	0.34
(B)	117.4	117.4	18.2	18.21	60.68	56.88	3.91	4.2	2.09	1.69
(C)	136.4	136.4	15.9	15.72	67.01	64.84	3.56	3.8	3.32	3

Op.: Operating; Sim.: Simulated; Me.: Measured

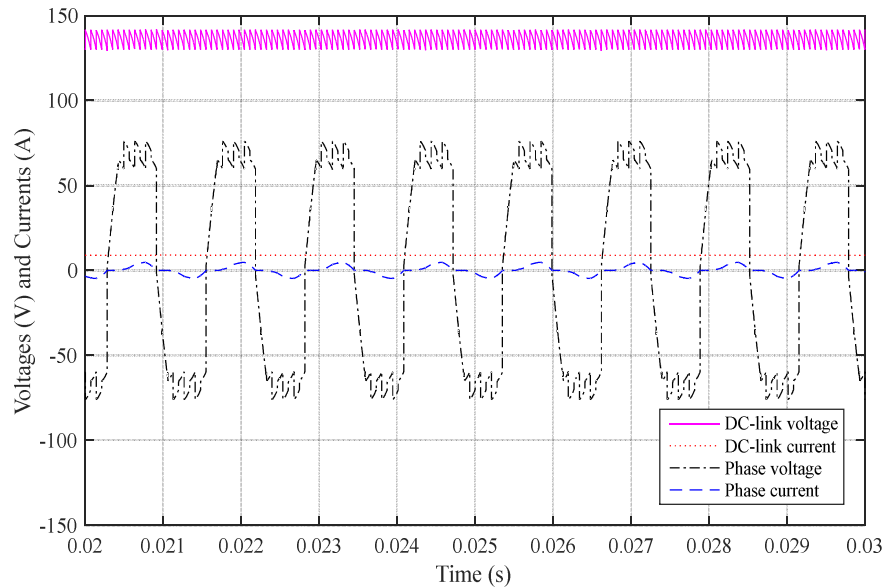


(a) DC-link voltage=93.6 V, point (A).

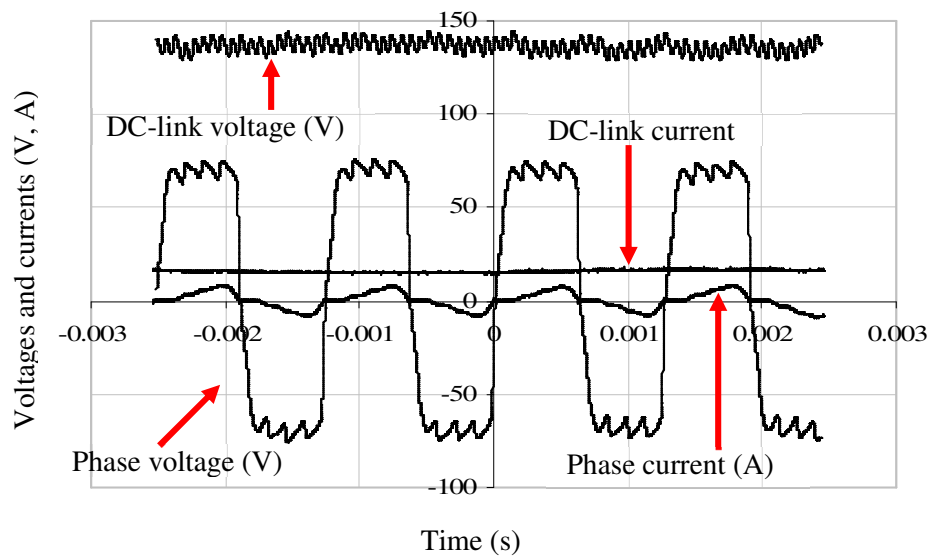


(b) DC-link voltage=117.4 V, point (B).

Fig. 4.13. HG simulated phase voltage and current, DC-link voltage and current at 3000 RPM for a delivered power of 2 kW.



(a) Simulated waveform.



(b) Measured waveforms.

Fig. 4.14. HG simulated and measured phase voltage and current, DC-link voltage and current at 3000 RPM for a delivered power of 2 kW, point (C).

4.4 High Voltage Benchmark Synchronous Generator (SG)

4.4.1 General Details

The HG proposed in this study is a high voltage, high power machine. However, it is out of scope of this thesis to build and test validate a high voltage, high power machine. Therefore, in order to have a sensible and viable design consistent with industry practice, a high voltage SG manufactured by Siemens whose design specifications and performance data are available to the author is selected as benchmark machine. Design of the HG is developed based on the benchmark SG specifications. Hence, the benchmark SG is analyzed and compared to the performance data to verify the analysis procedures and tools. The electromagnetic characteristics of the benchmark SG are investigated using finite element analysis (FEA) to obtain machine electromagnetic field distribution and flux-linkages. Analyses are carried out for no-load and full load conditions where the back-EMF, torque and machine performance is simulated. Once the benchmark SG characteristics are obtained they are used as acceptable measures for the subsequent HG design discussed in Chapter 5.

The benchmark SG is a 3-phase, 11 kV (line-to-line RMS voltage), synchronous generator which is in operation in a hydro generation plant. The benchmark SG is a salient pole machine rated at 5.52 MW with a nominal speed of 600 rpm. The machine is directly connected to the 3-phase, 50 Hz grid. Table 4.4 lists the main machine specifications. The high pole, low speed design was chosen to be compatible with the HG concept.

Table 4.4. Benchmark SG specifications

Parameter	Description/Value
Generator type	Salient pole synchronous generator (SG)
Rated power (MW)	5.52
Rated RMS line-to-line voltage (kV)	11
Rated RMS phase current (A)	362
Field DC current at rated power (A)	486.23
Rated speed (RPM)	600
Number of poles	10
Frequency (Hz)	50
Number of phases	3

The benchmark SG stator outer diameter is 2700 mm with an inner diameter of 2150 mm and active axial length of 400 mm, as illustrated in Fig. 4.15. The benchmark SG main dimensions are summarized in Table 4.5 and for the purpose of comparison specification details for the IG used in the Walney wind turbines are listed in Table 4.6.

Table 4.5. Benchmark SG dimensions

Parameter	Value
Machine axial length (mm)	400
Machine outer diameter (mm)	2700
Machine inner diameter (mm)	2150
Minimum air-gap length (mm)	7
Maximum air-gap length (mm)	11
Maximum rotor diameter of body (mm)	2136
Shaft diameter (mm)	400
Bearing diameter (mm)	250
Bearing length (mm)	200
Rotor pole body height (mm)	195 mm
Rotor pole body width (mm)	350 mm
Rotor pole shoe minimum height (mm)	43.7 mm
Number of stator slots/teeth	135
Stator tooth tip width (mm)	31.35
Stator slot width (mm)	18.50
Stator slot length from air-gap (mm)	90
Stator slot length for winding (mm)	87
Wedge length (mm)	5
Stator back-iron thinness (mm)	180
Stator slot area available for winding (mm ²)	1609.5

Table 4.6. Walney wind farm IG specifications

Parameter	Description
Generator type:	IG
Rated power (MW)	3.6 MW
Rated voltage (V)	690
Rated current (A)	3075.7
Rated speed (RPM)	1500
Number of poles	4
Frequency (Hz)	50
Number of phases	3
Machine length (m)	2.17
Machine outer diameter (m)	1.15
Machine inner diameter (m)	0.57

The front-end cross-section of the benchmark SG is illustrated in Fig. 4.15 with annotated main dimensions. The stator tooth/slot and rotor pole geometries are presented in Fig. 4.16 and Fig. 4.17 respectively. As seen from Fig. 4.17 (a) the rotor has a salient pole whose “shoe” length varies from 70 mm at the middle of the pole to 43.7 mm at the corners. Therefore, the air-gap length changes from a minimum of 7 mm in the middle of the pole to a maximum of 11 mm at the pole corners. Hence, the benchmark SG does not have a constant air-gap over the pole-face, referred to here as ‘adjusted’ air-gap. To test contribution of this design feature a modified rotor topology was modelled having a constant air-gap at the rotor pole-to-stator interface as illustrated in Fig. 4.17 (b). It will be shown later that the adjusted air-gap rotor topology reduces cogging torque. The stator slot length is 95 mm out of which 5 mm is the wedge length to keep the winding inside the slot, 3 mm the stator tip and 87 mm the stator main body. The stator slot width is 18.5 mm and the tooth width is 31.53 mm. Therefore, the stator slot/tooth pitch is 50.03 mm.

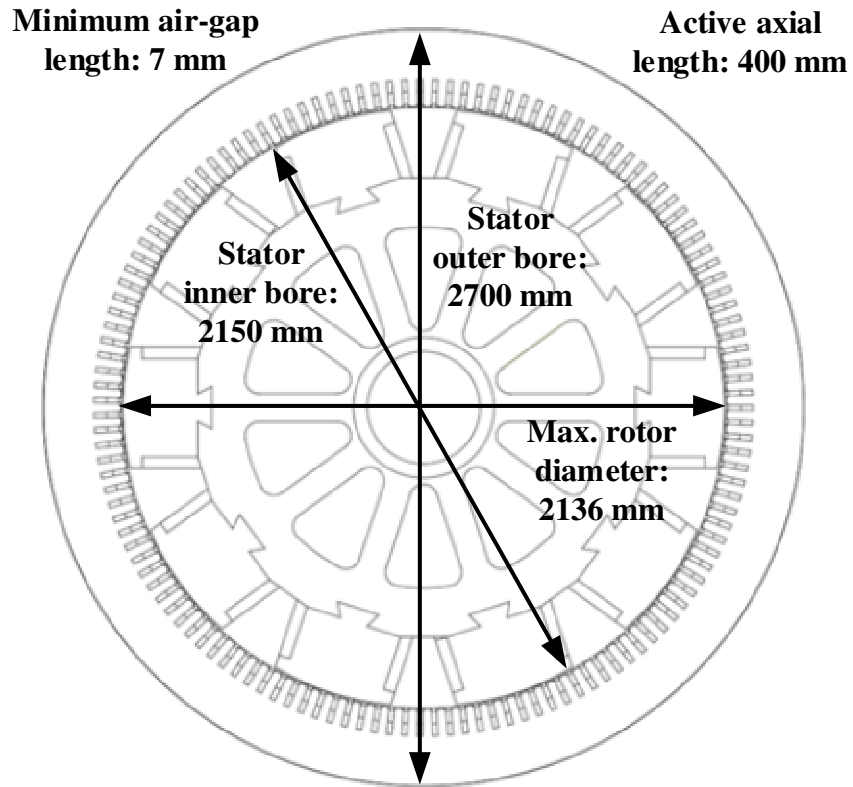


Fig. 4.15. Front-end cross-section of the benchmark SG.

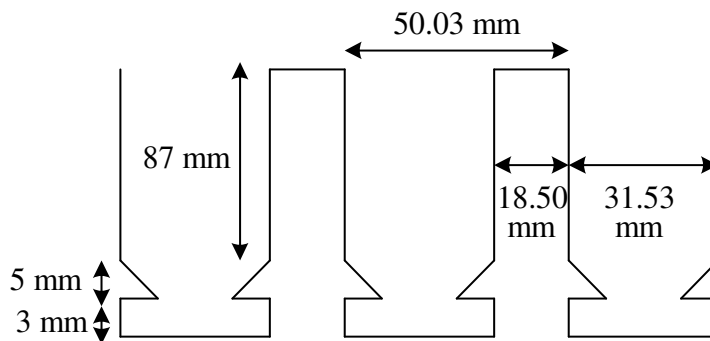
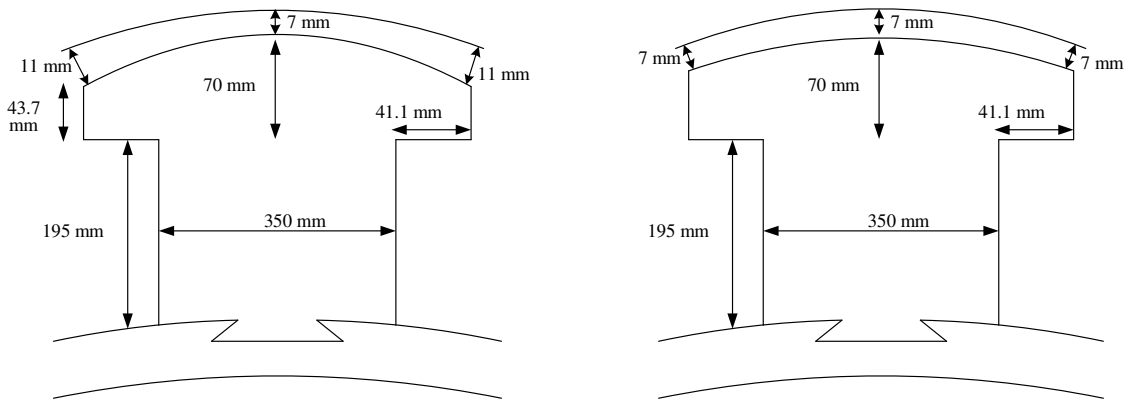


Fig. 4.16. Benchmark SG stator tooth/slot details.



(a) Benchmark machine rotor with “adjusted” air-gap. (b) Constant air-gap rotor topology to test “adjusted” air-gap feature.

Fig. 4.17. Benchmark SG rotor pole structure.

4.4.2 Winding Arrangement

The benchmark SG stator has 135 slots with a 3-phase distributed winding. The pole pitch (number of slots per pole) is 13.5 slots while the coil pitch (span) is 12 slots. Therefore, since the coil pitch is less than the pole pitch the winding is short-pitched. The winding phase band (sometimes called phase belt) is:

$$\text{Phase band} = \text{slots} / \text{pole} / \text{phase} = 135 / 10 / 3 = 4.5 \quad (4.1)$$

Since the phase band is not an integer the winding is a double layer fractional-slot winding [104]. In order to form a fractional slot winding a pattern needs to be found. Over the years, motor designers have developed a set of rules that will produce a balanced 3-phase fractional slot winding. Using the set of rules described in [104] a pattern of 5 and 4 coils for the benchmark SG stator winding is found as illustrated in Fig. 4.18. A set of 5 coils are connected in series where one side of the coil is placed into the top layer and the other side is in the bottom layer. The 4-set coils are also laid out similarly and the two sets, 5-set and

4-set, are then connected in series to form a complete pattern. Fig. 4.18 presents the winding pattern for one phase, this pattern being repeated five times for all the 135 slots to form the complete phase winding. Therefore, there are 45 coils per phase which are connected in series. Fig. 4.19 shows connection of the coils in one phase. The pattern is repeated for the other two phases in the final 3-phase winding.

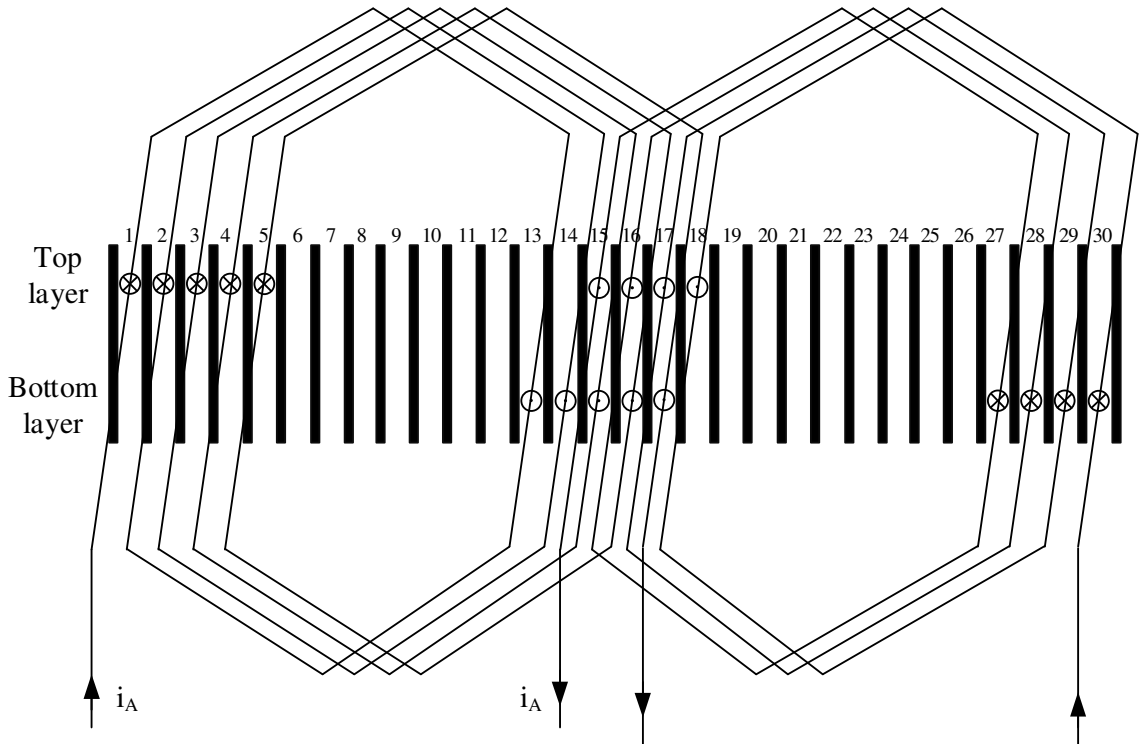


Fig. 4.18. Fractional-slot, short-pitched stator winding for the benchmark SG.

In each stator slot there are two coils. Each coil consists of four conductors (turns) and each conductor has a total of six strands electrically connected in parallel. The cross-section of a stator slot including cross-section of coils, conductors and strands for the benchmark SG is shown in Fig. 4.20. The two coils in the slot are separated using a 4 mm insulating material. The insulation systems for the windings will be discussed in Chapter 6.

The DC benchmark SG rotor winding consists of 10 coils each wound around one salient pole. Each coil has 51 turns and the 10 coils are connected in series. Fig. 4.21 shows the

rotor winding as well as stator slot windings. The rotor winding connections are shown in Fig. 4.22.

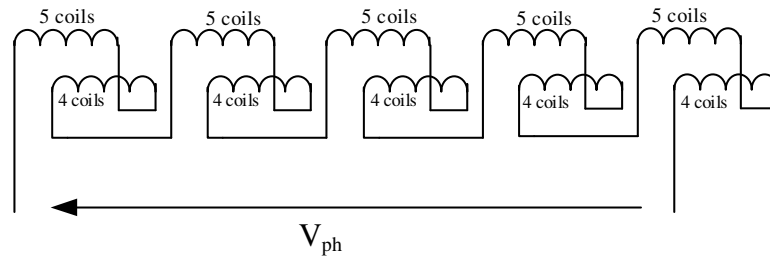


Fig. 4.19. Stator phase coil connections for benchmark SG.

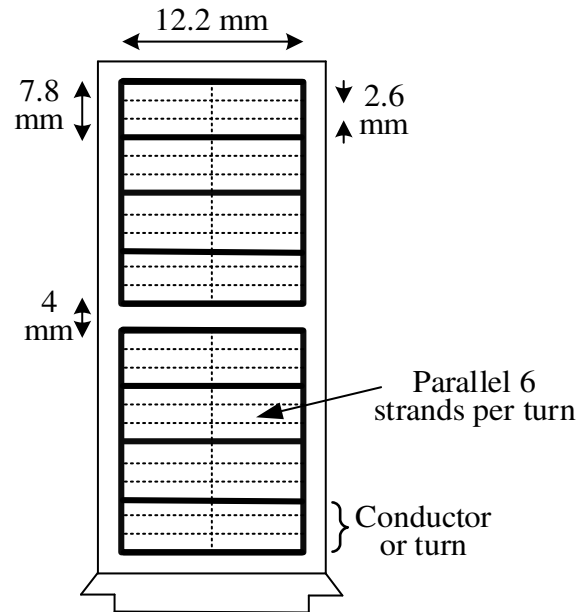


Fig. 4.20. Stator slot showing cross section of coil, conductor and strands.

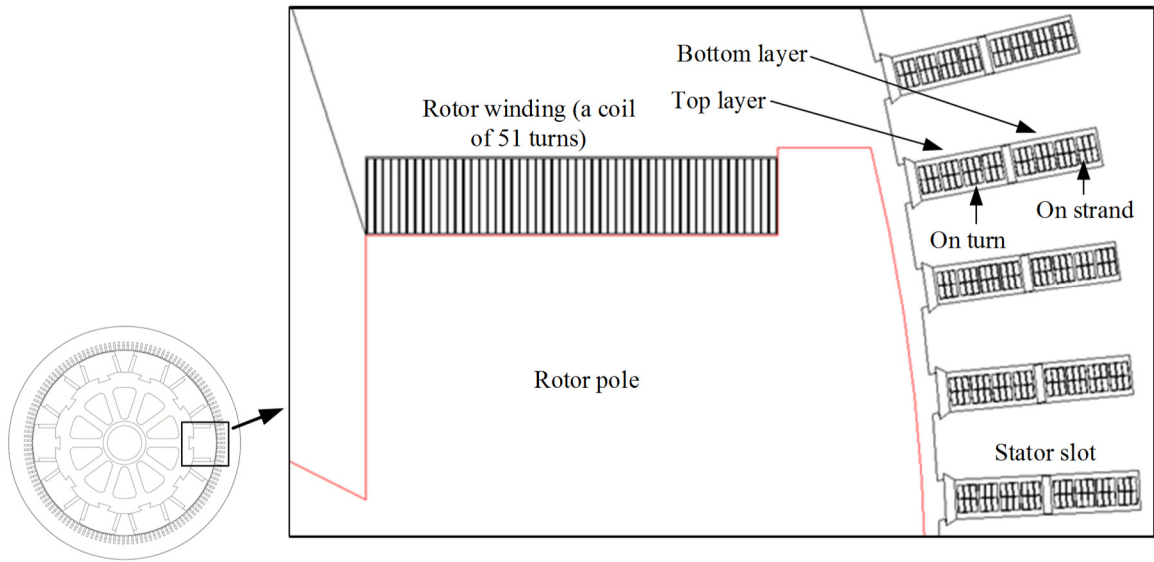


Fig. 4.21. Rotor and stator windings.

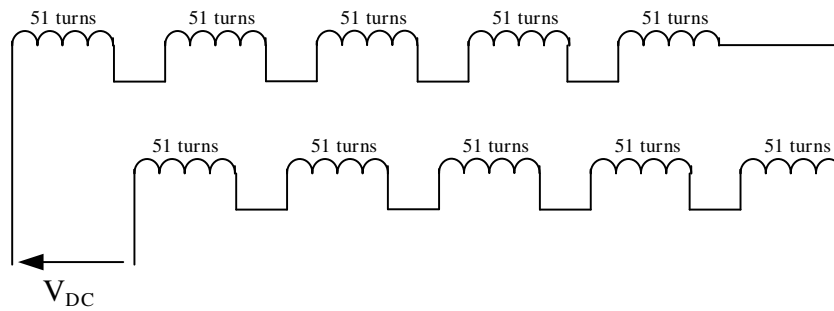


Fig. 4.22. Rotor coil connections for benchmark SG.

4.4.3 Magnetic Field Distribution and Flux-density

Using FEA the benchmark SG open circuit (O.C.) flux distribution at zero rotor angle and for a full-field current of 486.23 A is shown in Fig. 4.23. It is seen that some parts of the stator back-iron and rotor laminations operate at flux-densities close to 2 T and hence are saturated. Indeed, the machine operates at high flux-density at full-load facilitating reduced inductance and hence better power capability. Higher flux-density implies higher iron losses, however, loss management, or cooling is accommodated to maintain machine performance.

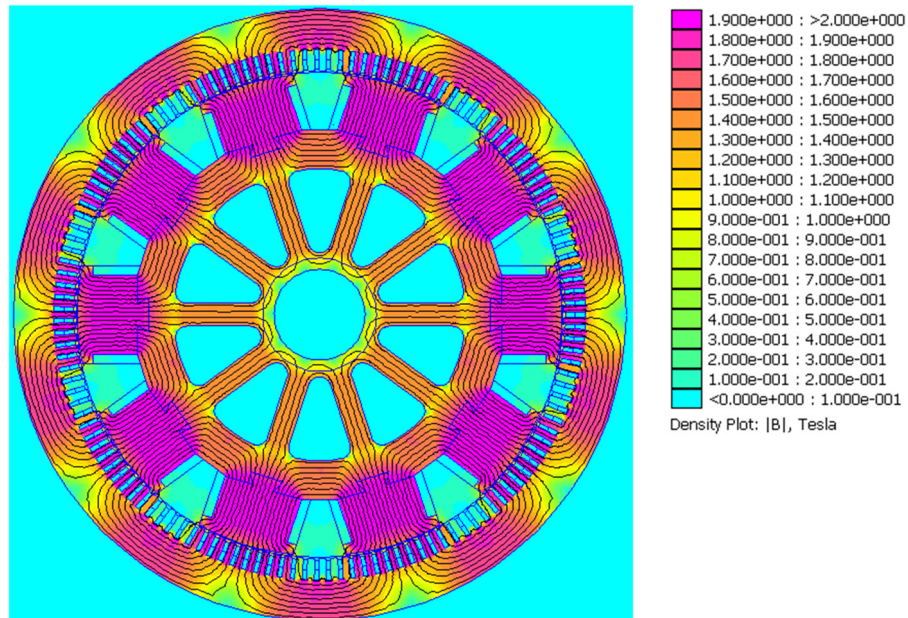


Fig. 4.23. Benchmark SG field distribution at full field.

Fig. 4.24 illustrates the normal and tangential component of the air-gap flux-density with respect to rotor electrical angle and for two electrical cycles. The perturbations at the peak flux-density plot is caused by the stator slots and are called ‘slot effects’. The flux crossing the air-gap faces a magnetically uneven surface of slots and teeth combination with variant reluctance which causes the slot effect. Flux-densities for different parts of the machine

laminations are listed in Table 4.7 with reference to machine sections shown in Fig. 4.25. The flux-densities are measured perpendicular to the dashed/solid line for each section.

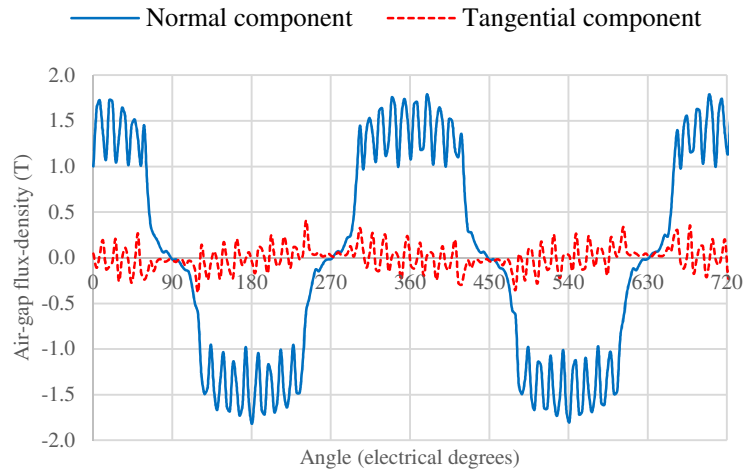


Fig. 4.24. Air-gap flux-density versus rotor electrical angle for two electrical cycles.

Table 4.7. Flux-density for different machine sections

Section	Flux-density (T)
Average air-gap over half a cycle (normal component)	0.998
Average air-gap over half a cycle (tangential component)	0.11
A	1.69
B	2.1
C	2
D	1.8
E	1.5
F	1.85
G	1.87
H	1.76
I	1.3

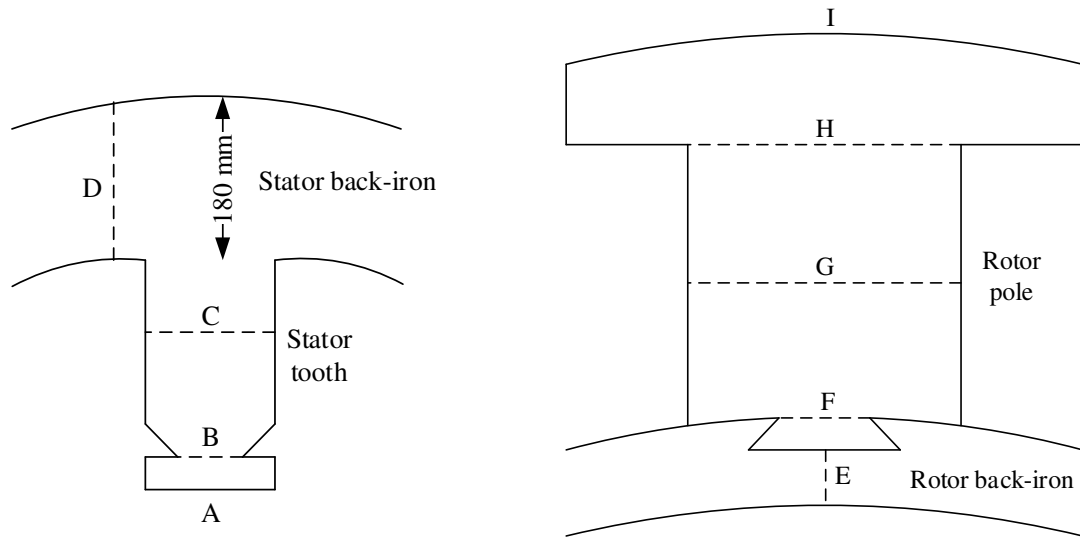


Fig. 4.25. Stator and rotor sections for flux-density measurement.

The average air-gap flux-density over half a cycle that is an indication of machine magnetic loading is 0.998 T (for the normal component). As seen from Table 4.7 the tooth tip operates at the highest flux-density in the machine i.e. 2.1 T. However, the mid-tooth and back-iron flux-density is 2 T and 1.8 T respectively. These numbers confirm that the machine operates at high flux-densities at full-field current excitation. In order to define how much the machine is operating into saturation the FEA analysis at different field currents is performed and plots for average air-gap, tooth and back-iron flux-densities are presented in Fig. 4.26 with their value listed in Table 4.8. The tooth flux-density is measured at the middle of the tooth i.e. section ‘C’ in Fig. 4.25. Also, the back-iron flux-density is measured at points with highest saturation.

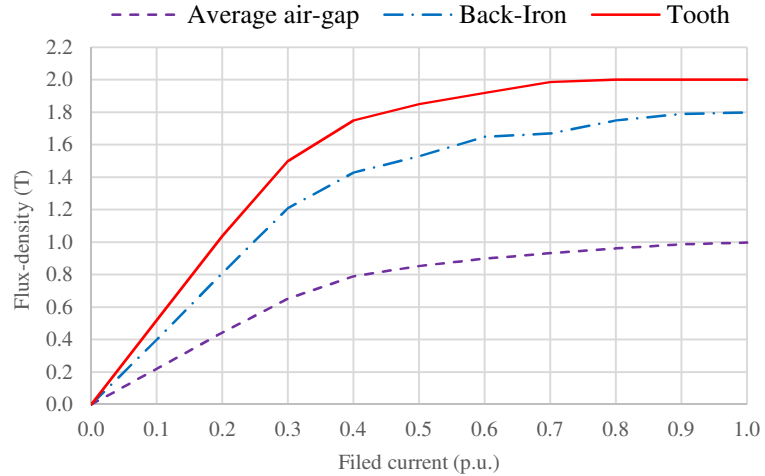


Fig. 4.26. Flux-density versus rotor field current for air-gap, back-iron and tooth.

Table 4.8. Flux-density for different field currents

Field current		Flux-density (T)		
(A)	(p.u.)	Average air-gap	Back-iron	Tooth
0	0.00	0	0	0
48.623	0.10	0.222	0.4	0.52
97.246	0.20	0.445	0.81	1.04
145.869	0.30	0.653	1.21	1.5
194.492	0.40	0.79	1.43	1.75
243.115	0.50	0.854	1.53	1.85
291.738	0.60	0.9	1.65	1.92
340.361	0.70	0.932	1.67	1.986
388.98	0.80	0.962	1.75	2
437.61	0.90	0.988	1.79	2
486.23	1.00	0.998	1.8	2

4.4.4 Flux-linkage and Back-EMF

The open-circuit flux-linkage over one electrical cycle for one phase winding and at a full-field current of 486.23 A is shown in Fig. 4.27. As discussed previously, the benchmark SG has an adjusted air-gap, Fig. 4.17 (a). The flux-linkage from the adjusted air-gap machine is compared with that for the constant air-gap machine shown in Fig. 4.17 (b), and the results presented in Fig. 4.27, where it can be noted that there is little difference.

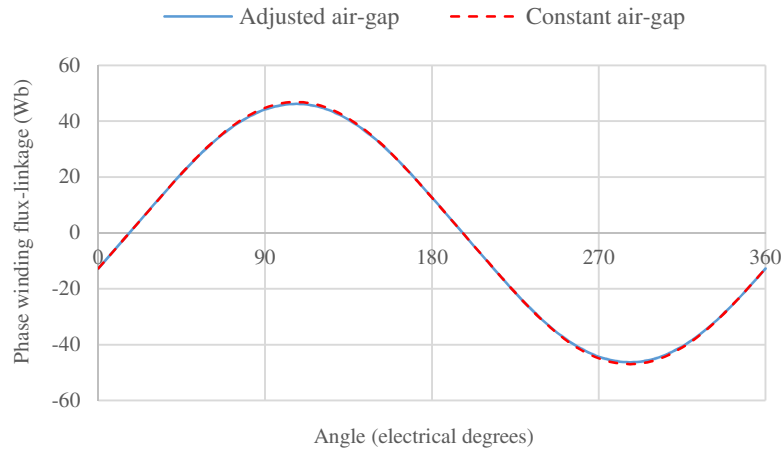


Fig. 4.27. Phase winding open-circuit flux-linkage for the benchmark SG at full-field.

The stator phase winding induced open-circuit back-EMF is calculated from Faraday and Lenz's laws viz:

$$E = -N \frac{d\phi}{dt} \quad (\text{V}) \quad (4.2)$$

where ϕ is the flux-linkage per phase winding. The rate of change in flux-linkage with respect to rotor electrical angle can be expressed in terms of machine speed:

$$\begin{aligned} \frac{d\phi}{dt} &= \frac{d\phi}{d\theta_e} \frac{d\theta_e}{dt} \\ \frac{d\theta_e}{dt} &= \omega_e \end{aligned} \quad (4.3)$$

Therefore, the phase winding open-circuit back-EMF is:

$$E = -N \omega_e \frac{d\phi}{d\theta_e} \quad (\text{V}) \quad (4.4)$$

also,

$$\omega_e = \frac{P}{2} \omega_m \quad (\text{electrical rad/s}) \quad (4.5)$$

$$\omega_m = \frac{2 \pi n}{60} \quad (\text{Mechanical rad/s}) \quad (4.6)$$

where,

N : is the total number of phase turns

ω_e : Machine electrical rotor speed (rad/s)

ω_m : Machine mechanical rotor speed (rad/s)

θ_e : Rotor electrical angle (rad)

n : Rotor speed (RPM)

P : Number of poles

Fig. 4.28 shows the phase winding back-EMF for full-field current and nominal rotor speed of 600 RPM. Here the back-EMF is plotted for both the adjusted and constant air-gap rotor designs. It is observed that there is no substantial difference in the open-circuit back-EMF between the two topologies. However, it will be shown later that the cogging torque for the adjusted air-gap is significantly smaller. The phase winding open-circuit back-EMF for different rotor currents is shown in Table 4.9 while Fig. 4.29 illustrates these results graphically. Fig. 4.29 also confirms that the machine is magnetically saturated at full-field. In fact, the linear region only extends to field currents up to 150 A; field current above 150 A progressively moving into the saturated region. Note that the rotor speed is kept at 600 RPM at all field currents. The phase winding open-circuit back-EMF is not a pure sinusoidal waveform and hence the RMS values are calculated accordingly.

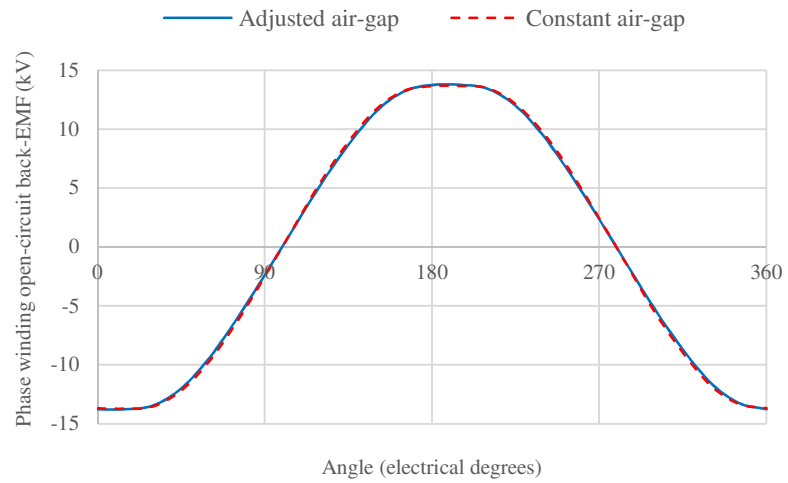


Fig. 4.28. Phase winding open-circuit back-EMF at full-field and nominal rotor speed of 600 RPM.

Table 4.9. Phase winding open-circuit back-EMF for different rotor field currents

Field current (A)	Phase back-EMF (kV)	
	Peak	RMS
0.00	0.00	0
30.00	2.03	1.44
60.00	4.09	2.91
90.00	6.14	4.36
122.32	8.25	5.87
149.09	9.80	7.02
193.97	11.32	8.26
235.22	11.98	8.81
298.43	12.66	9.35
382.20	13.29	9.87
486.23	13.77	10.32

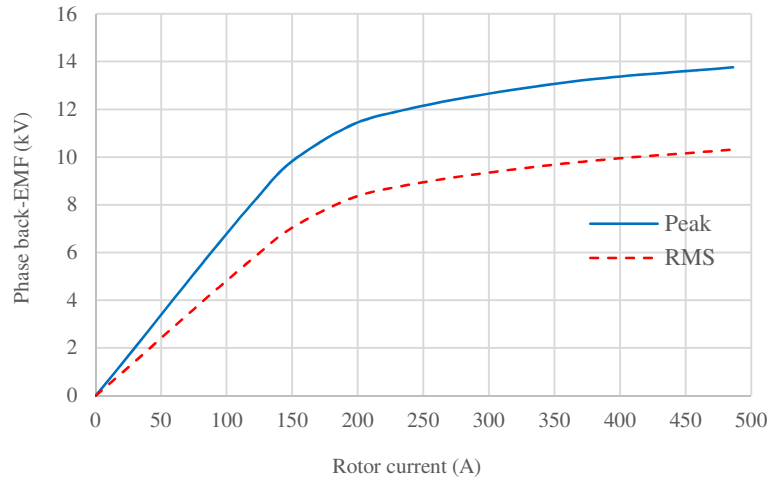


Fig. 4.29. Phase winding open-circuit back-EMF versus rotor field current.

4.4.5 Torque Calculations

Cogging torque for the benchmark SG is plotted in Fig. 4.30. The cogging torque is calculated at no-load (zero stator current) and full-field rotor current for both the adjusted and constant air-gap rotor topologies. It is seen that for the adjusted air-gap rotor the machine cogging torque is substantially lower. Therefore, the effect of adjusting the air-gap is a lower cogging torque in the benchmark SG under study.

The machine torque versus rotor angle at full-load stator phase winding current (512 A peak) and full-field field current (486.23 A) is presented in Fig. 4.31. The benchmark SG has a salient rotor therefore the total torque has two components; (i) excitation torque and (ii) salient torque. The excitation torque is as a result of the interaction of the rotor and stator magnetic fields. The rotor magnetic field is produced by the rotor field current and stator magnetic field is produced by the stator 3-phase winding currents. The salient torque however, is only dependent on the machine geometry and the stator currents. As an estimate of each contribution, the excitation torque can be obtained by subtracting the salient torque

from the total torque, the results of which is shown in Fig. 4.31. However, the results of Fig. 4.31 is not as would be expected from contemporary machines theory. This feature was investigated further by varying the stator current amplitude and then the rotor field current amplitude. Fig. 4.32 presents machine total torque at full-field and for full, three-quarter, half and one-quarter stator current excitation. It is seen that there appears little-to no saliency torque component at full rotor field current at any stator loading. In order to see this clearer, Fig. 4.33 shows the near linear variation of peak torque with respect to stator load current. Fig. 4.34 shows total torque for different rotor field currents and at full-load stator current excitation. It is seen that as the rotor field current reduces the effect of saliency, i.e. the twice fundamental component, becomes clear in the total torque. Therefore, as the rotor field current decreases the machine magnetics move from saturation and the salient torque becomes more apparent in the machine torque versus angle characteristics. Fig. 4.35 presents the peak torque variations with respect to rotor field current. Thus, at full rotor field, saturation in the machine rotor (and to some extent the stator) negates the salient torque contribution.

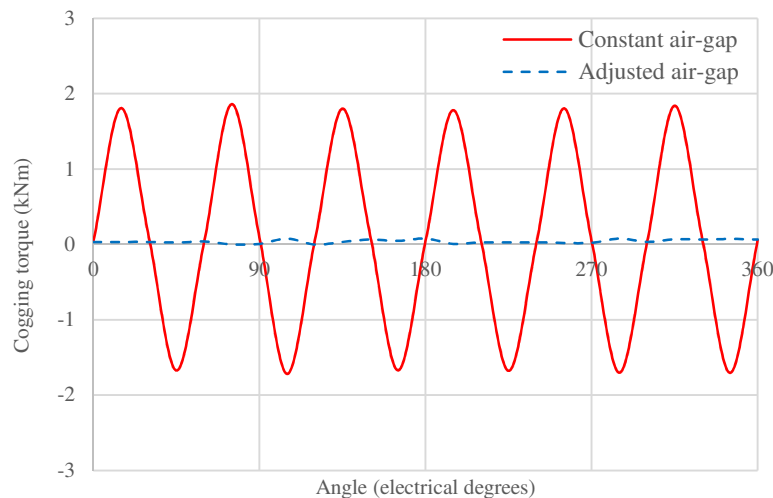


Fig. 4.30. Benchmark SG cogging torque for the adjusted and constant air-gap rotor topologies.

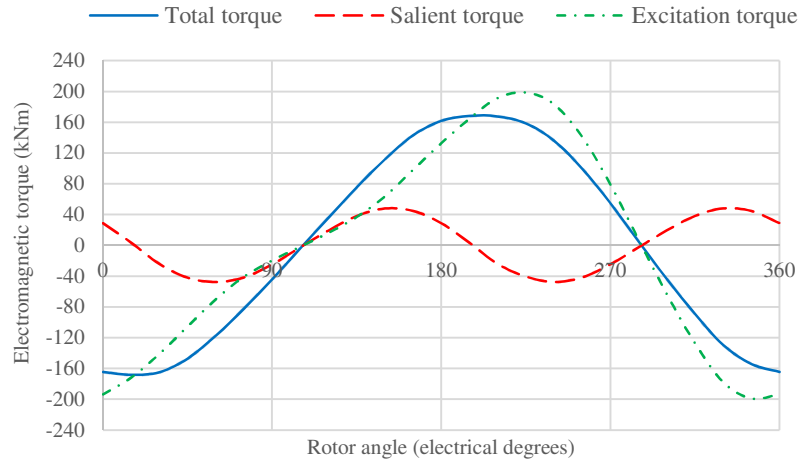


Fig. 4.31. Benchmark SG torque components at full rotor field current and full-load stator winding currents.

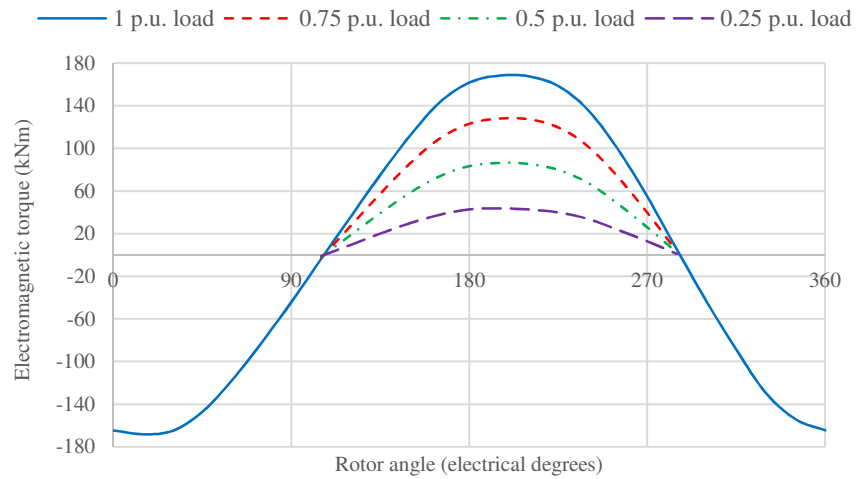


Fig. 4.32. Benchmark SG total torque at full-field and varying load.

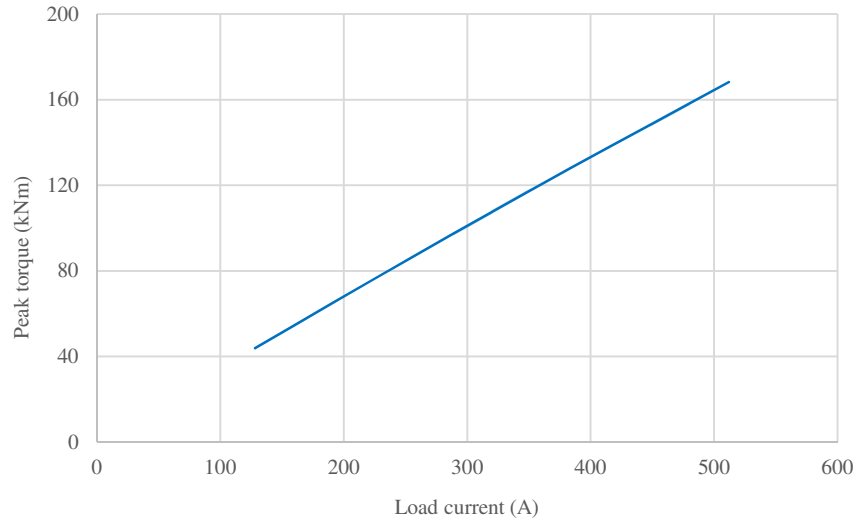


Fig. 4.33. Peak torque variation with-respect-to stator load current.

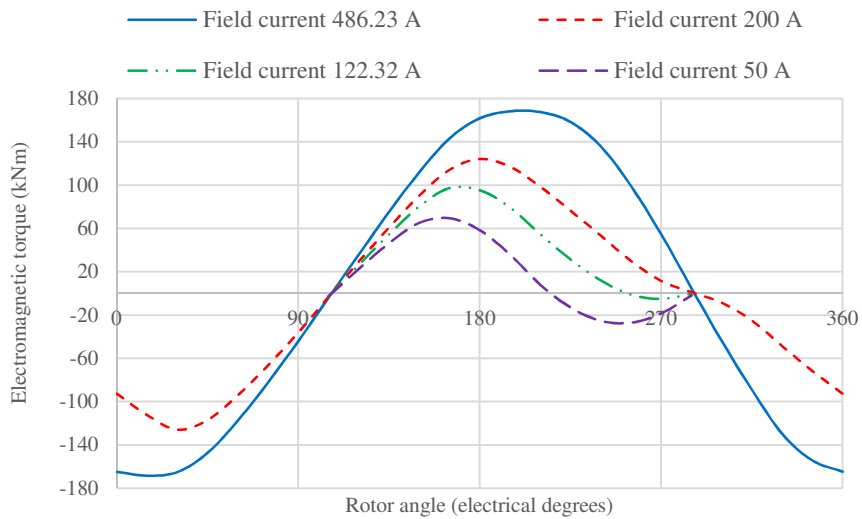


Fig. 4.34. Benchmark SG total torque at full-load stator current and varying rotor field current.

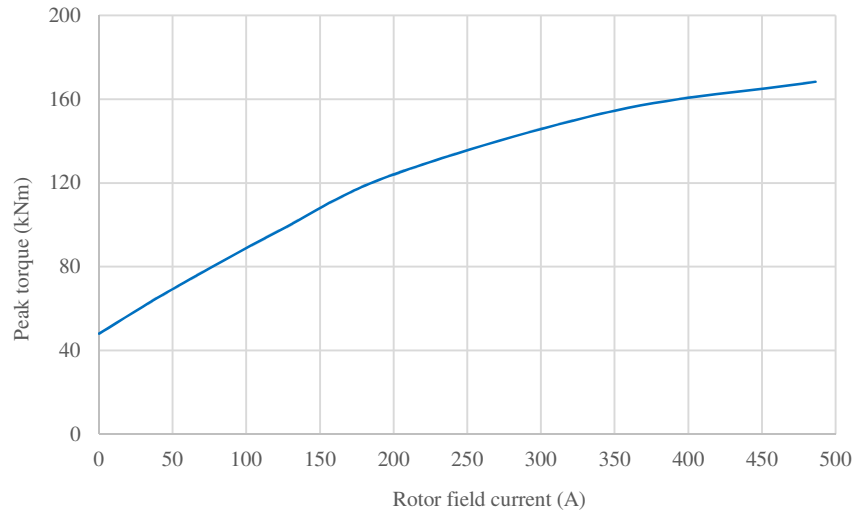


Fig. 4.35. Benchmark SG total torque at full-load stator current and varying rotor field current.

4.4.6 Inductances

As discussed previously, the benchmark SG operates in saturation at rated full-field current and full-load stator current. One of the saturation effects is reduced machine inductance which contributes to the machine power capability. The SG synchronous reactance is a function of the rotor field current once the machine is outside the linear (magnetic) operation region, as shown in Fig. 4.36 [105]. Machine output power has a reciprocal relationship with the machine reactance hence the machine output power increases as the machine goes into saturation as result of reduced inductance. Fig. 4.37 presents the per phase unsaturated self-inductance for the benchmark SG. The inductance is a function of rotor angle due to the rotor saliency, as discussed.

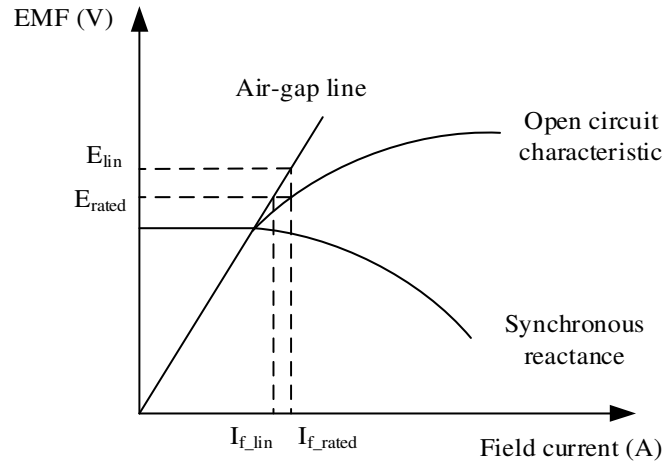


Fig. 4.36. SG synchronous reactance as function of field current.

The machine phase inductances are expressed as follows [106]:

$$\begin{aligned}
 L_a &= L_0 + L_2 \cos(2\theta_e) \\
 L_b &= L_0 + L_2 \cos\left(2\theta_e + \frac{2\pi}{3}\right) \\
 L_c &= L_0 + L_2 \cos\left(2\theta_e - \frac{2\pi}{3}\right)
 \end{aligned} \tag{4.7}$$

and the mutual coupling between phases are:

$$\begin{aligned}
 M_{ab} &= -\frac{1}{2} L_0 + L_2 \cos\left(2\theta_e - \frac{2\pi}{3}\right) \\
 M_{ac} &= -\frac{1}{2} L_0 + L_2 \cos\left(2\theta_e + \frac{2\pi}{3}\right) \\
 M_{bc} &= -\frac{1}{2} L_0 + L_2 \cos(2\theta_e)
 \end{aligned} \tag{4.8}$$

where,

L_a , L_b , L_c : Phase inductances for phase A, B and C respectively

M_{ab} , M_{ac} , M_{bc} : Mutual inductances between phases

L_0 : Average phase self-inductance (including leakage)

L_2 : Phase inductance amplitude variations above average

The d-q axis inductances shown in Fig. 4.37 are defined as follows [106]:

$$\begin{aligned} L_d &= \frac{3}{2} (L_0 + L_2) \\ L_q &= \frac{3}{2} (L_0 - L_2) \end{aligned} \quad (4.9)$$

The variation of inductances with rotor angle for a cylindrical rotor SG are generally neglected and hence the term with angular variation, i.e. L_2 , is assumed zero. Hence, the machine synchronous inductance for a cylindrical SG is calculated as follows:

$$L_s = L_d = L_q = \frac{3}{2} L_0 \quad (4.10)$$

Note, when leakage inductance is neglected, the synchronous inductance for a cylindrical SG with an identical sinusoidally distributed winding can be calculated as follows [102]:

$$L_s = \frac{m}{2} L_0 \quad (4.11)$$

where,

m : Number of phases

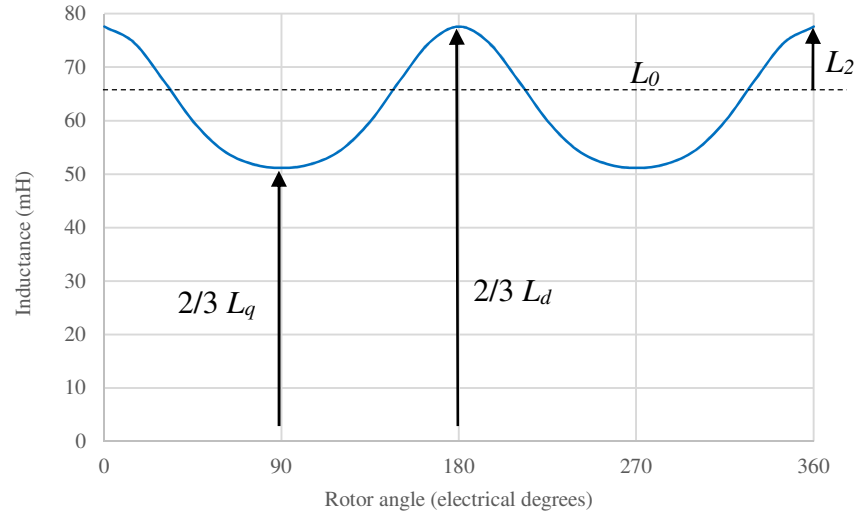


Fig. 4.37. Unsaturated phase self-inductance for the benchmark SG.

To account for saturation in subsequent modelling a saturation factor is calculated using the machine open circuit characteristics [107]. Referring to Fig. 4.36 the saturation factor is defined as:

$$k_s = \frac{I_{f_rated}}{I_{f_lin}} = \frac{E_{lin}}{E_{rated}} \quad (4.12)$$

where,

I_{f_rated} : Field current at rated stator load current (produces rated back-EMF)

I_{f_lin} : Field current that produces rated back-EMF on the linear air-gap characteristic

E_{lin} : Back-EMF produced by rated rotor field current on the air-gap linear characteristic

E_{rated} : Rated back-EMF

The saturated inductance is obtained by dividing the unsaturated inductance by a saturation factor [107]:

$$L_{ss} = \frac{L_{su}}{k_s} \quad (4.13)$$

where,

L_{ss} : Saturated inductance

L_{su} : Unsaturated inductance

Machine inductances for the benchmark SG are listed in Table 4.10 along with the machine per phase resistance quoted at an operational steady-state winding temperature of 75°C.

Table 4.10. Benchmark SG inductances and resistance

Parameter	Value
L_0 (mH)	64.42
L_2 (mH)	13.22
L_d (mH)	116.45
L_q (mH)	76.8
L_{su} (mH)	96.63 (1 p.u.)
L_{ss} (mH)	42.76 (0.44 p.u.)
k_s	2.26
Phase resistance at 75°C (Ω)	0.102

4.4.7 Modelling of Benchmark SG

The finite element parameters obtained for the benchmark SG are input to a MATLAB/Simulink simulation model of the machine. The benchmark SG is an industrial HV generator that is designed to connect to a three-phase, 50 Hz grid as shown in Fig. 4.38. Hence, the grid is modeled as an 11 kV line-to-line infinite bus-bar. The MATLAB model for the benchmark SG is shown in Fig. 4.39. The machine is analyzed with saturated

and unsaturated inductance for result comparison. The unsaturated inductance is regarded here as 1 p.u., hence the saturated inductance is 0.44 p.u.

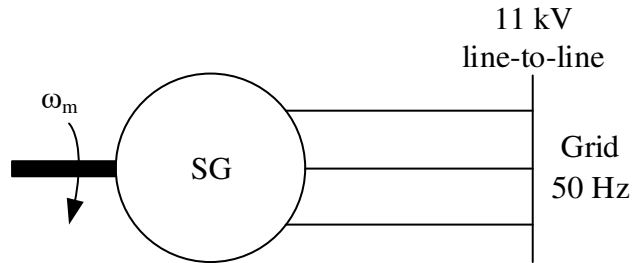


Fig. 4.38. Benchmark SG connected to 11 kV infinite bus-bar.

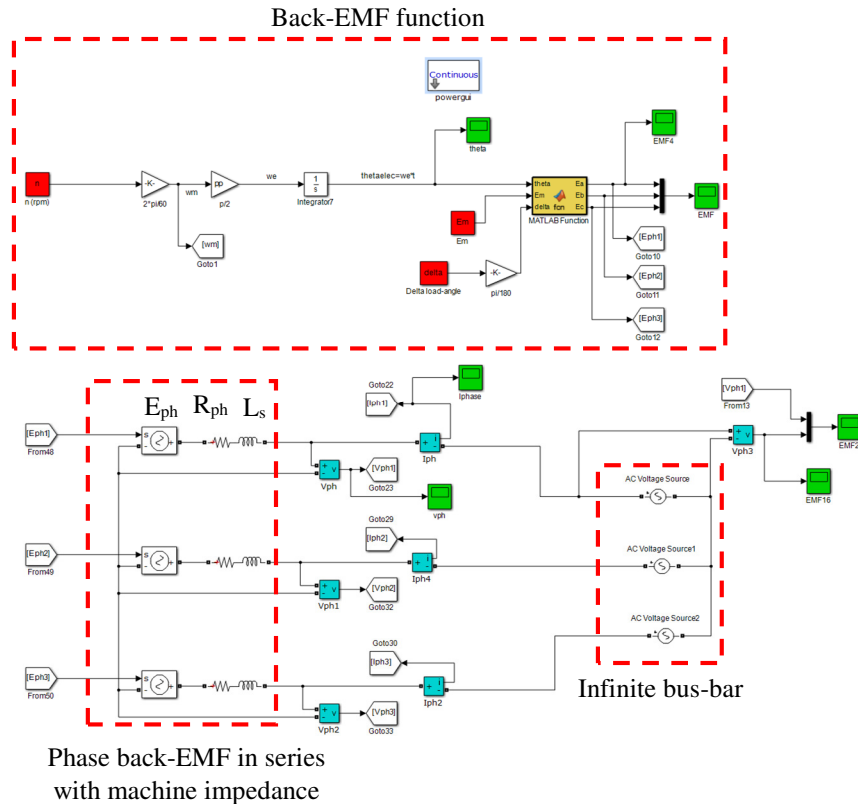


Fig. 4.39. MATLAB model for benchmark SG connected to 11 kV infinite bus-bar.

The SG output power is related to the sine of the load angle [108]. Fig. 4.40 shows power-angle characteristics for the benchmark SG. As seen the power increases as the inductance reduces. Therefore, a machine operating in the saturation region has a better power

capability due to reduced inductance. Machine phase back-EMF, phase voltage and current for a load angle of 22.15 electrical degrees are plotted in Fig. 4.41. In generator mode of operation, the back-EMF leads the phase voltage and power is injected to the bus-bar. The phase current lags the phase voltage by 35.57 degrees i.e. a power factor of 0.81. Table 4.11 compares simulation results against the published datasheet values for the benchmark SG, illustrating a good agreement between the two sets of data.

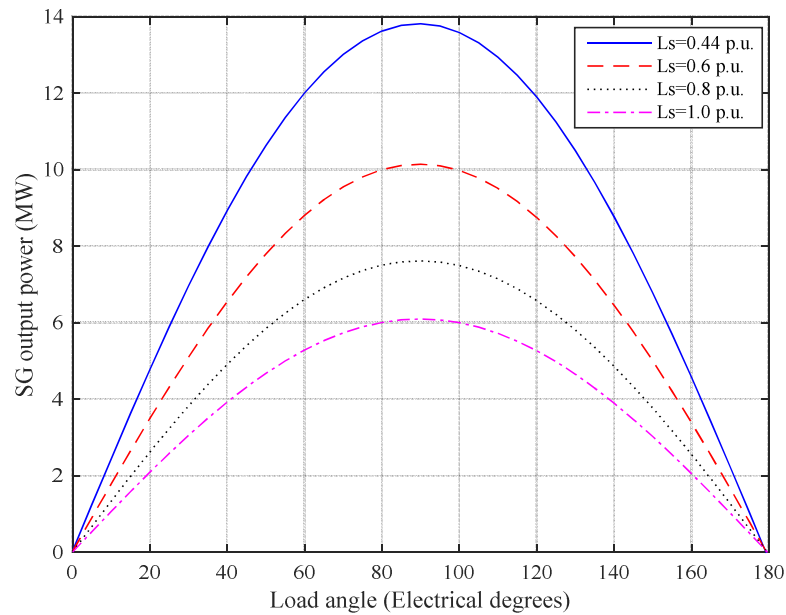


Fig. 4.40. Power-angle characteristics for the benchmark SG connected to an infinite bus-bar.

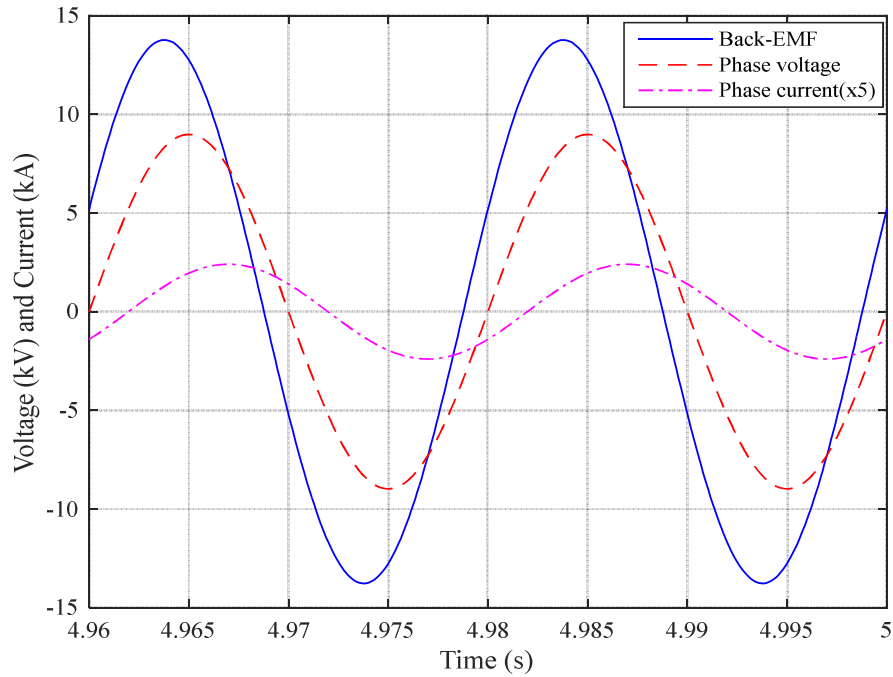


Fig. 4.41. Benchmark SG back-EMF, phase voltage and current.

Table 4.11. Comparison between benchmark SG simulated results and datasheet

Parameter	Simulated	Datasheet
Rated output power (MW)	5.52	
Full-field rotor current (at rated power) (A)	486.23	
Open circuit phase RMS back-EMF at full-field current (kV)	10.32	8.25
Grid line-to-line RMS voltage (kV)	11	
Full-load stator RMS current (A)	357.2	362
Load angle (degrees)	22.15	29.9
Power factor at full-load stator current (p.u.)	0.81	0.8
Grid frequency (Hz)	50	
Synchronous inductance (Ω)	13.43	14.2
Phase resistance (Ω) at 75 °C	0.102	0.131
Rotor winding resistance (Ω) at 75 °C	0.13	0.1260

4.5 Summary

In this Chapter different machine topologies and power conversion schemes for wind generation systems are reviewed. The hybrid generator concept is discussed and results from a laboratory prototype HG are presented. The prototype HG is a 3 kW machine with 88.5 V maximum peak phase voltage and nominal speed of 3000 RPM. A brushless exciter provides DC supply for the HG wound field. A MATLAB/Simulink model is developed to simulate the HG operational characteristics at various DC-link voltages and wound field currents. The simulation results are compared with HG prototype measured results and show a good agreement hence confidence in model accuracy. An industrial 11 kV, 5.52 MW synchronous generator is chosen as benchmark machine based on which the high voltage hybrid generator is designed in Chapter 5. The benchmark SG is analyzed and simulated to validate the machine published data. Benchmark SG air-gap flux-density, flux-linkage, back-EMF, torque and inductance are evaluated using finite element analysis. It is shown that machine operates in saturation region at full-load stator current and full-field rotor current. This results in a reduced inductance and improved power capability. The good agreement between the simulated benchmark SG and its associated published data gave confidence to progress the high voltage HG design using the finite element and MATLAB/Simulink circuit simulation tools.

Chapter 5

Hybrid Generator (HG) Design

5.1 Introduction

In this Chapter the benchmark SG presented in Chapter 4 will be used to develop HG designs suitable for the proposed wind generation scheme discussed in Chapter 3. The HG designs are evolved from benchmark machine design maintaining magnetic and electric loading equivalence so as to realize designs that have some practical validation, since the build and test of a full-size machine is out of the scope of this thesis study. As discussed in preceding Chapters, the HG has two rotor parts, a WF and a PM. Both rotors are mounted on the same shaft hence rotate with the same speed and share one stator. The HG WF and HG PM rotors can be designed as separate machines that are then combined with an appropriate split ratio to form a HG. The HG stator is the same as the benchmark SG, i.e. the same number of slots and geometry. However, two options will be considered for the stator winding:

- A 3-phase winding, as per the benchmark SG, and,
- A 9-phase winding within the same stator slot and geometry.

The 3- and 9-phase designs will be compared to illustrate the benefits of the multiphase solutions. The rotor geometry for the WF is the same as the benchmark SG rotor with 10 salient poles. The rotor geometry for the PM section is also 10 poles with suitable magnet dimensions. The design study will consider a full WF and a full PM solutions and a HG having a WF:PM split ratio.

5.2 HG Design Philosophies

In Chapter 2 the wind turbine operation was divided into two regions:

- (i) Limited speed region of operation, and
- (ii) High speed region of operation.

For the limited speed region, the HG speed is rated at 1 p.u., Fig. 2.15, while HG speed in the high speed region could be as high as 1.67 to 2.66 p.u. (≈ 3 p.u.), Fig. 2.17, depending on the pitch angle. Therefore, design of the HG varies depending on the choice of wind turbine operational region. In this section different design philosophies for the HG in both limited and high speed regions are investigated to address the wind turbine and system requirements. However, as it was discussed in Chapter 2, the high speed region of operation is not an industry practice for the wind turbine-generator. Hence, the remaining section of this Chapter only considers HG design for limited speed operation of the wind turbine.

5.2.1 HG Design Philosophy for Limited Speed Region

In a wind farm the wind turbines experience varying wind velocity with time. This is due to uneven distribution of the wind mass, uncertainty of the wind direction and also the location of the wind turbines. Therefore, in a large farm such as Walney, the output voltage and power of the wind turbine generators will vary slightly from one another [27], [109] - [114]. As discussed previously, for systems typical of the Walney wind farm, the two back-to-back VSCs decouple the generator from the grid and control the voltage and frequency to match that of grid. However, in the proposed HG system there are no VSC's, instead the HG is connected to a passive rectifier that has no inherent control functionality. Therefore, the WF of the HG must control the output voltage. Since the HG rectifiers for all the turbines in the farm are electrically connected in parallel any voltage disparity between generators will cause the rectification stage potentially to turn-off. Therefore, the WF must be designed for the largest wind velocity variations between the wind turbines in the wind

farm. A maximum of less than 20% wind velocity variation between wind turbines throughout a wind farm are reported in the literature [110]. In this study a maximum wind velocity variation of 25% is considered for the HG design to assure some margin in design. The HG WF design is dependent on voltage and hence speed variations. Therefore, the split ratio between PM and WF rotor sections of the HG can be considered as varying from a fully WF rotor or traditional SG, to some ratio of PM to WF excitation. To satisfy the 25% wind velocity variation a HG with a PM:WF ratio of 0.75:0.25 is considered and compared with a (100%) WF (or SG). Here, the 100% WF (or SG) machine is considered to be a reference 1 p.u. machine.

First consider a fully WF (or SG) machine. Fig. 5.1 presents total terminal voltage of a SG against rotor speed while the wind turbine is operating within the limited speed operation region. The output voltage of the SG is considered to be proportional to the rotor speed since the rotor WF current is fixed. As discussed in Chapter 2, Fig. 2.15, there are some speed and power perturbations around the rotor base speed which explains the voltage and current perturbations around base speed of Fig. 5.1.

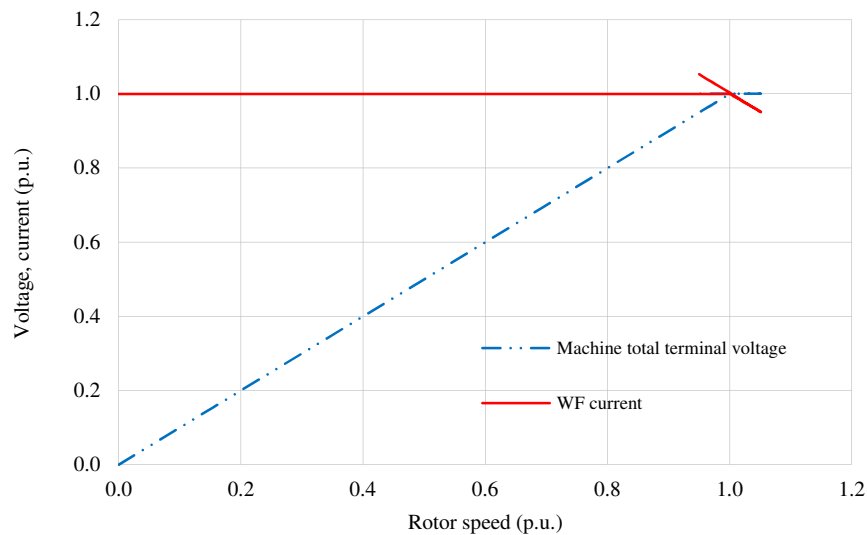


Fig. 5.1. Voltage variation of a fully WF (SG) for a turbine operating in the limited speed region.

Now consider that the SG is scaled down to act as the WF rotor of the HG. Therefore, the WF rotor provides 25% of the maximum HG terminal voltage and the PM rotor induces the remaining 75%. The HG total terminal voltage versus rotor speed variation is depicted in Fig. 5.2 when the HG is operating in the limited speed range. This WF boost voltage ensures that the HG is in a safe operating condition in the event of loss of rotor field, as opposed to a design where the WF voltage ‘bucked’ (reduced) that of the PM field. Loss of rotor field also acts as a protection feature in the event of generator faulted operation.

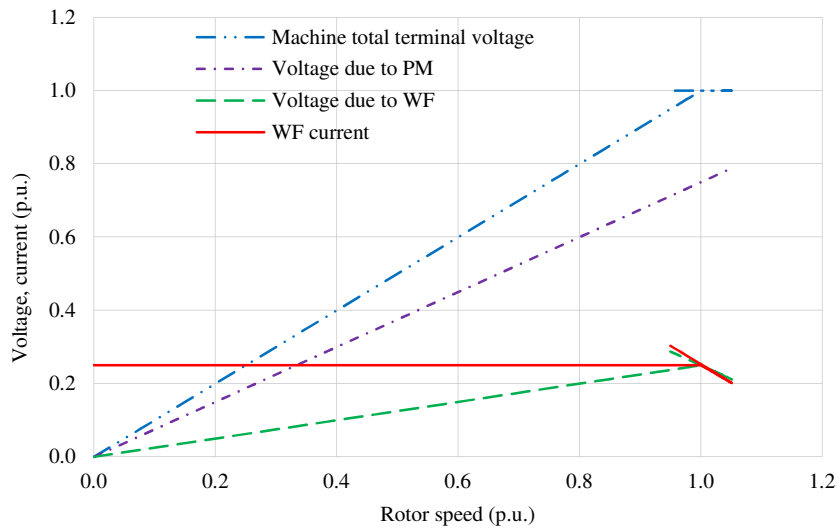


Fig. 5.2. Voltage variations for a HG with 75% induced voltage due to PM rotor and 25% induced voltage due to WF rotor for a turbine operating in the limited speed region.

5.2.2 HG Design Philosophy for High Speed Region

In the high speed region of operation, the rotor speed can exceed beyond the nominal rated (1.0 p.u.) depending on the pitch angle chosen to match the wind velocity. Note that the nominal 1.0 p.u. references the design to the limited speed region concept. In practice, the wind turbine mechanics will have to be designed for speeds above 1.0 p.u. hence the maximum rated speed will be higher and could be between 1.0 and 3.0 p.u. (2.66 p.u. for the Enercon E-82 system discussed in Chapter 2) depending on pitch angle control implementation for the turbine under study.

First consider a SG in the high speed region of operation. In the high speed region, the terminal voltage of the generator increases up to rated speed since it is assumed that the machine terminal voltage is proportional to the rotor speed. Above the rated speed, the output voltage of the generator stays constant at its nominal 1.0 p.u. value. Fig. 5.3 shows output voltage and WF current for the SG. The WF current is at its maximum from zero to rated speed and as the machine speed increase above 1.0 p.u. the WF current reduces to realize a constant voltage at the terminals of the SG. For the HG it is assumed that the HG terminal voltage at the highest rotor speed (3.0 p.u.) is only due to the PM excitation to ensure that there is no system over voltage should there be loss of WF. The induced voltage due to PM and terminal voltages are plotted in Fig. 5.4. The WF voltage is therefore calculated by subtracting the induced voltage due to PM rotor from the total required machine terminal voltage. The PM and WF induced voltages together with HG terminal voltage and WF current are shown in Fig. 5.4. The WF current is kept at a maximum value up to rated speed and reduced as the speed goes beyond the rated speed to maintain a constant terminal voltage.

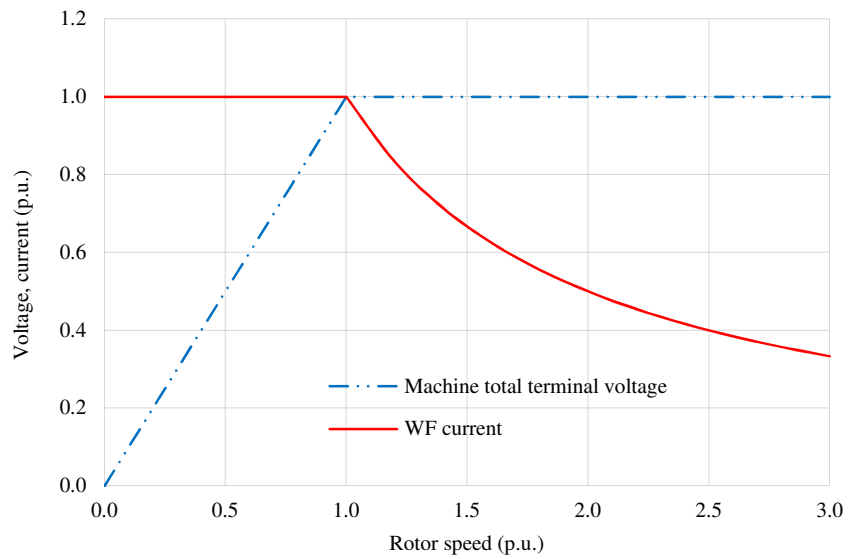


Fig. 5.3. Voltage variations for a fully WF (SG) for a turbine operating in the high speed region.

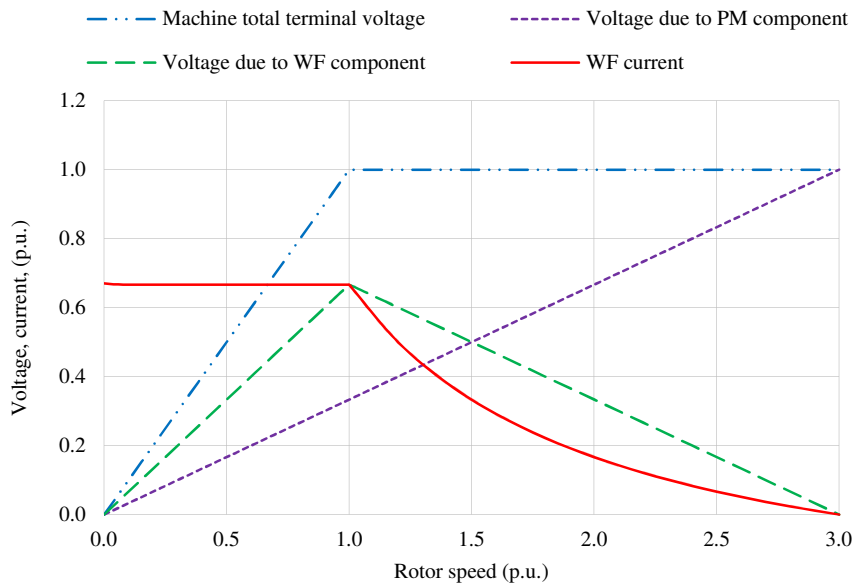


Fig. 5.4. Voltage variations for a HG with PM and WF rotor parts for a turbine operating in the high speed region.

5.3 Design of 3-phase HG with 100% Wound Field (WF)

5.3.1 Generator Connected to a Passive Rectifier

The 3-phase HG with 100% WF is essentially the same machine as the benchmark SG presented in Chapter 4. However, the benchmark SG is connected to a three-phase grid while here connected to a passive rectifier. The SG output power varies with the rotor angle when the machine is connected to an infinite bus-bar grid. However, for the HG connected to a rectifier, the rotor angle variation is constrained by the action of the diode bridge rectifier, hence some performance assessment has to be performed. Fig. 5.5 shows a schematic diagram of the 3-phase HG with 100% WF, referred to as 3-phase HG WF, connected to a passive rectifier.

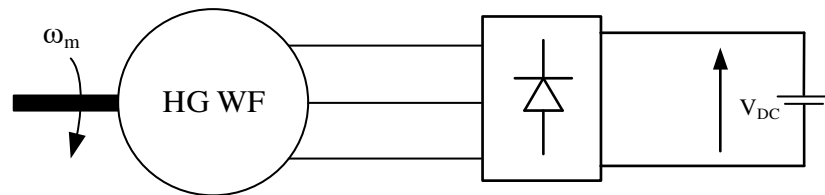


Fig. 5.5. 3-phase HG WF connected to a passive rectifier.

A MATLAB model is set up for the 3-phase HG WF to evaluate the machine performance, as shown in Fig. 5.6. The DC-link is connected to a DC power supply (battery) acting as the load. The model is set up to simulate a HG WF connected to rectifier and also a voltage source converter (VSC) so that the machine performance can be evaluated when connected to an uncontrolled passive rectifier and to a fully controlled VSC and the two schemes compared. For passive rectifier operation the gates of the IGBT's in the model are disabled. Therefore, the converter acts as a rectifier using the parallel diodes of the IGBTs's. The average of the rectified DC-link voltage can be analytically calculated as follows [77]:

$$V_{dc}^{ave} = \frac{3}{\pi} \sqrt{2} V_{LL}^{rms} \quad (5.1)$$

where,

V_{LL}^{rms} : RMS line-to-line voltage

The no-load DC-link voltage for the rectifier output is plotted in Fig. 5.7. The average of the simulated no-load DC-link is 22.77 kV, which is consistent with the analytical value calculated from (5.1). Table 5.1 lists the DC-link and HG WF main voltages.

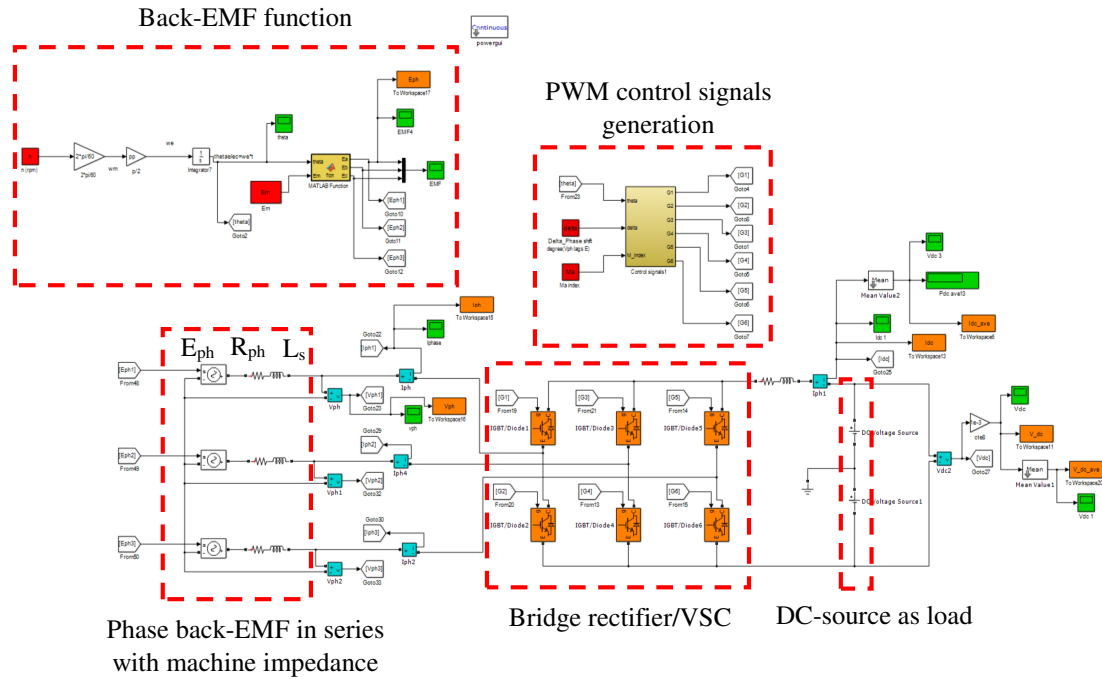


Fig. 5.6. MATLAB model for the 3-phase HG WF connected to a rectifier or VSC.

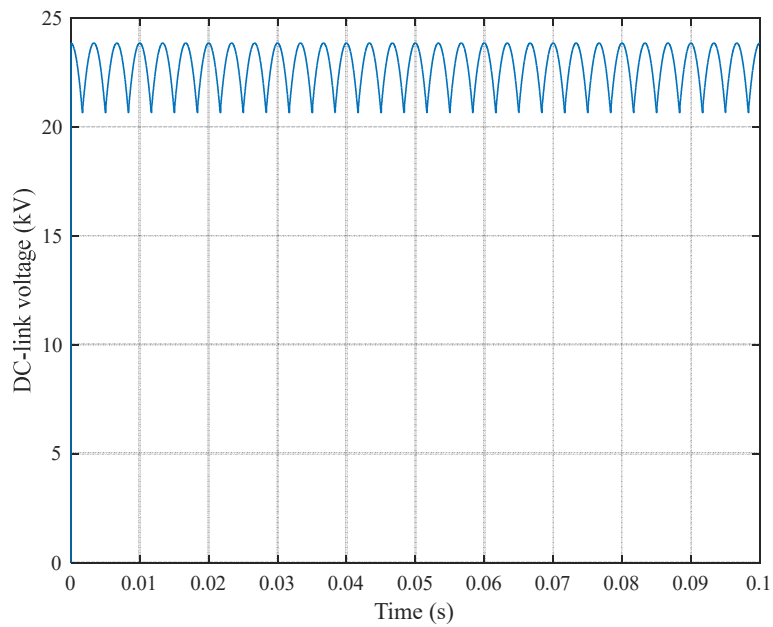


Fig. 5.7. No-load DC-link voltage at the rectifier output.

Table 5.1. DC-link and machine voltages for the 3-phase HG WF connected to a passive rectifier

Parameter	Value (kV)
Phase peak voltage	13.77
Line-to-line RMS voltage	16.86
Average no-load DC-link voltage	22.77
Peak no-load DC-link voltage	23.85
Minimum no-load DC-link voltage	20.65
No-load DC-link voltage variations	3.2

Fig. 5.8 shows the DC-link power with respect to DC-link voltage variations for different inductances when the 3-phase HG WF is connected to passive rectifier. The phase back-EMF, phase voltage and current for a DC-link voltage of 14 kV and machine inductance of 0.44 p.u. are plotted in Fig. 5.9. At a DC-link voltage of 14 kV the fundamental component of the phase current lags the fundamental of the phase voltage by 5.12 degrees, i.e. a power factor of 0.996 for the fundamental components. The phase current is defined by the load, i.e. the battery voltage. Therefore, the power factor is defined by the load and cannot be controlled via passive diode rectifier. The phase back-EMF is a sine wave generate by the HG WF but the phase voltage is a 6-step quasi square waveform with $\pm 2/3 V_{DC}$ and $\pm 1/3 V_{DC}$ voltage levels, Fig. 5.9. The instantaneous DC-link power and current are plotted in Fig. 5.10. The DC-link power perturbations are due to the ripples in the DC-link current.

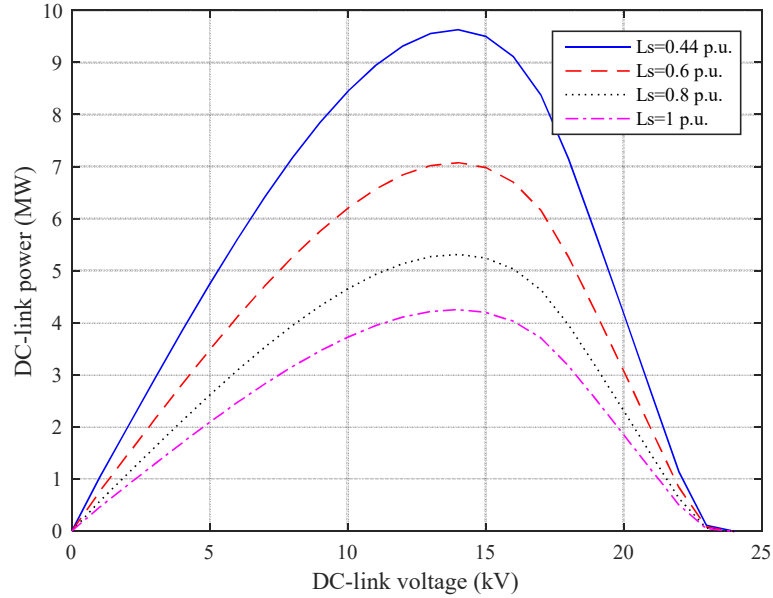


Fig. 5.8. DC-link power vs. DC-link voltage variations at the rectifier output.

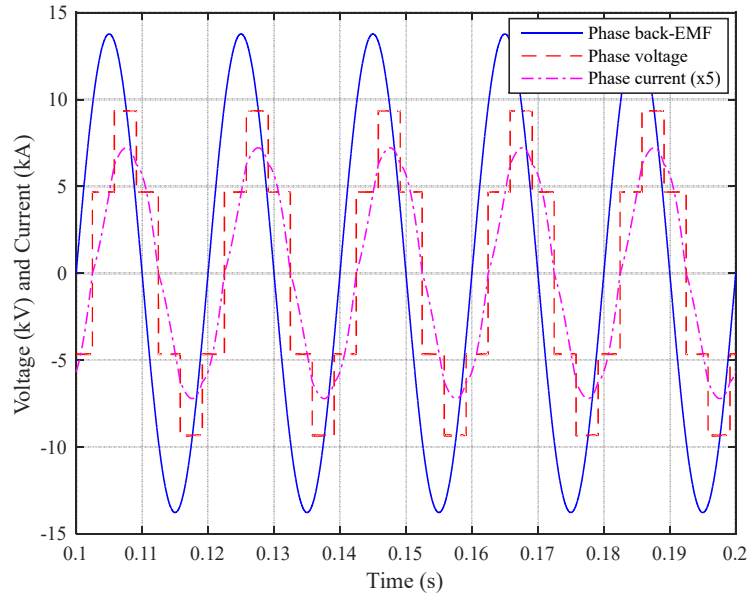


Fig. 5.9. Phase back-EMF, phase voltage and current for a DC-link voltage of 14 kV and 0.44 p.u. inductance for a 3-phase HG WF connected to a passive rectifier.

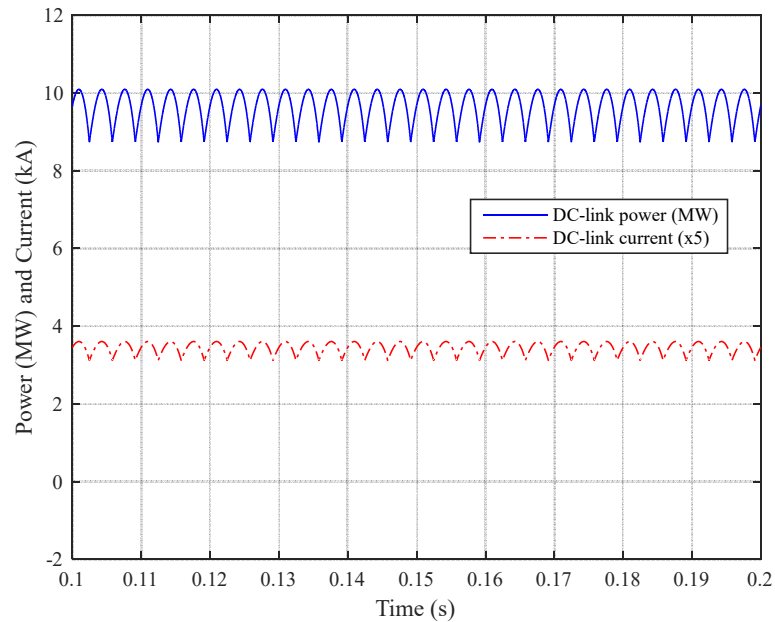


Fig. 5.10. DC-link power and current for a DC-link voltage of 14 kV and 0.44 p.u. inductance for a 3-phase HG WF connected to a passive rectifier.

5.3.2 Generator Connected to a VSC

In the previous section performance of the 3-phase HG WF connected to a rectifier was discussed. In commercial wind turbines, the Walney wind turbines for instance, the generator is sometimes connected to an active power electronic converter i.e. VSC. The VSC allows vector control of the HG WF hence improving the output power capability of the machine. In this section the performance of the HG WF connected to a three-phase VSC with two control schemes, PWM control and over modulated, is evaluated and results are compared with that of rectifier connected HG WF. Fig. 5.11 shows the 3-phase HG WF connected to a VSC and a battery as load.

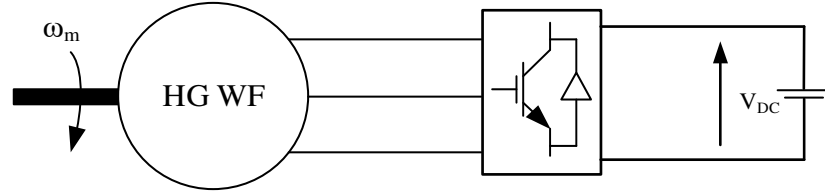


Fig. 5.11. Three-phase stator HG WF connected to a VSC.

The IGBT's gate signals shown in the MATLAB model in Fig. 5.6 are generated via comparing a 3 kHz saw-tooth carrier signal with a sine wave control (modulating) signal. The phase fundamental component is synthesized based on the switching sequences hence will be proportional to the control signal, i.e. a sine waveform. An amplitude modulation index is defined as follows [77]:

$$m_a = \frac{\hat{V}_{ctrl}}{\hat{V}_{saw-tooth}} \quad (5.2)$$

where,

\hat{V}_{ctrl} : Control signal amplitude

$\hat{V}_{saw-tooth}$: Carrier signal amplitude

The amplitude of the phase voltage fundamental component is controlled via the modulation index. Moreover, the phase angle and frequency of the phase voltage fundamental component is proportional to the control signal phase angle and frequency. Therefore, amplitude, angle and frequency of the phase voltage fundamental component are controlled by the control signal. For a sinusoidal PWM control scheme the modulation index varies between 0 and 1 and the output phase voltage envelope is a 6-step quasi-square wave with $\pm 2/3 V_{DC}$ and $\pm 1/3 V_{DC}$ voltage levels. Fig. 5.12 shows phase back-EMF, phase voltage and phase current of the 3-phase HG WF when connected to a VSC with PWM control, modulation index of 0.95, DC-link voltage of 14 kV and for an angle of 60 degrees between the fundamental voltage component and the back-EMF, i.e. the load angle. For

this load angle, the phase current lags the fundamental component of the phase voltage by 0.11 degrees i.e. a power factor of ≈ 1.0 p.u.

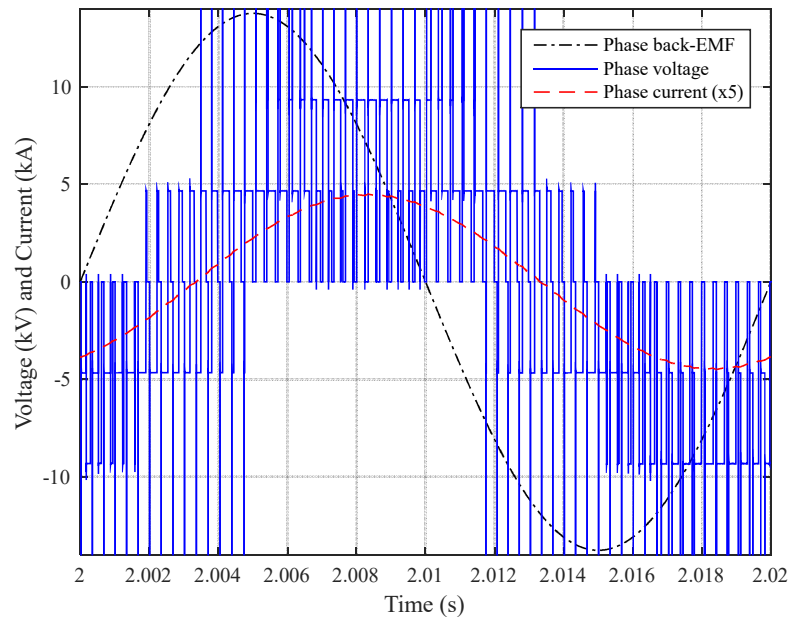


Fig. 5.12. Phase back-EMF, voltage and current for a 3-phase HG WF connected to a VSC with PWM control, modulation index 0.95, DC-link voltage 14 kV, inductance 0.44 p.u. and load angle 60° .

DC-link power and current for the same conditions stated in Fig. 5.12 are plotted in Fig. 5.13. The average power and current in the DC-link are constant while the instantaneous values vary with time as result of PWM switching. For the over-modulated control scheme, the modulation index is greater than 1.0. For a modulation index from 0 to 1.0, the phase voltage increases linearly. Above a modulation index of 1.0, the phase voltage increases non-linearly to a maximum value of 1.273 p.u. as shown in Fig. 5.14. The machine phase back-EMF, voltage and current for over-modulated control scheme for the same conditions as PWM control scheme but with a modulation index of 100 are plotted in Fig. 5.15. The phase voltage is a 6-step square wave with $\pm 2/3 V_{DC}$ and $\pm 1/3 V_{DC}$ voltage levels.

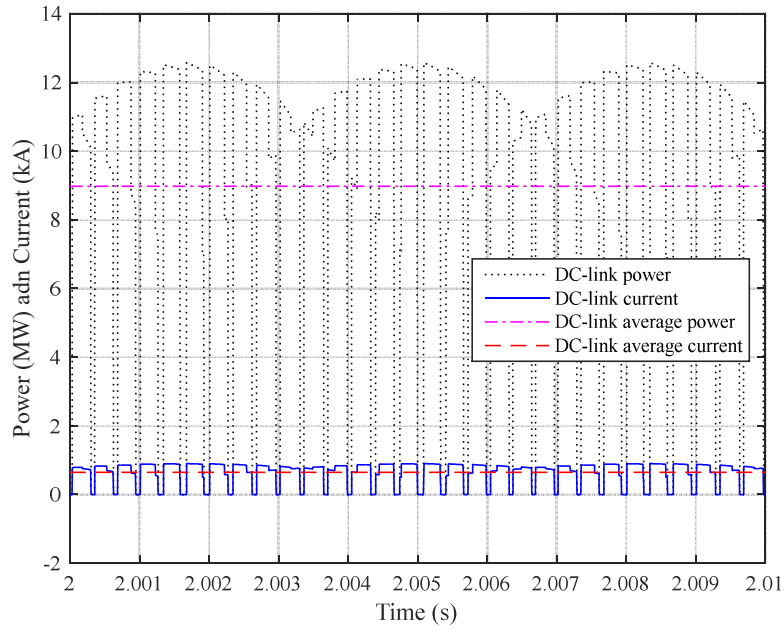


Fig. 5.13. DC-link power and current for the same conditions as in Fig. 5.12.

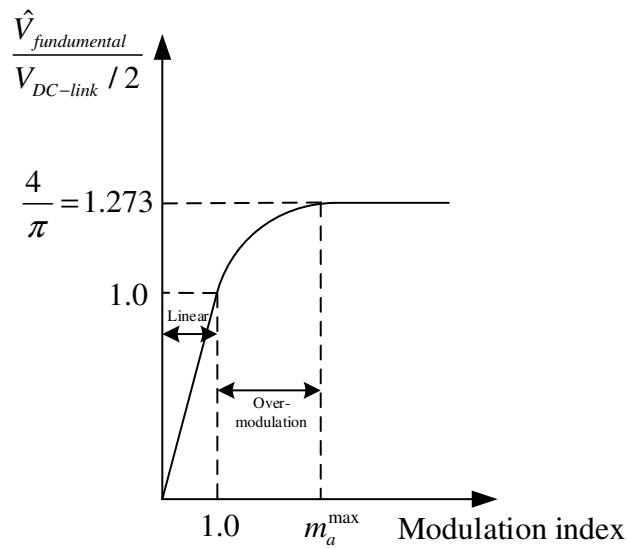


Fig. 5.14. Amplitude of the phase voltage fundamental component variations with respect to modulation index.

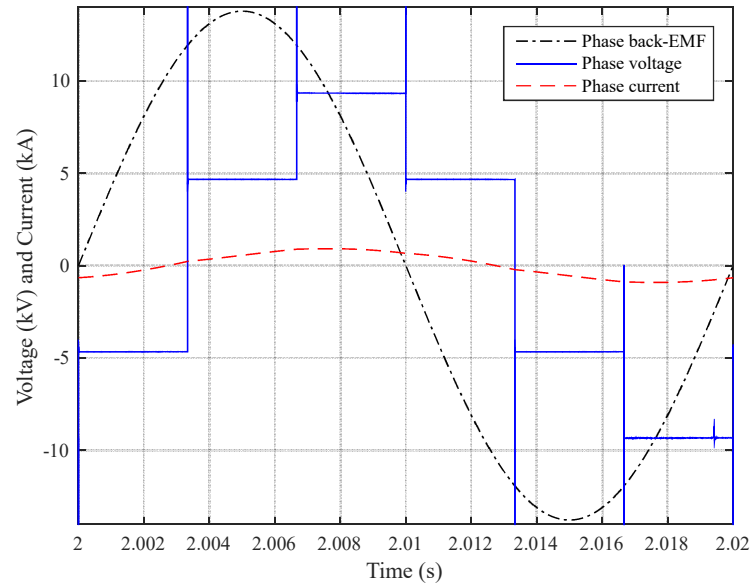


Fig. 5.15. Phase back-EMF, voltage and current for a 3-phase HG WF connected to a VSC with over-modulated control, modulation index 100, DC-link voltage 14 kV, inductance 0.44 p.u. and load angle 60° .

In the over-modulated scheme, the phase current lags 10.06 degrees behind the phase voltage fundamental component, i.e. a 0.98 power factor. Note that the load angle in both PWM and over-modulated is kept at 60 degrees. The DC-link power and current for the over-modulated control scheme are shown in Fig. 5.16. The DC-link average power for the over modulated VSC control is 11.91 MW while for the PWM control scheme and the same load angle is 8.98 MW. This is due to a maximum 0.95 modulation index for the PWM control scheme (to maintain sinusoidal phase current control) and also the 1.273 factor increase in phase voltage for the over-modulated case. Fig. 5.17 illustrates the DC-link power with respect to load angle for PWM and over-modulated control schemes. It is seen that the power gain for the over-modulated control scheme occurs at all load angles. However, in the over-modulated scheme the amplitude of the phase voltage fundamental component cannot be controlled. The switching frequency for the over-modulated control is low which makes it desirable for high power applications.

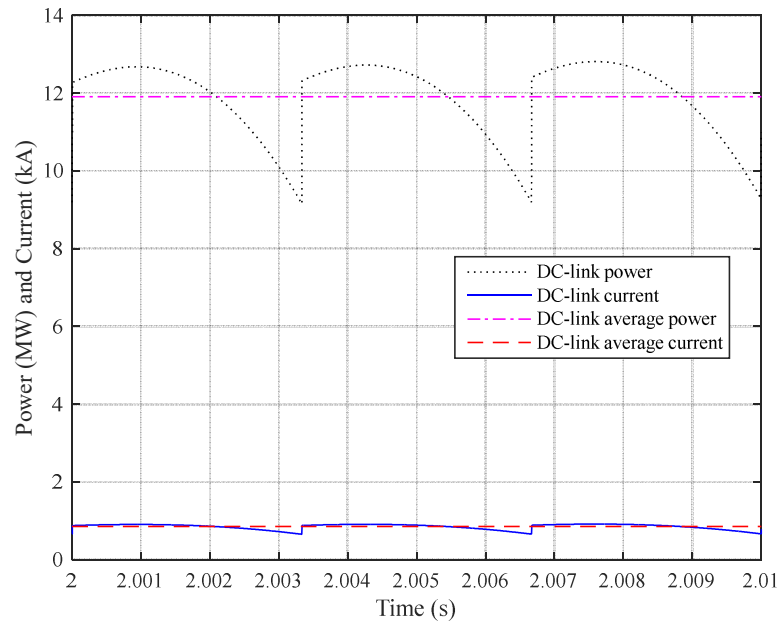


Fig. 5.16. DC-link power and current for the same conditions as in Fig. 5.15.

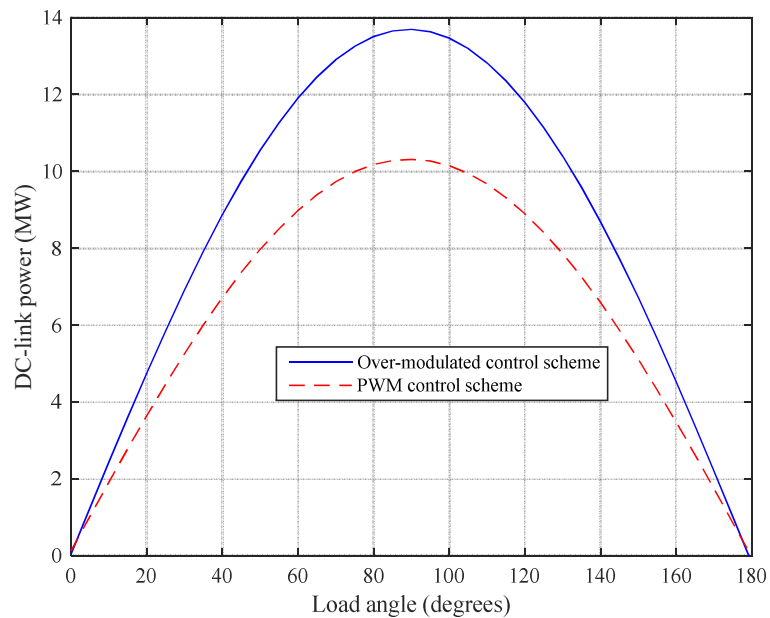


Fig. 5.17. DC-link power with respect to load angle for PWM and over-modulated control for a 3-phase HG WF connected to a VSC, DC-link voltage 14 kV, inductance 0.44 p.u.

Table 5.2 shows the maximum DC-link power for a 3-phase HG WF connected to a passive rectifier and VSC. The DC-link power in the rectifier case is lower due to passive rectifier inability to control load angle, whereas with a VSC the load angle can be controlled to 90 degrees. Therefore, when a passive rectifier replaces a VSC (or active rectifier), then in order to get the same DC-link power the 3-phase HG WF needs to be redesigned for a factor of 1.42 and 1.1 higher power for over-modulated and PWM schemes respectively. Hence, for the same application and DC-link power, it can be concluded that the machine rating must be larger if interfaced by a passive rectifier than when interfaced by a VSC.

Table 5.2. Maximum DC-link power for the 3-phase HG WF connected to a passive rectifier and VSC

3-phase HG WF connected to	Maximum DC-link power (MW)	DC-link power ratio (VSC/Rectifier)	
		Over-modulated	PWM
Passive rectifier	9.63	1.42	1.1
VSC with over-modulated control scheme	13.70		
VSC with PWM control scheme	10.31		

5.4 Design of 9-phase HG with 100% Wound Field (WF)

In this section the 3-phase HG with 100% WF i.e. 3-phase HG WF is rewound as a 9-phase stator winding, referred to as 9-phase HG WF. The machine rotor and stator geometries, number of poles (10), number of stator slots (135) and physical specifications are maintained the same for the purpose of comparison. For the 9-phase winding, the phase band from equation (4.1) and is 1.5. The winding is short-pitched and also fractional-slot. Therefore, in order to rewind the stator to include 9 phases a pattern of 2 and 1 coils is

required. Fig. 5.18 illustrates a pattern for the 9-phase stator winding for the HG WF. The 2-set and 1-set coils are connected in series to form a pattern. The pattern is repeated five times, therefore there are 15 coils per phase for the 9-phase winding. The coil span is 12 slots and the winding is double layer. For the 3-phase winding each coil had 4 turns (conductors) but for the 9-phase winding each coil has 12 turns. Therefore, having the same coil span the number of turns per phase for the 3- and 9-phase windings is 180; for 3-phase 45 coils and 4 turns per coil while for the 9-phase 15 coils and 12 turns per coil. The turn cross-sectional area in the 9-phase winding is one third that of the turn cross-sectional area in the 3-phase winding. Therefore, the per-phase resistance of the 9-phase winding is 3 times that of the 3-phase winding. Based on the value listed in Table 4.10 for the per-phase resistance of the 3-phase winding, the per-phase resistance for the 9-phase winding at the operational temperature of 75°C is $0.305\ \Omega$. Note that although the phase resistance is 3 times higher for the 9-phase design, the copper loss, for the 3- and 9-phase winding schemes is equitable since the 9-phase currents are reduced by a factor of 3.

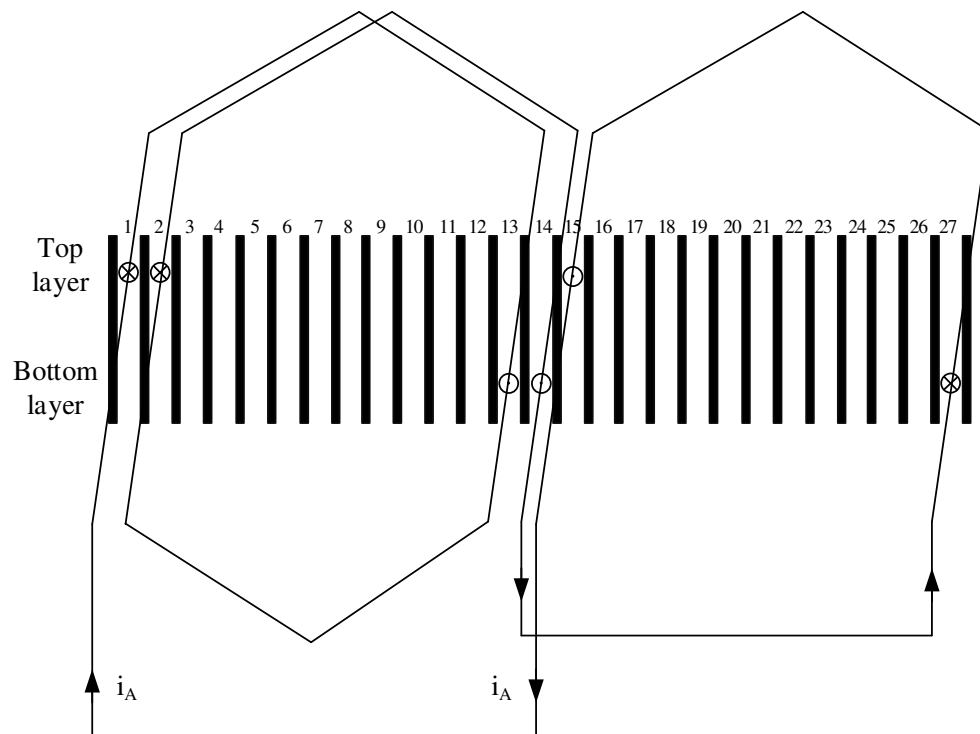


Fig. 5.18. Fractional-slot, short-pitched stator winding for the 9-phase HG WF.

For the purpose of verification, the per-phase resistance of the 9-phase winding is also calculated from the geometry of the machine as follows. The turn resistance is:

$$R_{turn}^{9\phi} = \frac{\rho_{cu} l_{turn}}{A_{turn}} \quad (5.3)$$

and,

$$l_{turn} = 2 l_a + 4 \sqrt{2} \frac{(\text{coil pitch})}{2} \quad (5.4)$$

where,

ρ_{cu} : Copper electrical resistivity ($\Omega.m$)

l_{turn} : Length of a turn in a coil (mm)

A_{turn} : Cross section of a turn in a coil (mm^2)

l_a : Axial length (mm)

Each turn in a coil has two sides plus end winding. The two sides have the same length as the machine axial length. According to Fig. 5.18, the end winding has a diamond (triangular) shape whose base length is the same as the coil pitch and height is half of the coil pitch, where the coil pitch is 12 slots. There are two such triangles, one at each end of the machine.

Therefore, for an N-turn coil:

$$R_{coil}^{9\phi} = N_{stator} R_{turn}^{9\phi} \quad (5.5)$$

There are 12 turns per coil and a total of 15 coils per phase. These 15 coils are connected in series using 9 interconnections. The interconnection also has a diamond shape with the base length of 13 slots and a height 13/2 slots:

$$l_{interconnection} = 2 \sqrt{2} \frac{(13 \text{ slots})}{2} \quad (5.6)$$

$$R_{interconnection}^{9\phi} = \frac{\rho_{cu} l_{interconnection}}{A_{turn}} \quad (5.7)$$

where,

$l_{interconnection}$: Interconnection length (mm)

$R_{interconnection}^{9\phi}$: Interconnection resistance (Ω)

Therefore, the phase resistance is:

$$R_{ph}^{9\phi} = 15 R_{coil}^{9\phi} + 9 R_{interconnection}^{9\phi} \quad (5.8)$$

Table 5.3 lists the winding specifications. Note that the calculated resistances are at 20°C.

The resistance at the operational temperature of the machine, 75°C, is given by [115]:

$$R_{ph(T_2)}^{9\phi} = R_{ph(T_1)}^{9\phi} [1 + \alpha_T (T_2 - T_1)] \quad (5.9)$$

where,

T_2 : Machine operational temperature 75°C

T_1 : Room temperature 20°C

α_T : Temperature coefficient of resistance °C⁻¹

Table 5.3. 9-phase winding specifications for the HG WF

Item	Value
Copper electrical resistivity ($\Omega \cdot m$)	1.68×10^{-8}
Turn length (mm)	2498.1
Turn cross-section area (mm^2)*	31.72
Axial length (mm)	400
Coil pitch (12 slots) (mm)	600.36
Turn resistance (Ω)	0.00137
Coil resistance (Ω)	0.0165
Interconnection length (mm)	919.79
Interconnection resistance (Ω)	0.0005
Phase resistance (Ω) at 20°C	0.252
Temperature coefficient of resistance ($^{\circ}C^{-1}$)	0.003862
Phase resistance (Ω) at 75°C	0.306

*Turn cross-section for 3-phase winding (with 6 strands)= 95.16 mm^2 ($= 6.1 \times 2.6 \times 6$)

The phase resistance calculated for the 9-phase winding from the machine geometry is the same as that estimated using the 3-phase resistance confirming the accuracy of the method. The rotor WF resistance is calculated from the rotor and coil geometry. Rotor winding has 10 coils each wound around the 10 salient rotor poles and connected in series. Each rotor coil has 51 turns. Each turn has two sides, each the same length as the machine active axial length (400 mm) plus end windings that have the same length as the width of the rotor poles (350 mm). Also, the length of the interconnection between the series coils is the same as the pole-pitch. The turn resistance and length of a rotor coil turn is calculated via (5.10) and (5.11):

$$R_{turn}^{rotor} = \frac{\rho_{cu} l_{turn}^{rotor}}{A_{turn}^{rotor}} \quad (5.10)$$

$$l_{turn}^{rotor} = 2 l_a + 2 l_w^{poles} \quad (5.11)$$

Hence:

$$R_{coil}^{rotor} = N_{rotor} R_{turn}^{rotor} \quad (5.12)$$

$$R_{interconnection}^{rotor} = \frac{\rho_{cu} l_{interconnection}^{rotor}}{A_{turn}^{rotor}} \quad (5.13)$$

Therefore, the rotor resistance is:

$$R_{rotor} = 10 R_{coil}^{rotor} + 9 R_{interconnection}^{rotor} \quad (5.14)$$

where,

R_{turn}^{rotor} : Turn resistance for the rotor coil (Ω)

l_{turn}^{rotor} : Length of a turn in a rotor coil (mm)

A_{turn}^{rotor} : Cross-section of a turn in rotor coil (mm^2)

l_w^{poles} : Width of rotor pole (mm)

R_{coil}^{rotor} : Rotor coil resistance (Ω)

N_{rotor} : Number of turns in a rotor coil

$l_{interconnection}^{rotor}$: Length of rotor winding interconnection (mm)

$R_{interconnection}^{rotor}$: Rotor interconnection resistance (Ω)

Rotor winding specifications are listed in Table 5.4.

Table 5.4. Rotor field winding specifications for the HG WF

Item	Value
Length per turn (mm)	1500
Turn cross-sectional area (mm ²)	112
Turn resistance (mΩ)	0.225
Number of turns per coil	51
Coil resistance (mΩ)	11
Winding interconnection length (mm)	675.44
Winding interconnection resistance (mΩ)	0.1
Resistance (Ω) at 20°C	0.11
Resistance (Ω) at 75°C	0.13

5.4.1 Comparison of 3-phase and 9-phase Machines

The flux-linkage per-phase and open-circuit induced back-EMF at a full-field current of 486.23A for the HG WF are presented in Figs. 5.19 and 5.20 respectively. For the purpose of comparison, the 3- and 9-phase waveforms are shown. It is seen that the back-EMF for the 9-phase winding is less sinusoidal compared to that of the 3-phase back-EMF. This is due to a lower number of coils per phase in the 9-phase winding. Note that the angular difference (phase shift) between the two windings is simply due to a shift in the coil center reference. Since the HG is connected to a passive rectifier in the proposed wind generation scheme, it is no longer necessary to have a sinusoidal output voltage, indeed a move towards a more trapezoidal waveform would be beneficial. Table 5.5 shows the peak and RMS values for the induced back-EMF for the 3-phase HG WF and 9-phase HG WF. It is seen from Table 5.5 that the 9-phase winding results in higher peak and RMS values for the phase voltage. This is explained using the phasor diagram.

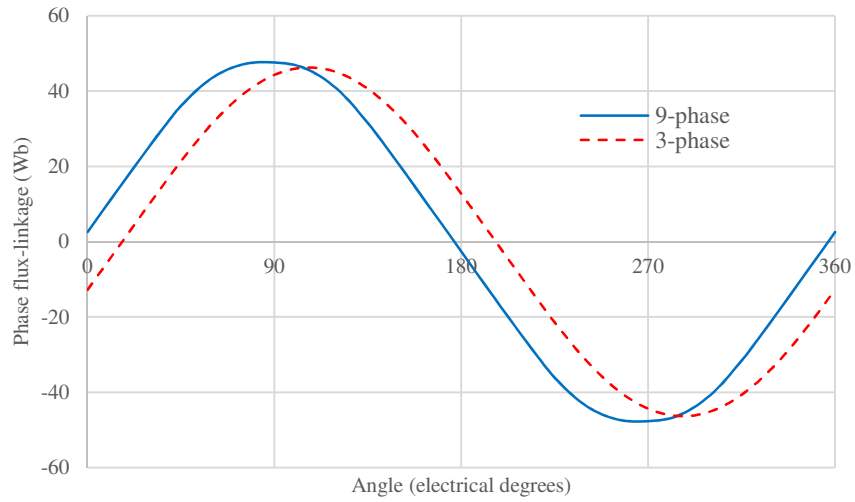


Fig. 5.19. Phase flux-linkage for the HG WF at a full-field current 486.23 A.

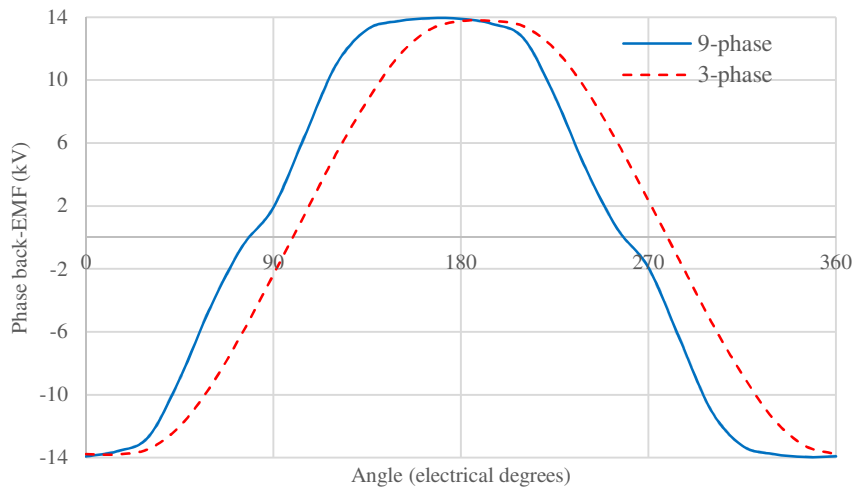


Fig. 5.20. Phase back-EMF for the HG WF at a full-field current 486.23 A.

Table 5.5. RMS and peak voltages for 3- and 9-phase HG WF at full-field of 486.23 A and 600 RPM

HG WF with	3-phase stator winding	9-phase stator winding	Voltage ratio (9-phase)/(3-phase)
Peak phase voltage (kV)	13.77	13.94	1.0123
RMS phase voltage (kV)	10.37	10.80	1.0415

Assuming that individual coils have sinusoidal back-EMF's (which is not the case), the winding coil distribution factor can be estimated from the phasor diagram for a pattern of 5-set and 4-set coils for the 3-phase winding, as shown in Fig. 5.21. Each coil is represented as a single phasor and the first coil is set as zero angle. The angles of other coils are defined with-respect-to the zero reference by the slot number in which the coil is laid in. Note that each slot is 2.67 degrees mechanical which equates to 13.33 degrees electrical. For the 4-set coils the phasors lie between 180 degrees and 270 degrees but since the current is reversed in the 4-set coils (due to the coil interconnections) a 180 degrees is deducted from their angles such that they lie in the first quadrant. In Fig. 5.21 the 4-set coil phasors have lighter color for clarity. Also, note that the amplitude of the voltages for each coil is normalized to 1.0 p.u.

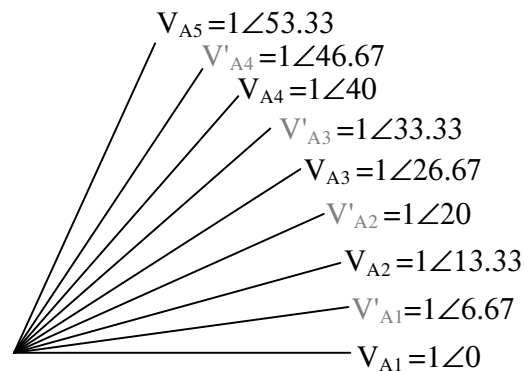


Fig. 5.21. Phasor diagram for 3-phase winding, 5-set and 4-set pattern.

The pattern is repeated 5 times, and considering 4 turns per coil, the per unit phase voltage for the 3-phase winding is:

$$\begin{aligned} V_{ph(3)} &= 4 \times 5 (V_{A1} + V_{A2} + V_{A3} + V_{A4} + V_{A5} - V'_{A1} - V'_{A2} - V'_{A3} - V'_{A4}) \\ &= 171.98 \angle 26.67^\circ \end{aligned} \quad (5.15)$$

Employing the same method, then for the 9-phase winding the phasor diagram for a pattern of 2-coils and 1-coil is shown in Fig. 5.22. The same process explained for the 3-phase winding phasors is used here to obtain the phase voltage. Therefore, the per-phase voltage for the 9-phase winding including 12 turns per coil is:

$$\begin{aligned} V_{ph(9)} &= 12 \times 5 (V_{A1} + V_{A2} - V'_{A1}) \\ &= 179.16 \angle 6.67^\circ \end{aligned} \quad (5.16)$$

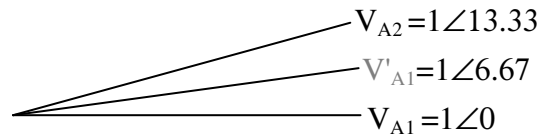


Fig. 5.22. Phasor diagram for 9-phase winding, 2-set and 1-set patterns.

The ratio of 9-phase to 3-phase voltages from the phasor diagram is 1.0417 (179.16/171.98). Hence, the increased voltage in the 9-phase case is due to an improved winding factor. Therefore, an important conclusion here is that compared to the 3-phase stator winding for the HG WF, the 9-phase winding results in 4.2% higher output voltage at the machine terminals.

5.4.2 Generator Connected to a Passive Rectifier

Fig. 5.23 shows the per-phase self-inductance of the 9-phase winding. The machine inductance changes with rotor angle since the rotor poles are salient. Fig. 5.24 shows nine coils each representing one phase where the displacement between adjacent coils is 40 electrical degrees.

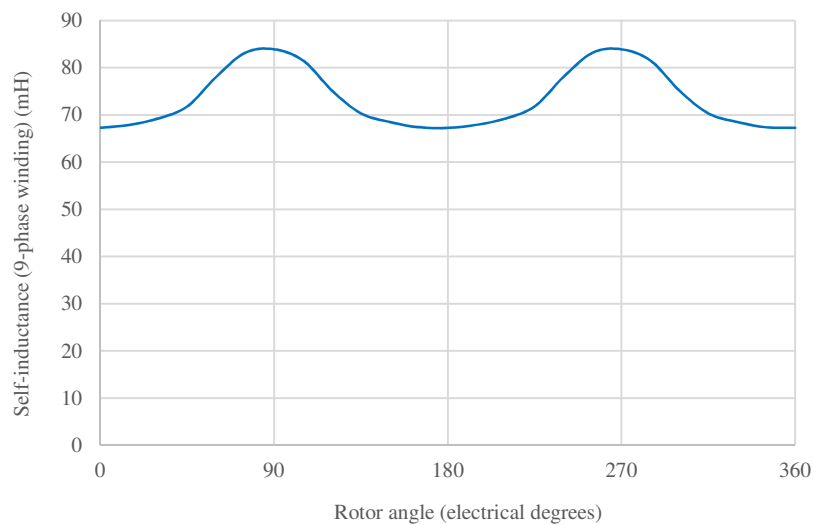


Fig. 5.23. Per-phase self-inductance for one phase of the 9-phase HG WF.

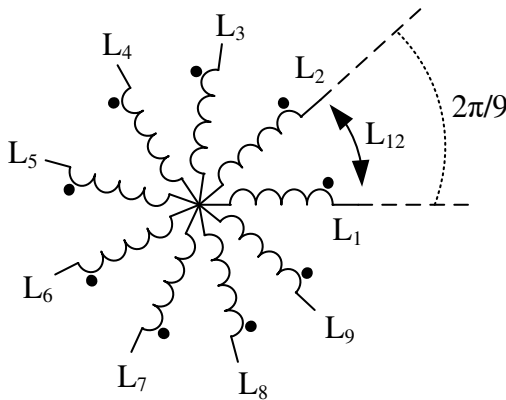


Fig. 5.24. Coil representation for 9-phase inductance calculations.

Equation 5.17 gives the self- and mutual-inductances for the 9-phase winding. Only the mutual inductance between phase 1 and other phases are shown in equation 5.17. Mutual inductances between other phases are obtained similarly.

$$\begin{aligned}
 L_1 &= L_0^9 + L_g^9 \cos(2\theta_e) & M_{12} &= L_0^9 \cos\left(\frac{2\pi}{9}\right) + L_g^9 \cos\left(2\theta_e - \frac{2\pi}{9}\right) \\
 L_2 &= L_0^9 + L_g^9 \cos\left(2\theta_e + \frac{2\pi}{9}\right) & M_{13} &= L_0^9 \cos\left(\frac{4\pi}{9}\right) + L_g^9 \cos\left(2\theta_e - \frac{4\pi}{9}\right) \\
 L_3 &= L_0^9 + L_g^9 \cos\left(2\theta_e + \frac{4\pi}{9}\right) & M_{14} &= L_0^9 \cos\left(\frac{6\pi}{9}\right) + L_g^9 \cos\left(2\theta_e - \frac{6\pi}{9}\right) \\
 L_4 &= L_0^9 + L_g^9 \cos\left(2\theta_e + \frac{6\pi}{9}\right) & M_{15} &= L_0^9 \cos\left(\frac{8\pi}{9}\right) + L_g^9 \cos\left(2\theta_e - \frac{8\pi}{9}\right) \\
 L_5 &= L_0^9 + L_g^9 \cos\left(2\theta_e + \frac{8\pi}{9}\right) & M_{16} &= L_0^9 \cos\left(\frac{10\pi}{9}\right) + L_g^9 \cos\left(2\theta_e - \frac{10\pi}{9}\right) \\
 L_6 &= L_0^9 + L_g^9 \cos\left(2\theta_e + \frac{10\pi}{9}\right) & M_{17} &= L_0^9 \cos\left(\frac{12\pi}{9}\right) + L_g^9 \cos\left(2\theta_e - \frac{12\pi}{9}\right) \\
 L_7 &= L_0^9 + L_g^9 \cos\left(2\theta_e + \frac{12\pi}{9}\right) & M_{18} &= L_0^9 \cos\left(\frac{14\pi}{9}\right) + L_g^9 \cos\left(2\theta_e - \frac{14\pi}{9}\right) \\
 L_8 &= L_0^9 + L_g^9 \cos\left(2\theta_e + \frac{14\pi}{9}\right) & M_{19} &= L_0^9 \cos\left(\frac{16\pi}{9}\right) + L_g^9 \cos\left(2\theta_e - \frac{16\pi}{9}\right) \\
 L_9 &= L_0^9 + L_g^9 \cos\left(2\theta_e + \frac{16\pi}{9}\right) & &
 \end{aligned} \tag{5.17}$$

where,

L_i : Self-inductance for phase i ($i = 1, \dots, 9$)

M_{ij} : Mutual inductance between phase i and j ($i = 1, \dots, 9$ and $j = 1, \dots, 9$)

L_0^9 : Average phase inductance for the 9-phase winding

L_g^9 : Phase inductance amplitude variations above average for the 9-phase winding

The phase inductance shown in Fig. 5.23 is unsaturated and its equivalent synchronous inductance is calculated from equation (4.11). However, the saturated synchronous inductance using equation (4.13) for the 9-phase HG WF is 112.33 mH. The MATLAB Simulink model for the 9-phase HG WF is shown in Fig. 5.25. Note that the gate signals are disabled so that the converter operates as a passive rectifier. The model embeds 3×3-phase converter that are connected to form a 9-phase converter. On the DC-link a battery

is used as a load. The no-load rectified DC-link voltage for the 9-phase and 3-phase windings of the HG WF are shown in Fig. 5.26. The simulated average DC-link voltage is consistent with the analytical value i.e. 27.32 kV, giving confidence in the model accuracy. The rectified voltage for the 9-phase system is higher than the 3-phase rectified voltage as seen from Fig. 5.26. Moreover, the peak-to-peak voltage ripple is reduced in the 9-phase rectified voltage, hence lower requirements for filtering. Table 5.6 compares 3- and 9-phase voltages. Therefore, the 9-phase HG not only results in 4.2% higher RMS voltage but also 19.98% higher DC-link rectified voltage. Therefore, a justified option for the HG stator. Phase voltage, current and also back-EMF for the 9-phase HG WF connected to a passive rectifier are shown in Fig. 5.27. DC-link power and current are shown in Fig. 5.28. Compared to the 3-phase the 9-phase system results in 4.2% higher power which is results of higher phase voltage due to improved winding factor. The important conclusion here is that by going from a 3-phase stator design to a 9-phase design the HG WF results is 4.2% higher power, higher DC-link voltage and reduced ripple hence improvement in power and voltage quality i.e. lower filtering requirement. From machine design point of view, the 9-phase machine is more power dense.

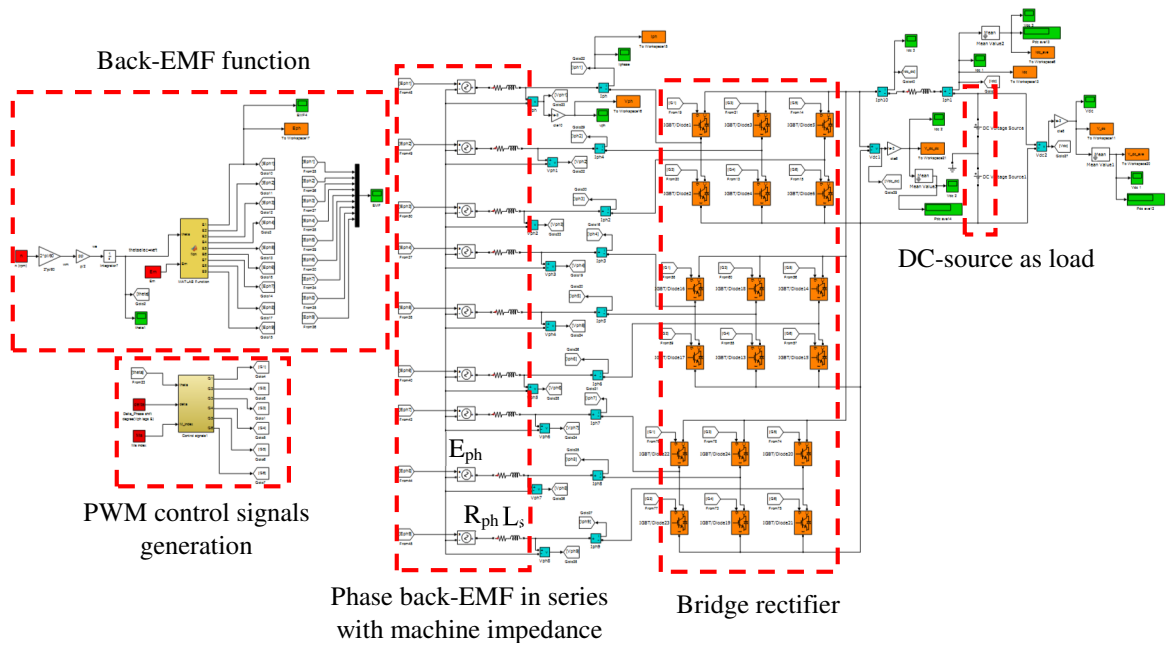


Fig. 5.25. MATLAB model for the 9-phase HG WF connected to a rectifier.

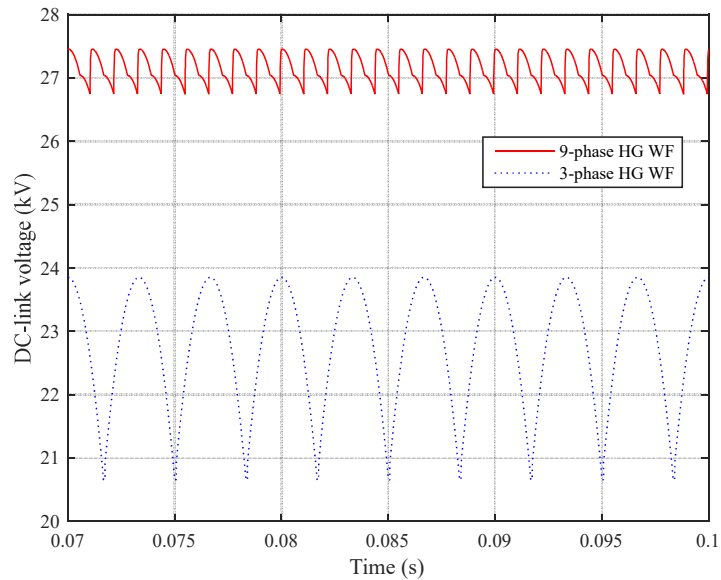


Fig. 5.26. No-load rectified DC-link voltage for the 3- and 9-phase HG WF.

Table 5.6. Comparison of three-phase and nine-phase machines at an average DC-link voltage of 14 kV

HG WF with	3-phase stator winding	9-phase stator winding	Ratio (9-phase)/(3-phase)
No-load peak phase voltage (kV)	13.77	13.94	1.0123
No-load RMS voltage (kV)	10.37	10.80	1.0415
RMS phase current (A)	512.23	179.28	0.35
Average phase power (MW)	3.21	1.115	0.35
No-load average DC-link voltage (kV)	22.77	27.32	1.1998
No-load peak DC-link voltage (kV)	23.85	27.45	1.151
No-load minimum DC-link voltage (kV)	20.65	26.74	1.295
No-load peak to peak ripples (kV)	3.2 (13.4%)	0.71 (2.6%)	0.22
Average DC current (A)	687.93	715.06	1.04
Peak DC current (A)	721.1	718.7	0.997
Average DC power (MW)	9.63	10.03	1.042
Peak DC power (MW)	10.685	10.06	0.94

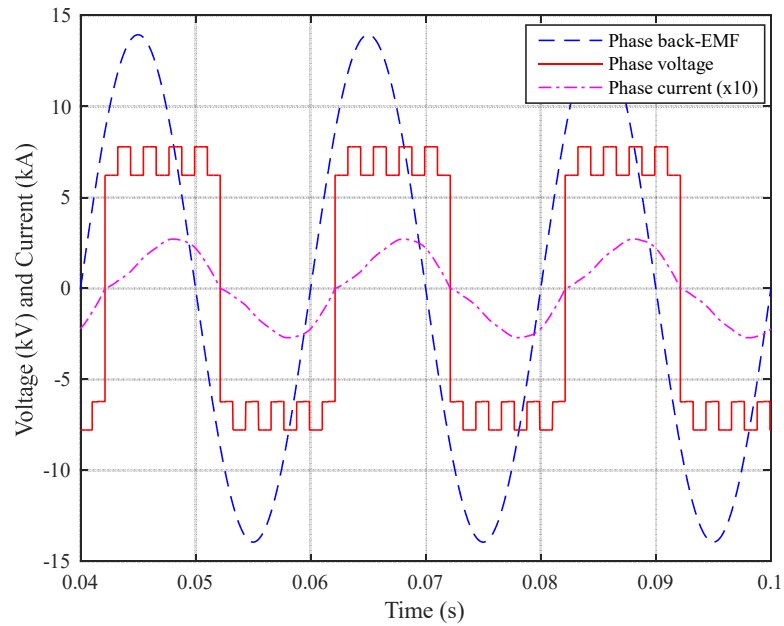


Fig. 5.27. Phase back-EMF, phase voltage and current for a 9-phase HG WF connected to a passive rectifier and a DC-link voltage of 14 kV.

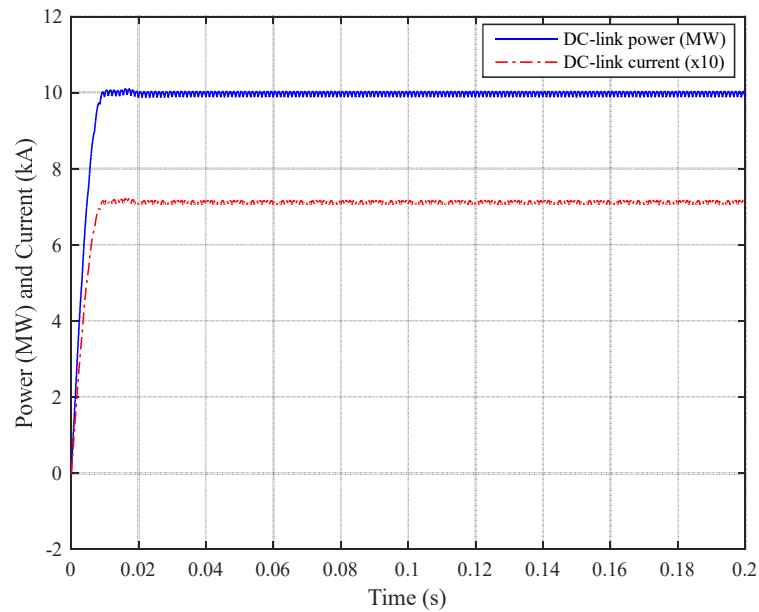


Fig. 5.28. DC-link power and current for a 9-phase HG WF connected to a passive rectifier and with a DC-link voltage of 14 kV.

5.5 Design of HG PM Rotor with NdFeB Surface Magnets

Previously design of the HG with 100% WF i.e. HG WF was discussed. In this section design of the HG with surface magnet rotor is addressed. The two machines, HG WF and HG with PM rotor, referred to as HG PM, are then combined to form the HG. The HG shares a common stator between WF and PM rotors. Therefore, the 9-phase stator winding designed for the HG WF is used for the HG PM machine. Two different designs for the PM rotor are discussed:

- A surface magnet PM rotor, and
- An interior magnet PM rotor design.

Two different commercially available magnet materials are considered, sintered Neodymium-Iron-Boron (NdFeB) and sintered Ferrite. NdFeB is a rare-earth magnet material that has been used in wind applications due to its high energy density [116-117]. However, there was a supply issue in 2008 that raised many uncertainties in the source of all rare-earth materials [118-119], hence the investigation into a sintered Ferrite rotor topology.

5.5.1 Sintered NdFeB Characteristics

The intrinsic and normal characteristics for a typical high energy sintered NdFeB magnet supplied by Arnold Magnetics UK [120], referred to as N35H, is shown in Fig. 5.29. The magnet characteristics are a function of temperature hence the machine internal and external operating ambient are important to understand. The magnet operating point lies on the linear characteristic and its intersection with the open-circuit load line. The slope of the linear B-H characteristic is related to the relative permeability and vacuum permeability, hence at machine operating temperature 80 °C (dotted line in Fig. 5.29):

$$\mu_r = \left(\frac{1}{\mu_0} \right) \left(\frac{B_2 - B_1}{H_2 - H_1} \right) \quad (5.18)$$

where,

μ_r : Magnet relative permeability

μ_0 : Vacuum permeability (H/m)

B : Flux-density (T)

H : Demagnetizing field intensity (kA/m)

Relevant properties of N35H are detailed in Table 5.7.

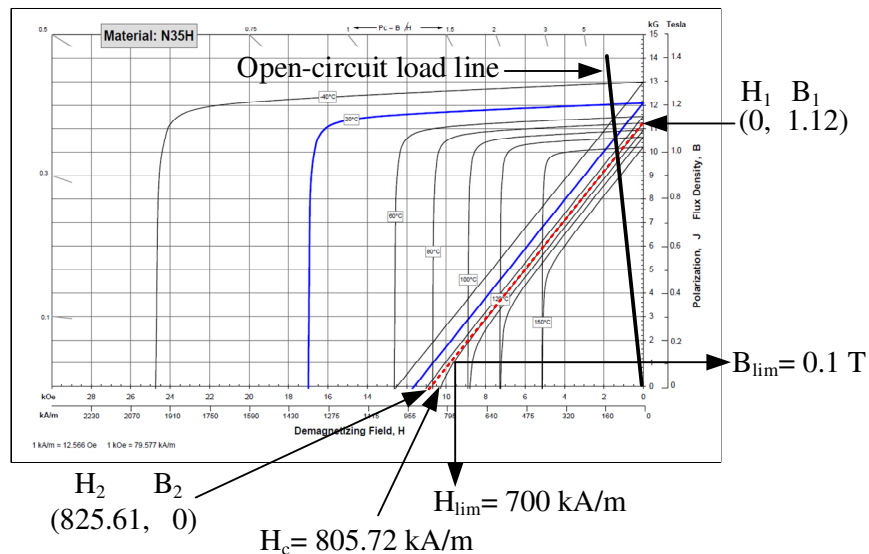


Fig. 5.29. B-H characteristic for NdFeB N35H [120].

Table 5.7. Neodymium-Iron-Boron magnet N35H properties at 80 °C

Parameter	Symbol	Value
Remanence (T)	B_r	1.12
Relative permeability	μ_r	1.08
Vacuum permeability (H/m)	μ_0	$4\pi \times 10^{-7}$
Coactivity (kA/m)	H_c	805.72
Magnetic intensity demagnetization limit (kA/m)	H_{lim}	700
Flux-density demagnetization limit (T)	B_{lim}	0.1
Magnet electrical conductivity (MS/m)	σ_m	0.556

For the surface magnet PM rotor the magnets are mounted on the rotor surface as shown in Fig. 5.30. The surface magnet PM machine is designed to have 10 poles, as for the WF, but the poles are full-pitched, i.e. cylindrical rotor as opposed to the salient WF rotor. Due to the circumferentially long magnet length (670.968 mm), each magnet is split into 6 equal sections with each section magnetized separately. This will prevent the magnet being magnetized unevenly which would result in lower flux-density in some locations in the magnet pole.

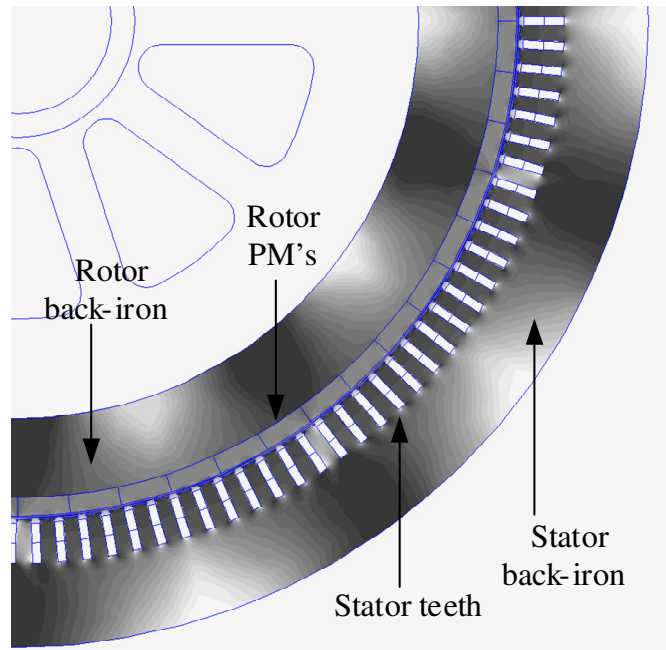


Fig. 5.30. Surface PM rotor structure.

For this large diameter machine, the magnet and air-gap surface areas can be assumed equal. Hence, the magnet flux-density can be estimated from [115]:

$$B_m = \frac{B_r}{1 + \mu_r \frac{l_g}{l_m}} \quad (\text{T}) \quad (5.19)$$

By rearranging equation (5.19) the magnet thickness is:

$$l_m = \frac{\mu_r l_g}{\frac{B_r}{B_m} - 1} \quad (\text{mm}) \quad (5.20)$$

where,

l_g : Air-gap radial thickness (mm)

The air-gap length is 7 mm, consistent with the minimum air-gap dimension for the WF rotor. Using the values in Table 5.7 the magnet thickness in terms of the magnet flux-density is plotted in Fig. 5.31.

The average air-gap flux-density for the WF rotor was 0.998 T, as previously shown in Table 4.8. For this average air-gap flux-density the magnet length from equation (5.20) would be 61.84 mm. At this flux-density the stator back-iron and tooth are saturated for the HG WF as seen from Fig. 4.26. While the WF is highly loaded it is not sensible to run the PM stator to the same load since this is an effective waste of the rotor magnet material. Hence, considering reduced magnet volume the magnet length is reduced and the stator tooth flux-density reduced to 1.85 T, corresponding to an average air-gap flux-density of 0.854 T, as detailed in Table 4.8 (Chapter 4). The magnet thickness is now analytically calculated to be 25 mm. However, FEA results show that with a magnet thickness of 25 mm the average air-gap flux-density is 0.77 T which is 10% lower than the targeted 0.854 T. This is due to flux-leakage not accounted for by the simple analytic expression of equation (5.19). Therefore, the magnet thickness is increased to obtain the target average flux-density. Table 5.8 lists different magnet thicknesses and the average air-gap flux-density calculated analytically and from FEA. The magnet thickness is therefore chosen to be 40 mm which produces an average flux-density of 0.842 T in the air-gap. Fig. 5.32 presents the air-gap flux-density for the surface magnet rotor design for both tangential and normal components. Fig. 5.33 illustrates a typical open-circuit field distribution for the machine with surface magnets while Table 5.9 presents average flux-density in different sections of the machine. The flux-density for the tooth and back-iron are denoted for the sections with the highest density.

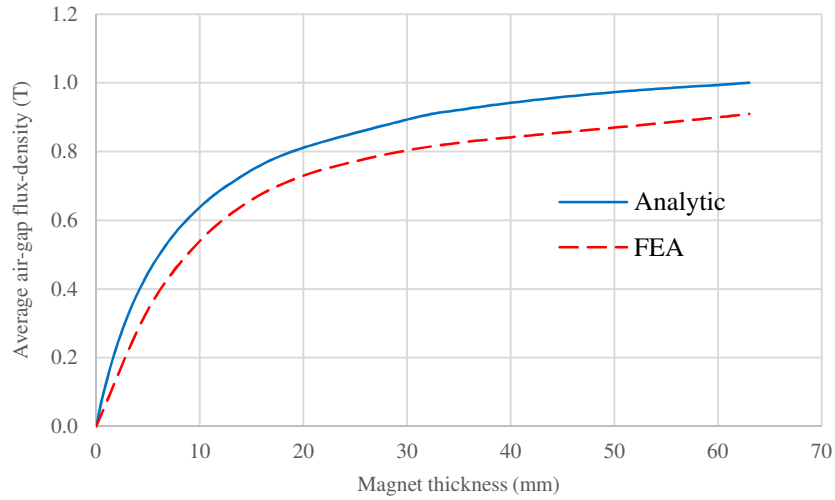


Fig. 5.31. Air-gap flux-density versus magnet thickness for sintered NdFeB surface magnet PM rotor.

Table 5.8. Magnet thickness and average air-gap flux-density for NdFeB surface magnet PM rotor

Magnet thickness, l_m (mm)	Average air-gap flux-density, B_m (T)	
	Analytic	FEA
25	0.86	0.772
30	0.9	0.804
35	0.92	0.826
40	0.94	0.842

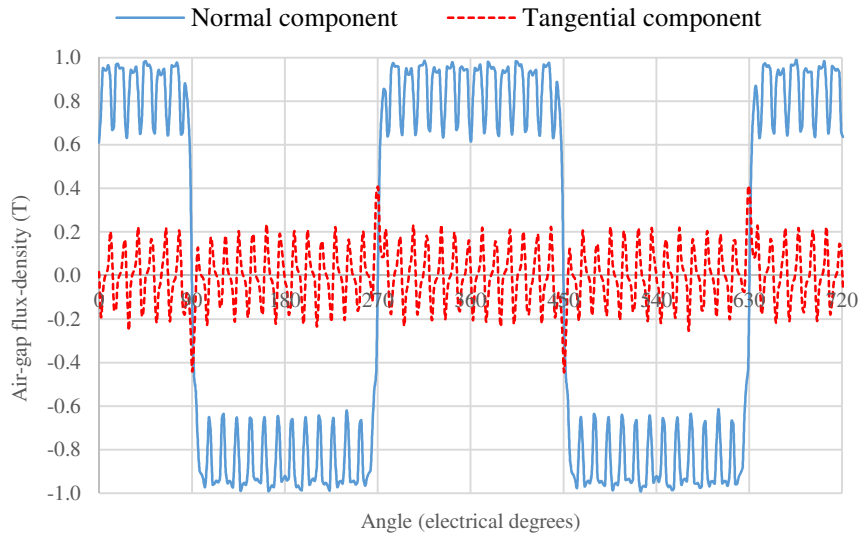


Fig. 5.32. Air-gap flux-density for NdFeB surface magnet PM rotor.

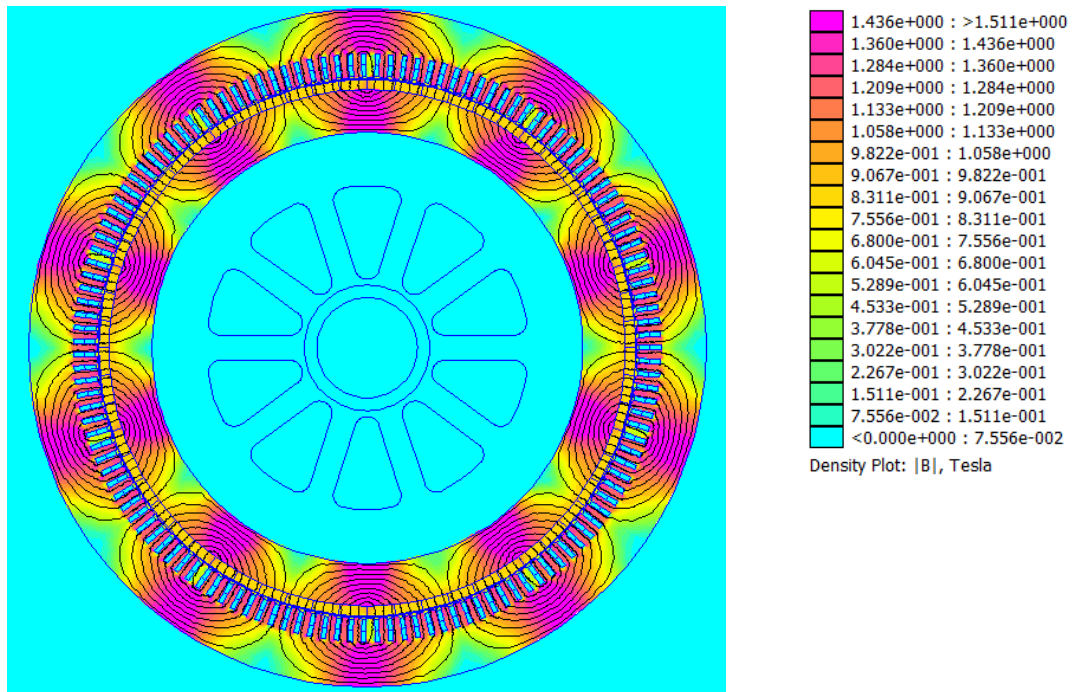


Fig. 5.33. Field distribution for NdFeB surface magnet PM rotor.

Table 5.9. Flux-density for different sections for NdFeB surface magnet PM rotor

Section	Flux-density (T)
Average air-gap	0.842
Stator tooth	1.27
Stator back-Iron	1.44
Rotor back-iron	1.72

From the N35H characteristics the minimum flux-density for the magnet is 0.1 T as stated in Table 5.7. The minimum magnet thickness in order to prevent magnet demagnetization is calculated as follows:

$$l_m^{\min} = \frac{-I_g}{\mu_0 H_{\lim}} - \mu_r l_g \quad (\text{mm}) \quad (5.21)$$

yielding a minimum magnet length of 0.4 mm to prevent demagnetization a value much below the 40 mm design length. In order to verify this a FEA file is set up, Fig. 5.34, with full-load stator current in the 9-phase winding (peak phase current = 170.67 A). The PM rotor is rotated such that the magnet field is directly opposed by the stator field at each pole. This condition represents a direct symmetrical short circuit at the machine terminals. After solution the FEA results file is scrutinized and the weakened magnet flux-density is obtained at different locations inside the magnet. The minimum FEA measured flux-density in the magnet is 0.35 T, which is higher than the demagnetization limit of 0.1 T. Therefore, the magnets will not be demagnetized under this worst load condition. Note that the seeming high magnet length is not to counter worst case stator reaction field but to achieve the average air-gap flux-density while maintaining a mechanical air-gap of 7 mm. This air-gap may be reduced with the ensuing reduction of magnet length (l_m), however, it was thought prudent to maintain the working mechanical air-gap as per the benchmark SG.

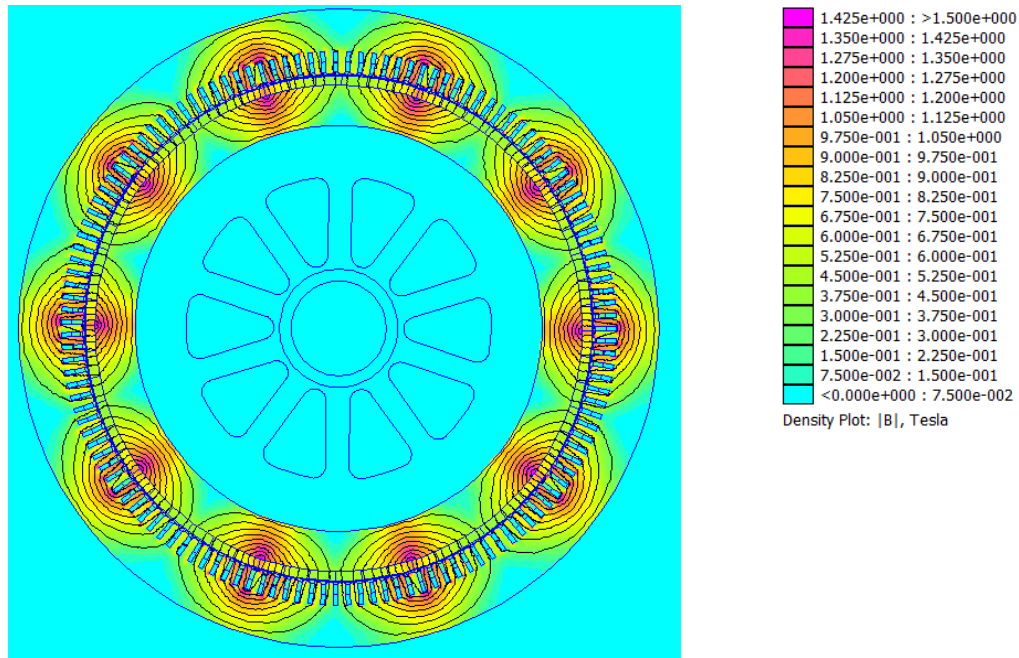


Fig. 5.34. Demagnetizing field distribution for NdFeB surface magnet PM rotor.

5.5.2 Flux-linkage, Back-EMF and Torque

The surface magnet PM machine has 10 rotor poles each split into 6 sections and magnetized separately in a fixed axis relative to the magnet piece center-line. The air-gap thickness, stator inner and outer diameter and stator structure for the HG PM is the same as the HG WF. In order to facilitate the comparison, the axial length for the HG PM is chosen to be the same as the HG WF, i.e. 400 mm. Later on these two machines, i.e. WF and PM, are combined and scaled accordingly to obtain the final HG design. Table 5.10 lists magnet length and thickness for the surface magnet PM machine. In order to protect the magnets from damages due to centrifugal forces the periphery of the surface PM rotor is covered with a layer of banding applied under tensile of stress. Table 5.10 shows maximum stress in the banding for two different banding thicknesses and two typical banding materials,

Carbon Fiber and Kevlar. The peripheral velocity of the rotor at the nominal rotor speed of 600 RPM is 67.5 m/s. A 20% over speed, i.e. 720 RPM, is considered to give a margin for safety.

Table 5.10. Sintered NdFeB magnet dimensions for the surface magnet PM machine

Item	Value (mm)	
Magnet length	670.968	
Magnet radial thickness, l_m	40	
Maximum banding material stress (MPa)	Banding thickness (mm)	
	1.50	2.00
Carbon Fiber*	1011.20	765.51
Kevlar*	1016.30	770.62

*The yield stress is taken as 1100 MPa

FEA results for the winding per-phase flux-linkage for the HG PM with NdFeB surface magnets is presented in Fig. 5.35, while Fig. 5.36 shows the phase open-circuit back-EMF at a nominal rotor speed of 600 RPM. For the purpose of comparison, waveforms for the 3-phase HG WF and 9-ph HG WF are also shown. The difference in shape of the 9-phase HG PM and HG WF back-EMF arises from the different rotor structures, i.e. cylindrical rotor with full-pitched magnets for the HG PM compared to salient pole rotor for the HG WF. The peak back-EMF for 9-phase HG PM is lower compared to the 9-phase HG WF because the HG PM operates at lower air-gap flux-density (0.842 T) compared to 0.998 T for the HG WF.

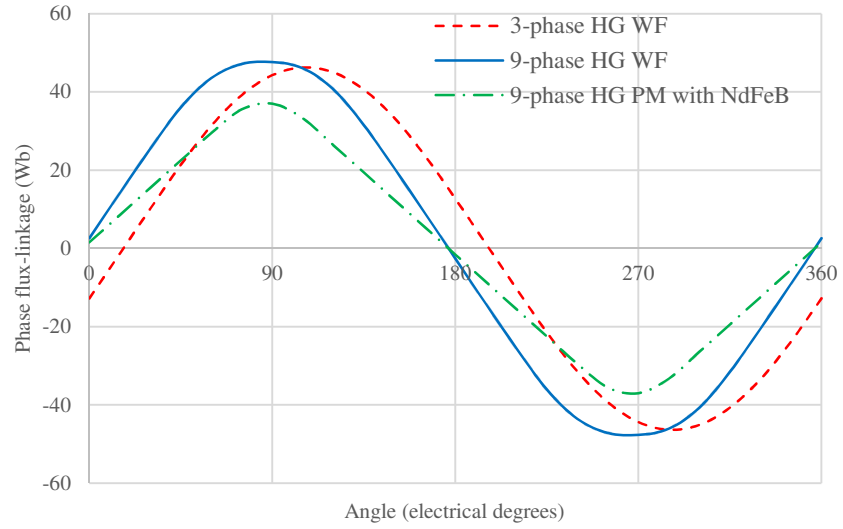


Fig. 5.35. Phase winding flux-linkage versus rotor position.

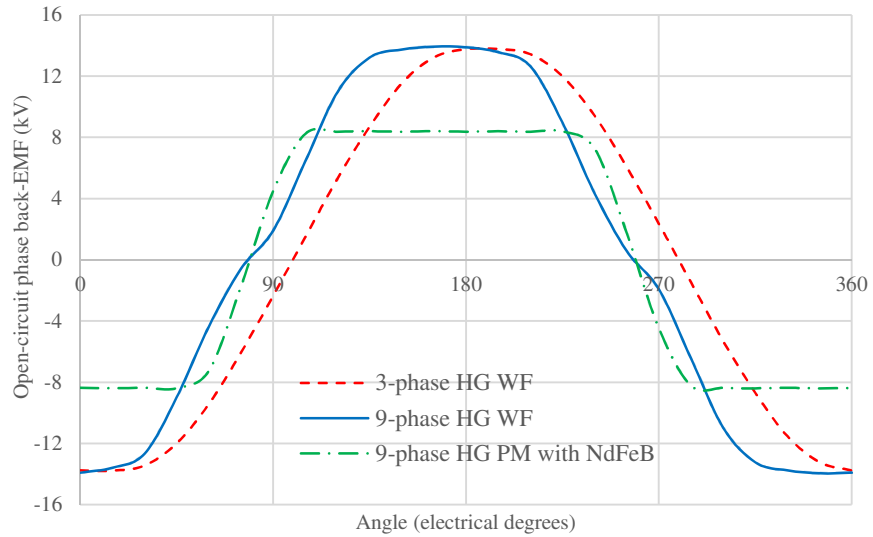


Fig. 5.36. Phase winding open-circuit back-EMFs.

The cogging torque (at zero stator current) for the HG PM is plotted in Fig. 5.37. For the purpose of comparison, the HG WF cogging torque for both constant and adjusted air-gaps are shown in Fig. 5.37. The peak cogging torque is lower for the HG PM due to lower air-gap flux-density. However, the HG PM is higher than that of the adjusted air-gap HG WF. This cogging torque could be reduced by reducing the rotor pole-arc to pole pitch [115], but since this would not significantly affect the total torque or machine power capability, no further work was carried out here. Needless-to-say, this would be a future modification to any final machine design.

The FEA results for the machine electromagnetic torque at full-load stator sinusoidal current excitation are presented in Fig. 5.38. The 9-phase full-load peak stator current for the HG PM and 9-phase HG WF is 170.67 A, while it is 512 A for the 3-phase HG WF. The nominal field current for the 3- and 9-phase HG WF is 486.23 A. The peak torque for the 9-phase HG WF is 4.2% higher than that of the 3-phase HG WF, due to the improved winding factor as discussed previously. However, the HG PM torque is lower due to lower air-gap flux-density.

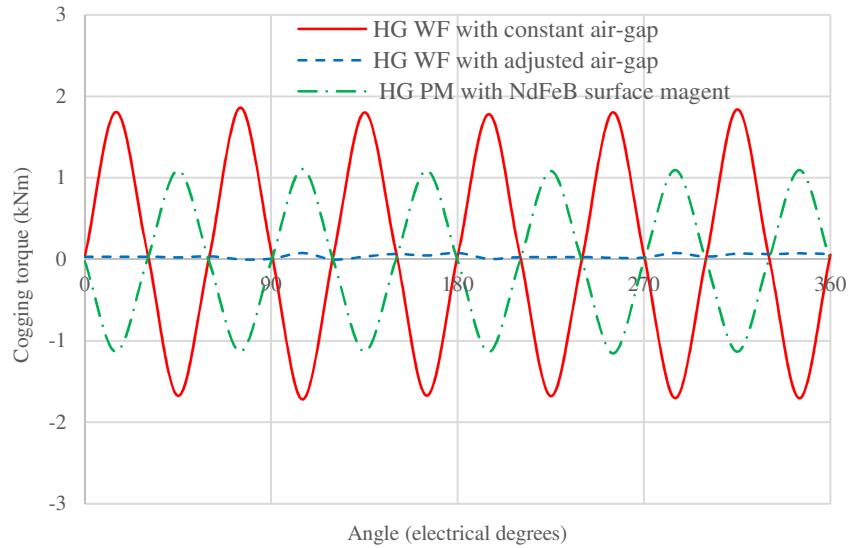


Fig. 5.37. Cogging torque waveforms.

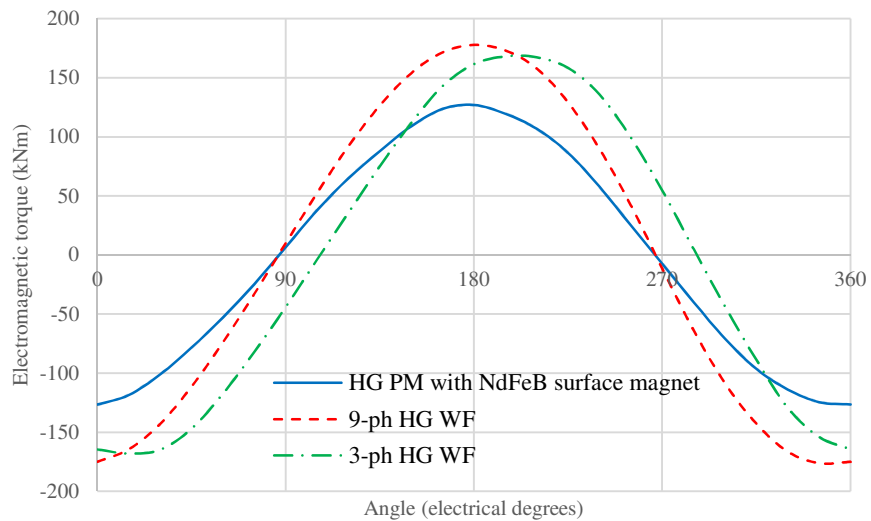


Fig. 5.38. Electromagnetic torque at full-load peak stator current 170.67 A for 9-phase and 512 A for 3-phase, and rotor field current 486.23 A for the HG WF.

5.5.3 Inductances

The HG PM with a surface magnet design has a cylindrical rotor. Therefore, the machine per phase inductance is essentially constant with respect to rotor position. Indeed, any perturbations due to stator slots are neglected by the large effective magnetic air-gap posed by the NdFeB magnets and mechanical air-gap. In order to calculate the machine inductance, the magnets are set to air and the rotor is rotated while one phase is excited with full-load stator current. Fig. 5.39 shows the per-phase self-inductance and mutual inductances between phase 1 and other phases for the HG PM with surface magnets. It is seen that the HG PM inductances are constant as expected.

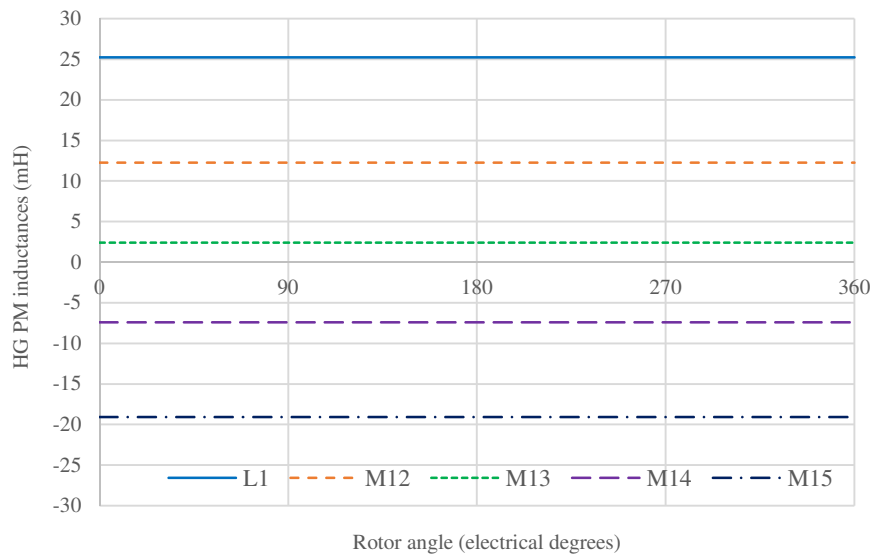


Fig. 5.39. Self- and mutual-inductances for the HG PM with surface magnets.

By setting the variable part of inductance to zero in equation (5.17) the self and mutual inductances for the 9-phase winding are obtained:

$$\begin{aligned}
 L_1^{PMs} &= L_2^{PMs} = L_3^{PMs} = L_4^{PMs} & M_{12}^{PMs} &= L_1^{PMs} \cos\left(\frac{2\pi}{9}\right) & M_{13}^{PMs} &= L_1^{PMs} \cos\left(\frac{4\pi}{9}\right) \\
 &= L_5^{PMs} = L_6^{PMs} = L_7^{PMs} & M_{14}^{PMs} &= L_1^{PMs} \cos\left(\frac{6\pi}{9}\right) & M_{15}^{PMs} &= L_1^{PMs} \cos\left(\frac{8\pi}{9}\right) \\
 &= L_8^{PMs} = L_9^{PMs} & M_{16}^{PMs} &= L_1^{PMs} \cos\left(\frac{10\pi}{9}\right) & M_{17}^{PMs} &= L_1^{PMs} \cos\left(\frac{12\pi}{9}\right) \\
 & & M_{18}^{PMs} &= L_1^{PMs} \cos\left(\frac{14\pi}{9}\right) & M_{19}^{PMs} &= L_1^{PMs} \cos\left(\frac{16\pi}{9}\right)
 \end{aligned} \tag{5.22}$$

Note that:

$$\begin{aligned}
 M_{12}^{PMs} &= M_{19}^{PMs} & M_{13}^{PMs} &= M_{18}^{PMs} \\
 M_{14}^{PMs} &= M_{17}^{PMs} & M_{15}^{PMs} &= M_{16}^{PMs}
 \end{aligned}$$

Referring to Fig. 5.24 the mutual inductances for the HG PM with surface magnets can be generalized as follows:

$$\begin{aligned}
 M_{i,i+1}^{PMs} &= M_{i,i+8}^{PMs} = L_1^{PMs} \cos\left(\frac{2\pi}{9}\right) & M_{i,i+2}^{PMs} &= M_{i,i+7}^{PMs} = L_1^{PMs} \cos\left(\frac{4\pi}{9}\right) & M_{ij}^{PMs} &= M_{ji}^{PMs} \\
 M_{i,i+3}^{PMs} &= M_{i,i+6}^{PMs} = L_1^{PMs} \cos\left(\frac{6\pi}{9}\right) & M_{i,i+4}^{PMs} &= M_{i,i+5}^{PMs} = L_1^{PMs} \cos\left(\frac{8\pi}{9}\right)
 \end{aligned} \tag{5.23}$$

where,

L_i^{PMs} : Self-inductance for i^{th} phase for the HG PM with surface magnets

M_{ij}^{PMs} : Mutual inductance between phases i and j for the HG PM with surface magnets

The synchronous inductance for the HG PM with surface magnet is calculated from equation (4.11). The HG PM is designed such that operates in the linear magnetic region, hence the unsaturated inductance is only considered in the machine analysis. Table 5.11 lists inductances for the HG PM with surface magnets.

Table 5.11. Inductances for the HG PM with surface magnets

Item	Symbol	Value (mH)
Self-inductance	L_i^{PMs}	25.23
Mutual-inductances	$M_{i,i+1}^{PMs} = M_{i,i+8}^{PMs}$	12.26
	$M_{i,i+2}^{PMs} = M_{i,i+7}^{PMs}$	2.42
	$M_{i,i+3}^{PMs} = M_{i,i+6}^{PMs}$	-7.39
	$M_{i,i+4}^{PMs} = M_{i,i+5}^{PMs}$	-19.06
Synchronous inductance	L_s^{PMs}	113.35

5.6 Design of HG PM Rotor with Ferrite Embedded Magnets

In this section design of a HG PM machine with embedded magnet rotor using sintered Ferrite magnets is addressed. The B-H characteristics for a typical sintered Ferrite magnet manufactured by Arnold Magnetics, referred to as Ferrite AC-5, is shown in Fig. 5.40. The dotted line shows the desired characteristics at a nominal machine operating temperature of 80 °C. Properties of the Ferrite magnet at 80 °C are detailed in Table 5.12. Ferrite relative permeability is calculated using two points on the graph in Fig. 5.40 and equation (5.18).

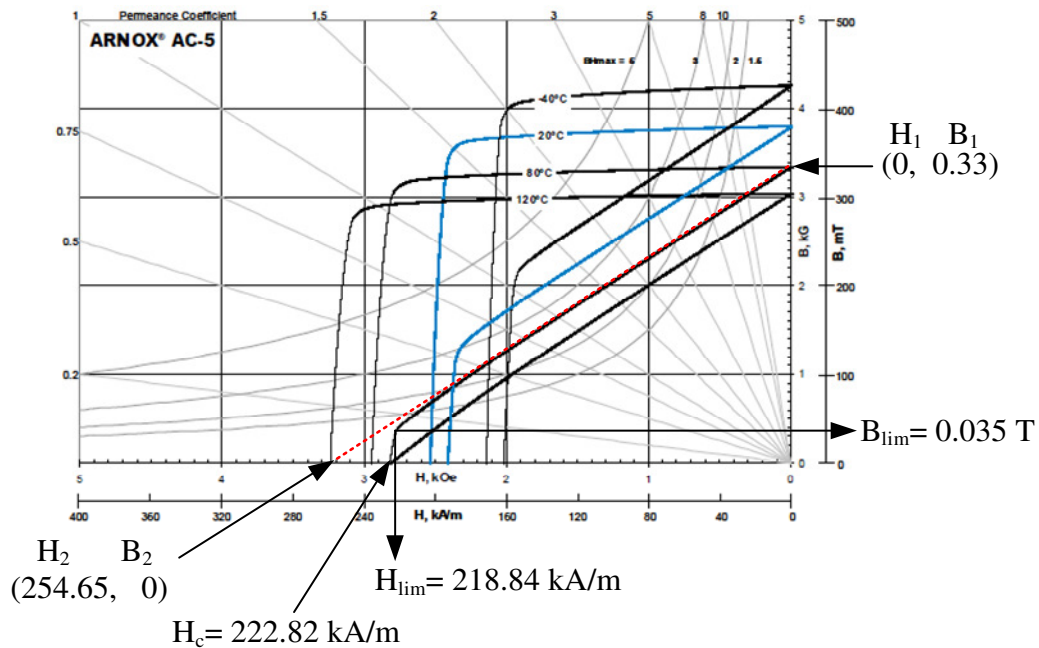


Fig. 5.40. B-H characteristic for Ferrite AC-5 [120].

The sintered Ferrite magnet remanence at 80 °C (0.33 T) is much lower than that of the sintered NdFeB magnet (1.12 T). Therefore, if the Ferrite magnets are to replace the surface magnets in the HG PM design the air-gap flux-density will be lower than that of HG PM with NdFeB surface magnets by a factor close to the ratio of their respective remanences. This would require a longer machine axial length in order to obtain the same back-EMF and therefore not an ideal option for the HG PM design. However, the HG PM with

embedded Ferrite magnets in a ‘high field’ topology is studied here to investigate the feasibility of such design. Fig. 5.41 shows a HG PM with Ferrite ‘high field’ embedded rotor design.

Table 5.12. Ferrite magnet AC-5 properties at 80 °C

Parameter	Value
Remanence (T)	0.33
Relative permeability	1.03
Coactivity (kA/m)	222.82
Magnetic intensity demagnetization limit (kA/m)	218.84
Flux-density demagnetization limit (T)	0.035
Magnet electrical conductivity (MS/m)	0

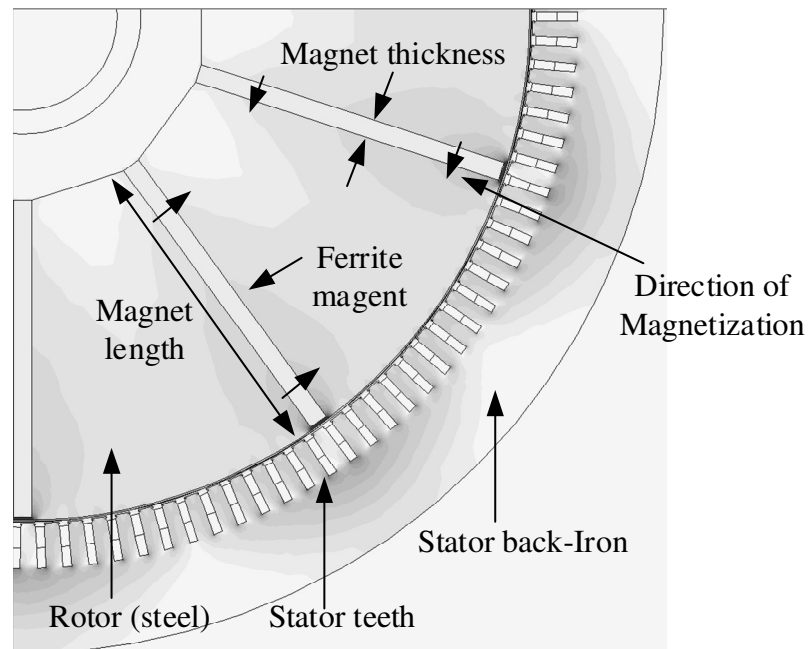


Fig. 5.41. Ferrite magnet arrangement in HG PM ‘high field’ embedded rotor design.

The Ferrite magnets are arranged to realize a 10-pole rotor field. Basic analytic sizing are used to estimate the initial thickness and length of the Ferrite magnets for the embedded PM rotor design. The outer diameter of the rotor for the embedded magnet design is the same as surface magnet rotor but the inner rotor diameter has to be larger to accommodate the embedded magnets hence the amount of rotor material is greater compared to that of surface magnet rotor. There are 10 poles, hence 10 Ferrite magnets displaced 36 mechanical degrees from one another. Each Ferrite magnet is magnetized circumferentially as indicated in Fig. 5.42. The air-gap thickness is maintained at 7 mm, as per the other machine designs. The no-load field distribution for the HG PM with an embedded magnet rotor is shown in Fig. 5.42.

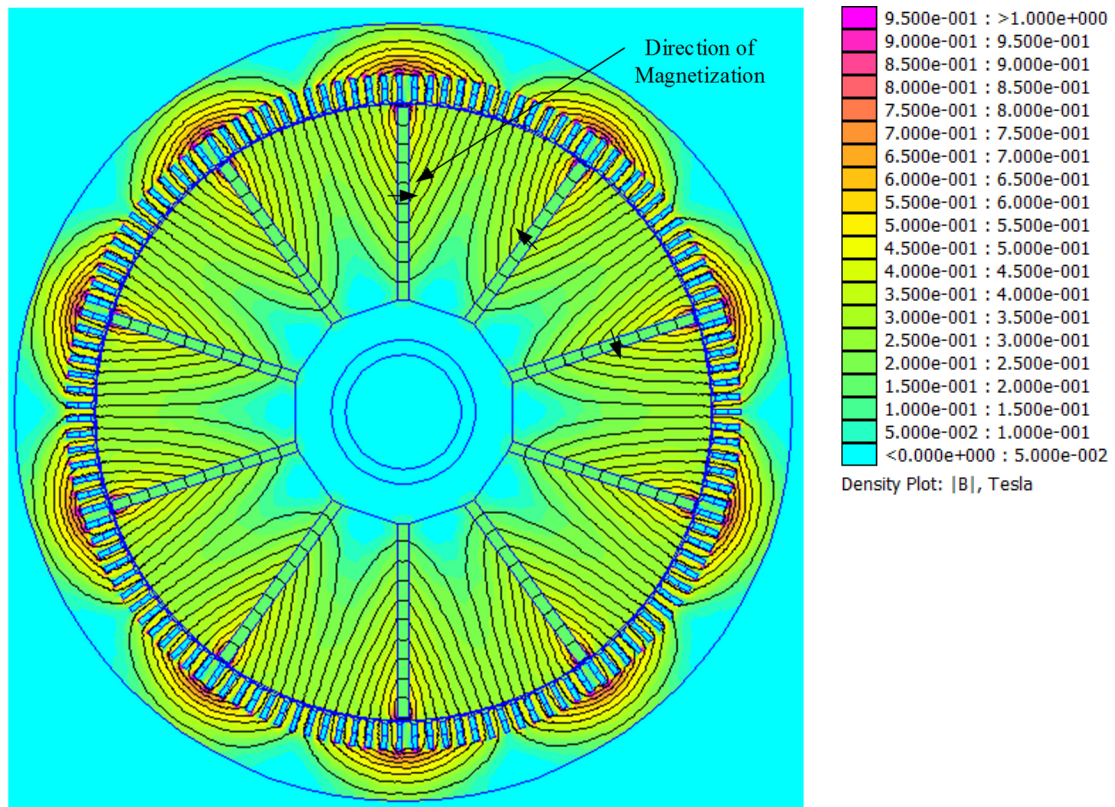


Fig. 5.42. Typical no-load magnetic field distribution for the HG PM with embedded sintered Ferrite magnets.

Ideally it is expected that fluxes due to two adjacent Ferrites add up in the air-gap to increase the air-gap flux-density. However, for the same magnet thickness and length as in NdFeB magnets the average air-gap flux-density is 0.274 T. As seen from Fig. 5.42 the fluxes don't add up. Therefore, in order to increase the air-gap flux-density the Ferrite magnet's thickness is increased and average air-gap flux-density is calculated using FEA. Table 5.13 shows average air-gap flux-density for different Ferrite thickness's and for two different lengths, (i) a full magnet length of 670.968 mm and (ii) a half magnet length of 335.484 mm, while Fig. 5.43 plots these results graphically.

From Fig. 5.43 it is evident that the air-gap flux-density does not increase linearly with the Ferrite magnet thickness. Indeed, it is concluded that the geometry of the rotor is such that the flux due to adjacent Ferrites do not add up. In order to investigate the effect of geometry on the air-gap flux-density the number of poles are increased. Table 5.14 shows average air-gap flux-density for different pole numbers and Fig. 5.44 illustrates this graphically. As seen, when the number of poles is increased the air-gap flux-density is increased. Note that the additional poles have the same shape, length (670.968 mm) and thickness (40 mm) and when adding new poles the angular distance between poles are calculated accordingly to accommodate appropriate amount of Ferrite magnets in the rotor constraint. Thus, for the machine dimensions fixed by the benchmark machine design, a 10-pole solution would not be a suitable one for employing a sintered Ferrite rotor design.

Therefore, it is concluded that the embedded magnet rotor design with sintered Ferrite magnets for the HG PM rotor is not an ideal option hence will not be investigated further in this study.

Table 5.13. Magnet size and average air-gap flux-density for the HG PM with embedded sintered Ferrite PM rotor

Magnet thickness (mm)	Average air-gap flux-density (T)	
	Magnet length=670.968 mm (full-length)	Magnet length=335.484 mm (half-length)
40	0.274	0.163
60	0.324	0.183
80	0.357	0.196
100	0.38	0.204
120	0.4	0.211
140	0.411	0.216
160	0.422	0.220

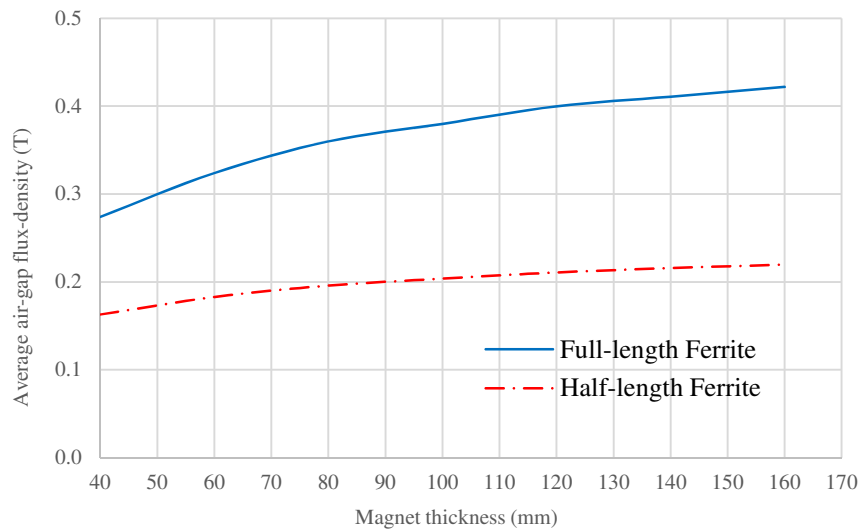


Fig. 5.43. HG PM average air-gap flux-density with respect to embedded Ferrite magnet size.

Table 5.14. Average air-gap flux-density for the HG PM with embedded PM rotor and different number of poles (Ferrite length 670.968 mm and thickness 40 mm)

Number of poles	Average air-gap flux-density (T)
10	0.274
12	0.299
14	0.32
16	0.337
18	0.351
20	0.361

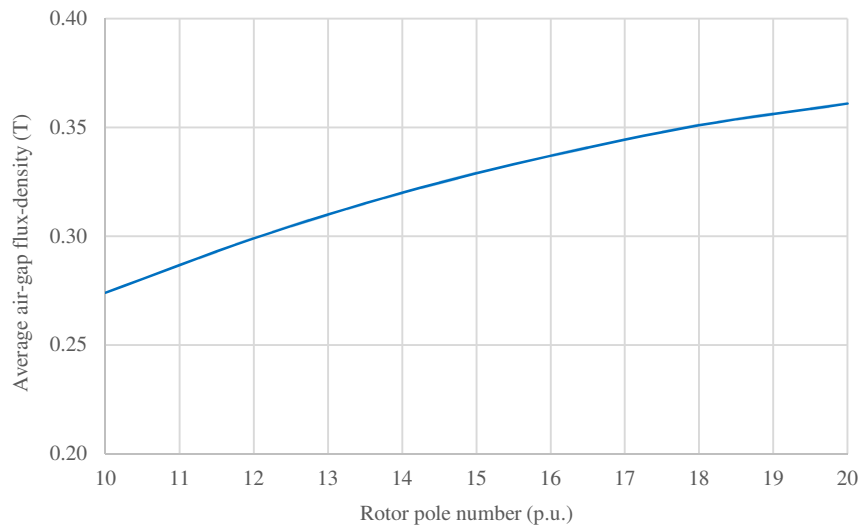


Fig. 5.44. HG PM average air-gap flux-density with respect to number of embedded Ferrite magnet rotor poles.

5.7 Design of HG PM Rotor with NdFeB Embedded Magnets

A HG PM rotor design with sintered NdFeB surface magnets was discussed previously. It was also concluded that the embedded rotor design with sintered Ferrite magnets is not a suitable option for the HG PM. In this section a HG PM rotor design with embedded sintered NdFeB magnets is discussed to give some assessment for this rotor topology. The same NdFeB magnet grade as in surface rotor design, i.e. N35H manufactured by Arnold is chosen. The magnets are laid out within the rotor assembly as with the Ferrites design. The magnet length (670.968 mm) and thickness (40 mm) are as for the surface magnet design. Fig. 5.45 shows the no-load flux distribution for the HG PM with embedded NdFeB rotor design, while Fig. 5.46 presents machine air-gap flux-density for two electrical cycles. Comparing Fig. 5.46 with Fig. 5.32 it is seen that the air-gap flux-density is higher for the embedded design with the same magnet length and thickness. Table 5.15 shows average air-gap flux-density for three PM rotor designs, (i) HG PM with surface NdFeB magnets, (ii) HG PM with embedded Ferrite magnets, and (iii) HG PM with embedded NdFeB magnets. Average air-gap flux-density for the embedded NdFeB rotor design is 1.0 T, i.e. 18.8% higher than that of surface magnet design hence a suitable option for the HG PM rotor design.

Table 5.16 lists average flux-density for different sections of the HG PM machine with embedded NdFeB rotor. The tooth flux-density is measured in the middle of the tooth and rotor and stator back-iron flux-densities are for the areas with highest saturation. Note that the average air-gap and stator back-iron flux-density for the HG PM with embedded NdFeB is the same as HG WF. However, the stator tooth and rotor back-iron flux-density is higher in the HG WF machine due to the higher field loading. The RMS air-gap flux-density for the HG PM with embedded NdFeB magnets is 1.04 T which is 11% lower compared to 1.17 T for the HG WF machine.

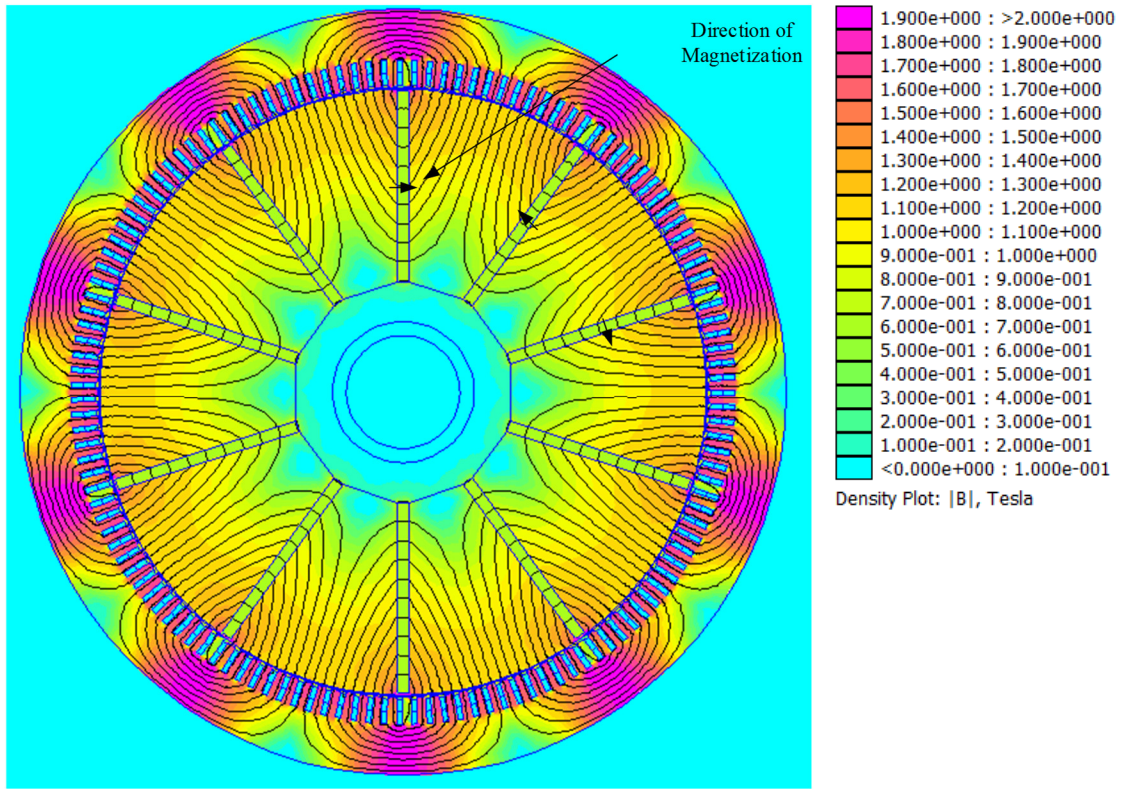


Fig. 5.45. No-load flux distribution for the HG PM with embedded NdFeB rotor design.

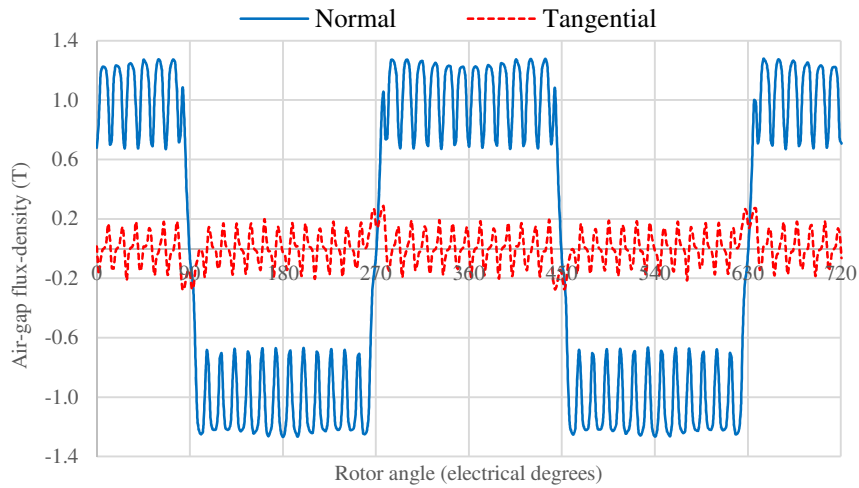


Fig. 5.46. No-load air-gap flux-density with respect to rotor electrical angle for the HG PM embedded NdFeB rotor design.

Table 5.15. Average air-gap flux-density for the HG PM with different rotor designs
(for all designs magnet length is 670.968 mm, and thickness 40 mm)

HG PM with	Average air-gap flux-density (T)
Surface NdFeB magnets	0.842
Embedded Ferrite magnets	0.274
Embedded NdFeB magnets	1.00

Table 5.16. Flux-density for different sections for the HG PM with NdFeB magnets

Section	Flux-density (T)		
	HG PM with surface NdFeB	HG PM with Embedded NdFeB	HG WF
Average air-gap	0.842	1.00	0.998
Stator tooth	1.27	1.54	2
Stator back-Iron	1.44	1.81	1.8
Rotor back-iron	1.72	1.12	1.5

5.7.1 Flux-linkage, Back-EMF and Torque

The HG PM with embedded NdFeB magnets has the same machine stator as the HG PM with surface magnets, i.e. a 9-phase design with distributed windings. The air-gap thickness, stator inner and outer diameter is also the same as the HG PM with surface magnets. The outer diameter of the rotor for the embedded magnet design is the same as surface magnet rotor but the inner rotor diameter is larger for the embedded rotor. For comparison purposes, the machine axial length is the same as HG PM with surface magnets i.e. 400 mm. Fig. 5.47 shows per-phase flux-linkage while the open-circuit back-EMF's at the nominal rotor speed of 600 RPM is presented in Fig. 5.48. The peak phase back-EMF

for the HG PM with embedded NdFeB is 20.6% higher than that of HG PM with surface magnets. However, the HG PM has lower peak back-EMF compared to the HG WF due to lower flux-linkage. Table 5.17 lists peak and RMS voltages for the HG WP and HG WF.

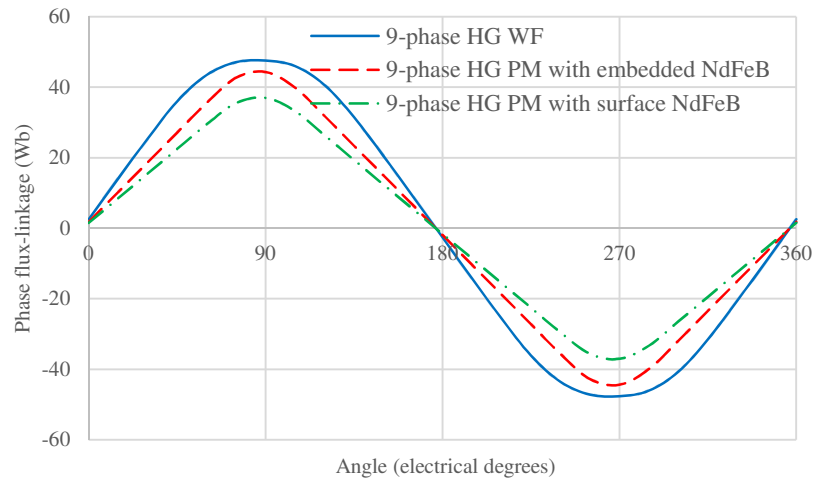


Fig. 5.47. Per-phase flux-linkage for the 9-phase HG WF, 9-phase HG PM with surface NdFeB magnets and 9-phase HG PM with embedded NdFeB magnets.

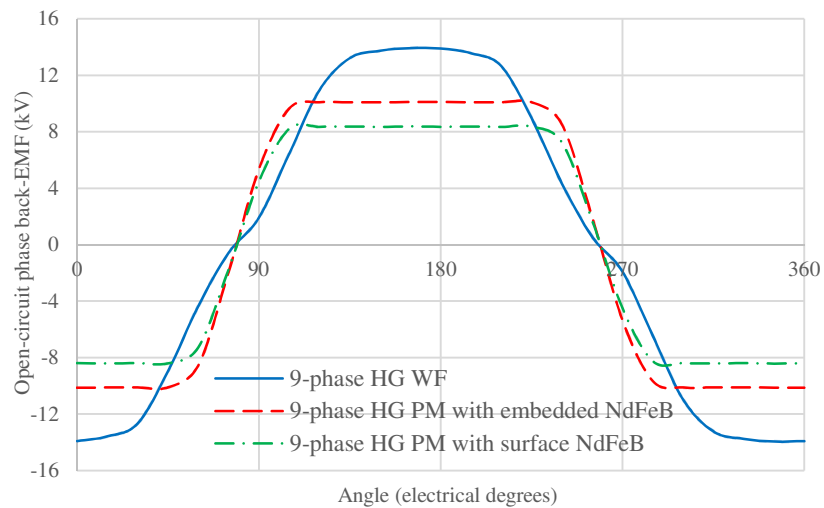


Fig. 5.48. Per-phase open-circuit back-EMF for the 9-phase HG WF, 9-phase HG PM with surface NdFeB magnets and 9-phase HG PM with embedded NdFeB magnets.

The machine cogging torque at no-load stator current is plotted in Fig. 5.49. Compared to the surface magnet design the cogging torque in the embedded rotor has more harmonics with larger amplitudes. Table 5.18 shows peak cogging torque for HG PM with surface and embedded magnets and also for the HG WF. For the HG PM with embedded NdFeB magnets, the peak cogging torque is 2.6% of the machine total torque whereas the cogging torque in the HG PM with surface magnets is only 0.9% of its total torque. However, the adjusted air-gap HG WF cogging torque is much smaller, i.e. 0.05% of the total torque. Further improvement of the cogging torque is out of scope of this study and hence will not be discussed further.

The FEA results for machine electromagnetic torque at full-load stator current are presented in Fig. 5.50. The embedded magnet rotor design is electromagnetically a salient pole rotor hence has two torque components; salient torque and excitation torque. The excitation torque is due to interactions between magnet and stator fields while the salient torque depends on the machine geometry. The HG PM with surface magnets has a cylindrical rotor hence machine torque is only due to excitation. The HG PM with embedded PM has higher torque compared to surface magnet design due to increased air-gap flux-density and saliency component of torque. The HG WF has a salient rotor however, the machine is highly saturated and the excitation torque dominates the shape of the torque waveform in Fig. 5.50. In order to estimate the salient torque for the HG PM with embedded NdFeB rotor the magnets are set to air and the FEA results are plotted in Fig. 5.51. By setting the magnets to air the machine operating point on the B-H curve changes hence the steel operates at a lower flux-density. Therefore, the salient torque calculated is an estimate of the actual machine salient torque. By subtracting the salient torque from the total machine torque the estimation for excitation torque is obtained, as shown in Fig 5.50. Table 5.19 details peak excitation, salient and total torque for the HG PM and HG WF.

The peak salient torque is 25.52% of the total peak torque in the HG PM machine with embedded magnets. For the purpose of comparison, the torque components for HG WF and HG PM with surface magnets are also shown in Table 5.19.

Table 5.17. RMS and peak voltages for 9-phase HG with various rotors

9-phase stator machine	Voltage (kV)	
	Peak	RMS
HG WF	13.94	10.80
HG PM with surface NdFeB magnets	8.40	7.70
HG PM with embedded NdFeB magnets	10.13	9.28

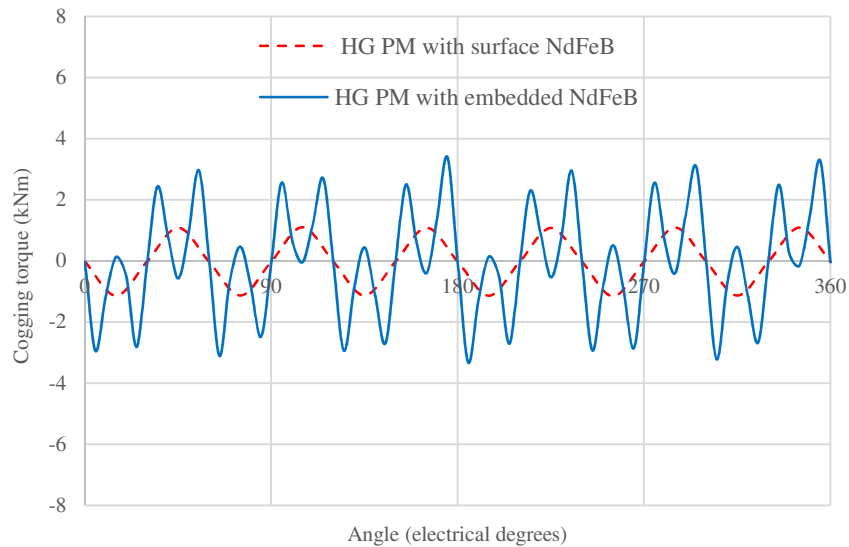


Fig. 5.49. Cogging torque (at zero stator current).

Table 5.18. Peak cogging and total torque for different designs

9-phase stator machine	Peak torque (kNm)		Torque Ratio (%) (Cogging/Total)
	Cogging	Total	
HG WF	0.08	177.90	0.05
HG PM with surface NdFeB magnets	1.11	127.05	0.9
HG PM with embedded NdFeB magnets	3.40	130.93	2.6

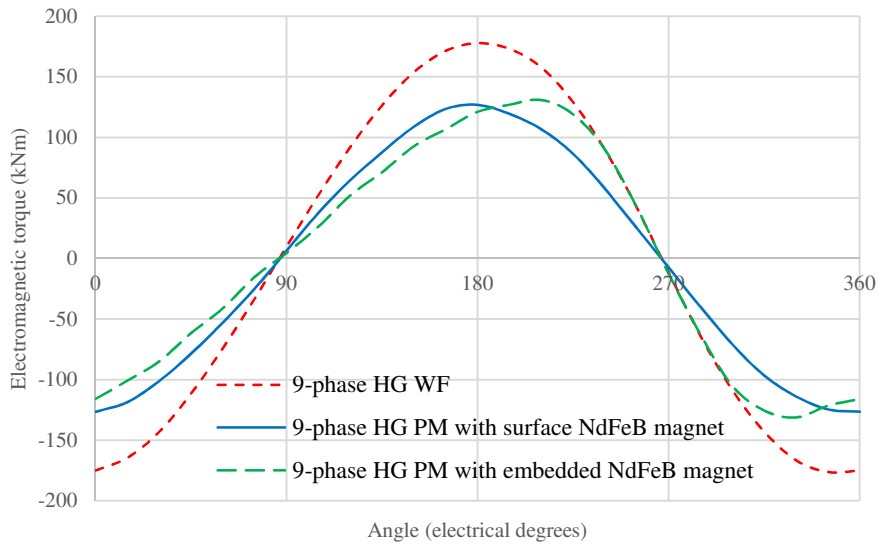


Fig. 5.50. Electromagnetic torque at full-load peak stator current of 170.67 A for the 9-phase stator winding.

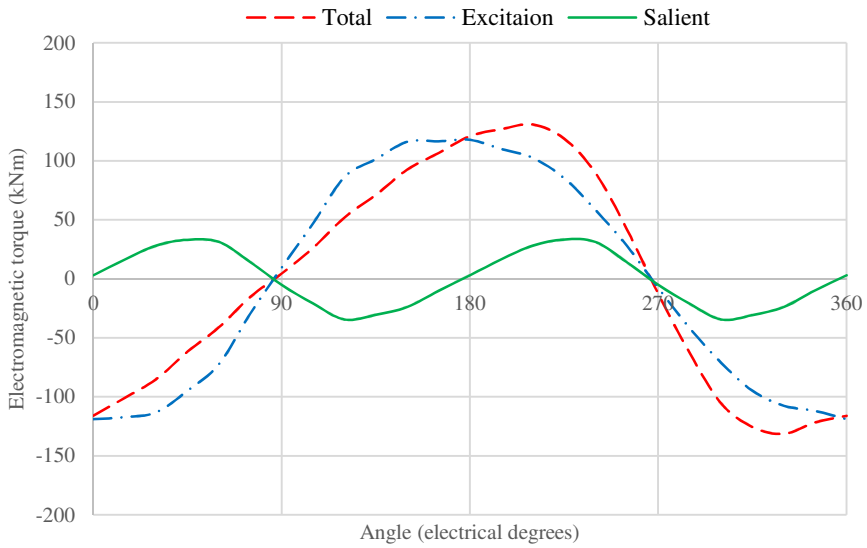


Fig. 5.51. Salient and excitation torque components in the 9-phase HG PM with embedded NdFeB.

Table 5.19. Peak salient, excitation and total torque for different designs

9-phase stator machine	Peak torque (kNm)			Torque Ratio (%) (Salient/Total)
	Salient	Excitation	Total	
HG WF	52.38	206.40	177.90	29.44
HG PM with surface NdFeB magnets	-	127.05	127.05	0
HG PM with embedded NdFeB magnets	33.41	118.02	130.93	25.52

5.7.2 Inductances

The HG PM with embedded NdFeB magnets rotor design has a magnetically salient rotor. Therefore, the machine per phase inductance varies with respect to rotor position. In order to calculate the machine inductance the magnets are set to air and the rotor is rotated while one phase is excited with full-load stator current. Fig. 5.52 shows the per-phase machine inductance. The HG PM with embedded NdFeB self-inductance with respect to rotor electrical angle can be expressed as:

$$L_{self}^{PM_e} = L_0^{PM_e} + L_2^{PM_e} \cos(2\theta_e) \quad (5.24)$$

where,

$L_0^{PM_e}$: Average phase inductance

$L_2^{PM_e}$: Phase inductance amplitude variations above average

Compared to the HG WF self-inductance the d-q axis is switched in the HG PM with embedded NdFeB. Therefore:

$$\begin{aligned}
 L_q^{PM_e} &= \frac{3}{2} (L_0^{PM_e} + L_2^{PM_e}) \\
 L_d^{PM_e} &= \frac{3}{2} (L_0^{PM_e} - L_2^{PM_e})
 \end{aligned}
 \tag{5.25}$$

The machine equivalent synchronous inductance is calculated from equation (4.11). Table 5.20 lists different inductances for the HG PM with embedded NdFeB.

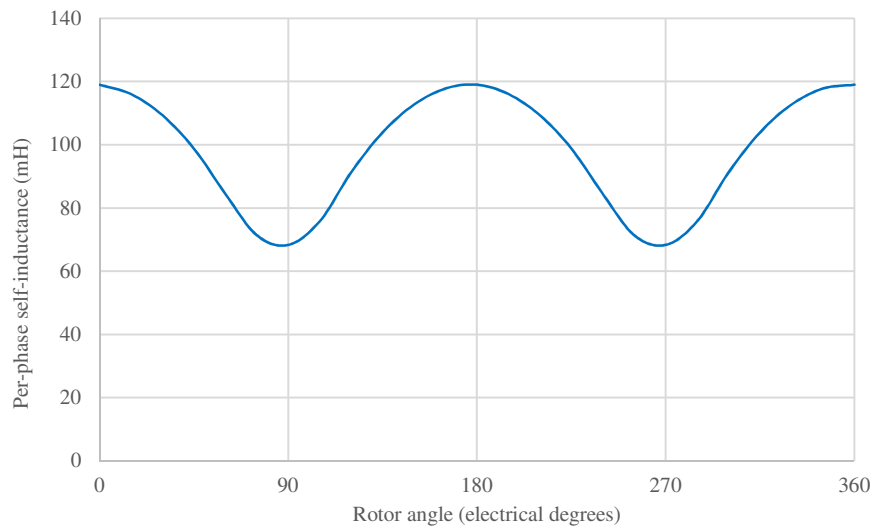


Fig. 5.52. Per-phase self-inductance for the HG PM with embedded NdFeB magnets.

Table 5.20. HG PM with embedded NdFeB inductances

Parameter	Value (mH)
$L_0^{PM_e}$	93.68
$L_2^{PM_e}$	25.31
$L_d^{PM_e}$	102.56
$L_q^{PM_e}$	178.49
$L_s^{PM_e}$	421.56

5.8 Final HG Considerations

The 3-phase benchmark SG is rated at 5.52 MW. Therefore, the nominal power of the 3-phase HG WF, which is essentially the same machine as the benchmark SG, is 5.52 MW. However, as discussed previously when the machine is rewound with a 9-phase stator the output voltage increases by 4.2%, hence the 9-phase HG WF nominal power is 5.75 MW. As shown in Table 5.17 the RMS phase voltage of the 9-phase HG WF is 10.80 kV, higher than that of HG PM with surface and embedded magnets, i.e. 7.70 kV and 9.28 kV respectively due to their reduced air-gap flux-densities relative to the benchmark machine. All three machines, HG WF, HG PM with surface NdFeB and HG PM with embedded NdFeB have the same active axial length, i.e. 400 mm and the same number of turns per coil, i.e. 12. Therefore, for the same stator current the machine output power is linearly changed with the voltage. The output power of the HG PM with surface magnet is reduced by a factor of 0.71 (7.70/10.80) while the output power of the HG PM with embedded magnets is reduced by a factor of 0.86 (9.28/10.80). In order to facilitate the comparison, the three machines are scaled to the same voltage and power i.e. 10.80 kV and 5.75 MW. The machine voltage is a function of axial length and number of turns in each coil i.e.:

$$EMF \propto N l_a \quad (5.26)$$

where,

N : Number of turns per coil (p.u.)

l_a : Active axial length (mm)

Therefore, to obtain an RMS phase voltage of 10.80 kV while keeping the same number of turns, the initial axial length of 400 mm for the HG PM with surface magnets is increased to 560 mm (by a factor 1.4) while the axial length of the HG PM with embedded magnets is increased to 464 mm (by a factor of 1.16). Since the stator current is maintained the same the machine output power is linearly increased for both HG PM with surface and embedded magnets to 5.75 MW. Table 5.21 summarizes the main specification of the three machines at 5.75 MW.

The HG in the proposed wind generation scheme in Chapter 3 is rated at 3.6 MW. Therefore, the 9-phase 5.75 MW machines need to be scaled to deliver a nominal power of 3.6 MW. The machine torque can be expressed as [115]:

$$T = \frac{\pi D^2}{2} l_a Q B_{ave} \quad (5.27)$$

where,

D : Air-gap diameter (mm)

l_a : Active axial length (mm)

Q : Electric loading (A/mm)

B_{ave} : Air-gap average flux-density (magnetic loading) (T)

The machine power is related to its torque via rotational speed. Keeping the same air-gap diameter, electric loading and air-gap average flux-density the machine axial length is adjusted to obtain desired output power. However, by changing the axial length the machine output voltage changes. In order to keep the same output voltage while scaling the machine power the number of turns need to be changed. The 5.75 MW 9-phase HG WF axial length is 400 mm hence the axial length for a 3.6 MW rated power is 250.43 mm, viz:

$$l_a = \frac{3.6}{5.75} (400) = 250.43 \text{ mm}$$

The number of turns per coil for the 5.75 MW HG WF is 12, therefore, the adjusted number of turns for the 3.6 MW machine and for the same output voltage is 19.2, viz:

$$N = \frac{400}{250.43} (12) = 19.2$$

However, the number of turns need to be an integer, i.e. 19. This requires the 3.6 MW HG WF axial length to be tuned to 253 mm to obtain the same output voltage. Note that the total coil cross-section is kept the same hence increasing the number of turn reduces the cross-section per turn. Similarly with 19 turns per coil the axial length for the HG PM with surface NdFeB and the HG PM with embedded NdFeB is 354.3 mm 293.6 mm respectively. Table 5.22 summarizes the 3.6 MW machines axial length, number of turns, coil and turn cross-section.

Table 5.21. Main machine specifications at 5.75 MW

Parameter	9-phase Machine		
	HG WF	HG PM with surface magnets	HG PM with embedded magnets
Output power (MW)	5.75		
RMS phase voltage (kV)	10.80		
Number of turns per coil (p.u.)	12		
Coil cross-section (mm ²)	380.64		
Turn cross-section (mm ²)	31.72		
Active axial length (mm)	400	560	464

Table 5.22. Main machine specifications at 3.6 MW

Parameter	9-phase Machine		
	HG WF	HG PM with surface magnets	HG PM with embedded magnets
Output power (MW)	3.6		
RMS phase voltage (kV)	10.80		
Number of turns per coil (p.u.)	19		
Coil cross-section (mm ²)	380.64		
Turn cross-section (mm ²)	20.03		
Active axial length (mm)	253	354.3	293.6
Mass (kg)⁽¹⁾			
Stator steel (back-iron + teeth)	3536.14	4952	4103.6
Rotor pole steel	1912.68	-	-
Rotor back-iron steel	2182.82	2701.73	6406.94
Rotor pole PM ⁽²⁾	-	699.58	589.78
Stator copper	1036	1129.23	1073.41
Rotor copper	774.14	-	-
Total steel	7631.64	7653.73	10510.54
Total copper	1810.14	1129.23	1073.41
Exciter	1141.25	-	-
Total ⁽³⁾ (tonnes)	10.58	9.48	12.18

⁽¹⁾ Steel (lamination) density = 7650 kg/m³; Copper density = 8960 kg/m³

⁽²⁾ PM mass density 7500 kg/m³

⁽³⁾ Excluding shaft, machine casing, end caps, cooling system and other support structure

5.8.1 WF and PM Split Ratio

As discussed the HG has two rotor sections; WF and PM rotors. The HG output voltage is 75% due to the PM and 25% due to WF sections as discussed previously. Therefore, the separate machines analyzed as HG WF and HG PM need to be combined with appropriate ratios to obtain the HG output voltage at 3.6 MW rated power. The machine RMS output voltage is 10.80 kV. Therefore, the PM rotor section provides 75% of this voltage, i.e. 8.1 kV, while the WF rotor section provides the 25%, i.e. 2.7 kV. The machine axial length is linearly related to its output voltage as expressed in equation (5.26). Therefore, the WF rotor section axial length is 25% of the HG WF axial length i.e. 63.25 mm (0.25×253). The axial length of the PM rotor section is 75% of the HG PM i.e. 265.73 mm (0.75×354.3) providing the rotor is the PM with surface magnet NdFeB. If the rotor is PM with embedded NdFeB magnets the axial length is 220.2 mm (0.75×293.6). Therefore, two different designs for the final HG is considered:

- Design 1: a HG with surface NdFeB PM rotor, and
- Design 2: a HG with embedded NdFeB PM rotor.

The WF is the same for both designs. The total HG axial length for HG with surface NdFeB PM rotor is 328.98 mm while for the HG PM with embedded PM rotor it is 283.45 mm.

Table 5.23 summarizes the two designs. Note that the HG has a single stator shared between the PM and WF rotor sections. Therefore, the machine power is split between PM and WF by their respective voltage ratio since the stator current is the same for both sections. For both HG Design 1 and Design 2 the permanent magnet material used in the machine is NdFeB. Both designs have the same WF rotor however, manufacturing the PM rotor is different in embedded and surface designs. The HG with embedded magnet PM rotor results in 14% lower axial length which in turn results in lower machine mass. The end winding for the WF rotor is extended by 20 mm beyond the WF axial length. Therefore, the stator axial length needs to be increased to account for the WF end winding extension as seen from Fig. 5.53. The HG axial length including the end winding extension is listed in Table 5.23.

Table 5.23. Specification details for the HG Designs

HG Design 1 with surface NdFeB PM rotor			
Parameter	WF section	PM section	HG
Output power (MW)	0.9	2.7	3.6
RMS phase voltage (kV)	2.7	8.1	10.80
Active axial length (mm)	63.25	265.73	328.98
Axial length with end winding extension (mm)	83.25	256.73	349
Number of turns per stator coil (p.u.)	19		
Coil cross-section (mm ²)	380.64		
Turn cross-section (mm ²)	20.03		
HG Design 2 with embedded NdFeB PM rotor			
Output power (MW)	0.9	2.7	3.6
RMS phase voltage (kV)	2.7	8.1	10.80
Active axial length (mm)	63.25	220.2	283.45
Axial length with end winding extension (mm)	83.25	220.2	304
Number of turns per stator coil (p.u.)	19		
Coil cross-section (mm ²)	380.64		
Turn cross-section (mm ²)	20.03		

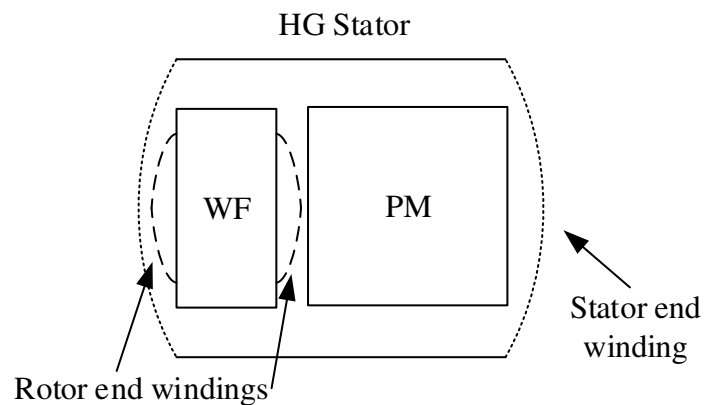


Fig. 5.53. HG rotor and stator end winding extension.

The WF rotor of the final HG is the same as the 9-phase HG WF with a scaled axial length. Therefore, the WF rotor winding resistance is calculated from equations (5.10) -(5.14) and listed in Table 5.24. The HG stator is basically the same as stator for the 9-phase HG WF and HG PM with a scaled axial length. The stator per phase winding resistance is presented in Table 5.25. The stator per-phase inductance is the sum of the inductances due to WF and PM sections. The inductance is a function of machine axial length and square of number of turns [115]:

$$L \propto N^2 l_a \quad (5.28)$$

Therefore, the inductances for the HG WF and HG PM machines are scaled and added to obtain the HG per-phase inductance. Table 5.26 lists the HG equivalent per-phase synchronous inductance.

Table 5.24. HG wound field rotor winding specifications

Item	Design 1 and Design 2
Rotor turn length (mm)	826.5
Rotor turn cross-section area (mm ²)	112
Rotor turn resistance (Ω)	0.000124
Number of rotor coil turns	51
Rotor coil resistance (Ω)	0.0063
Rotor winding interconnection length (mm)	675.44
Rotor winding interconnection resistance (Ω)	0.0001
Rotor resistance (Ω) at 20°C	0.064
Rotor resistance (Ω) at 75°C	0.078

Table 5.25. HG stator winding specifications

Item	Design 1	Design 2
Stator turn length (mm)	2396.07	2306.07
Stator coil cross section (mm ²)	380.64	
Number of stator coil turns	19	
Stator turn cross-section area (mm ²)	20.03	
Turn resistance (Ω)	0.002	0.0019
Coil resistance (Ω)	0.038	0.036
Interconnection length (mm)	919.79	
Interconnection resistance (m Ω)	0.8	
Phase resistance (Ω) at 20°C	0.58	0.55
Phase resistance (Ω) at 75°C	0.70	0.67

Table 5.26. HG per-phase stator equivalent synchronous inductance

Item	Design 1	Design 2
Inductance due to WF rotor (mH)	44.53	
Inductance due to PM rotor with surface NdFeB (mH)	182.38	-
Inductance due to PM rotor with embedded NdFeB (mH)	-	581.26
Total stator per-phase (synchronous) inductance (mH)	226.91	625.79

5.8.2 HG Loss Audit

The losses in the HG is split into stator and rotor copper loss, stator iron (or core) loss and mechanical losses such as windage and friction. The copper losses for the stator and rotor windings are calculated via:

$$\begin{aligned} P_{cu}^s &= 9 R_s I_s^2 \\ P_{cu}^r &= R_r I_r^2 \end{aligned} \quad (5.29)$$

where,

R_s : Stator per phase resistance at 75°C (Ω)

R_r : Rotor winding resistance at 75°C (Ω)

I_s : Stator RMS full-load phase current (A)

I_r : Rotor DC field current at full-load (A)

Since the HG rotational speed and stator structure is the same as the benchmark SG the windage and friction losses for the HG is scaled by the axial length from their original values for the benchmark SG. Table 5.27 details the HG copper, friction and windage losses at nominal speed (600 RPM), full-load RMS stator phase current (120.67 A) and rotor full-field DC current (486.23 A).

Table 5.27. HG copper, friction and windage losses at nominal speed, full-load RMS stator current and rotor full-field DC current

Item	Design 1	Design 2
Stator copper loss (kW)	91.7	87.80
Rotor copper loss (kW)	18.44	
Windage and friction loss (kW)	54.62	47.58

The estimation of iron losses in electric machines have been studied in many research publications [121-131]. However, much of the work is linked back to the early work of Steinmetz [132] on the measurement and characterization of hysteresis loss in lamination steels. Some studies divide the iron losses into three main components namely hysteresis, eddy current and excess losses [131]. Separation of the losses by linear magnetization, rotational magnetization and higher harmonics is also studied among the loss analysis publications [127] while the losses calculated in [125] are proportional to the square of the rate of change of flux-density. Finite element analysis has been used to improve the loss predictions. In this study the iron losses are predicted via polynomial regression which is used to fit the curve of actual iron loss data of the United Laminated steel material (0.47 mm, 26 gauge) [133] at different frequencies. The manufacture's iron loss curves are shown in Fig. 5.54 where the core losses are measured in Watts per kilogram, i.e. loss density (W/kg) at different peak flux-densities and for two frequencies, 50 Hz and 60 Hz.

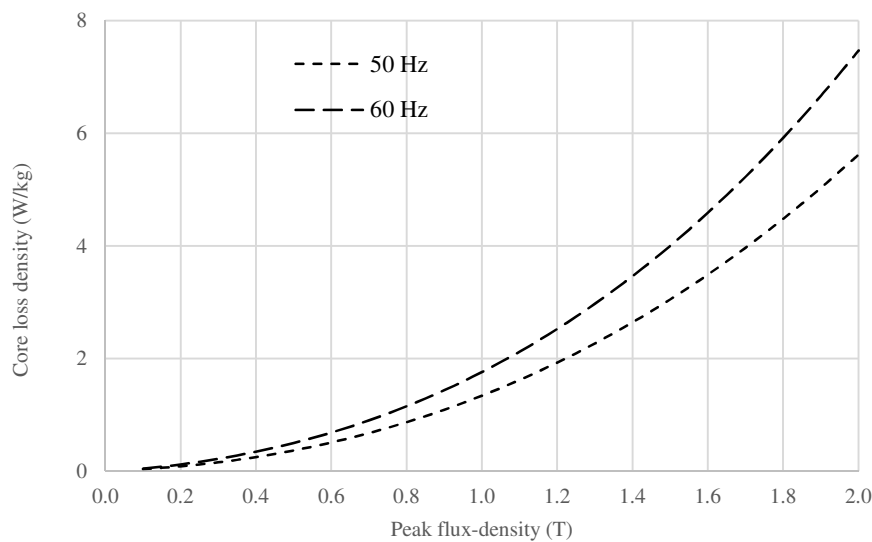


Fig. 5.54. Manufacturer's iron loss data for United Laminated Steel.

A third-order polynomial equation is fit into the manufacturer's iron loss curves:

$$P_{iron}^d = k_e B_m^3 + k_h B_m^2 + k_a B_m + k_d \quad (5.30)$$

Second order polynomial functions are used to estimate the coefficients in the loss formula:

$$\begin{aligned} k_e &= a_{e2} f^2 + a_{e1} f + a_{e0} \\ k_h &= a_{h2} f^2 + a_{h1} f + a_{h0} \\ k_a &= a_{a2} f^2 + a_{a1} f + a_{a0} \\ k_d &= a_{d2} f^2 + a_{d1} f + a_{d0} \end{aligned} \quad (5.31)$$

where,

P_{iron}^d : Core/iron loss density (W/kg)

B_m : Maximum/peak flux-density (T)

k_e, k_h, k_a, k_d : Frequency dependent loss-coefficients (p.u.)

$a_{ei}, a_{hi}, a_{ai}, a_{di}$: Constants of the loss coefficients where $i=0, 1, 2$

The constants of the frequency dependent loss coefficients are listed in Table 5.28 while Fig. 5.55 compares the predicted and manufactures iron loss density. As seen the predicted loss curves fit the datasheet with good agreement. The machine frequency is calculated via:

$$f_s = \frac{P}{120} n_s \quad (5.32)$$

where,

n_s : Rotational speed (RPM)

P : Number of poles

The HG nominal rated rotational speed is 600 RPM hence having 10 poles the machine frequency is 50 Hz.

Table 5.28. Constants of the loss coefficients

Item	Value (p.u.)
a_{e2}	0.0001
a_{e1}	0.0041
a_{e0}	-0.2873
a_{h2}	0.00004
a_{h1}	0.0002
a_{h0}	0.8743
a_{a2}	-0.00001
a_{a1}	0.0259
a_{a0}	-1.0767
a_{d2}	0.000007
a_{d1}	-0.003
a_{d0}	0.148

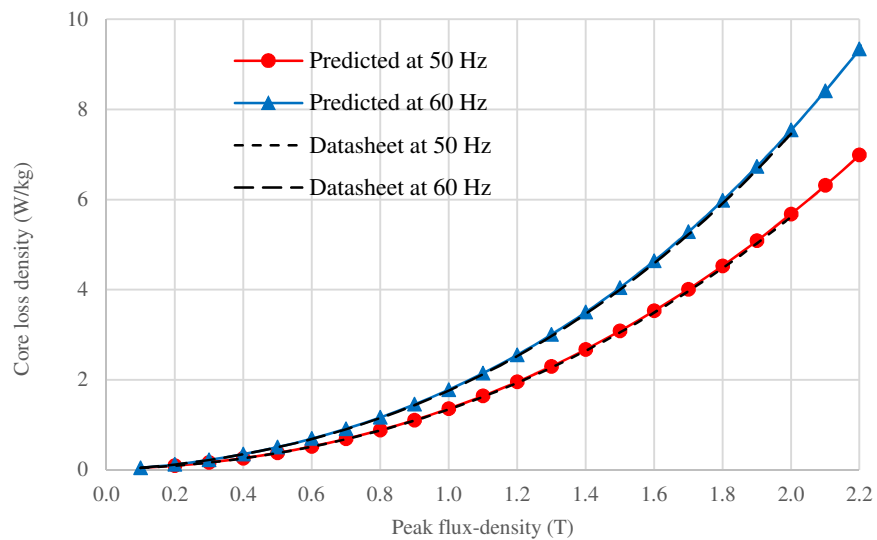


Fig. 5.55. Predicted versus manufacturer's datasheet iron loss density.

The stator tooth and back-iron operate at different flux-density as listed in Table 5.29. Therefore, iron losses for 3 sections namely stator tooth tip, stator tooth body and stator back-iron are calculated separately. The total iron loss is sum of the losses for the 3 sections. The stator core losses for the PM and WF sections are calculated separately due to different flux-densities.

Table 5.29. Flux-density for different sections for the HG

Section	Flux-density (T)		
	Surface NdFeB PM	Embedded NdFeB PM	WF
Stator tooth tip	1.04	1.3	1.77
Stator tooth body	1.27	1.54	2.0
Stator back-iron	1.44	1.81	1.8

The iron losses calculated from equation (5.30) are per kilogram iron. The iron loss for each section is obtained via multiplying the section mass by the loss density. The mass of each section is calculated by using the United Steel Lamination density and multiplying it to the section volume. Table 5.30 shows the volume and mass of different section while the HG iron losses for different sections are presented in Table 5.31. Compared to the fully wound filed machine (i.e. SG) the HG Design 1 results in 3.9% lower mass while the HG Design 2 results in 15.2% higher mass. This is due to the fact that rotor back-iron in the embedded PM design is increased. Note that mass of the shaft, machine casing, end caps, cooling system and other support structures are not included in the analysis. The total losses for the HG for both Design 1 and Design 2 are listed in Table 5.32. For Design 1 the stator and rotor copper losses contribute to 50.8% and 10.2% of the total loss, the windage and friction contribute to 30.3% and the iron loss is 8.7% of the total machine losses. For Design 2 the stator and rotor copper loss are 50.8% and 10.7% of the total loss while windage and friction is 27.5% and iron loss contributes to 11% of the total losses. The HG efficiency at 3.6 MW output for Design 1 and Design 2 is 95.23% and 95.42% respectively while the efficiency of fully wound field SG is 94.98% as seen from Table 5.32.

Table 5.30. Volume and mass audit of the HG designs

Item	Sections					
	Surface NdFeB PM		Embedded NdFeB PM		WF	
	Volume (m ³)	Mass (kg)	Volume (m ³)	Mass (kg)	Volume (m ³)	Mass (kg)
Stator tooth tip	0.0086	65.79	0.0072	55.08	0.0027	20.66
Stator tooth body	0.106	810.9	0.088	673.2	0.033	252.45
Stator back-iron	0.376	2876.4	0.313	2394.45	0.118	902.7
Rotor pole steel	-	-	-	-	0.0625	478.17
Rotor back-iron	0.2649	2026.3	0.628	4805.21	0.0713	545.71
Rotor pole PM	0.06859	524.69	0.0578	442.34	-	-
Stator Copper	0.09452	846.92	0.08985	805.06	0.038	340.9
Rotor copper	-	-	-	-	0.0216	193.54
Total stator steel	0.49	3753.09	0.41	3122.73	0.15	1175.81
Total rotor steel	0.2649	2026.3	0.628	4805.21	0.1338	1032.88
Total copper	0.09452	846.92	0.08985	805.06	0.0595	533.54
Exciter	-	-	-	-	-	285.31
Total mass (tonnes)	6.63		8.73		3.03	
Section	HG					
	Design 1		Design 2			
	Volume (m ³)	Mass (kg)	Volume (m ³)	Mass (kg)		
Stator tooth tip	0.0113	86.45	0.0099	75.74		
Stator tooth body	0.193	1063.35	0.121	925.65		
Stator back-iron	0.494	3779.1	0.431	3297.15		
Rotor pole steel	0.0625	478.17	0.0625	478.17		
Rotor back-iron	0.3362	2572.01	0.06993	5350.92		
Rotor pole PM	0.06859	524.69	0.0578	442.34		
Stator Copper	0.13252	1187.82	0.12785	1145.96		
Rotor copper	0.0216	193.54	0.0216	193.54		
Total stator steel	0.64	4928.9	0.56	4298.54		
Total rotor steel	0.3989	3050.18	0.13243	5829.09		
Total copper	0.15412	1381.36	0.14945	1339.5		
Brushless exciter	-	285.31	-	285.31		
Total mass* (tonnes)	10.17		12.19			

Steel (lamination) density = 7650 kg/m³; Copper density = 8960 kg/m³; PM mass density 7500 kg/m³

*Excluding shaft, machine casing, end caps, cooling system and other support structure

Table 5.31. HG iron losses

Item	Core loss (kW)				
	Surface NdFeB PM	Embedded NdFeB PM	WF	HG Design 1	HG design 2
Stator tooth tip	0.10	0.13	0.09	0.19	0.22
Stator tooth body	1.78	2.19	1.43	3.21	3.62
Stator back-iron	8.16	10.98	4.09	12.25	15.07
Total	10.03	13.30	5.61	15.64	18.91

Table 5.32. HG total losses

Item	Design 1		Design 2		9-phase SG	
	(kW)	(%)	(kW)	(%)	(kW)	(%)
Stator copper	91.7	50.8	87.80	50.8	85.18	44.8
Rotor copper	18.44	10.2	18.44	10.7	26.7	14.8
Windage and friction	54.62	30.3	47.58	27.5	39.6	20.8
Iron	15.64	8.7	18.91	11	38.58	19.6
Total	180.4	100	172.73	100	190.1	100
Efficiency (%)	95.23		95.42		94.98	

5.9 Summary

This Chapter discusses design of the HG. The HG design is based on an industrial 3-phase SG manufactured by Siemens and referred to as benchmark SG. The benchmark machine is rewound for a 9-phase stator and FEA analysis are carried out. It is shown that compared to the 3-phase the 9-phase machine for the same ampere-turn, coil cross-section area and stator copper loss results in 4.2% higher voltage and hence power. Performance of the machine connected to an active power electronic VSC with two control methods, PWM and over-modulated, is evaluated and compared to the case where the machine is connected to a passive rectifier. It is concluded that when a passive rectifier replaces a VSC with PMW or over-modulated control the machine needs to be redesigned for 10% and 42% higher rated power. Three designs for the PM rotor section is investigated; a surface PM rotor with NdFeB magnets, an embedded PM rotor with Ferrite magnet and an embedded PM rotor with NdFeB magnets. It is shown that due to machine geometry the PM rotor with Ferrite magnets is not a suitable option for the machine. The air-gap flux-density for the surface PM rotor is 0.842 T compared to 0.998 T for the WF rotor. However, using the embedded PM rotor the air-gap flux-density is boosted to 1 T. The HG losses are split into stator and rotor copper, windage and friction and iron losses. The benchmark SG windage and friction losses are scaled by the axial length ratio to obtain the values for the HG. The machine copper losses are calculated at rated stator current and full-field rotor current. The HG iron losses are estimated using polynomial equation fitted to the manufacturer loss datasheet. The iron losses are calculated for stator tooth tip, stator tooth body and back iron separately and added up to obtain the total iron losses. For Design 1 the stator and rotor copper losses contribute to 50.8% and 10.2% of the total loss, the windage and friction contribute to 30.3% and the iron loss is 8.7% of the total machine losses. For Design 2 the stator and rotor copper loss are 50.8% and 10.7% of the total loss while windage and friction is 27.5% and iron loss contributes to 11% of the total losses. The HG efficiency with 3600 kW output for Design 1 and Design 2 is 95.23% and 95.42% respectively.

Chapter 6

HG High Voltage Insulation Systems

6.1 Introduction

The proposed wind generation scheme in Chapter 3 uses a 9-phase HG with 38.1 kV RMS phase voltage. However, design of the HG in Chapter 5 was based on a SG with 6.35 kV RMS phase voltage (11 kV RMS line-to-line). Therefore, the HG windings specified in Chapter 3 need to be redesigned to accommodate a nominal phase RMS voltage of 38.1 kV. The first part of this Chapter considers system analysis of the proposed wind generation scheme using a HG with a phase RMS voltage of 6.35 kV, as previously designed from the benchmark SG, and then compares this machine with the results obtained at 38.1 kV in Chapter 3. The benchmark SG, an example of high voltage machines in industry, has a phase voltage of 6.35 kV hence the system analysis at the machine voltage of 6.35 kV is carried out to verify the system performance, benefits and gains at a voltage level already practiced by industry. The rest of this Chapter discusses insulation system design for the HG windings suitable for a 38.1 kV RMS phase voltage machine. The machine initial 6.35 kV voltage is scaled in steps to obtain the targeted 38.1 kV and appropriate winding insulations for each design step is proposed. Various industry practice for the HV windings are introduced and insulation systems for different parts of a winding i.e. turn, strand and ground insulations are addressed in this Chapter. Semiconductor and stress grading insulations are also investigated. The voltage stress between different insulations and the grounded machine core is modeled using lumped capacitors to illustrate the voltage withstand strength of the insulations.

6.2 Analysis of the Proposed HV System Employing a 6.35 kV HG

For an RMS phase voltage of 6.35 kV (peak voltage of 8.98 kV) the rectified DC voltage at the output of the 9-phase HG calculated from equation (3.17) is 17.6 kVDC. This voltage is 1/6th of the DC voltage for the original proposed system i.e. 105.6 kVDC. The voltage ratio is indeed the ratio of the RMS phase voltages ($6.35/38.1=1/6$). For a 3.6 MW nominal turbine power, the DC current at the rectifier output is 204.55 A i.e. 6 times the currents in the original system. The DC voltage for the transmission cable connecting the off-shore to the on-shore substations is the same as the original system i.e. 420 kV. Therefore, the DC/DC converter step-up ratio is increased to 23.86 ($420/17.6$). Assuming the same current densities for the cables as in the Walney system discussed in Chapter 3, the cable cross-sections and resistances are respectively 6 and 1/6 times than their respective original values. Therefore, the resistances are reduced by a factor of 1/6 except for the transmission cable resistance. Table 6.1 lists the related cable cross-sections, current densities and resistances for the proposed system operating with a 6.35 kV HG. The results of the proposed system analysis at full-load and with a 6.35 kV HG is presented in Table 6.2.

Table 6.1. Proposed system cable specifications with a 6.35 kV HG

Description	Tower	Circuit 2		Off-shore substation to on-shore
		Inter-array between turbines	Inter-array to off-shore substation	
Cable length (km)	0.0835	0.750	0.458	44.4
Material	Copper			
Copper resistivity ($\mu\Omega\text{m}$)	0.0172			
Rated voltage (kVDC)	20	20	20	425
Current density (A/mm^2)	1.58	1.58	0.6	1.2
Cross-section area (mm^2)	129.48	517.86	1705.2	362.31
DC cables resistance (Ω)	0.022	0.05	0.0092	4.2

Table 6.2. Proposed system full-load analysis with a 6.35 kV HG

Turbine					
Turbine No.	1	2	3	4	5
HG phase voltage (kV)	6.35	6.35	6.34	6.33	6.33
HG DC voltage (kV)	17.60	17.59	17.57	17.54	17.54
HG DC current output (A)	197.41	197.57	197.79	198.13	198.13
DC voltage at the tower base, kV	17.60	17.59	17.57	17.54	17.50
Interconnection and Transmission					
Input DC voltage at the off-shore substation (kV)				17.49	
Input DC current, Circuit 2 at off-shore sub. (A)				989.04	
Output DC voltage at the off-shore sub. (kV)				417.27	
Output DC current at the off-shore sub. (A)				416.57	
Input DC voltage at the on-shore sub. (kV)				415.52	
Input DC current at the on-shore sub. (A)				416.57	
Power and losses in the nacelle and tower					
Turbine power (kW)				3,600	
HG output power (kW)				3,492	
Rectifier output power (kW)				3,474.54	
HG efficiency (%) and losses (kW)				97	108
Rectifier efficiency (%) and losses (kW)				99.5	17.46
Tower cable power loss (kW)				0.86	
Turbine link cable					
From--to		1 to 2	2 to 3	3 to 4	4 to 5
Inter-array cable loss (kW)		1.95	7.80	17.57	31.28
Cable loss, Circuit 2 to the off-shore substation (kW)				9.00	
Input power and losses at off-shore sub. from Circuit 2					
Power (kW)	17,300.80		Losses (kW)	699.20	
Input power and losses at off-shore sub. from Circuits 1-6					
Power (kW)	176,468.17		Losses (kW)	7,131.83	
DC/DC converters efficiency at off-shore sub. (%)				98.5	
Loss at off-shore substation (kW)				2647.02	
Cable losses, Off-shore to on-shore sub. (kW)				728.83	
Total power at on-shore substation (kW)				173,092.31	
Total losses at on-shore substation (kW)				10,507.69	
Total system efficiency (%)				94.28	

Table 6.3 presents a comparison between the two systems i.e. proposed system with a 6.35 kV HG and with a 38.1 kV HG at full-load. It is seen that the total system efficiency is similar for both systems resulting in similar benefits and gains in the new system. For the 38.1 kV HG the mass is increased by 7.5% due to increase in the machine outer diameter, this will be discussed in detail at the end of this Chapter after insulation considerations. However, the total mass for the proposed system with 6.35 kV HG is 40.9% higher than the system with 38.1 kV HG.

Table 6.3. Comparison between system with a 6.35 kV HG and with a 38.1 kV HG at full-load

Items	Proposed system	
	6.35 kV HG	38.1 kV HG
Number of HG phases	9	
HG RMS phase voltage (kV)	6.35	38.1
Rectified DC voltage (kVDC)	17.6	105.6
Turbine power (kW)	3,600	
System total losses (kW)	10,507.69	9,894.10
Total system efficiency (%)	94.28	94.61
DC/DC step-up ratio (p.u.)	23.86	4
Active power conversion mass (Tonnes)		
HG	24.2	26.02
Tower Cable	0.18	0.03
Inter-array cables' between turbines	72	12
Cables from Circuits to off-shore substation	59.34	9.89
Transmission cable	215.33	
Total cable	346.85	237.25
Total system mass	371.05	263.27

These results form an interesting conclusion. One of the objectives of the proposed HV HG wind generation scheme is to remove active power electronic converters from the turbine towers. Effectively, the individual tower power electronic converters are rationalized into larger DC/DC converters that can be located at the central off-shore substation. These HV DC/DC converters are still the subject of research and development. However, it is assumed here that they will be realized in due course as a natural progression of HVDC sub-systems. Certainly, for HVDC transmission, high step-up, step-down ratio DC/DC converters are a technical requirement for future systems. Consequently, the results presented in Tables 6.2 and 6.3 illustrate the HV HG system concept could be technically realized at an accepted industry standard voltage level (11 kV line-to-line), albeit with higher interconnecting cable mass and higher step-up ratio for off-shore DC/DC converter. This being accepted, the challenge herein is to therefore investigate the potential design changes necessary to increase operating voltages from 11 kV line-to-line, or 6.35 kV phase up to 38.1 kV phase. Note, phase voltages are quoted here since there are 4 different line-to-line voltages specified for a 9-phase system.

6.3 HV Winding Types

Fig. 6.1 schematically shows a 3-phase HG stator winding connections. Each phase is connected to the neutral point in one end and to the machine terminals at the other. The neutral point is solidly connected to the surrounding ground along with the stator core. This provides a level of equipment protection as well as referencing the winding coils to ground and the stator core, which is also grounded.

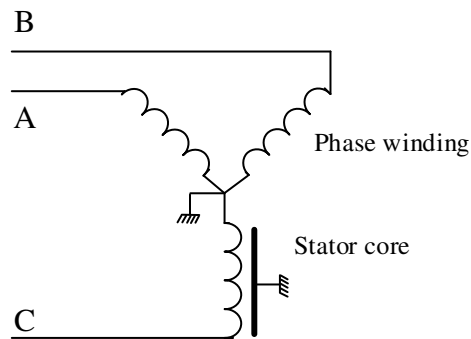


Fig. 6.1. Stator winding connections.

The winding insulations becomes more significant as machine nominal voltage increases. Insulation does not contribute to the machine torque production [134] however, it is required to prevent short circuits between the copper conductors and also between conductors and ground. Insulations also provide mechanical strength and help protect conductors from damage in the process of coil insertion into the stator slots and also prevent the coils from movements during operation. Main types of stator windings are [135]:

- Random-wound coils
- Form-wound coils
- Roebel bar coils

In random-wound coils the insulated conductors are usually round cross-section wires that are randomly and continuously wound to form a multi-turn coil. In this type of winding it

does not matter if the turn with the highest voltage is placed adjacent to a turn with the lowest voltage. This type of winding is not used for high voltage applications. Random-wound stators could have coils wound beforehand and inserted into slots or wound directly into the coils around stator teeth. Fig. 6.2 shows a random-wound stator winding for a low voltage (300 V) machine.

Form-wound coils consist of individually insulated copper wires or rectangular bars that are wound and pre-formed to a fixed shape for subsequent insertion into the machine stator or wound rotor. The rectangular shape allows better packing factor for the slots. In form-wound coils each turn consists of a few to several copper strands. Fig. 6.3 shows a form-wound stator coil.

Form-wound coils are used for higher voltage machines. Unlike random-wound coils, care has to be taken when designing form-wound coils such that each turn is next to a turn with least voltage difference. This results in minimized insulation between turns.

Roebel bar is another windings scheme, as shown in Fig. 6.4, that is sometimes used for high voltage and high power machines such as turbo generators over 50 MW [135]. The Roebel bar winding implementation transposes the winding turns to minimize parasitic winding effects such as eddy current and proximity effects, cross-slot leakage, un-balanced turn-voltage etc. In this study, form-wound coils are considered for the HV HG windings hence other types of windings will not be studied.

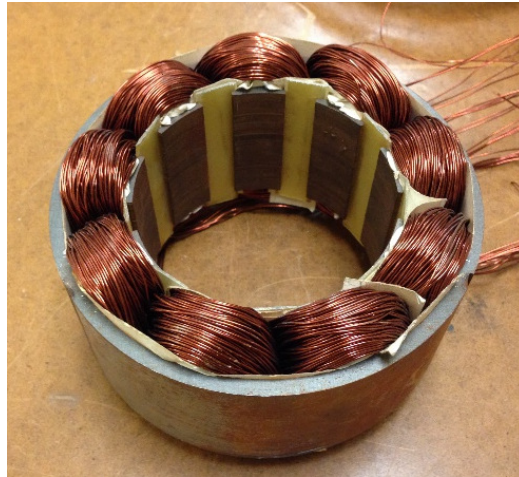


Fig. 6.2. A Random-wound stator.



Fig. 6.3. A form-wound coil.



Fig. 6.4. A typical Roebel bar winding (Photo courtesy Partzsch Group) [136].

6.4 Insulation Systems

In order to have a sensible design for the HG insulation systems that is comparable and verifiable with industry practice HV windings, the 11 kV insulations for the benchmark SG (3-phase HG WF) are used as a design base, against which new insulations systems are compared. Fig. 6.5 shows the cross-section of a stator slot for the 3-phase benchmark SG. The slot has two layers each representing the cross-section of one coil side. The two coils are either from the same phase or different phases. Therefore, the voltage difference between the two layers is different depending on the coil voltages. Each coil has 4 turns, each turn of which is referred to as conductor; each conductor has 6 strands that are transposed from coil to coil and connected at the machine terminals in parallel. There is no or may be small voltage difference between the strands therefore they require minimum insulation.

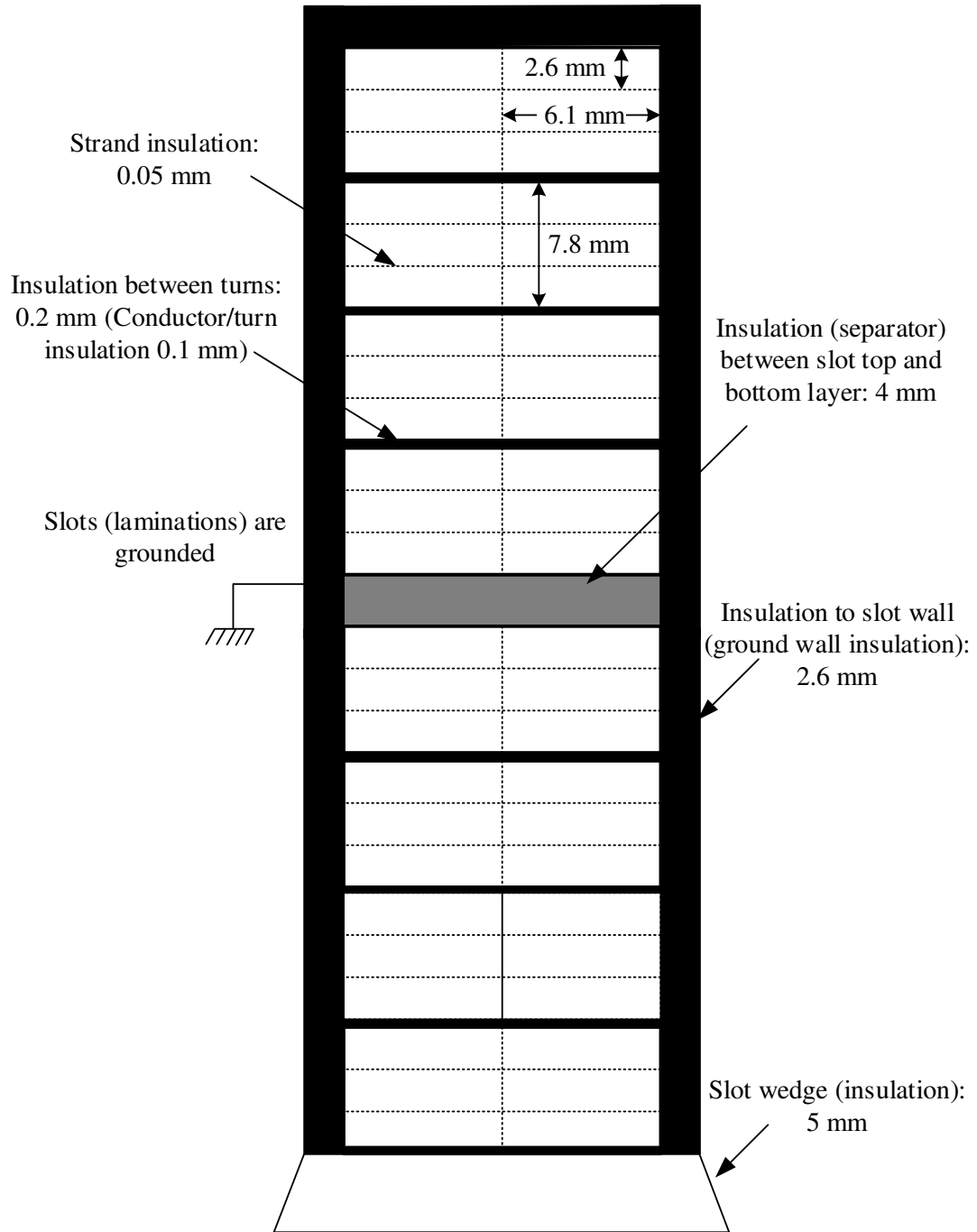


Fig. 6.5. Three-phase benchmark SG or HG WF slot insulation system.

Strands have an insulation thickness of 0.05 mm while conductor insulation thickness is 0.1 mm. Top and bottom coils are separated from each other in the slot by a 4 mm thick insulation. The slot has a wedge made of insulating material of 5 mm thickness. The slot wedge helps to keep the coils tightly placed in the slot and prevents their movements. The laminations are grounded and between the slot wall and coils there is an insulation of 2.6 mm thickness, this is referred to as ground wall insulation. Main insulation components in a HV winding include [135]:

- Strand insulation
- Turn insulation
- Groundwall insulation
- Semiconductive slot insulation
- Voltage stress grading insulation

6.4.1 Strand, Turn and Groundwall Insulation

Each conductor in the 3-phase HG WF has 6 strands that are formed and electrically connected in parallel to form a single turn. Splitting a big conductor cross-section into smaller strand cross-sections has three main advantages:

- Mechanical and manufacturing ease
- Reduction of eddy current effects and losses, and hence
- Reduction of copper losses

Mechanically, a conductor with large cross-section is difficult to bend and insert into slots. Forming a conductor from smaller strands facilitates bending and manufacturing. Moreover, by reducing conductor cross-section area to smaller strands the skin effect is reduced [135] providing the conductor strands are transposed when interconnecting the individual phase coil. Unlike DC current that is uniformly distributed in the conductor cross-section area, AC current tends to flow in the periphery of a conductor resulting in a

smaller effective cross-section which results in a perceived higher AC resistance than the conductor DC resistance. The higher the conductor resistance the higher the copper losses. By splitting a conductor into smaller cross-sections and transposing at inter-coil connections, the skin effect is reduced and hence more of the available conductor cross-section is used. The 3-phase HG WF is rated at 11 kV line-to-line RMS voltage (6.35 kV RMS phase voltage). For each phase there are 45 coils therefore the individual coil voltage is 140 V. Each coil has 4 turns therefore, the turn voltage is 35 V. Each turn is made up of 6 parallel strands hence the voltage across each strand is the same as turn voltage, as shown in Fig. 6.6. Table 6.4 summarizes coil, turn and strand voltages.

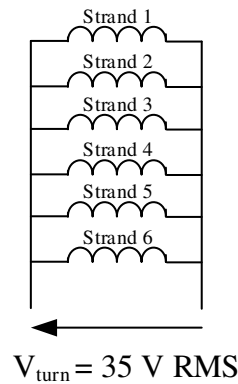


Fig. 6.6. 3-phase HG WF strand voltage.

Table 6.4. Turn, coil and strand voltages

Description	RMS	Peak
Line-to-line voltage (kV)	11	15.56
Phase-to-ground voltage (kV)	6.35	8.98
Voltage across each coil (V)	140	200
Voltage across each turn (V)	35	50
Voltage across each strand in each turn (V)	35	50

Turn insulations prevent short circuits between turns that are in contact. In order to minimize the turn insulations, each turn in a coil is placed next to the turn with smallest voltage difference. Turn insulations are normally thicker than strand insulations since they have to withstand higher voltages. However, some manufacturers combine turn and strand insulations to facilitate manufacturing process [135]. The turn voltage build-up for the 3-phase HG WF is illustrated in Fig. 6.7(a).

Once the turns are placed together and a coil is formed, a layer of insulation referred to as groundwall insulation, usually a tape, is applied on the coil surface. The groundwall insulation protects coils from contact to the grounded laminations. It also holds the turns tightly together and prevents them from moving due to the forces in the machine acting on conductors. For random-wound windings the turn insulation also acts as groundwall insulation. Therefore, the turn insulation in random-wound coils is designed to withstand phase-to-phase voltages. However, for form-wound coils in high voltage machines, groundwall insulation is normally different from turn insulation. The coils depending on their position in a phase experience different voltages with respect to the grounded laminations. The first coil in a phase, i.e. the coil that is connected to the ground, referred to as neutral-end coil, is subject to zero voltage and as the coils are connected in series their voltage to ground increases. Therefore, the last coil in a phase, referred to as the terminal-end coil is subject to full phase-to-ground voltage. Therefore, the groundwall insulations need to protect the coils from voltages as high as phase voltage against the grounded laminations. Although different coils experience different voltages, the groundwall insulations are normally designed for the same insulation thickness for all coils. Fig. 6.7(b) shows the phase voltage build-up for the benchmark SG (or 3-phase HG WF).

A design for the HV windings for the ABB Powerformer was proposed where coils have different insulation thickness depending on their voltage and hence the slot size varies as the insulation thickness increases [137]. The coil insulation has to be applied coil-by-coil as the machine is wound, making the winding process somewhat involved. Fig. 6.8 shows the machine stator slots, highlighting the variation in slot shape to accommodate the “cable” winding [137].

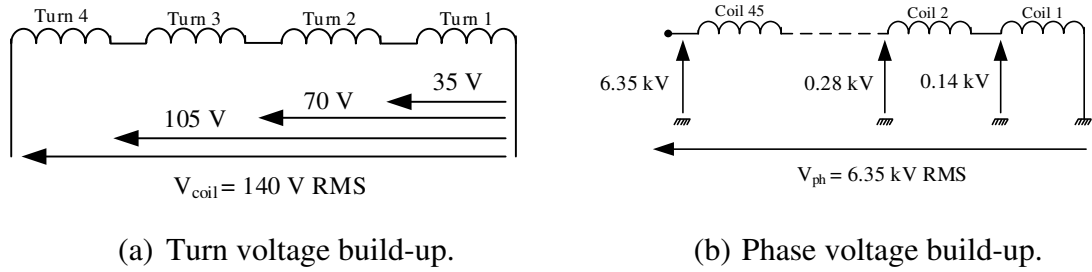
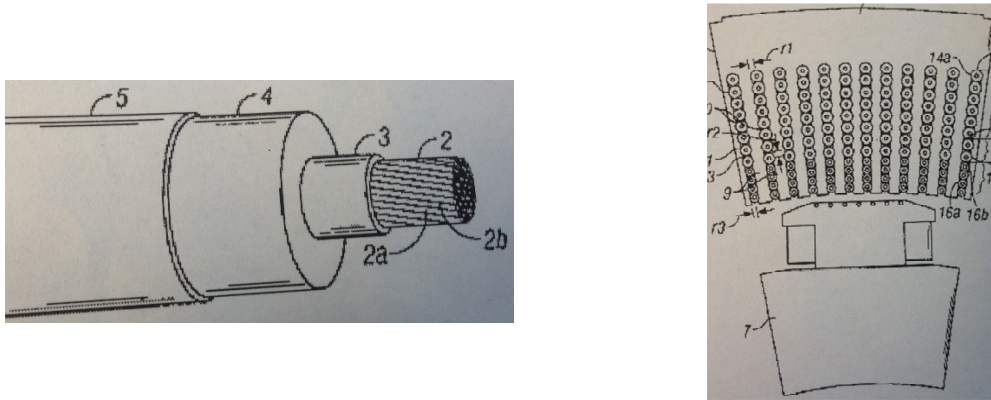
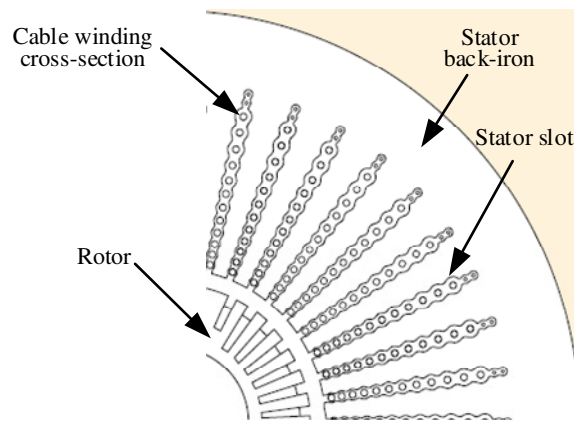


Fig. 6.7. 3-phase benchmark SG (or HG WF) turn and phase voltages.



(a) Cable structure. (b) Slot/tooth cross-section.



(c) Machine cross-section

Fig. 6.8. AB Powerformer stator slots [137].

Air pockets (also known as voids) can occur in the insulation system during the manufacturing process and when the machine is in service. If air pockets are subject to high voltages, they break down and a spark or discharge is initiated. Repeated electric breakdowns, referred to as partial discharge (PD), leave a hole in the insulation system hence the copper becomes exposed to the grounded laminations or other conductors and a short circuit ultimately occurs. The electric breakdown depends on the strength of the electric field, also referred to as electric stress or voltage gradient. The electric field between two surfaces displaced at a distance of d and with a voltage difference of V is [135]:

$$E = \frac{V}{d} \quad (\text{kV/mm}) \quad (6.1)$$

If the voltage across two surfaces is increased above break-down point conduction occurs. In such case the material between the surfaces (which could be air or an insulation material) is ionized and conducts current which ultimately creates a short circuit. For air the break-down strength at room temperature, low humidity and one atmosphere is 3 kV/mm [135]. In order to evaluate voltage across insulations, each section of insulation is modeled as a capacitor circuit. The capacitance between two surfaces is:

$$C = \frac{\varepsilon A}{d} \quad (\mu\text{F}) \quad (6.2)$$

$$\varepsilon = \varepsilon_r \varepsilon_0$$

where,

ε : Insulating material permittivity (F/m)

ε_r : Insulating material relative permittivity

ε_0 : Air permittivity (8.854×10^{-12} F/m)

A lumped capacitance circuit model for the capacitors between copper strands to the grounded stator core for the HG winding is presented in Fig. 6.9. There are three sections between the copper strand and grounded stator core:

- (i) Strand insulation modelled as C_s ,
- (ii) Conductor insulation modelled as C_c , and
- (iii) Groundwall insulation modelled as C_g .

Using the insulation thicknesses for the 3-phase HG WF shown in Fig. 6.5 and equation (6.2) the capacitors parametric values are calculated and detailed in Table 6.5.

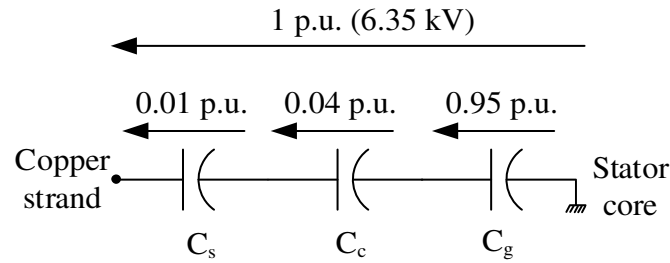


Fig. 6.9. Lumped capacitance circuit model between strands and grounded stator core.

Table 6.5. Strand-to-groundwall capacitors parametric values

Symbol	Description	Parametric value
C_s	Strand insulation capacitor	$C_s = \frac{\epsilon A}{0.05} = 20 \epsilon A$
C_c	Conductor insulation capacitor	$C_c = \frac{\epsilon A}{0.1} = 10 \epsilon A$
C_g	Groundwall insulation capacitor	$C_g = \frac{\epsilon A}{2.6} = 0.38 \epsilon A$

As discussed, stands of the terminal-end coil are subject to the highest voltage i.e. 6.35 kV phase RMS voltage noted as 1 p.u. voltage. This voltage is divided between capacitors based on their capacitance as shown in Fig. 6.9. It is seen that the voltage across the groundwall insulation is highest due to its lowest capacitance. In order to study insulation failure, it is assumed there is an air pocket with 0.3 mm thickness in the groundwall insulation. The air pocket is modelled as a capacitor, C_{air} , hence the circuit model from the groundwall to the grounded insulation is shown in Fig. 6.10.

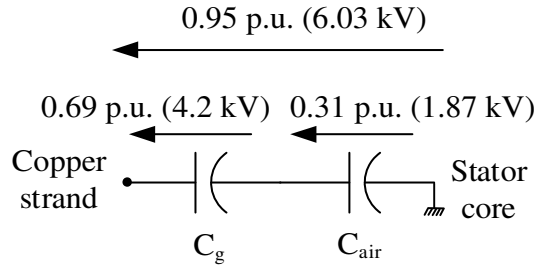


Fig. 6.10. Groundwall-to-grounded stator core model with an air pocket.

Groundwall insulating material used for the machine has a permittivity of four times larger than air [135], therefore:

$$C_{air} = \frac{A}{d_{air}} = \frac{A}{0.3} = 3.33 A$$

$$C_g = \frac{4A}{d_g} = \frac{4A}{2.6} = 1.54 A$$

The total voltage between the groundwall insulation and grounded stator core is 6.03 kV (0.95 p.u.) as calculated in Fig. 6.9. This voltage is split between the groundwall insulation and air pocket based on their capacitance. Therefore, the voltage across the air pocket is 1.87 kV as shown in Fig. 6.10. The electric field across the air pocket is:

$$E_{air} = \frac{1.87}{0.3} = 6.23 \text{ kV/mm}$$

Air breaks down at 3 kV/mm [135], therefore the air pocket breaks down and a discharge occurs in the groundwall insulation. In order to prevent this, air pockets are avoided during the manufacturing process by careful procedures in vacuum pressure impregnation (VPI) of the machine stator with insulating resins post winding. The HG stator has two coils in each slot. Fig. 6.11 shows a capacitor circuit model for the insulation between the two coils. Insulations between the two coils include strand, conductor and groundwall insulation. The separator between the two coils in the slot shown in Fig. 6.5 is modeled as C_{sep} , where

$$C_{sep} = \frac{\epsilon A}{4} = 0.25 \epsilon A.$$

The voltage difference between the two coils is as high as the line-to-line voltage if terminal-end coils of two different phases are placed in one slot. The voltages across insulations are split based on their capacitance. As shown in Fig. 6.11 the highest voltage appears across the slot separator. Fig. 6.12 illustrates a circuit model for a coil along the axial length of the HG. Each capacitor in Fig. 6.12 is an equivalent capacitor ($C_{eqs} = 0.36 \epsilon A$) for three series capacitors C_s , C_c and C_g . The winding axial length has been divided into four arbitrary sections each with the same resistance. The voltage profile at each point along machine winding axial length is shown in Fig. 6.12, as seen the terminal-end has the highest voltage.

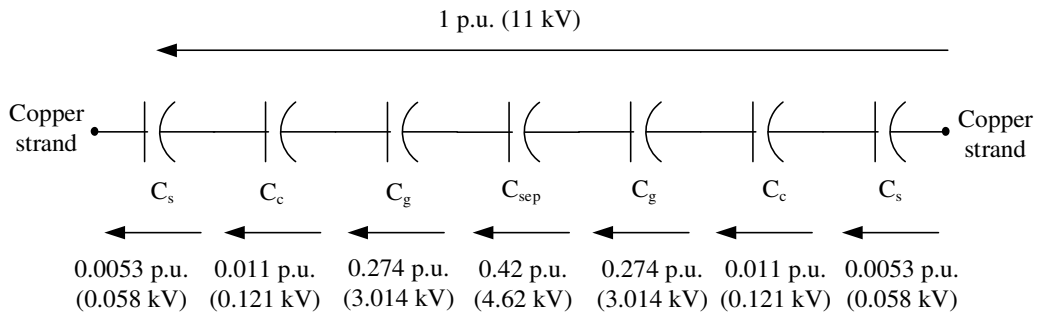


Fig. 6.11. Coil-to-coil capacitor core model.

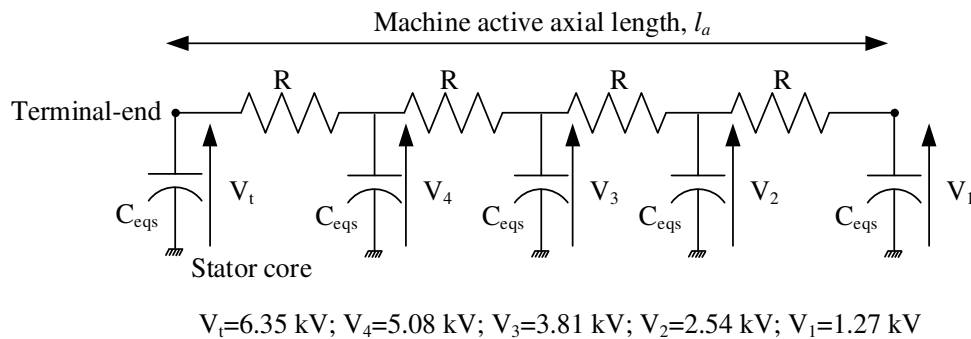


Fig. 6.12. Coil capacitor model along the HG axial length.

6.4.2 Semiconductive Slot and Voltage Stress Grading Insulation

For the 3-phase HG WF the copper packing factor is 0.457 p.u. Note that there are other definitions for copper packing factor, hence copper packing factor is defined here as total slot copper area divided by total slot area. The total slot area is always larger than the total winding cross-sectional area including the coil insulations to facilitate practical placement of the coils. Therefore, there is an air gap between coil surface and the grounded slot. At high voltages a PD can occur in this air gap for the same reason that a PD occurs in an air pocket in the insulation if not properly insulated. In order to fill the air gaps some manufacturers use varnish/resin applied via VPI [135], [138-141]. However, if the voltage across the air gap exceeds 3 kV/mm the air breaks down and a PD occurs. In order to prevent a PD between coil surface and grounded slot a semiconductive coating is applied on the coil groundwall insulation. This is also known as semiconductive slot coating or sometimes called conductive coating/tape/material [135], [142-143]. The semiconductive coating has a low resistance and it is at ground voltage since it is in contact with the grounded slots. Semiconductive coating essentially puts a conductive layer in the air gap, hence a low electric field is created and no PD occurs. A circuit model for the semiconductive resistance, R_{semi} , in parallel with the air gap capacitor is shown in Fig. 6.13.

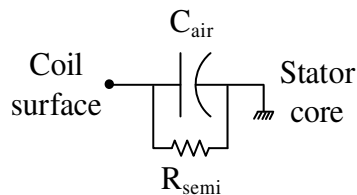


Fig. 6.13. Semiconductive resistance and air gap capacitor model.

Semiconductive coating is not generally used if the machine is rated at voltages below 6 kV [135] because the electric stress for such voltages will not exceed the 3 kV/mm limit. Higher conductivity coatings are not usually used because it short circuits the laminations and will result in eddy currents [135], [142]. Semiconductive coating is usually extended

a few 10's of millimeters from the end of the slot [144] to neglect any end effects. Note that semiconductive coating should not be extended close to the end of the coil because the grounded surface will be too close to the connection of the coil to the next coil. Also, if the end winding is grounded by semiconductive tape, chances of a PD increases in the air pockets in the end winding as result of high electric field due to bringing the ground close to air pocket. Semiconductive insulations come usually as paint or tapes. Semiconductive slot insulations and groundwall insulation for the 3-phase HG WF stator coil are shown in Fig. 6.14.

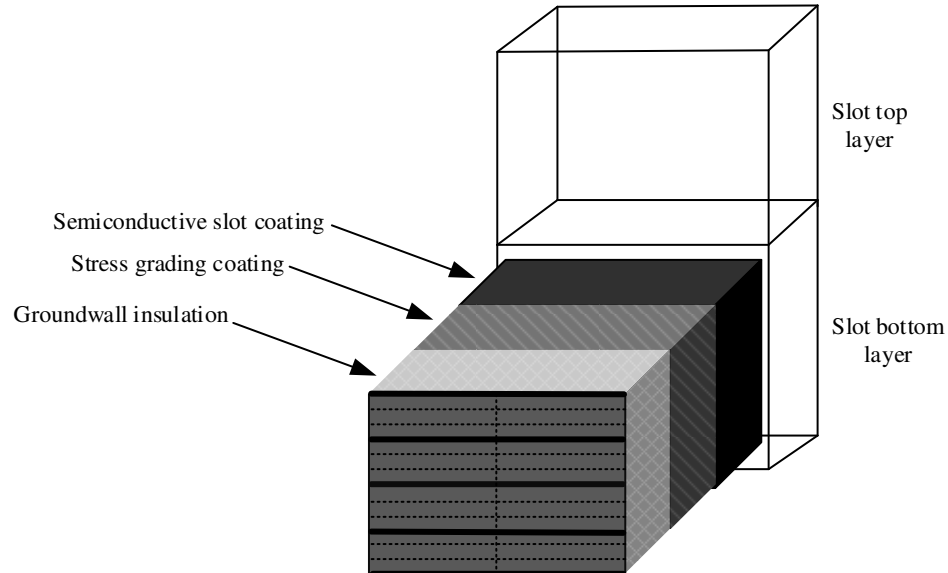


Fig. 6.14. Semiconductive, stress grading and groundwall insulations for the 3-phase HG WF stator coil.

The semiconductive coating cannot end abruptly since the voltage difference between the coils surface and grounded semiconductive tape creates an electric field that could exceed 3 kV/mm and starts a PD [142-143]. Therefore, the end of semiconductive coatings are either terminated [144] or in most cases a voltage stress grading material is continued to cover the end winding [142-143], [145-147]. The voltage stress grading coating is started at the end of the semiconductive slot coating and often it overlaps with the semiconducting

slot coating. The stress grading coating is used to create a smooth transition from the grounded semiconductive slot coating to the high voltage surface of the coil. The voltage stress grading material has lower conductivity than the semiconductive slot coatings [143]. Silicon carbide is a common material that is used as stress grading material [135]. The stress grading insulation comes usually as tapes. The stress grading insulation for the 3-phase HG WF stator coil is shown in Fig. 6.14.

6.4.3 Transposition

As discussed previously, turns in a coil are often transposed to reduce eddy current losses and also gain mechanical strength [147-148]. The stator cross-section for the coil start and coil end is shown in Fig. 6.15. Turn 1 is at the bottom of the start-side of the coil but is transposed to the top at the end-side. Turn 4 at the coil start-side is the bottom turn, while Turn 4' is transposed to the end-side. Other turns in the coil also change places at the coil end-side. This procedure is done for all the coils in each phase. In order to change the location of turns the coil end winding is twisted, referred to as transposition via knuckle, as shown in Fig. 6.16.

In the transposition, turns with lowest voltage difference are placed next to each other. For instance, if the turn voltage is 0.25 p.u. (coil voltage 1 p.u.) and if Turn 4 is next to Turn 1 the voltage between them is 0.75 p.u. but if turns are arranged as shown in Fig. 6.15, the voltage between each consecutive turn is 0.25 p.u., and would hence require thinner insulation. Sometimes supporting materials are used to mechanically support end windings for twisting actions, for instance a cloth tape as shown in Fig. 6.16. The above discussed is a basic transposition via knuckle to reduce the eddy current loss and circulating current loss of the conductor. To further reduce such losses, there are other more complicated transposition [144] which are not considered here since they are out of scope of this study.

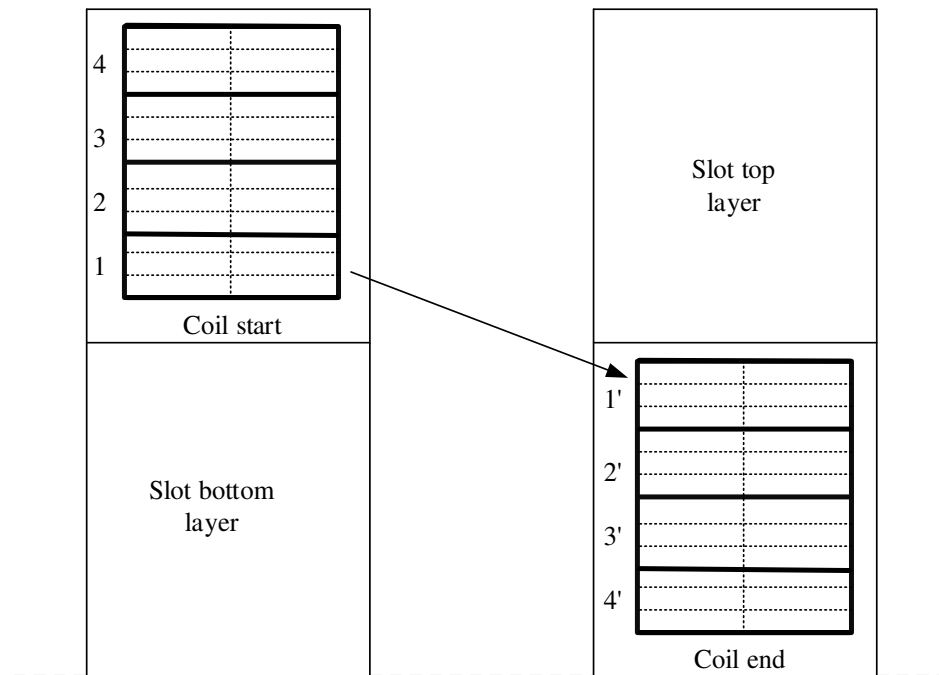


Fig. 6.15. Coil transposition.

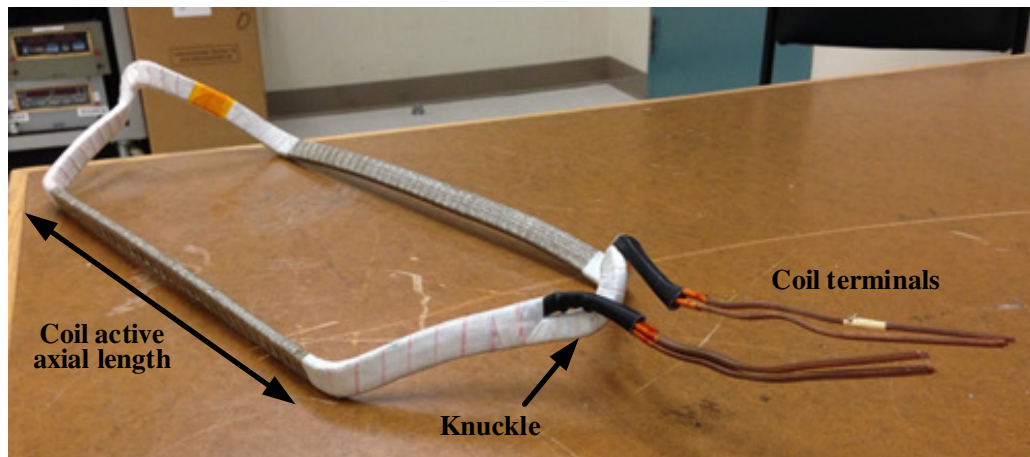


Fig. 6.16. Coil transposition via knuckle.

6.5 HG Insulation

The 9-phase HG stator structure is the same as the benchmark 3-phase SG. However, 9-phase winding has 15 coils per phase as compared to 45 coils per phase for the 3-phase winding. The total slot copper cross-section for the 9-phase HG winding is the same as for in the 3-phase SG. However, the number of turns per coil has increased to 19, reducing the turn voltage and cross-section area. Table 6.6 shows the RMS phase, coil, turn and strand voltage for the 3-phase SG and the 9-phase HG. Fig. 6.17 illustrates the coil cross-section for 3-phase SG and 9-phase HG. The strands are shown as dotted lines while solid lines define turns. Each turn in the 9-phase system has 2 strands compared to 6 strands per turn for the 3-phase system. The strands and conductors in the 9-phase coil have the same width but reduced height. However, the voltage across strands and conductors in the 9-phase system is reduced by a factor of 0.66 ($=0.023/0.035$). Therefore, assuming that the strand and conductor insulation thickness varies linearly with voltage, the 9-phase strand and conductor insulation is 0.033 mm and 0.066 mm respectively. However, it is assumed that the groundwall insulation thickness does not vary with the voltage hence at higher phase voltages a better groundwall insulation material is used.

Table 6.6. RMS phase, coil, turn and strand voltage

Description	3- phase SG	9-phase HG
No. of coils	45	15
No. of turns	4	19
No. of strands per turn	6	2
No. of strands per coil	24	38
Phase voltage (kV)	6.35	6.6
Coil voltage (kV)	0.14	0.44
Conductor/turn voltage (kV)	0.035	0.023
Strand voltage (kV)	0.035	0.023

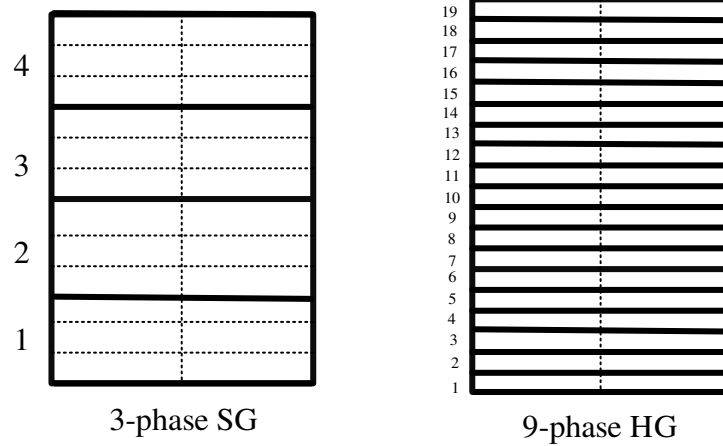


Fig. 6.17. Coil cross-section for 3-phase SG and 9-phase HG.

For the benchmark SG the strand copper height and width excluding insulations is 2.6 mm and 6.1 mm respectively, i.e. strand cross-section area is 15.85 mm^2 . There are 24 strands per coil hence the coil copper cross-section is 380.64 mm where the coil copper width is 12.2 mm (2 strands) and coil copper height is 31.2 mm (12 strands). Having the same coil copper width and hence height for the HG and 19 conductors/turns per coil, the conductor copper height is 1.64 mm. The HG conductor copper and coil copper width is the same as the benchmark SG coils. However, since the insulation thickness for strands and conductors is changed the total coil dimension is changed. Table 6.7 lists coil, conductor and strand specifications for 9-phase and 3-phase coils. Compared to the benchmark SG the HG total coil height is increased by 4.58% but its width is decreased by 0.39% the total coil cross-section is however increased by 4.17%.

In order to minimize the voltage difference between consecutive turns (conductors), they are placed on top of each other. In the arrangement shown in Fig. 6.17 the voltage difference between two adjacent turns in the HG coil is 0.023 kV. However, if turn 6 was to be placed next to turn 1 the voltage difference would be 0.115 kV and thicker conductor insulation would be required. Therefore, in designing the high voltage coils, proper arrangement of turns needs to be taken into account.

Table 6.7. Coil, turn and strands for 9-phase HG with phase RMS voltage 6.6 kV

Description	3-phase benchmark SG	9-phase HG
Strand insulation thickness (mm)	0.05	0.033
Conductor insulation thickness (mm)	0.1	0.066
Strand height excluding insulation (mm)	2.6	1.64
Strand width excluding insulation (mm)	6.1	6.1
Coil copper cross-section (mm ²)	380.64	
Strand height including insulation (mm)	2.7	1.71
Strand width including insulation (mm)	6.2	6.2
Conductor height including insulation (mm)	8.3	1.84
Conductor width including insulation (mm)	12.6	12.53
Groundwall insulation thickness (mm)	2.6	
Coil height including insulation (mm)	38.4	40.16
Coil width including insulation (mm)	17.8	17.73
Total coil cross-section including insulation (mm)	683.52	712.04

The RMS phase voltage of the HG is 6.6 kV whereas the proposed wind generation scheme requires a HG with RMS phase voltage of 38.1 kV. Table 6.8 lists steps in which the machine voltage is increased from its initial 6.6 kV to obtain the desired voltage. In the first step the initial 6.6 kV voltage is doubled i.e. 13.2 kV. Therefore, with the same number of coils, i.e. 15 the coil voltage is doubled, i.e. 0.88 kV from its initial 0.44 kV. Therefore, maintaining the same voltage per turn, i.e. 0.023 kV, the number of turns need to be doubled to 38 turns per coil. By maintaining the same voltage per turn the conductor insulation thickness is the same hence a verifiable design.

Table 6.8. Voltage scaling steps for the 9-phase HG

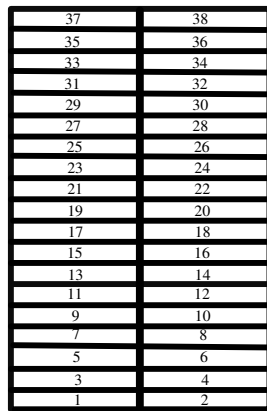
Description	RMS phase voltage (kV)	Step voltage multiplier
Initial phase voltage	6.6	-
Step 1	13.2	2
Step 2	26.4	2
Step 3	38	1.44

Each turn in the 6.6 kV machine has 2 parallel strands which makes up to a total of 38 strands per coil as shown in Fig. 6.17. By insulating strands using conductor insulation each strand is used as one turn and the coil voltage is increased to 0.88 kV hence the machine voltage increases to 13.2 kV. The coil cross-section for the 13.2 kV machine is shown in Fig. 6.18(a).

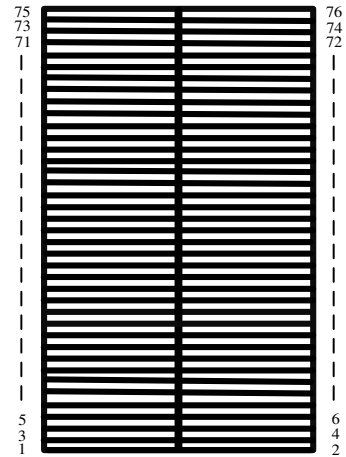
In the 13.2 kV HG coil the voltage difference between vertically adjacent turns is 0.046 kV (2×0.023 kV) while the maximum voltage difference between adjacent turns is 0.069 kV (3×0.023 kV). For the initial 6.6 kV machine the conductor insulation is 0.066 mm. Therefore, for the 13.2 kV machine the conductor insulation is increased to 0.13 mm and a layer of insulation with a thickness of 0.13 mm needs to be added in the middle of the coil to account for maximum 0.069 kV voltage difference between turns. Table 6.9 shows the size of coil and turns for the 13.2 kV machine. As seen the coil height and width is increased by 2.83% and 1.8% respectively. The coil total cross-section area is however increased by 4.7%.

In order to step-up phase voltage to 26.4 kV while maintaining the same turn voltage, i.e. 0.023 kV, the number of turns is increased to 76, i.e. double the number of turns for the 13.2 kV coils. Therefore, each turn in Fig. 6.18(a) is split vertically into two turns and with the same turn arrangement the coil cross-section for the 26.4 kV HG is shown in Fig. 6.18(b). The voltage difference between turns is the same as 13.2 kV HG hence the same insulation is used as shown in Table 6.9. Compared to the initial values the coil height, width and cross-section area for the 26.4 kV HG is increased by 15.14%, 1.8% and 17.22% respectively.

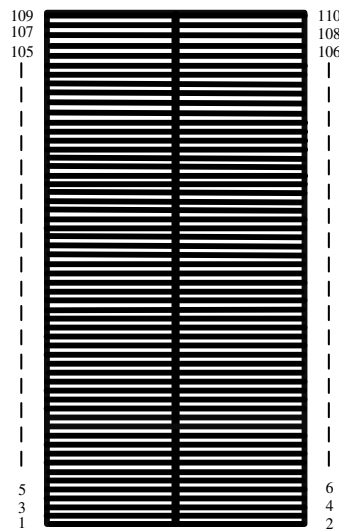
To achieve a 38.1 kV RMS phase voltage while maintaining a turn voltage of 0.023 kV, the number of turns per coil needs to increase to 110. Therefore, by keeping the same copper cross-section area, i.e. 380.64 mm², the same coil copper width and height, i.e. 12.2 mm and 31.2 mm, and also by having the same turn arrangements as in Fig. 6.18(a) the conductor copper height for the coils in the 38.1 kV machine is 0.57 mm. Therefore, for the same turn arrangements as in 13.2 kV and 26.4 kV HG coils the conductor insulation thickness stays the same i.e. 0.13 mm. However, due to added number of turns the coil height, width and cross-section area is increased by 26.6%, 1.8% and 28.9% respectively. The coil cross-section for the 38.1 kV HG is shown in Fig. 6.18(c) while Fig. 6.19 shows stator slot and back-iron cross-sectional view for different designs. Table 6.9 summarizes the winding insulation systems. In order to account for the coil height increase the slot depth is increased by 26.6% and to ensure the same machine magnetic performance the stator back-iron is increased by 26.6% to maintain the same back-iron thickness as in the 6.6 kV HG. Therefore, the stator inner diameter is the same while the stator outer diameter is increased by 26.6%. As a result the machine mass is increased by 7.5%.



(a) Coil cross-section for 13.2 kV HG.



(b) Coil cross-section for 26.4 kV HG.



(c) Coil cross-section for 38.1 kV HG.

Fig. 6.18. Coil cross-section for 13.2 kV, 26.4 kV and 38.1 kV HG.

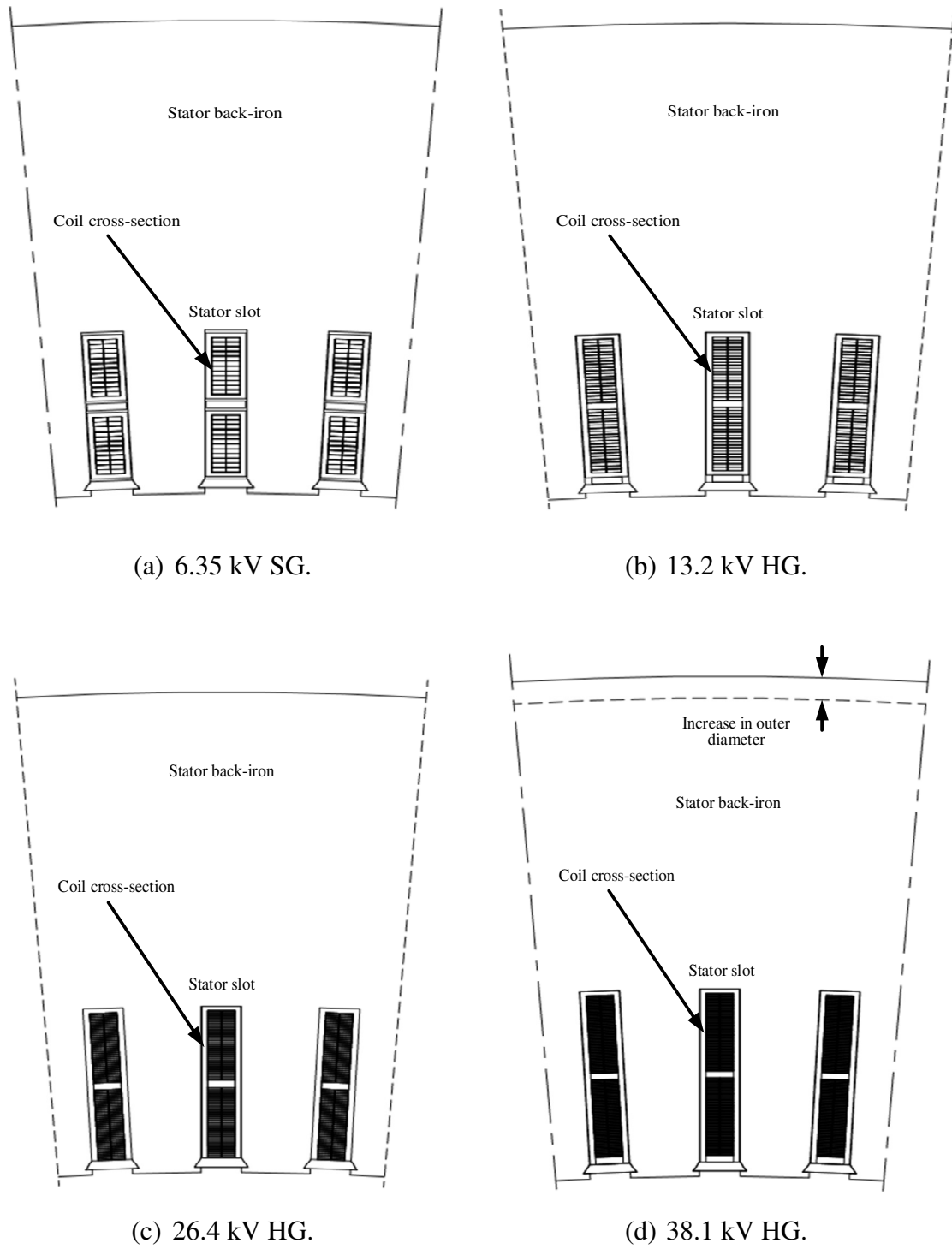


Fig. 6.19. Stator cross-sectional view for different HG winding designs.

Table 6.9. HG coil and turn insulations

Description	Initial	Step 1	Step 2	Step 3
Phase voltage (RMS kV)	6.6	13.2	26.4	38.1
Coil voltage (RMS kV)	0.44	0.88	1.76	2.54
Turn voltage (RMS kV)	0.023			
No. of coils per phase	15			
No. of turns per coil	19	38	76	110
Conductor height excluding insulation (mm)	1.64	1.64	0.8279	0.57
Conductor width excluding insulation (mm)	12.2	6.1	6.1	6.1
Conductor insulation (mm)	0.066	0.13	0.13	0.13
Conductor height including insulation (mm)	1.84	1.9	1.08	0.83
Conductor width including insulation (mm)	12.53	6.36	6.36	6.36
Added insulation in the middle of the coil (mm)	-	0.13	0.13	0.13
Groundwall insulation thickness (mm)	2.6			
Coil height (mm)	40.16	41.3	46.24	50.85
Coil width (mm)	17.73	18.05	18.05	18.05
Total coil cross-section including insulation (mm)	712.04	745.47	834.63	917.84
Increase in coil height (%)	-	2.83	15.14	26.6
Increase in coil width (%)	-	1.8	1.8	1.8
Increase in coil cross-section area (%)	-	4.7	17.22	28.9

6.6 Summary

The insulation systems for the HV machines are discussed in this Chapter. Three different types of windings for the machines are introduced namely, random-wound coils, form-wound coils and Roebel bars. The form-wound coils common between the high voltage machine manufacturers is chosen for the HG windings. Insulation systems for the strand, conductor and coils are considered and the insulations for the benchmark SG are chosen as the bases of the insulation design for the HG. The importance of the groundwall insulation, semiconductive and voltage stress grading insulations are illustrated. The winding insulation systems are modelled as capacitor circuits and the importance of avoiding air pockets is illustrated via an example. The groundwall insulation for the HG is the same as the benchmark SG while the strand and conductor insulations increase linearly with the voltage. The RMS phase voltage increase from 6.6 kV to the desired 38.1 kV is explained using three steps to illustrate the impact of winding voltage on the machine stator design. In step one and two the voltage is doubled while in step 3 the voltage is increased by a factor of 1.44. The turns in each coil are arranged such that the voltage difference between consecutive coils is minimized hence minimizing the insulation requirements. It is shown that for the same number of coils per phase and the same turn voltages, the coil height is increased by 26.6% from its original value for the 6.6 kV HG. To account for the coil height increase the stator slots are made deeper while stator back-iron thickness is kept the same. Therefore, the 38.1 kV HG has an outer diameter 26.6% longer than that of the 6.6 kV HG which results in 7.5% increase in machine mass.

Chapter 7

Conclusions and Future Work

7.1 Summary and Conclusions

This Ph.D. study proposes a new off-shore wind generation scheme incorporating high voltage hybrid generator (HG), HVDC interconnection and transmission. In Chapter 2 wind turbine basics are discussed. Analytical expressions for the harvested power from a free-stream wind by wind turbines are presented and the Betz limit discussed. After considering different turbine configurations, the 3-blade wind turbine is chosen as it results in higher harvested power. Turbine power coefficient from different references are studied and a commonly used expression is chosen for further analysis. Turbine power-speed, torque-speed, power-wind velocity and torque-wind velocity mathematical models are derived. In order to confirm the mathematical models, characteristics of a commercial 2MW wind turbine manufactured by Enercon is studied using published datasheet and operational data to confirm the developed models. In this study two operational regions for the wind turbines are considered, one practiced by the wind industry at large, termed the limited speed region and a new scheme, termed the high speed region. In the limited speed region, the wind turbine rotor speed and power increase with the wind velocity until a rated wind velocity is reached. For velocities above nominal rated, the turbine power and rotor speed is controlled at their nominal values via turbine blade pitch control and power delivery. For the new scheme introduced in this study, the high speed region of operation, the turbine rotor speed is allowed to exceed the rated speed at a constant output power, a feature that results in reduced torque for the electric generator. The wind turbine mechanics may need to be

redesigned for higher speeds, this and other mechanical and aerodynamic considerations are not further analyzed and assessed in this thesis and are left for future studies.

The analysis of the proposed wind generation scheme is presented in Chapter 3. The proposed system is compared against a commercial wind generation system, Walney 1 which is representative of existing industry practice for off-shore systems. The analysis results show that the proposed system results in 3.8% higher energy conversion efficiency assuming all turbines are operating at their full-load rating. Analysis at other loads i.e. three-quarter, half and one quarter loads shows similar efficiency gains. The proposed scheme also results in 2.3% lower mass for the turbine and 75.8% lower mass for the cable systems.

Perhaps the most important contribution of the new scheme is the removal of two fully rated VSC's in the turbine tower and nacelle and the turbine transformer. Hence, the system complexity and number of component count is reduced which potentially improves the serviceability and maintenance of the wind farm over time for the proposed system compared to the existing state of the art, i.e. Walney. It is envisaged that these savings contribute to overall cost reduction of the wind farm and system, although this is not assessed nor quantified in this study. In the proposed system the interconnection cable's voltage is controlled to vary compared to the essentially fixed interconnection voltage for the benchmark Walney system. The off-shore substation transformers in the Walney system is replaced with high voltage, high power DC/DC converters. The proposed system uses a high voltage HG compared to the low voltage (690 V) IG in the Walney system. The HG has two rotor sections, a WF and a PM rotor which share a 9-phase stator. The 9-phase HG yields improved power density while eliminating the smoothing DC-link capacitors that would otherwise be required. In Chapter 4 a low voltage laboratory prototype HG is tested and results are compared with simulations which show good agreement. A commercial 3-phase 5.2 MW, 11 kV, SG manufactured by Siemens is chosen as a benchmark for the HG design. FEA analysis and MATLAB simulations are carried out for the benchmark SG which confirm the machine datasheet hence providing validation for the subsequent high power machine studies.

Design of the high voltage HG is studied in Chapter 5. Machine operational philosophies and concept is investigated and illustrated using a fully wound field synchronous generator example. The benchmark SG 3-phase stator is rewound as 9-phase winding. The 9-phase stator winding results in 4.2% higher output voltage and hence power due to improved winding factor.

It is shown that when an electric generator is interfaced via a passive rectifier as opposed to a fully active VSC, the DC-link power is reduced. The reduction in performance is assessed and input to the machine design procedure. For the benchmark generator connected to a rectifier, the design rating would have been higher by a factor of 1.1 and 1.4 compared to a generator interfaced by a PWM and over-modulated controlled VSC respectively for the same DC-link power.

Two final designs for the HG are proposed (i) a HG with WF and surface NdFeB PM rotor and (ii) a HG with WF and embedded NdFeB PM rotor. A discussion of the split ratio between the WF and PM sections is made. The WF section operates in the nonlinear portion of the B-H curve where the stator teeth and back-iron are saturated. The PM rotor section operates in the B-H linear region where the stator iron is not saturated. The phase inductance for the WF and PM section is calculated with a constant value for the surface PM section and variable value for the WF and embedded PM rotor due to saliency. The machine copper losses are calculated at the rated stator and rotor current while the stator iron loss is calculated for tooth tip, tooth body and back-iron separately since they operate at different flux-densities. The iron losses are predicted via polynomial regression that is used to fit the loss curves provided by lamination manufacturer. The loss analysis for the HG Design 1 shows that the machine losses are 50.8% and 10.2% due to stator and rotor copper loss respectively, 8.7% due to iron loss and the remaining 30.3% due to windage and friction loss. However, for the HG Design 2, 50.8% and 10.7% of the losses are due to stator and rotor copper loss, 11% due to stator iron loss and the remaining 27.5% due to friction and windage losses. The HG efficiency is 95.23% and 95.42% for Design 1 and Design 2 respectively.

The HG insulation system is studied in Chapter 6. Different winding schemes are presented and form-wound HV coils are chosen as the HV winding scheme for the HG. Various insulation components in a HV coil are studied with the SG coils being a representative industry example of high voltage winding. Lumped capacitor models for the insulations are illustrated for different insulation sections.

As a starting point for the insulation study, a 9-phase progressive of the benchmark SG is analyzed. The results illustrate the HV HG system concept could be technically realized at an accepted industry standard voltage level (11 kV line-to-line), albeit with higher interconnecting cable mass and higher step-up ratio for off-shore DC/DC converter.

The machine initial 6.6 kV RMS phase voltage is scaled to 38.1 kV in three steps. For each step proper insulation is designed by linearly increasing the conductor and strand insulation while the groundwall insulation is maintained the same. However, it is assumed that a better quality groundwall insulation with the same thickness is used for higher voltages. The turns in each coil are placed next to each other such that minimum voltage difference between two adjacent turns is assured. The height of the coils in the 38.1 kV machine is increased by 26.6% compared to its original height. Therefore, the stator slot depth is increased and by keeping the same stator back-iron thickness the stator outer diameter is increased by 26.6%. This results in 7.5% mass increase for the machine stator.

7.2 Publications

This Ph.D. study has resulted in following publications to-date.

Journal Papers:

1. **Omid Beik**, Nigel Schofield, “An Off-Shore Wind Generation Scheme with High Voltage Hybrid Generator, HVDC Interconnections and Transmission” *IEEE Transactions on Power Delivery*, vol. 31, no. 2, pp. 867-877, April 2016.

Conference Papers:

1. **Omid Beik**, Nigel Schofield, “High Voltage Generator for Wind Turbines”, *The 8th IET international conference on Power Electronics, Machines and Drives (PEMD 2016)*, Manchester, UK, April 19-21, 2016.
2. **Omid Beik**, Nigel Schofield, “Hybrid Generator for Wind Generation Systems”, *IEEE Energy Conversion Congress and Exposition (ECCE 2014)*, Pittsburgh, PA, USA, Sept 14-18, 2014.
3. **Omid Beik**, Nigel Schofield, Ahmad Al-Adsani, “Variable Speed Brushless Hybrid Permanent Magnet Generator for Hybrid Electric Vehicles”, *IEEE Transportation Electrification Conference and Expo (ITEC 2014)*, Michigan, USA, June 15-18, 2014.
4. Nigel Schofield, Xin Niu, **Omid Beik**, “Multiphase Machines for Electric Vehicle Traction”, *IEEE Transportation Electrification Conference and Expo (ITEC 2014)*, Michigan, USA, June 15-18, 2014.
5. **Omid Beik**, Nigel Schofield, “A Brushless Exciter Design for a Hybrid Permanent Magnet Generator Applied to Series Hybrid Electric Vehicles”, *The 7th IET international conference on Power Electronics, Machines and Drives (PEMD 2014)*, Manchester, UK, April 8-10, 2014.

7.3 Future Work

Following recommendations are suggested for future work:

- In Chapter 2 a high speed region of operation for the wind turbine is proposed where the wind turbine operates at higher speeds than rated. Therefore, turbines mechanics and aerodynamics may need to be re-designed which are not included in this study. Design and operation of a wind turbine for higher rotor speeds and its effect on blade, shaft and other mechanical parts can be included in future studies.
- The high voltage, high power DC/DC converters are used in the proposed system in Chapter 3. Investigating different topologies and circuits for such converters with high step-up ratio can be studied in future work. Indeed, design of high voltage, high power bidirectional DC/DC converters for off-shore wind generation systems is an interesting topic for a Ph.D. thesis.
- In this study system performance is evaluated at steady-state to identify the system envelope, rating specification requirements, key technology gaps, benefits and system performance. Investigating system dynamics and transients and their effects on the component ratings is the logical extension of this research. A future system dynamic study can include transient and small signal analysis considering HG wound field control response including brushless exciter.
- Thermal analysis of the HG with different cooling systems practiced by industry for high voltage and high power machines can be studied in future work. Cooling methods such as internally ventilated and cooled with an air-to-air heat exchange system or air-to-air eternal fan with centrifugal flow direction (that are two common methods used in the Siemens wind turbine systems) can be considered for the HG.
- The WF of the HG is fed by a DC voltage and current. The DC voltage is feedback from the rectified HG output. Design of a system to control the WF current in order to regulate and fast track the machine output voltage and coordinate control of all the generators in a wind farm can be considered in future studies.

References

- [1] [Online] Brazos on-shore wind farm, Texas, US. Available: https://en.wikipedia.org/wiki/Brazos_Wind_Farm. Last accessed on Jan. 2016.
- [2] [Online] Walney Off-shore Windfarms. Available: <http://www.dongenergy.com/>. Last accessed on Jan. 2016.
- [3] [Online] Alstom wind turbines. Available: <http://alstomenergy.gepower.com/>. Last accessed on Jan. 2016.
- [4] W.-L. Chen, Y.-Y. Hsu, "Controller design for an induction generator driven by a variable-speed wind turbine," IEEE Transactions on Energy Conversion, vol.21, no.3, pp.625-635, Sept. 2006.
- [5] W. Yang, P.J. Tavner, M.R. Wilkinson, "Condition monitoring and fault diagnosis of a wind turbine synchronous generator drive train," IET Renewable Power Generation, vol.3, no.1, pp.1-11, March 2009.
- [6] S. Muller, M. Deicke, R. W. De Doncker, "Doubly fed induction generator systems for wind turbines," IEEE Industry Applications Magazine, vol. 8, no. 3, pp. 26-33, May/Jun 2002.
- [7] K. Tan, S. Islam, "Optimum control strategies in energy conversion of PMSG wind turbine system without mechanical sensors," IEEE Transactions on Energy Conversion, vol.19, no.2, pp.392-399, June 2004.
- [8] [Online] Article. Available: <http://cleantechnica.com/2014/05/07/wind-power/>. Last accessed on Jan. 2016.
- [9] E. Hau, Wind Turbines: Fundamentals, Technologies, Application, Economics. Springer, 2006.
- [10] [Online] Siemens wind turbine SWT-3.6-107. Available: <http://www.siemens.com>. Last accessed on Jan. 2016.

- [11] [Online] Enercon E-82 wind turbine. Available: <http://www.enercon.de>. Last accessed on Jan. 2016.
- [12] S.V. Bozhko, R. Blasco-Gimenez, R. Li, J.C. Clare, "Control of Offshore DFIG-Based Wind Farm Grid With Line-Commutated HVDC Connection," *IEEE Transactions on Energy Conversion*, vol.22, no.1, pp.71-78, March 2007.
- [13] [Online] Direct-Connected Induction (Asynchronous) Generator. Available: <http://www.uwig.org/>. Last accessed on Jan. 2016.
- [14] Z. Tan, X. Song, W. Cao, Z. Liu, Y. Tong, "DFIG Machine Design for Maximizing Power Output Based on Surrogate Optimization Algorithm," *IEEE Transactions on Energy Conversion*, vol.30, no.3, pp.1154-1162, Sept. 2015.
- [15] V. Delli Colli, F. Marignetti, C. Attaianesi, "Analytical and Multiphysics Approach to the Optimal Design of a 10-MW DFIG for Direct-Drive Wind Turbines," *IEEE Transactions on Industrial Electronics*, vol.59, no.7, pp.2791-2799, July 2012.
- [16] M. Fazeli, S.V Bozhko, G.M. Asher, L. Yao, "Voltage and frequency control of offshore DFIG-based wind farms with line commutated HVDC connection," *4th IET Power Electronics, Machines and Drives (PEMD)*, pp.335-339, 2-4 April, 2008.
- [17] A. Boumassata, D. Kerdoun, "Direct powers control of DFIG through direct converter and sliding mode control for WECS," *3rd International Conference on Control, Engineering & Information Technology (CEIT)*, May 2015.
- [18] S. Ghosh, "Closed loop control of a DFIG based wind power system," *IEEE Innovative Smart Grid Technologies - Asia (ISGT Asia)*, 10-13 Nov. 2013.
- [19] W. Srirattanawichaikul, Y. Kumsuwan, S. Premrudeepreechacharn, S.; Wu, B., "A vector control of a grid-connected 3L-NPC-VSC with DFIG drives," *International Conference on Electrical Engineering/Electronics Computer Telecommunications and Information Technology (ECTI-CON)*, pp.828-832, 19-21 May 2010.

- [20] Y. Lei, A. Mullane, G. Lightbody, R. Yacamini, "Modeling of the wind turbine with a doubly fed induction generator for grid integration studies," *IEEE Transactions on Energy Conversion*, vol.21, no.1, pp.257-264, March 2006.
- [21] H. Liu, J. Sun, "Voltage Stability and Control of Offshore Wind Farms with AC Collection and HVDC Transmission," *IEEE Journal of Emerging and Selected Topics in Power Electronics*, vol.2, no.4, pp.1181-1189, Dec. 2014.
- [22] D. Yoon, H. Song, G. Jang, S. Joo, "Smart Operation of HVDC Systems for Large Penetration of Wind Energy Resources," *IEEE Transaction on Smart Grid*, vol.4, no.1, pp.359-366, March 2013.
- [23] E. Selvaraj, C.P. Sugumaran, Krishnamoorthi, M.R. Kumar, M.R. Joshi, J. Ganesan, S. Geethadevi, S.D. Kumar "A Review on Fundamentals of HVDC Transmission," *Journal Club for Electrical Engineering (JCEE)*, vol.1, 2014.
- [24] R. Feldman, M. Tomasini, E. Amankwah, J.C. Clare, P.W. Wheeler, D.R. Trainer, R.S. Whitehouse, "A Hybrid Modular Multilevel Voltage Source Converter for HVDC Power Transmission," *IEEE Transaction on Industry Applications*, vol.49, no.4, pp.1577-1588, July-Aug. 2013.
- [25] J. A. Baroudi, V. Dinavahi. A.M. Knight, "A review of power converter topologies for wind generators", *Renewable Energy*, vol.32, pp.2369-2385, 2007.
- [26] O. Anaya-Lara, N. Jenkins, J. Ekanayake, P. Cartwright, M. Hughes, *Wind Energy Generation: Modelling and Control*, Wiley, West Sussex, UK, 2009.
- [27] D. Jovicic, N. Strachan, "Offshore wind farm with centralised power conversion and DC interconnection," *IET Generation, Transmission & Distribution*, vol.3, no.6, pp.586-595, 2009.
- [28] E. Veilleux, P.W. Lehn, "Interconnection of Direct-Drive Wind Turbines Using a Series-Connected DC Grid," *IEEE Transaction on Sustainable Energy*, vol.5, no.1, pp.139-147, Jan. 2014.

- [29] M. Dahlgren, H. Frank, M. Leijon, F. Owman, L. Walfridsson, "Windformer," ABB Review, Tech. Rep., vol. 3 pp.31-37, 2000.
- [30] S.M. Muyeen, R. Takahashi, J. Tamura, "Operation and Control of HVDC-Connected Offshore Wind Farm," IEEE Transactions on Sustainable Energy, vol.1, no.1, pp.30-37, April 2010.
- [31] C. Zhan, C. Smith, A. Crane, A. Bullock, D. Grieve, "DC transmission and distribution system for a large offshore wind farm," 9th IET International Conference AC and DC Power Transmission, pp.1-5, 19-21 Oct. 2010.
- [32] S.D. Wright, A.L. Rogers, J.F. Manwell, A.Ellis, "Transmission options for offshore wind farms in the United States" Proceedings of the American Wind Energy Association Annual Conference, pp.1-12, 2002.
- [33] V.G. Agelidis, G.D. Demetriades, N. Flourentzou, "Recent Advances in High-Voltage Direct-Current Power Transmission Systems," IEEE International Conference on Industrial Technology (ICIT) 2006, pp.206-213, 15-17 Dec. 2006.
- [34] P. Bresesti, W.L. Kling, R.L. Hendriks, R. Vailati, "HVDC Connection of Offshore Wind Farms to the Transmission System," IEEE Transactions on Energy Conversion, vol.22, no.1, pp.37-43, March 2007.
- [35] C. Meyer, M. Hoing, A. Peterson, R.W. De Doncker, "Control and Design of DC Grids for Offshore Wind Farms," IEEE Transaction on Industry Applications, vol.43, no.6, pp.1475-1482, 2007.
- [36] R. Steigerwald and R. Tompkins, "A comparison of high-frequency link schemes for interfacing a DC source to a utility grid," IEEE IAS Annual Meeting, pp. 759–766, 1982.
- [37] R.W De Doncker, D.M. Divan, M.H. Kheraluwala, "A three-phase soft-switched high-power-density DC/DC converter for high-power applications," IEEE Transaction on Industry Applications, vol.27, no.1, pp.63-73, Jan/Feb 1991.

- [38] D. Jovcic, "Bidirectional, High-Power DC Transformer," *Transaction on Power Delivery*, vol.24, no.4, pp.2276-2283, Oct. 2009.
- [39] D. Jovcic, L. Zhang, "LCL DC/DC Converter for DC Grids," *IEEE Transaction on Power Delivery*, vol.28, no.4, pp.2071-2079, Oct. 2013.
- [40] C. Meyer, R. W. De Doncker, "Design of a Three-Phase Series Resonant Converter for Offshore DC Grids," *IEEE Industry Applications Conference, 42nd IAS Annual Meeting*, pp.216-223, 23-27 Sept. 2007.
- [41] L. Max, T. Thiringer, "Control method and snubber selection for a 5 MW wind turbine single active bridge DC/DC converter," *European Conference on Power Electronics and Applications*, pp.1-10, 2-5 Sept. 2007.
- [42] W. Chen, A.Q. Huang, C. Li, G. Wang, W. Gu, "Analysis and Comparison of Medium Voltage High Power DC/DC Converters for Offshore Wind Energy Systems," *IEEE Transactions on Power Electronics*, vol.28, no.4, pp.2014-2023, April 2013.
- [43] M. Hajian, J. Robinson, D. Jovcic, B. Wu, "30 kW, 200 V/900 V, Thyristor LCL DC/DC Converter Laboratory Prototype Design and Testing," *IEEE Transactions on Power Electronics*, vol.29, no.3, pp.1094-1102, March 2014.
- [44] N. Denniston, A. M. Massoud, S. Ahmed, P.N. Enjeti, "Multiple-Module High-Gain High-Voltage DC–DC Transformers for Offshore Wind Energy Systems," *IEEE Transactions on Industrial Electronics*, vol.58, no.5, pp.1877-1886, May 2011.
- [45] G. Ortiz, J. Biela, D. Bortis, J.W. Kolar, "1 Megawatt, 20 kHz, isolated, bidirectional 12kV to 1.2kV DC-DC converter for renewable energy applications," *International Power Electronics Conference (IPEC)*, pp.3212-3219, 21-24 June 2010.

- [46] K.T. Chau, Y.B. Li, J.Z. Jiang, S. Niu, "Design and Control of a PM Brushless Hybrid Generator for Wind Power Application," *IEEE Transaction on Magnetics*, vol.42, no.10, pp.3497-3499, 2006.
- [47] C. Liu, K.T. Chau, J.Z. Jiang, L. Jian, "Design of a New Outer-Rotor Permanent Magnet Hybrid Machine for Wind Power Generation," *IEEE Transaction on Magnetics*, vol.44, no.6, pp.1494-1497, 2008.
- [48] R. Pillai, S. Narayanan, G. Swindale, "Benefits and challenges of a grid coupled wound rotor synchronous generator in a wind turbine application," *Technical Information from Cummins Generator Technologies*, Issue number: WP102.
- [49] I.D. Margaris, N.D. Hatzargyriou, "Direct drive synchronous generator wind turbine models for power system studies," *7th Mediterranean Conference and Exhibition on Power Generation, Transmission, Distribution and Energy Conversion*, pp.1-7, 7-10 Nov. 2010.
- [50] S. Achilles, M. Poller, 'Direct drive synchronous machine models for stability assessment of wind farms'. *Fourth Int. Workshop on Large Scale Integration of Wind Power and Transmission Networks for Offshore Windfarms*, Billund, Denmark, Oct. 2003.
- [51] M.R. Behnke, E. Muljadi, "Reduced order dynamic model for variable-speed wind turbine with synchronous generator and full power conversion topology," *International Conference on Future Power Systems*, Nov. 2005.
- [52] E. Spooner, P. Gordon, J.R. Bumby, C.D. French, "Lightweight ironless-stator PM generators for direct-drive wind turbines," *IEE Proceedings Electric Power Applications*, vol.152, no.1, pp.17-26, Jan. 2005.
- [53] S. Brisset, D. Vizireanu, P. Brochet, "Design and Optimization of a Nine-Phase Axial-Flux PM Synchronous Generator With Concentrated Winding for Direct-Drive Wind Turbine," *IEEE Transactions on Industry Applications*, vol.44, no.3, pp.707-715, May-June 2008.

- [54] H. Li, Z. Chen, "Overview of different wind generator systems and their comparisons," IET Renewable Power Generation, vol.2, no.2, pp.123-138, June 2008.
- [55] D. J. Bang, H. Polinder, G. Shrestha, and J. A. Ferreira, "Review of generator systems for direct-drive wind turbines," Eur. Wind Energy Conf. Exhib., Belgium, Mar. 31–Apr. 3, 2008.
- [56] H. Polinder, F. van der Pijl, G. de Vilder, P.J. Tavner, "Comparison of direct-drive and geared generator concepts for wind turbines," IEEE Transaction on Energy Conversion, vol.21, no.3, pp.725-733, 2006.
- [57] M. Liserre, R. Cardenas, M. Molinas, J. Rodriguez, "Overview of Multi-MW Wind Turbines and Wind Parks," IEEE Transactions on Industrial Electronics, vol.58, no.4, pp.1081-1095, April 2011.
- [58] [Online] DeWind D8.2 2000 kW wind turbine. Available: <http://www.dewindco.com>. Last accessed on Jan. 2016.
- [59] A. Betz, Wind-Energie und ihre Ausnutzung durch Windmühlen (Wind energy and its utilization through windmills), Öko-Buchverlag Kassel, 1982.
- [60] G. L. Johnson, Wind Energy Systems, Prentice Hall, 1985.
- [61] S. Heier, Grid Integration of Wind Energy Conversion Systems. New York: Wiley, 1998.
- [62] R. Gasch, J. Tvele, Wind Power Plants: Fundamentals, Design, Construction and Operation. Solarpraxis AG, 2002.
- [63] Z. Lubosny, Wind Turbine Operation in Electric Power Systems, Springer, 2003.
- [64] O. Wasynczuk, D.T. Man, J.P. Sullivan, "Dynamic Behavior of a Class of Wind Turbine Generators during Random Wind Fluctuations," IEEE Power Engineering Review, vol: PER-1, no.6, pp.47-48, June 1981.

- [65] P.M. Anderson, A. Bose, "Stability Simulation of Wind Turbine Systems," IEEE Transactions on Power Apparatus and Systems, vol: PAS-102, no.12, pp.3791-3795, Dec. 1983.
- [66] Department of Energy, NASA, "The Mod-2 Wind Turbine Development Project," Report No. DOE/NASA/20305-5 NASA TM-82681, July 1981.
- [67] B. Amlang, D. Arsurdis, W. Leonhard, W. Vollstedt, K. Wefelmeier, "Elektrische Energieversorgung mit Windkraftanlagen", Abschlußbericht BMFT-Forschungsvorhaben 032-8265-B, Braunschweig, 1992.
- [68] Y. Xia, K.H. Ahmed, B.W. Williams, "Wind Turbine Power Coefficient Analysis of a New Maximum Power Point Tracking Technique," IEEE Transactions on, Industrial Electronics, vol.60, no.3, pp.1122-1132, March 2013.
- [69] MATLAB software Powersim Simulink help.
- [70] V. Quaschnig, Understanding Renewable Energy Systems. Earthscan, 2005.
- [71] M. Chinchilla, S. Arnaltes, J.C. Burgos, "Control of permanent-magnet generators applied to variable-speed wind-energy systems connected to the grid," IEEE Transactions on Energy Conversion, vol.21, no.1, pp.130-135, March 2006.
- [72] N. Milivojevic, N. Schofield, I. Stamenkovic, Y. Gurkaynak, "Field weakening control of PM generator used for small wind turbine application," IET Conference on Renewable Power Generation (RPG 2011), 6-8 Sept. 2011.
- [73] Department of Defense, "The Military Handbook for Reliability Prediction of Electronic Equipment," Tech. Rep. MIL-HDBK-217F-2, 1995.
- [74] [Online] Xian Electric Transformer, "Transformer & Reactor 10kV~500kV," Available: <http://www.xianelectric.com>. Last accessed on Jan. 2016.
- [75] [Online] NKT Cables, "Product Catalogue Australia Medium and High Voltage Cables," Available: <http://www.nktcables.com>. Last accessed on Jan. 2016.

- [76] [Online] Prysmian Cables, “High Voltage Cables,” Available: <http://prysmiangroup.com/>. Last accessed on Jan. 2016.
- [77] N. Mohan, T. Undeland, W. Robbins, Power Electronics: Converters, Applications, and Design, 3rd ed., John Wiley & Sons, 2003.
- [78] J. D. Glover, S. M. Sarma, and T. J. Overbye, Power System Analysis and Design. 5th ed, Cengage Learning, Stamford, CT, USA, 2012.
- [79] W.L. Kling, P. Bresesti, I. Valade, D. Canever, and R.L. Hendriks, “Transmission systems for offshore wind farms in the Netherlands”, International Conference & Exhibition “Offshore wind”, Copenhagen, Denmark, October 2005.
- [80] H. Li, Z. Chen, "Design optimization and evaluation of different wind generator systems," International Conference on Electrical Machines and Systems (ICEMS), Oct. 2008.
- [81] H. Li, Z. Chen, H. Polinder, "Optimization of Multibrid Permanent-Magnet Wind Generator Systems," IEEE Transactions on Energy Conversion, , vol.24, no.1, pp.82-92, March 2009.
- [82] Y.-S. Xue, L. Han, H. Li, L.-D. Xie, "Optimal design and comparison of different PM synchronous generator systems for wind turbines," International Conference on Electrical Machines and Systems (ICEMS), Oct. 2008.
- [83] D. Kowal, L. Dupre, P. Sergeant, L. Vandenbossche, M. De Wulf, "Influence of the Electrical Steel Grade on the Performance of the Direct-Drive and Single Stage Gearbox Permanent-Magnet Machine for Wind Energy Generation, Based on an Analytical Model," IEEE Transactions on Magnetics, vol.47, no.12, pp.4781-4790, Dec. 2011.
- [84] G. Bywaters, V. John, J. Lynch, P. Mattila, G. Norton, J. Stowell, M. Salata, O. Labath, A. Chertok, and D. Hablanian, Northern Power Systems WindPACT drive train alternative design study report. NREL, Golden, CO, Rep. Number NREL/SR-500-35524, 2004.

- [85] [Online] Available: <https://www.motiondynamics.com.au/gearboxes-which-type.html>. Last accessed on Jan. 2016.
- [86] R. P. Severns, G. Bloom, Modern DC-to-DC switchmode power converter circuits, Van Nostrand Reinhold Co., 1985.
- [87] D. Jovcic, “Step-up DC–DC converter for megawatt size applications,” IET Power Electronics, vol.2, no.6, pp.675-685, Nov. 2009.
- [88] D. Jovcic, “High gain DC transformer,” U.K. Patent office, PCT Patent application no. GB 0724369.4, Dec. 2007.
- [89] L. Max, S. Lundberg, “System Efficiency of a DC/DC Converter-based Wind Farm,” Journal of Wind Energy, vol.11, pp. 109–120, 2008.
- [90] Y. Zhou, D.E. Macpherson, W. Blewitt, D. Jovcic, “Comparison of DC-DC converter topologies for offshore wind-farm application,” IET International Conference on Power Electronics, Machines and Drives (PEMD), 2012.
- [91] [Online] Vestas wind turbines. Available: <http://www.vestas.com>. Last accessed on Jan. 2016.
- [92] [Online] Siemens wind turbine. Available: <http://www.offshorewind.biz/>. Last accessed on Jan. 2016.
- [93] [Online] Liquid filled transformers. Available: <http://new.abb.com/products/transformers>. Last accessed on Jan. 2016.
- [94] [Online] ABB Converter, “Low voltage wind turbine converter ACS880, 800 kW – 8 MW,” Document No. 3AXD10000303002 02.2014. Available: www.abb.com/converters-inverters. Last accessed on Jan. 2016.
- [95] [Online] Available: <http://hvdiode.en.alibaba.com/>. Last accessed on Jan. 2016.

- [96] R. Pena, J.C. Clare, G.M. Asher, "Doubly fed induction generator using back-to-back PWM converters and its application to variable-speed wind-energy generation," IEE Proceedings-Electric Power Applications, vol.143, no.3, pp.231-241, May 1996.
- [97] R. Datta, V.T. Ranganathan, "Variable-speed wind power generation using doubly fed wound rotor induction machine-a comparison with alternative schemes," IEEE Transactions on Energy Conversion, vol.17, no.3, pp.414-421, Sep 2002.
- [98] [Online] Alstom Haliade 150–6MW wind turbines. Available: <http://alstomenergy.gepower.com/>. Last accessed on Jan. 2016.
- [99] [Online] SG in a wind turbine. Available: <http://www.alternative-energy-tutorials.com/wind-energy/synchronous-generator.html>. Last accessed on Jan. 2016.
- [100] J. Hansson, "Analysis and control of a hybrid vehicle powered by a free-piston energy converter", PhD Thesis, Royal Institute of Technology (KTH), Stockholm, Sweden 2006.
- [101] S. Jordan, C.D. Manolopoulos, J. Apsley, "Winding Configurations for Five-Phase Synchronous Generators with Diode Rectifiers," IEEE Transactions on Industrial Electronics, vol. 63, No. 1, January 2016.
- [102] A. S. Al-Adsani, "Hybrid Permanent Magnet Machines for Electric Vehicles", PhD Thesis, The University of Manchester, Manchester, UK, 2006.
- [103] O. Beik, N. Schofield, "A Brushless Exciter Design for a Hybrid Permanent Magnet Generator Applied to Series Hybrid Electric Vehicles," The 7th IET International Conference on Power Electronics, Machines and Drives PEMD'14, Manchester, UK, April 2014.
- [104] S. Smith, "Electric Machine Design," M.Sc. lecture notes, Power Conversion Group, School of Electrical and Electronics Engineering, The University of Manchester, Manchester, UK, 2012.

- [105] S. J. Chapman, *Electric machinery Fundamentals*. Fifth edition, McGraw-Hill, New York, 2012.
- [106] I. Boldea, S. A. Nasar, *Electric machine dynamics*. Macmillan, 1986.
- [107] V. Del Toro, *Electric Machines and Power Systems*. Prentice-Hall, N. J., 1985.
- [108] J. I. Grainger, W. Stevenson Jr., *Power System Analysis*, McGraw-Hill, 1994.
- [109] J.L. Rodriguez-Amenedo, S. Arnalte, J.C. Burgos, "Automatic generation control of a wind farm with variable speed wind turbines," *IEEE Transactions on Energy Conversion*, vol.17, no.2, pp.279,284, Jun 2002.
- [110] T. Surinkaew, I. Ngamroo, "Coordinated Robust Control of DFIG Wind Turbine and PSS for Stabilization of Power Oscillations Considering System Uncertainties," *IEEE Transactions on Sustainable Energy*, vol.5, no.3, pp.823-833, July 2014.
- [111] A. D. Hansena, P. Sørensen, F. Iovb, F. Blaabjerg, "Centralised power control of wind farm with doubly fed induction generators," *Renewable Energy*, vol.31, no.2, pp.935-951, 2006.
- [112] L.M. Fernandez, C.A. Garcia, F. Juradob, "Comparative study on the performance of control systems for doubly fed induction generator (DGIG) wind turbines operating with power regulation," *Energy*, vol. 33, no.2, pp.1438-1452, 2008.
- [113] W. Lu, B.T. Ooi, "Multi-terminal LVDC system for optimal acquisition of power in wind-farm using induction generators," *IEEE Transactions on Power Electronics*, vol.17, no.4, pp.558-563, 2002.
- [114] W. Lu, B.T. Ooi, "Optimal acquisition and aggregation of offshore wind power by multiterminal voltage-source HVDC," *IEEE Transactions on Power Delivery*, vol.18, no.1, pp.201-206, Jan 2003.
- [115] N. Schofield, "Electric Machine Design and Operation," Ph.D. and M.Sc. lecture notes, Department of Electrical and Computer Engineering, McMaster University, Hamilton, Ontario, Canada, 2015.

- [116] J. F. Gieras, *Advancements in Electric Machines*. Springer, Netherlands, 2010.
- [117] S.J. Sugimoto, “Current status and recent topics of rare-earth permanent magnets,” *Journal of Physics D: Applied Physics*, Volume 44, Issue 6, 2011.
- [118] M. Humphries, “Rare Earth Elements: The Global Supply Chain,” CRS Report for Congress, Report No. R41347, Congressional Research Service, 2013.
- [119] C. Hurst, “China’s rare earth elements industry: what can the west learn?” Institute for the Analysis of Global Security (IAGS), Washington D.C., 2010.
- [120] [Online] Arnold Magnetics permanent magnets datasheet. Available: <http://www.arnoldmagnetics.com/en-us/>. Last accessed on Jan. 2016.
- [121] D. Ishak, A.Q. Zhu, D. Howe “Eddy-current loss in the rotor magnets of permanent-magnet brushless machines having a fractional number of slots per pole”, *IEEE Transactions on Magnetics*, Vol. 41, No. 9, pp. 2462- 2469, Sept. 2005.
- [122] A. Boglietti, A. Cavagnino, M. Lazzari, M. Pastorelli, “Two simplified methods for the iron losses prediction in soft magnetic materials supplied by PWM inverter”, *IEEE International on Electric Machines and Drives Conference (IEMDC 2001)*, pp. 391-395, 2001.
- [123] L. Li, X. Huang, B. Kao, B. Yan, “Research of core loss of permanent magnet synchronous motor (PMSM) in AC servo system”, *International Conference on Electrical Machines and Systems (ICEMS 2008)*, pp. 602-607, 17-20 Oct. 2008.
- [124] G. Bertotti, A. Boglietti, M. Chiampi, D. Chiarabaglio, F. Fiorillo, M. Lazzari, “An improved estimation of iron losses in rotating electrical machines”, *IEEE Transactions on Magnetics*, Vol. 27, No. 6, pp. 5007-5009, Nov. 1991.
- [125] G. R. Slemon and X. Liu, “Core Losses in Permanent Magnet Motors”, *IEEE Transactions on Magnetics*, Vol. 26, No. 5, pp 1653–1655, Sept. 1990.
- [126] A. Krings, J. Soulard, “Overview and Comparison of Iron Loss Models for Electrical Machines,” *Journal of Electrical Engineering*, 2010.

- [127] K. Atallah, Z. Q. Zhu, D. Howe, “An improved method for predicting iron losses in brushless permanent magnet DC drives,” *IEEE Transactions on Magnetics*, vol. 28, pp. 2997-2999, 1992.
- [128] W. A. Roshen, “A Practical, Accurate and Very General Core Loss Model for Nonsinusoidal Waveforms,” *IEEE Transactions on Power Electronics*, vol. 22, pp. 30-40, 2007.
- [129] I. Mayergoyz, “Mathematical models of hysteresis,” *IEEE Transactions on Magnetics*, vol. 22, pp. 603-608, 1986.
- [130] L. R. Dupre, O. Bottauscio, M. Chiampi, M. Repetto, J. A. A. Melkebeek, “Modeling of electromagnetic phenomena in soft magnetic materials under unidirectional time periodic flux excitations,” *IEEE Transactions on Magnetics*, vol. 35, pp. 4171-4184, 1999.
- [131] G. Bertotti, “General properties of power losses in soft ferromagnetic materials”, *IEEE Transactions on Magnetics*, vol. 24, no. 1, pp. 621-630, Jan. 1988.
- [132] C. P. Steinmetz, “On the law of hysteresis,” *Proceedings of the AIEEE*, Vol. 72, pp. 197-221, 1884.
- [133] Lamination Steel Third Edition CD-ROM, Electric Motor Education and Research Foundation, ISBN 0-9714391-3-3, Second Printing 2009.
- [134] B. J. Moore, R. H. Rehder, and R. E. Draper, “Utilizing Reduced Build Concepts in the Development of Insulation Systems for Large Motors,” In *Proceedings of IEEE Electrical Insulation Conference*, Cincinnati, pp. 347–352, October 1999.
- [135] G. C. Stone, E. A. Boulter, I. Culbert, and H. Dhirani, “Electrical Insulation for Rotating Machines,” p.5, IEEE Press, 2004.
- [136] [Online] Partzsch Group. Available: <https://en.partzsch.de/roebel-bars>. Last accessed on Jan. 2016.
- [137] M. Leijon, “ABB Powerformer,” Report No: ABB Review 2/1998.

- [138] X. Yu, W. Wu, W. Pan, S. Han, L. Wang, J. Wei, L. Liu, S. Du, Z. Zhou, A. Foussat, P. Libeyre, "Development of Insulation Technology With Vacuum-Pressure-Impregnation (VPI) for ITER Correction Coil," *IEEE Transactions on Applied Superconductivity*, vol.22, no.3, pp.7700504-7700504, June 2012.
- [139] M. K. W. Stranges, D. A. Snopek, A. K. Younsi, J. H. Dymond, "Effect of surge testing on unimpregnated ground insulation of VPI stator coils," *IEEE Transactions on Industry Applications*, vol.38, no.5, pp.1460-1465, Sep/Oct 2002.
- [140] W. Grubelnik, C. Stiefmaier, "Un-impregnated vpi tape testing and effects on dielectric performance of VPI insulation systems," *Electrical Insulation Conference (EIC)*, pp.359-362, 8-11 June 2014.
- [141] A. Nakayama, H. Haga, M. Muraoka, "Development of generator stator coil with 22kV global VPI insulation," *Conference on Electrical Insulation and Dielectric Phenomena (CEIDP '04)*, pp.224-227, 17-20 Oct. 2004.
- [142] F. P. Espino-Cortes, E. A. Cherney, S. Jayaram, "Effectiveness of stress grading coatings on form wound stator coil groundwall insulation under fast rise time pulse voltages," *IEEE Transactions on Energy Conversion*, vol.20, no.4, pp.844-851, Dec. 2005.
- [143] D. J. Conley, N. Frost, "Fundamentals of semi-conductive systems for high voltage stress grading," *Electrical Insulation Conference and Electrical Manufacturing Expo*, pp.89-92, 26-26 Oct. 2005.
- [144] Private conversation with Dr. Yali (Natalie) Feng, HV insulation expert at Sulzer Dowding & Mills, Birmingham, UK, 2014.
- [145] F. T. Emery, D.C. Johnson, "Voltage grading model for high voltage electric generator stator coil end turn regions," *Conference on Electrical Insulation and Dielectric Phenomena*, pp.589-592, 25-28 Oct 1998.
- [146] A. Roberts, "Stress grading for high voltage motor and generator coils," *IEEE Electrical Insulation Magazine*, vol.11, no.4, pp.26-31, July-Aug. 1995.

- [147] M. Fujita, Y. Kabata, T. Tokumasu, K. Nagakura, M. Kakiuchi, S. Nagano, "Circulating Currents in Stator Coils of Large Turbine Generators and Loss Reduction," *IEEE Transactions on Industry Applications*, vol.45, no.2, pp.685-693, March-April 2009.
- [148] Y. Liang, X. Bian, H. Yu, L. Wu, B. Wang, "Analytical Algorithm for Strand End Leakage Reactance of Transposition Bar in AC Machine," *IEEE Transactions on Energy Conversion*, vol.30, no.2, pp.533-540, June 2015.

Appendices

A.1 MATLAB Program: Turbine Power Coefficient

```

clc
clf
clear all
c1=0.5176;
c2=116;
c3=0.4;
c4=5;
c5=21;
c6=0.0068;
k=1;
for beta=[0, 5, 10, 15, 20]
    i=1;
    for S=0.1:0.01:14
        lambda(i)=S;
        lambdai(i)=1/(1/(lambda(i)+0.08*beta)-0.035/(beta^3+1));
        Cp(i,k)=c1*(c2/lambdai(i)-c3*beta-c4)*exp(-
c5/lambdai(i))+c6*lambda(i);
        i=i+1;
    end
    Cpmax(k)=max(Cp(:,k));
    a=find(Cp(:,k)==Cpmax(k));
    lambdaopt(k)=lambda(a);
    figure(1)
    plot(lambda,Cp(:,k))
    grid on
    hold on
    k=k+1;
end
figure(2)
plot(lambda,Cp(:,1),'b',lambda,Cp(:,2),'r--',lambda,Cp(:,3),'g-
.',lambda,Cp(:,4),'c:',lambda,Cp(:,5),'k')
grid on
xlabel('Tip speed ratio, lambda')
ylabel('Turbine power coefficient, Cp')
title('Cp-lambda Curves')
legend('beta=0','beta=5','beta=10','beta=15','beta=20')
figure(3)
plot(lambda,Cp(:,1))
grid on
xlabel('Tip speed ratio, lambda')
ylabel('Turbine power coefficient, Cp')
title('Cp-lambda Curves')
legend('beta=0')

```

A.2 MATLAB Program: Turbine Power versus Speed

```

clc
clf
clear all
c1=0.5176;
c2=116;
c3=0.4;
c4=5;
c5=21;
c6=0.0068;

beta=0;
i=1;
for S=0.1:0.01:13
    lambda(i)=S;
    lambda(i)=1/(1/(lambda(i)+0.08*beta)-0.035/(beta^3+1));
    Cp(i)=c1*(c2/lambda(i)-c3*beta-c4)*exp(-
c5/lambda(i))+c6*lambda(i);
    i=i+1;
end

Cpmax=max(Cp);
a=find(Cp==Cpmax);
lambdaopt=lambda(a);

figure(1)
plot(lambda,Cp)
grid on
xlabel('Tip speed ratio, lambda')
ylabel('Turbine power coefficient, Cp')
title('Cp-lambda Curve')

R=4.75;
ro=1.225;

for k=1:1:25
    v(k)=k;
    w(:,k)=v(k)*1/R*lambda';
    y=w(:,k);
    Pt(:,k)=0.5*ro*pi*R^2*v(k)^3*1/1000*Cp;

    if v(k)<=15
        Ptmax(k)=max(Pt(:,k));
        a=find(Pt(:,k)==Ptmax(k));
        wo(k)=y(a);
    else
        Ptmax(k)=max(Pt(:,15));
    end
end

```

```
Cp2(k)=2*Ptmax(k)*1000/(ro*R^2*pi*v(k)^3);

figure(2)
plot(w(:,k),Pt(:,k))
hold on
grid on
end

figure(3)
plot(v,Ptmax)
grid on
xlabel('Wind velocity, m/sec')
ylabel('Shaft power, kW')

figure(4)
plot(v,Cp2)
grid on
xlabel('Wind velocity, m/sec')
ylabel('Turbine power coefficient')
ylim([0 0.5])
```

A.3 MATLAB Program: Walney Off-shore Wind Farm Full-load Analysis

```

clc
clear all
format bank

%Off-shore substation transformer used 130MVA 10.5/121kV
Zt_sub=0.002+0.089j;
Rt_sub=0.002;
Xt_sub=0.089;
Rc_sub=1741.71;
Xm_sub=213.5;
a_sub=132/33;

%Tower transformer used 4.5MVA Siemens 0.69/33kV
Zt_tower=0.001+6.77e-3j;
Rt_tower=0.001;
Xt_tower=6.77e-3;
Rc_tower=128.68;
Xm_tower=10.62;
a_tower=33/0.69;

%3x150mm2 33kV cable
R_array=0.16*0.750;
X_array=0.116*0.75;
C_array=0.191e-6*0.750;
Yc_array=2*pi*50*C_array*1j;
Yc_half_array=Yc_array/2;

%3x500mm2 33kV cable
R_circuit=0.0515*0.458;
X_circuit=0.0974*0.458;
C_circuit=0.3e-6*0.458;
Yc2_circuit=2*pi*50*C_circuit*1j;
Yc2_half_circuit=Yc2_circuit/2;

%3x630mm2 132kV cable
R_sub_shore=0.028*44.4;
X_sub_shore=2*pi*50*0.37e-3*44.4;
C_sub_shore=0.21e-6*44.4;
Yc_sub_shore=2*pi*50*C_sub_shore*1j;
Yc3_half_sub_shore=Yc_sub_shore/2;

%System Calculations
Eff_IG1=0.97; %efficiency of IG is 97%
Eff_conv1_1=0.985; %efficiency of Converter 1 is 98.5%
Eff_conv2_1=0.985; %efficiency of Converter 2 is 98.5%

P_turbine1=3600; %turbine power in kW
Ploss_IG1=(1-Eff_IG1)*P_turbine1; %IG losses

```

```

P_IG1=P_turbine1-Ploss_IG1; %power at the output of IG
Ploss_conv1_1=(1-Eff_conv1_1)*P_IG1; %Converter 1 losses, Note: The
resistanc of the cable connecting the generator to the Converter 1 is
neglected
P_conv1_1=P_IG1-Ploss_conv1_1; %power at the output of Converter 1 in
the nacelle,
V_IG1_LL=690; %RMS line voltage at the input of the Converter 1 in the
nacelle
PF_IG1=0.95; % leading; power factor at the output of IG1 is leading
since IG receives reactive power
I_IG1=P_IG1*1e3/(sqrt(3)*V_IG1_LL*PF_IG1);
V_dc1_1=2*sqrt(2)/sqrt(3)*V_IG1_LL; %DC voltage at the output of the
Converter 1 in the nacelle
I_dc_1=P_conv1_1*1e3/V_dc1_1; % DC current throughout the entire length
of the DC-link is the same
J_dc_1=1; %Current density of DC cables in the tower DC-link that is
assumed nearly the same as AC cables
A_dc_1=I_dc_1/J_dc_1; % tower cable cross section area in mm2
R_dc_1=1.72e-8*83.5/(A_dc_1*1e-6); % Resistance of tower DC cable using
the copper resistivity of 1.72e-8, cable length=hub height=83.3m
R_tower1=R_dc_1; %Resistance of DC cable
Ploss_tower1=2*R_tower1*I_dc_1^2*1e-3; %factor 2 is because we have 2
cables in the DC-link
V_dc2_1=V_dc1_1-2*R_tower1*I_dc_1; %DC voltage at the input of the
Converter 2 at the bottom of the tower
V_conv2_1_LL=sqrt(3)/(2*sqrt(2))*V_dc2_1; %RMS line voltage at the
output of the Converter 2 and at the input of the tower transformer
V_conv2_1_ph=V_conv2_1_LL/sqrt(3); %RMS phase voltage at the output of
the Converter 2 and at the input of the tower transformer
Ploss_conv2_1= (1-Eff_conv2_1)*(P_conv1_1-Ploss_tower1); %Converter 2
losses
P_conv2_1=P_conv1_1-Ploss_tower1-Ploss_conv2_1; % power at the output of
the converter 2 and input of the tower transformer, Note: The resistans
of the cable connecting the Converter 2 to the tower transformer is
neglected
PF_conv2_1=1; %PF at the output of all the turbines' converter2 is
considered 1
I_prim1_1=(P_conv2_1*1e3/(sqrt(3)*V_conv2_1_LL*PF_conv2_1))*(PF_conv2_1-
sin(acos(PF_conv2_1))*1j); %Phase current in the primary of the
transformer before magnetizing branch; assumed lagging PF; Note: the
Converter2 controls the PF at the input of the transformer.
I_prim1_1_abs=abs(I_prim1_1);
I_prim1_1_phi=angle(I_prim1_1)*180/pi;
I_prim2_1=I_prim1_1-(1/Rc_tower+1/(Xm_tower*1j))*V_conv2_1_ph; %phase
current in the primary of the transformer after magnetizing branch
Ploss_T1=(3*abs(V_conv2_1_ph)^2/Rc_tower)*1e-
3+(3*Rt_tower*abs(I_prim2_1)^2)*1e-3; % transformer loss
I1=1/a_tower*I_prim2_1; % phase current in the secondary of the
transformer
I1_abs=abs(I1);
I1_angle=angle(I1)*180/pi;
V_prim2_1=V_conv2_1_ph-Zt_tower*I_prim2_1; %phase voltage in the primary
of transformer after the magnetizing branch

```

```

V1_ph=a_tower*V_prim2_1; %phase voltage in the secondary of transformer
in volts
V1_ph_abs=abs(V1_ph)*1e-3;
V1_ph_angle=angle(V1_ph)*180/pi;
V1_LL=sqrt(3)*abs(V1_ph)*1e-3; %Line voltage in the secondary of
transformer in kV
PF_1=cos(V1_ph_angle*pi/180-I1_angle*pi/180);
I12_1=I1; %phase current for the line pi model between two turbines
before the capacitor
I12_between=I1-Yc_half_array*V1_ph; %phase current for the line pi model
between two turbines between the capacitor
Ploss_12=3*R_array*abs(I12_between)^2*1e-3; % losses for the line
between the two turbines
V2_ph=V1_ph-(R_array+X_array*1j)*I12_between; %phase voltage at the
secondary of the transformer 2
V2_ph_abs=abs(V2_ph)*1e-3;
V2_ph_angle=angle(V2_ph)*180/pi;
V2_LL=sqrt(3)*abs(V2_ph)*1e-3; %line voltage at the secondary of the
transformer 2
I12_2=I12_between-Yc_half_array*V2_ph; %phase current for the line pi
model between two turbines after the capacitor
I12_2_abs=abs(I12_2);
I12_2_angle=angle(I12_2)*180/pi;
Ploss_12_2=Ploss_IG1+Ploss_conv1_1+Ploss_tower1+Ploss_conv2_1+Ploss_T1+P
loss_12; %total losses up to the point where turbine 2 is joint to the
line
P_12_2=P_turbine1-Ploss_12_2; %power input at the point where turbine 2
is joint to the line

Ploss_IG2=Ploss_IG1;
Ploss_conv1_2=Ploss_conv1_1;
Ploss_tower2=Ploss_tower1;
Ploss_conv2_2=Ploss_conv2_1;
P_turbine2=P_turbine1;
P_IG2=P_turbine2-Ploss_IG2;
V_prim2_2=V2_ph*1/a_tower;
P_conv2_2=P_conv2_1; %Power at the output of converter 2 is the same
for all turbines
PF_conv2_2=1; %Power factor at the input of the transformer is
considered 1 for all turbines i.e. Converter 2 fixes the power factor to
1
bb2=-V_prim2_2/(1+Zt_tower*(1/Rc_tower+1/(Xm_tower*1j)));
cc2=-
1/3*P_conv2_2*1e3*Zt_tower/(1+Zt_tower*(1/Rc_tower+1/(Xm_tower*1j)));
delta2=bb2^2-4*cc2;
V_conv2_2_ph=(-bb2+sqrt(delta2))/2;
V_conv2_2_LL=sqrt(3)*abs(V_conv2_2_ph);
V_conv2_2_ph_abs=abs(V_conv2_2_ph);
V_conv2_2_ph_angle=angle(V_conv2_2_ph)*180/pi;
V_dc2_2=2*sqrt(2)/sqrt(3)*V_conv2_2_LL;
I_dc2=I_dc1;
V_dc1_2=2*R_dc1*I_dc2+V_dc2_2;
V_IG2_LL=sqrt(3)/(2*sqrt(2))*V_dc1_2;

```

```

PF_IG2=0.95; % leading; power factor at the output of IG1 is leading
since IG receives reactive power
I_IG2=P_IG2*1e3/(sqrt(3)*V_IG2_LL*PF_IG2);
I_prim1_2=(P_conv2_2*1e3/(sqrt(3)*V_conv2_2_LL*PF_conv2_2))*(PF_conv2_2-
sin(acos(PF_conv2_2))*1j); %lagging PF considered
I_prim2_2=I_prim1_2-(1/Rc_tower+1/(Xm_tower*1j))*V_conv2_2_ph;
Ploss_T2=(3*abs(V_conv2_2_ph)^2/Rc_tower)*1e-
3+(3*Rt_tower*abs(I_prim2_2)^2)*1e-3;
I2=1/a_tower*I_prim2_2;
I2_abs=abs(I2);
I2_angle=angle(I2)*180/pi;
PF_2=cos(V2_ph_angle*pi/180-I2_angle*pi/180);
I23_1=I2+I12_2;
I23_between=I23_1-Yc_half_array*V2_ph;
Ploss_23=3*R_array*abs(I23_between)^2*1e-3;
V3_ph=V2_ph-(R_array+X_array*1j)*I23_between;
V3_ph_abs=abs(V3_ph)*1e-3;
V3_ph_angle=angle(V3_ph)*180/pi;
V3_LL=sqrt(3)*abs(V3_ph)*1e-3;
I23_2=I23_between-Yc_half_array*V3_ph;
Ploss_23_2=Ploss_12_2+Ploss_IG2+Ploss_conv1_2+Ploss_tower2+Ploss_conv2_2
+Ploss_T2+Ploss_23;
P_23_2=P_turbine1+P_turbine2-Ploss_23_2;

Ploss_IG3=Ploss_IG1;
Ploss_conv1_3=Ploss_conv1_1;
Ploss_tower3=Ploss_tower1;
Ploss_conv2_3=Ploss_conv2_1;
P_turbine3=P_turbine1;
P_IG3=P_turbine3-Ploss_IG3;
V_prim2_3=V3_ph*1/a_tower;
P_conv2_3=P_conv2_1;
PF_conv2_3=1;
bb3=-V_prim2_3/(1+Zt_tower*(1/Rc_tower+1/(Xm_tower*1j)));
cc3=-
1/3*P_conv2_3*1e3*Zt_tower/(1+Zt_tower*(1/Rc_tower+1/(Xm_tower*1j)));
delta3=bb3^2-4*cc3;
V_conv2_3_ph=(-bb3+sqrt(delta3))/2;
V_conv2_3_LL=sqrt(3)*abs(V_conv2_3_ph);
V_conv2_3_ph_abs=abs(V_conv2_3_ph);
V_conv2_3_ph_angle=angle(V_conv2_3_ph)*180/pi;
V_dc2_3=2*sqrt(2)/sqrt(3)*V_conv2_3_LL;
I_dc_3=I_dc_1;
V_dc1_3=2*R_dc_1*I_dc_3+V_dc2_3;
V_IG3_LL=sqrt(3)/(2*sqrt(2))*V_dc1_3;
PF_IG3=0.95; % leading; power factor at the output of IG1 is leading
since IG receives reactive power
I_IG3=P_IG3*1e3/(sqrt(3)*V_IG3_LL*PF_IG3);
I_prim1_3=(P_conv2_3*1e3/(sqrt(3)*V_conv2_3_LL*PF_conv2_3))*(PF_conv2_3-
sin(acos(PF_conv2_3))*1j); %lagging PF considered
I_prim2_3=I_prim1_3-(1/Rc_tower+1/(Xm_tower*1j))*V_conv2_3_ph;

```



```

Ploss_T3=(3*abs(V_conv2_3_ph)^2/Rc_tower)*1e-
3+(3*Rt_tower*abs(I_prim2_3)^2)*1e-3;
I3=1/a_tower*I_prim2_3;
I3_abs=abs(I3);
I3_angle=angle(I3)*180/pi;
PF_3=cos(V3_ph_angle*pi/180-I3_angle*pi/180);
I34_1=I3+I23_2;
I34_between=I34_1-Yc_half_array*V3_ph;
Ploss_34=3*R_array*abs(I34_between)^2*1e-3;
V4_ph=V3_ph-(R_array+X_array*1j)*I34_between;
V4_ph_abs=abs(V4_ph)*1e-3;
V4_ph_angle=angle(V4_ph)*180/pi;
V4_LL=sqrt(3)*abs(V4_ph)*1e-3;
I34_2=I34_between-Yc_half_array*V4_ph;
Ploss_34_2=Ploss_23_2+Ploss_IG3+Ploss_conv1_3+Ploss_tower3+Ploss_conv2_3
+Ploss_T3+Ploss_34;
P_34_2=P_turbine1+P_turbine2+P_turbine3-Ploss_34_2;

Ploss_IG4=Ploss_IG1;
Ploss_conv1_4=Ploss_conv1_1;
Ploss_tower4=Ploss_tower1;
Ploss_conv2_4=Ploss_conv2_1;
P_turbine4=P_turbine1;
P_IG4=P_turbine4-Ploss_IG4;
V_prim2_4=V4_ph*1/a_tower;
P_conv2_4=P_conv2_1;
PF_conv2_4=1;
bb4=-V_prim2_4/(1+Zt_tower*(1/Rc_tower+1/(Xm_tower*1j)));
cc4=-
1/3*P_conv2_4*1e3*Zt_tower/(1+Zt_tower*(1/Rc_tower+1/(Xm_tower*1j)));
delta4=bb4^2-4*cc4;
V_conv2_4_ph=(-bb4+sqrt(delta4))/2;
V_conv2_4_LL=sqrt(3)*abs(V_conv2_4_ph);
V_conv2_4_ph_abs=abs(V_conv2_4_ph);
V_conv2_4_ph_angle=angle(V_conv2_4_ph)*180/pi;
V_dc2_4=2*sqrt(2)/sqrt(3)*V_conv2_4_LL;
I_dc_4=I_dc_1;
V_dc1_4=2*R_dc_1*I_dc_4+V_dc2_4;
V_IG4_LL=sqrt(3)/(2*sqrt(2))*V_dc1_4;
PF_IG4=0.95; % leading; power factor at the output of IG1 is leading
since IG receives reactive power
I_IG4=P_IG2*1e3/(sqrt(3)*V_IG4_LL*PF_IG4);
I_prim1_4=(P_conv2_4*1e3/(sqrt(3)*V_conv2_4_LL*PF_conv2_4))*(PF_conv2_4-
sin acos(PF_conv2_4))*1j); %lagging PF considered
I_prim2_4=I_prim1_4-(1/Rc_tower+1/(Xm_tower*1j))*V_conv2_4_ph;
Ploss_T4=(3*abs(V_conv2_4_ph)^2/Rc_tower)*1e-
3+(3*Rt_tower*abs(I_prim2_4)^2)*1e-3;
I4=1/a_tower*I_prim2_4;
I4_abs=abs(I4);
I4_angle=angle(I4)*180/pi;
PF_4=cos(V4_ph_angle*pi/180-I4_angle*pi/180);
I45_1=I4+I34_2;
I45_between=I45_1-Yc_half_array*V4_ph;

```

```

Ploss_45=3*R_array*abs(I45_between)^2*1e-3;
V5_ph=V4_ph-(R_array+X_array*1j)*I45_between;
V5_ph_abs=abs(V5_ph)*1e-3;
V5_ph_angle=angle(V5_ph)*180/pi;
V5_LL=sqrt(3)*abs(V5_ph)*1e-3;
I45_2=I45_between-Yc_half_array*V5_ph;
Ploss_45_2=Ploss_34_2+Ploss_IG4+Ploss_conv1_4+Ploss_tower4+Ploss_conv2_4
+Ploss_T4+Ploss_45;
P_45_2=P_turbine1+P_turbine2+P_turbine3+P_turbine4-Ploss_45_2;

Ploss_IG5=Ploss_IG1;
Ploss_conv1_5=Ploss_conv1_1;
Ploss_tower5=Ploss_tower1;
Ploss_conv2_5=Ploss_conv2_1;
P_turbine5=P_turbine1;
P_IG5=P_turbine5-Ploss_IG5;
V_prim2_5=V5_ph*1/a_tower;
P_conv2_5=P_conv2_1;
PF_conv2_5=1;
bb5=-V_prim2_5/(1+Zt_tower*(1/Rc_tower+1/(Xm_tower*1j)));
cc5=-
1/3*P_conv2_5*1e3*Zt_tower/(1+Zt_tower*(1/Rc_tower+1/(Xm_tower*1j)));
delta5=bb5^2-4*cc5;
V_conv2_5_ph=(-bb5+sqrt(delta5))/2;
V_conv2_5_LL=sqrt(3)*abs(V_conv2_5_ph);
V_conv2_5_ph_abs=abs(V_conv2_5_ph);
V_conv2_5_ph_angle=angle(V_conv2_5_ph)*180/pi;
V_dc2_5=2*sqrt(2)/sqrt(3)*V_conv2_5_LL;
I_dc_5=I_dc_1;
V_dc1_5=2*R_dc_1*I_dc_5+V_dc2_5;
V_IG5_LL=sqrt(3)/(2*sqrt(2))*V_dc1_5;
PF_IG5=0.95; % leading; power factor at the output of IG1 is leading
since IG receives reactive power
I_IG5=P_IG2*1e3/(sqrt(3)*V_IG5_LL*PF_IG5);
I_prim1_5=(P_conv2_5*1e3/(sqrt(3)*V_conv2_5_LL*PF_conv2_5))*(PF_conv2_5-
sin(acos(PF_conv2_5))*1j); %lagging PF considered
I_prim2_5=I_prim1_5-(1/Rc_tower+1/(Xm_tower*1j))*V_conv2_5_ph;
Ploss_T5=(3*abs(V_conv2_5_ph)^2/Rc_tower)*1e-
3+(3*Rt_tower*abs(I_prim2_5)^2)*1e-3;
I5=1/a_tower*I_prim2_5;
I5_abs=abs(I5);
I5_angle=angle(I5)*180/pi;
PF_5=cos(V5_ph_angle*pi/180-I5_angle*pi/180);
I56_1=I5+I45_2;
I56_between=I56_1-Yc2_half_circuit*V5_ph;
Ploss_56=3*R_circuit*abs(I56_between)^2*1e-3;
V6_ph=V5_ph-(R_circuit+X_circuit*1j)*I56_between;
V6_ph_abs=abs(V6_ph)*1e-3;
V6_ph_angle=angle(V6_ph)*180/pi;
V6_LL=sqrt(3)*abs(V6_ph)*1e-3;
I56_2=I56_between-Yc2_half_circuit*V6_ph;
I56_2_abs=abs(I56_2);
I56_2_angle=angle(I56_2)*180/pi;

```

```

Ploss_56_2=Ploss_45_2+Ploss_IG5+Ploss_conv1_5+Ploss_tower5+Ploss_conv2_5
+Ploss_T5+Ploss_56;
P_56_2=P_turbine1+P_turbine2+P_turbine3+P_turbine4+P_turbine5-
Ploss_56_2;

PF_6=cos(V6_ph_angle*pi/180-I56_2_angle*pi/180); % this is the PF for
circuit 2 at the point of connection to off-shore sub.; it is assumed
other circuits connect to off-shore sub. with the same PF

P_C2=P_56_2;
P_C1=6/5*P_C2; % It is assumed that the power is shared between circuits
with respect to number of turbines
P_C3=10/5*P_C2;
P_C4=10/5*P_C2;
P_C5=10/5*P_C2;
P_C6=10/5*P_C2;

Ploss_C2=Ploss_56_2; % It is assumed that the loss is shared between
circuits with respect to number of turbines
Ploss_C1=6/5*Ploss_56_2;
Ploss_C3=10/5*Ploss_56_2;
Ploss_C4=10/5*Ploss_56_2;
Ploss_C5=10/5*Ploss_56_2;
Ploss_C6=10/5*Ploss_56_2;

P_C1_C2_C3_C4_C5_C6=P_C1+P_C2+P_C3+P_C4+P_C5+P_C6;
Ploss_C1_C2_C3_C4_C5_C6=Ploss_C1+Ploss_C2+Ploss_C3+Ploss_C4+Ploss_C5+Plo
ss_C6;

P_C1_C3_C4_C5_C6=P_C1+P_C3+P_C4+P_C5+P_C6;
Ploss_C1_C3_C4_C5_C6=Ploss_C1+Ploss_C3+Ploss_C4+Ploss_C5+Ploss_C6;

I_sub_input=P_C1_C2_C3_C4_C5_C6/(sqrt(3)*V6_LL*PF_6)*(PF_6-
sin(acos(PF_6))*1j); % The same power factor for all circuits is
assumed

I_Tsub_parallel_branch=(1/Rc_sub+1/(Xm_sub*1j))*V6_ph; % there are 2
transformers in the sub.
I_Tsub_series=I_sub_input/2-I_Tsub_parallel_branch;
Ploss_Tsub=(3*2*abs(V6_ph)^2/Rc_sub)*1e-
3+(3*2*Rt_sub*abs(I_Tsub_series)^2)*1e-3;
V7_prim2=V6_ph-Zt_sub*I_Tsub_series;
V7_ph=V7_prim2*a_sub;
V7_ph_abs=abs(V7_ph)*1e-3;
V7_ph_angle=angle(V7_ph)*180/pi;
V7_LL=sqrt(3)*abs(V7_ph)*1e-3;

I78_1=2*I_Tsub_series*1/a_sub;
I78_1_abs=abs(I78_1);
I78_1_angle=angle(I78_1)*180/pi;
PF_7=cos(V7_ph_angle*pi/180-I78_1_angle*pi/180);

```

```
I78_between=I78_1-Yc3_half_sub_shore*V7_ph;  
V8_ph=V7_ph-(R_sub_shore+X_sub_shore*1j)*I78_between;  
V8_ph_abs=abs(V8_ph)*1e-3;  
V8_ph_angle=angle(V8_ph)*180/pi;  
V8_LL=sqrt(3)*abs(V8_ph)*1e-3;  
I78_2=I78_between-Yc3_half_sub_shore*V8_ph;  
I8=I78_2;  
I8_abs=abs(I8);  
I8_angle=angle(I8)*180/pi;  
  
PF_8=cos(V8_ph_angle*pi/180-I8_angle*pi/180);  
  
Ploss_78=3*R_sub_shore*abs(I78_between)^2*1e-3;  
Ploss_8=Ploss_C1_C2_C3_C4_C5_C6+Ploss_Tsub+Ploss_78;  
P8=sqrt(3)*V8_LL*I8_abs*PF_8;  
Eff_8=P8/(51*P_turbine1)*100;
```

A.4 MATLAB Program: Proposed Wind Generation Scheme Full-load Analysis

```

clc
clear all
format bank
% format shortg

R_tower=0.13/2;
R_array=0.3/2;
R_circuit=0.055/2;
R_sub_shore=4.2/2;

V1_ph=66/sqrt(3)*1e3; % Generator RMS phase voltage, RMS Line-to-Line
for 3-phase is 66 kV
V1_ph_peak=sqrt(2)*V1_ph; % Generator peak phase voltage
m=9; % number of phases for Hybrid generator
Vdc1=V1_ph_peak*2*m*sin(pi/m)/pi; % DC voltage at the output of
rectifier

Eff_HG1=0.97;
Eff_rect1=0.995;
Eff_sub=0.985;

P_turbine1=3600;
Ploss_HG1=(1-Eff_HG1)*P_turbine1;
P_HG1=P_turbine1-Ploss_HG1;
Ploss_rect1=(1-Eff_rect1)*P_HG1;
P_rect1=P_HG1-Ploss_rect1;
I1=P_rect1*1e3/Vdc1;
Ploss_tower1=2*R_tower*I1^2*1e-3;
Ploss_12=2*R_array*I1^2*1e-3;
Ploss_12_2=Ploss_HG1+Ploss_rect1+Ploss_tower1+Ploss_12;
P12_2=P_turbine1-Ploss_12_2;
V1=Vdc1-2*R_tower*I1;

P_turbine2=P_turbine1;
Ploss_HG2=Ploss_HG1;
Ploss_rect2=Ploss_rect1;
V2=V1-2*R_array*I1;
P_rect2=P_rect1;
bb2=-V2;
cc2=-2*R_tower*P_rect2;
delta2=bb2^2-4*cc2;
Vdc2=(-bb2+sqrt(delta2))/2;
V2_ph=pi/(2*m*sin(pi/m))*Vdc2/sqrt(2);
I2=P_rect2*1e3/Vdc2;
I23=I1+I2;
Ploss_tower2=2*R_tower*I2^2*1e-3;

```

```

Ploss_23=2*R_array*I23^2*1e-3;
Ploss_23_2=Ploss_12_2+Ploss_HG2+Ploss_rect2+Ploss_tower2+Ploss_23;
P23_2=P_turbine1+P_turbine2-Ploss_23_2;

```

```

P_turbine3=P_turbine1;
Ploss_HG3=Ploss_HG1;
Ploss_rect3=Ploss_rect1;
V3=V2-2*R_array*I23;
P_rect3=P_rect1;
bb3=-V3;
cc3=-2*R_tower*P_rect3;
delta3=bb3^2-4*cc3;
Vdc3=(-bb3+sqrt(delta3))/2;
V3_ph=pi/(2*m*sin(pi/m))*Vdc3/sqrt(2);
I3=P_rect3*1e3/Vdc3;
I34=I3+I23;
Ploss_tower3=2*R_tower*I3^2*1e-3;
Ploss_34=2*R_array*I34^2*1e-3;
Ploss_34_2=Ploss_23_2+Ploss_HG3+Ploss_rect3+Ploss_tower3+Ploss_34;
P34_2=P_turbine1+P_turbine2+P_turbine3-Ploss_34_2;

```

```

P_turbine4=P_turbine1;
Ploss_HG4=Ploss_HG1;
Ploss_rect4=Ploss_rect1;
V4=V3-2*R_array*I34;
P_rect4=P_rect1;
bb4=-V4;
cc4=-2*R_tower*P_rect4;
delta4=bb4^2-4*cc4;
Vdc4=(-bb4+sqrt(delta4))/2;
V4_ph=pi/(2*m*sin(pi/m))*Vdc4/sqrt(2);
I4=P_rect4*1e3/Vdc4;
I45=I4+I34;
Ploss_tower4=2*R_tower*I4^2*1e-3;
Ploss_45=2*R_array*I45^2*1e-3;
Ploss_45_2=Ploss_34_2+Ploss_HG4+Ploss_rect4+Ploss_tower4+Ploss_45;
P45_2=P_turbine1+P_turbine2+P_turbine3+P_turbine4-Ploss_45_2;

```

```

P_turbine5=P_turbine1;
Ploss_HG5=Ploss_HG1;
Ploss_rect5=Ploss_rect1;
V4=V3-2*R_array*I34;
V5=V4-2*R_array*I45;
P_rect5=P_rect1;
bb5=-V4;
cc5=-2*R_tower*P_rect5;
delta5=bb5^2-4*cc5;
Vdc5=(-bb5+sqrt(delta5))/2;
V5_ph=pi/(2*m*sin(pi/m))*Vdc5/sqrt(2);
I5=P_rect5*1e3/Vdc5;
I56=I5+I45;
Ploss_tower5=2*R_tower*I5^2*1e-3;
Ploss_56=2*R_circuit*I56^2*1e-3;

```

```

Ploss_56_2=Ploss_45_2+Ploss_HG5+Ploss_rect5+Ploss_tower5+Ploss_56;
P56_2=P_turbine1+P_turbine2+P_turbine3+P_turbine4+P_turbine5-Ploss_56_2;
V6=V5-2*R_circuit*I56;

P_C2=P56_2;
P_C1=6/5*P_C2;
P_C3=2*P_C2;
P_C4=2*P_C2;
P_C5=2*P_C2;
P_C6=2*P_C2;

Ploss_C2=Ploss_56_2;
Ploss_C1=6/5*Ploss_C2;
Ploss_C3=2*Ploss_C2;
Ploss_C4=2*Ploss_C2;
Ploss_C5=2*Ploss_C2;
Ploss_C6=2*Ploss_C2;

P_C1_C3_C4_C5_C6=P_C1+P_C3+P_C4+P_C5+P_C6;
Ploss_C1_C3_C4_C5_C6=Ploss_C1+Ploss_C3+Ploss_C4+Ploss_C5+Ploss_C6;

P_C1_C2_C3_C4_C5_C6=P_C1+P_C2+P_C3+P_C4+P_C5+P_C6;
Ploss_C1_C2_C3_C4_C5_C6=Ploss_C1+Ploss_C2+Ploss_C3+Ploss_C4+Ploss_C5+Ploss_C6;

Ploss_sub=(1-Eff_sub)*P_C1_C2_C3_C4_C5_C6;

P_sub_output=P_C1_C2_C3_C4_C5_C6-Ploss_sub;
Ploss_sub_output=Ploss_C1_C2_C3_C4_C5_C6+Ploss_sub;

V7=4*V6; %Step-up ratio of 4 is cosen for DC/DC converter. The sam as
walney sub 33/132=4
I78=P_sub_output*1e3/V7;
V8=V7-2*R_sub_shore*I78;
I8=I78;
Ploss_78=2*R_sub_shore*I78^2*1e-3;
P8=P_sub_output-Ploss_78;
Ploss_8=Ploss_sub_output+Ploss_78;
Eff_8=P8/(51*P_turbine1)*100;

```

A.5 Example of FEA Torque Analysis Coupled with MATLAB Program

%Note: to be able to run this code, all the parts of rotor must be indentified by group '1000' from properties of selected block

```

clc
clear all

addpath('C:\femm42\mfiles');
openfemm;

opendocument('OB_HG_Surface_N35H_9ph_40mm.fem');
mi_saveas('OB_HG_Surface_N35H_9ph_40mm_temp.FEM');

A_amp=0; % 12 turns per each top or bottom layaer
B_amp=0;
C_amp=0;
D_amp=0;
E_amp=0;
F_amp=0;
G_amp=0;
H_amp=0;
I_amp=0;

mi_setcurrent('A+',A_amp)
mi_setcurrent('A-',-A_amp)
mi_setcurrent('B+',B_amp)
mi_setcurrent('B-',-B_amp)
mi_setcurrent('C+',C_amp)
mi_setcurrent('C-',-C_amp)
mi_setcurrent('D+',D_amp)
mi_setcurrent('D-',-D_amp)
mi_setcurrent('E+',E_amp)
mi_setcurrent('E-',-E_amp)
mi_setcurrent('F+',F_amp)
mi_setcurrent('F-',-F_amp)
mi_setcurrent('G+',G_amp)
mi_setcurrent('G-',-G_amp)
mi_setcurrent('H+',H_amp)
mi_setcurrent('H-',-H_amp)
mi_setcurrent('I+',I_amp)
mi_setcurrent('I-',-I_amp)

n=26; % original n=26, step=3; you can put n=10 and the step=8 to
reduce the time of simulation but less accuracy
step=3; % one electrical cycle is 72 degrees mechanical.
theta(1)=0;

for k=1:n

```



```
k
mi_analyze;
mi_loadsolution;

T_A_pos=mo_getcircuitproperties('A+');
T_A_neg=mo_getcircuitproperties('A-');
T_A=T_A_pos-T_A_neg;
Flux_A(k)=T_A(3);

T_B_pos=mo_getcircuitproperties('B+');
T_B_neg=mo_getcircuitproperties('B-');
T_B=T_B_pos-T_B_neg;
Flux_B(k)=T_B(3);

T_C_pos=mo_getcircuitproperties('C+');
T_C_neg=mo_getcircuitproperties('C-');
T_C=T_C_pos-T_C_neg;
Flux_C(k)=T_C(3);

T_D_pos=mo_getcircuitproperties('D+');
T_D_neg=mo_getcircuitproperties('D-');
T_D=T_D_pos-T_D_neg;
Flux_D(k)=T_D(3);

T_E_pos=mo_getcircuitproperties('E+');
T_E_neg=mo_getcircuitproperties('E-');
T_E=T_E_pos-T_E_neg;
Flux_E(k)=T_E(3);

T_F_pos=mo_getcircuitproperties('F+');
T_F_neg=mo_getcircuitproperties('F-');
T_F=T_F_pos-T_F_neg;
Flux_F(k)=T_F(3);

T_G_pos=mo_getcircuitproperties('G+');
T_G_neg=mo_getcircuitproperties('G-');
T_G=T_G_pos-T_G_neg;
Flux_G(k)=T_G(3);

T_H_pos=mo_getcircuitproperties('H+');
T_H_neg=mo_getcircuitproperties('H-');
T_H=T_H_pos-T_H_neg;
Flux_H(k)=T_H(3);

T_I_pos=mo_getcircuitproperties('I+');
T_I_neg=mo_getcircuitproperties('I-');
T_I=T_I_pos-T_I_neg;
Flux_I(k)=T_I(3);
```

```
mo_selectpoint (1071.5, 0)
mo_selectpoint (1065.5, 112)
mo_selectpoint (1048, 222.8)
mo_selectpoint (1019, 331)
mo_selectpoint (979, 435.7)
mo_selectpoint (928.1, 535.7)
mo_selectpoint (866.86, 629.81)
mo_selectpoint (796.2, 717)
mo_selectpoint (717.2, 796.2)
mo_selectpoint (629.8, 866.7)
mo_selectpoint (536, 927.8)
mo_selectpoint (435.6, 978.8)
mo_selectpoint (331.2, 1019)
mo_selectpoint (222.8, 1048)
mo_selectpoint (112, 1065.5)
mo_selectpoint (0, 1071.5)

mo_selectpoint (-112, 1065.5)
mo_selectpoint (-222.8, 1048)
mo_selectpoint (-331.2, 1019)
mo_selectpoint (-435.6, 978.8)
mo_selectpoint (-536, 927.8)
mo_selectpoint (-629.8, 866.7)
mo_selectpoint (-717.2, 796.2)
mo_selectpoint (-796.2, 717)
mo_selectpoint (-866.86, 629.81)
mo_selectpoint (-928.1, 535.7)
mo_selectpoint (-979, 435.7)
mo_selectpoint (-1019, 331)
mo_selectpoint (-1048, 222.8)
mo_selectpoint (-1065.5, 112)
mo_selectpoint (-1071.5, 0)

mo_selectpoint (-1065.5, -112)
mo_selectpoint (-1048, -222.8)
mo_selectpoint (-1019, -331)
mo_selectpoint (-979, -435.7)
mo_selectpoint (-928.1, -535.7)
mo_selectpoint (-866.86, -629.81)
mo_selectpoint (-796.2, -717)
mo_selectpoint (-717.2, -796.2)
mo_selectpoint (-629.8, -866.7)
mo_selectpoint (-536, -927.8)
mo_selectpoint (-435.6, -978.8)
mo_selectpoint (-331.2, -1019)
mo_selectpoint (-222.8, -1048)
mo_selectpoint (-112, -1065.5)
mo_selectpoint (0, -1071.5)

mo_selectpoint (112, -1065.5)
mo_selectpoint (222.8, -1048)
mo_selectpoint (331.2, -1019)
mo_selectpoint (435.6, -978.8)
```

```
mo_selectpoint(536,-927.8)
mo_selectpoint(629.8,-866.7)
mo_selectpoint(717.2,-796.2)
mo_selectpoint(796.2,-717)
mo_selectpoint(866.86,-629.81)
mo_selectpoint(928.1,-535.7)
mo_selectpoint(979,-435.7)
mo_selectpoint(1019,-331)
mo_selectpoint(1048,-222.8)
mo_selectpoint(1065.5,-112)
mo_selectpoint(1071.5,0)

Airgap_arc=mo_lineintegral(4);
Torque(k)=Airgap_arc(1);

mi_clearselected();
mo_clearcontour;

Flux_print=[theta', Flux_A', Flux_B', Flux_C', Flux_D', Flux_E',
Flux_F', Flux_G', Flux_H', Flux_I', Torque'];
xlswrite('Surface_PM_From_Matlab.xlsx', Flux_print,1);

mi_seteditmode('group');
mi_selectgroup(1000);
mi_moverotate(0,0,step);
theta(k+1)=theta(k)+step;

end

closefemm;
```